Modèle d'ordre réduit de structures non-linéaires pour l'aéroélasticité des turbomachines

Théo Flament

▶ To cite this version:

Théo Flament. Modèle d'ordre réduit de structures non-linéaires pour l'aéroélasticité des turbomachines. Mécanique [physics]. HESAM Université, 2023. Français. NNT : 2023HESAC038 . tel-04590957

HAL Id: tel-04590957
https://theses.hal.science/tel-04590957v1

Submitted on 28 May 2024

ÉCOLE DOCTORALE Sciences des Métiers de l'Ingénieur
Laboratoire de Mécanique des Structures et des Systèmes Couplés

THÈSE

présentée par : **Théo FLAMENT**
soutenue le : **19 décembre 2023**

pour obtenir le grade de : **Docteur d'HESAM Université**

préparée au : **Conservatoire national des arts et métiers**
Discipline : **Génie Mécanique, Génie Civil**
Spécialité : **Mécanique**

Reduced order model of nonlinear structures for turbomachinery aeroelasticity

THÈSE dirigée par :
DEÜ Jean-François Professeur, Cnam

et co-encadrée par :
PLACZEK Antoine Ingénieur de Recherche, ONERA
BALMASEDA Mikel Ingénieur de Recherche, ONERA
TRAN Duc-Minh Ingénieur de Recherche HDR, ONERA

Jury

C. TOUZÉ	Professeur, ENSTA Paris	Président
E. CAPIEZ-LERNOUT	MCF HDR, Université Gustave Eiffel	Rapporteur
F. THOUVEREZ	Professeur, École Centrale de Lyon	Rapporteur
F. NYSSEN	Senior Research Engineer, Cenaero	Examinateur
M. MIGNOLET	Professeur, Arizona State University	Examinateur
J.-F. DEÜ	Professeur, Cnam	Examinateur
A. PLACZEK	Ingénieur de recherche, ONERA	Examinateur
M. BALMASEDA	Ingénieur de recherche, ONERA	Examinateur

T
H
È
S
E

à mes proches ...

Remerciements

Je tiens avant tout à remercier l'ensemble des membres du jury d'avoir accepté d'évaluer ce travail de thèse. Merci à Cyril Touzé d'en avoir assumé la présidence. Merci à Evangéline Capiez-Lernout et Fabrice Thouverez d'avoir accepté la lourde tâche de rapporteur pendant une période de l'année très chargée.

J'adresse de sincères remerciements à ceux sans qui cette thèse n'aurait pas été possible. Je remercie mon directeur de thèse Jean-François Deü pour son accompagnement toujours bienveillant tout au long de ces trois années. Il s'est montré très disponible et je savais pouvoir compter sur lui. Je remercie mes encadrants de l'ONERA Antoine Placzek, Mikel Balmaseda et Duc-Minh Tran pour leur aide précieuse et leurs conseils avisés. Je souhaite un tel encadrement à tout doctorant.

Je tiens également à exprimer ma gratitude aux différents chercheurs que j'ai eu la chance de rencontrer en congrès pour les échanges passionnants que nous avons eu et qui m'ont permis d'améliorer mon travail.

Je souhaite dire un grand merci à mes collègues de l'unité MSAE pour les bon moments passés ensembles, pour les discussions sur des sujets improbables en pauses café et les centaines de viennoiseries accumulées dans mon organisme. Je voudrais remercier les coéquipiers du volley qui m'ont permis de poursuivre ce sport formidable et à qui je souhaite de gagner le tournoi cette année, ainsi que les camarades de boxe pour m'avoir remis les idées en place entre deux calculs.

J'adresse mes profonds remerciements à ma famille. A mes parents pour leur soutien et aide sans faille tout au long de mon parcours. Merci à toi Camille, ma grande soeur, pour avoir affronté les obstacles de la vie avant moi et les conseils précieux que tu as. Merci Claire-Alice pour me rappeler régulièrement toutes ces références humoristiques que nous avons en commun et que nous sommes parfois bien seuls à comprendre. Je remercie de tout mon coeur ma femme Veronika pour m'avoir suivi dans cette aventure. Tu partages mon quotidien depuis bien des années déjà et me pousse à donner le meilleur de moi-même. Je te remercie pour ta patience et tes attentions particulières qui remplissent mon quotidien de bonheur.

Résumé

Ce travail concerne le développement d'un modèle d'ordre réduit non-intrusif de structures non-linéaires géométriques, en vue de remplacer le solveur non-linéaire structure dans le cadre d'un couplage partitionné pour la résolution numérique de problèmes d'interaction fluide-structure et en particulier la prédiction des phénomènes d'aéroélasticité rencontrés au sein des turbomachines. La formulation proposée pour construire ce modèle réduit est basée sur la projection des équations sur une base de dimension réduite, contenant à la fois des modes linéaires de la structure ainsi que des modes duaux. Ces derniers ont pour but d'enrichir la base de modes propres afin de capturer les comportements non-linéaires. Une méthode originale de calcul des coefficients des efforts non-linéaires projetés dans cette base est également proposée. Des efforts sont imposés à la structure contrairement aux déplacements imposés habituellement utilisés. Ainsi, les mêmes cas de chargement peuvent être utilisés à la fois pour la détermination des modes duaux et pour celle des coefficients des efforts non-linéaires projetés. Dans ce manuscrit, la méthodologie de construction du modèle réduit est détaillée. Elle est validée dans un premier temps sur un cas simple de poutre non-linéaire d'Euler-Bernoulli soumise à différents cas de chargement, y compris dans le cadre d'un couplage fluide-structure partitionné impliquant des vibrations induites par des vortex. La capacité de ce modèle réduit à remplacer un solveur éléments finis non linéaire y est démontrée. Une validation sur des cas d'application 3D est également proposée, dont le cas complexe d'une aube de soufflante d'un moteur réaliste soumise à un chargement aérodynamique instationnaire.

Mots clés : Dynamique des structures, vibrations, non-linéarités géométriques, réduction de modèle, interaction fluide-structure, aéroélasticité.

Abstract

This work concerns the development of a reduced order model for geometric nonlinear structures, to replace the nonlinear structure solver within the framework of partitioned coupling for the numerical resolution of fluid-structure interaction problems, and thus the prediction of aeroelasticity phenomena encountered in turbomachinery. The construction of the reduced order model is based on a projection of the equations into a basis of reduced dimension, containing both linear modes of the structure and dual modes. The purpose of the latter is to enhance the basis of linear normal modes in order to capture the non-linearity. An original method for calculating the coefficients of the non-linear forces projected into this basis is also proposed. Forces are imposed on the structure, as opposed to the usual approach of imposed displacements. The same loading cases can thus be used to determine both the dual modes and the coefficients of the projected non-linear forces. In this thesis, the methodology to build the reduced order model is detailed. It is first validated on a simple case of a nonlinear Euler-Bernoulli beam subjected to different loading conditions, including a partitioned fluid-structure coupling involving vortex-induced vibrations. The ability of this reduced order model to replace a nonlinear finite element solver is demonstrated in this last application. Validation on 3D cases is also proposed, including the complex geometry of a realistic engine fan blade subjected to unsteady aerodynamic loading.

Keywords : Structural dynamics, vibrations, geometric nonlinearity, reduced order model, fluid-structure interaction, aeroelasticity.

Contents

List of Figures

List of Tables

List of Acronyms and Symbols

Acronyms

CFD	Computational Fluid Dynamics
CSM	Computational Structural Mechanics
FE	Finite Element
IC	Implicit Condensation
ICE	Implicit Condensation and Expansion
ICDual	Reduced order model using dual modes along with the Implicit Condensation
dofs	Degrees of freedom
SVD	Singular Value Decomposition
ROM	Reduced Order Model
FOM	Full Order Model
FSI	Fluid-structure interaction
UHBR	Ultra High Bypass Ratio

Symbols

$\boldsymbol{\nabla}_{\boldsymbol{x}}, \boldsymbol{\nabla}_{\boldsymbol{X}}$	Gradients with respect to the current and reference configurations of the solid respectively
$\mathbf{I}$	Identity matrix
$\boldsymbol{n}$	Normal vector pointing outwards the volume
α_{HHT}	Coefficient of the HHT-α temporal integration method
$\mathcal{R}_{\mathrm{g}}$	Inertial frame
$\mathcal{R}_{\mathrm{m}}$	Moving frame
$\mathbf{R}$	Rotation matrix between the inertial and moving frames
$\boldsymbol{\omega}$	Rotation vector of the frame $\mathcal{R}_{\mathrm{m}}$
$\boldsymbol{\Omega}$	Matrix of the rotation given by the vector $\boldsymbol{\omega}$
$\boldsymbol{X}$	Position vector in the reference undeformed configuration
$\boldsymbol{x}$	Position vector with respect to the current frame
$\hat{\boldsymbol{y}}$	Position vector with respect to the inertial frame

$\ddot{\boldsymbol{y}}$	Acceleration vector with respect to the inertial frame
$\boldsymbol{u}$	Displacement vector
$\hat{\boldsymbol{s}}$	Translation between the inertial frame and the moving frame
$\boldsymbol{\sigma}$	Local stress tensor in the current configuration
$\boldsymbol{\varepsilon}$	Local strain tensor in the current configuration
$\boldsymbol{F}$	Deformation gradient
$\boldsymbol{E}$	Green lagrange strain tensor
$\boldsymbol{\Pi}$	Boussinesq stress tensor (first Piola-Kirchhoff stress tensor)
$\boldsymbol{S}$	Second Piola-Kirchhoff stress tensor
$\boldsymbol{\mathcal{H}}$	Elasticity fourth order tensor in Hooke's law
$\boldsymbol{b_v}$	Vector of the local volumic forces
$\boldsymbol{t}$	Vector of the local surface forces
Ω_0	Reference volume of the solid
$\Omega(t)$	Current volume of the solid
$\partial\Omega$	Total surface of the solid
Γ_0	Reference surface of the solid where the Neumann conditions are applied
S^d	Solid border where the Dirichlet boundary conditions are applied
Γ	Solid border where the Neumann boundary conditions are applied
Ω_S	Structural domain
$S_F(t)$	Surface of a fluid control volume
Ω_F	Fluid domain
δW_{int}	Virtual work of the internal forces
δW_{ext}	Virtual work of the external forces
δW_{acc}	Virtual work associated to the acceleration
$\boldsymbol{\delta u}$	Virtual displacement
$\boldsymbol{\delta}\mathbf{u}$	Discretized virtual displacement
$\mathbf{N}$	Shape functions
$\mathbf{N}_{\text{u}}, \mathbf{N}_{\text{v}}$	Shape functions for the beam problem
N	Number of degrees of freedom of the system
$\mathbf{u}, \dot{\mathbf{u}}, \ddot{\mathbf{u}}$	Displacement, velocity, acceleration of the degrees of freedom

$\mathbf{u_t}$	Total displacement $\mathbf{u_s} + \mathbf{u}$
$\mathbf{u_s}$	Prestressed displacement of the structure under centrifugal forces
$\mathbf{K_{mat}}, \mathbf{M}, \mathbf{C}$	Elastic stiffness, mass and viscous damping matrices
$\mathbf{K}$	Total stiffness matrix of the structure
$\mathbf{K_{tan}}(\mathbf{u})$	Total tangent stiffness matrix evaluated at the displacement $\mathbf{u}$
$\mathbf{K}_{\mathrm{e}}, \mathbf{M}_{\mathrm{e}}$	Elementary stiffness and mass matrices
$\mathbf{K}_{\mathrm{c}}^{e}$	Elementary centrifugal softening matrix
$\mathbf{f}_{\omega}^{e}$	Elementary vector of centrifugal forces
$\mathbf{D_g}$	Gyroscopic coupling matrix
$\mathbf{K_a}$	Centrifugal acceleration matrix
$\mathbf{K_c}$	Centrifugal softening stiffness matrix
$\mathbf{K_{nl}}(\mathbf{u})$	Tangent stiffness matrix of the purely nonlinear forces evaluated at the position $\mathbf{u}$
ξ	Damping coefficient: $\mathbf{C} = 2\xi\omega_0\mathbf{M}$
$\mathbf{f_{int}}$	Internal forces
$\mathbf{f_{nl}}$	Purely nonlinear components of the internal geometrical forces for all the degrees of freedom
$\mathbf{f}_{\mathrm{nl}}^{\mathrm{quad}}, \mathbf{f}_{\mathrm{nl}}^{\mathrm{cub}}$	Quadratic and cubic components of $\mathbf{f_{nl}}$
$\mathbf{g_{nl}}$	Purely nonlinear component of the internal geometrical forces of the centrifugally prestressed structure.
$\mathrm{f}_{\mathrm{nl}}^{\;k}$	Projection of $\mathbf{f_{nl}}$ on the k^{th} linear modes
$\mathrm{g}_{\mathrm{nl}}^{\;k}$	Projection of $\mathbf{g_{nl}}$ on the k^{th} linear modes
$\mathbf{f}_{\mathrm{ext}}$	External forces applied to the structure at the degrees of freedom
$\mathbf{f}_{\mathrm{a}}$	Aerodynamic forces
$\mathbf{f_v}$	Discretized vector of the volumic forces on all the degrees of freedom
$\mathbf{f_c}$	Discretized vector of the surface forces on all the degrees of freedom
$\mathbf{f}_{\boldsymbol{\omega}}$	Discretized vector of the centrifugal forces
$\mathbf{V}$	Reduction basis
$\mathbf{q}, \dot{\mathbf{q}}, \ddot{\mathbf{q}}$	Generalized coordinates/velocities/accelerations
$\widetilde{\mathbf{K}}, \widetilde{\mathbf{M}}, \widetilde{\mathbf{C}}$	Reduced stiffness, mass and damping matrices
$\widetilde{\mathbf{f}}_{\mathrm{a}}$	Generalized aerodynamic forces
$\widetilde{\mathbf{f}}_{\mathbf{nl}}, \widetilde{\mathbf{g}}_{\mathbf{nl}}$	Projected nonlinear forces with respect to the total $\mathbf{u_t}$ and relative $\mathbf{u}$ displacements

$\widetilde{f}_{\text{nl}}^{k}$	k^{th} component of the vector $\widetilde{\mathbf{f}}_{\mathbf{nl}}$
$\widetilde{g}_{\text{nl}}^{k}$	k^{th} component of the vector $\widetilde{\mathbf{g}}_{\mathbf{nl}}$
$\boldsymbol{\Phi}$	Basis of linear normal modes
$\boldsymbol{\phi}_i$	i^{th} linear normal mode in the basis $\boldsymbol{\Phi}$
ω_i	Pulsation of the i^{th} linear normal mode
n_{b}	Number of linear normal modes in the reduction basis
n	Number of modes in the reduction basis
n_{L}	Number of load cases for the construction of the ROM
$\mathbf{f}_{\text{ext}}^{(\ell)}$	External static forces applied to the structure for the construction of the ICE and ICDual models
$\boldsymbol{\psi}$	Reconstruction modes for the *Expansion* step of the ICE method
$\boldsymbol{\Psi}$	Basis of the ICE reconstruction modes
n_{m}	Number of ICE reconstruction modes
$\boldsymbol{\eta}$	Generalized coordinates associated to $\boldsymbol{\Psi}$
n_{p}	Number of SVD modes kept
$\mathbf{d}_i$	i^{th} mode resulting from the SVD
E_i	Linearized strain energy contribution of the SVD mode i
$\mathcal{E}_r$	Sum of the linearized strain energies E_i
$\boldsymbol{\Phi}_{\text{dual}}$	Basis of the dual modes only
$\boldsymbol{\theta}$	Basis of modal derivatives only
$\boldsymbol{\theta}_{ij}$	Modal derivative of the mode $\boldsymbol{\phi}_i$ with respect to the mode $\boldsymbol{\phi}_j$
p	Fluid pressure
$\boldsymbol{v}$	Fluid velocity
R_{specific}	Universal gas constant
$\boldsymbol{\tau}$	Viscous stress tensor
$\boldsymbol{q}$	Heat flux
$\boldsymbol{W}$	Fluid conservative variables
$\boldsymbol{\mathcal{F}}$	Flux of the conservative variables
$\hat{\boldsymbol{v}}$	Mesh velocity
$\boldsymbol{\xi}$	Mesh deformation degrees of freedom

Introduction

Context

The proven impact of human activity on global warming and the need to preserve the environment means reducing greenhouse gas emissions. With an average of 100,000 flights a day worldwide, the air transport sector is particularly concerned, and projects to reduce greenhouse gas emissions are underway. For example, the European Clean Sky project, renewed in 2014 as Clean Sky 2 [28], is an integral part of the European Commission's Horizon 2020 Research and Innovation Program, which aims to develop greener air transport technologies by improving engine efficiency and reducing CO2 emissions. These programs are continuing in Clean Aviation, particularly at the European level. The aim is to accelerate technological progress in the aviation sector to make the European aeronautics industry more competitive and environmentally friendly, through the development of disruptive technologies to replace the current fleet of aircraft and achieve the European Commission's Flightpath 2050 goals [48] set by ACARE (Advisory Council for Aeronautics Research in Europe). These goals include a 75% reduction in CO2 emissions per passenger kilometer, and a 90% reduction in nitrogen oxide (NOx) emissions.

As part of their drive to reduce engine fuel consumption, aerospace manufacturers are seeking to increase engine bypass ratios (the ratio between primary and secondary flows) by increasing the secondary flow, thereby boosting thrust and improving efficiency. This means increasing the size of the blades or propellers. Figure 1 illustrates an Ultra High Bypass Ratio (UHBR) jet engine, a ducted engine with an expected bypass ratio of 15:1. It means that for every volume of air passing through the combustion chamber (the primary flow), 15 volumes of air bypass it (the secondary flow). By contrast, the bypass ratio of the LEAP engine is 11:1, and that of the CFM56 is 6:1.

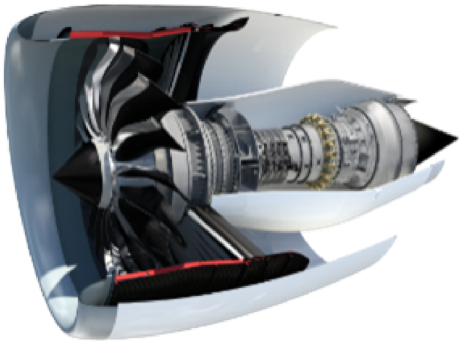

Figure 1: Ultra High Bypass Ratio engine developed jointly by Safran and GE Aerospace in the CFM company

To further increase the bypass ratio, unshrouded engine architectures called unducted fans are under study. Examples of unducted fans are presented in Figure 2. Safran proposed a demonstrator of an unducted fan with contra-rotating blades called Open-Rotor, illustrated in Figure 2b. The architecture of the latter aims to reduce fuel consumption by 15% compared with the ducted LEAP engine. The engine is only a demonstrator and not commercialized due to its complexity. On the contrary, the Revolutionary Innovation for Sustainable Engines (RISE) aircraft engine shown in Figure 2a consists of a rotating fan and a stator. It is under development jointly by Safran and GE Aerospace in the CFM company.

(a) RISE aircraft engine (Safran-GE)

(b) Open-rotor (Safran)

Figure 2: New generation of unducted fans (propfans): RISE (a) and Open-rotor (b) aircraft engines.

To guarantee excellent structural properties with limited weight, complex assemblies of lighter materials are used. Since the structures are light and slender, they are more flexible. As a result, these structures are prone to significant structural displacements outside the linear framework, known as geometric non-linearities. Non-linear effects due to the large-amplitude displacements of these flexible structures can significantly alter vibration levels under aerodynamic loads. A non-linear modeling of the structure is therefore necessary to accurately assess the levels of vibration and to characterize aeroelastic phenomena such as flutter and forced response, which require the resolution of a coupled problem taking into account both the fluid and the structural domains. One approach to solve large-scale aeroelastic problems is to couple two different nonlinear solvers, the first for the fluid domain and the second for the structure domain. The problem is twofold: on the one hand, the coupling between the solvers leads to computation times too significant to be acceptable in industry. On the other hand, coupling dedicated solvers (sometimes black box commercial solvers) is cumbersome to manage in terms of computer architecture and information transfer from one solver to the other. This is particularly highlighted in the case of dynamic computations.

Objectives

For industrial configurations, aeroelastic analyses are traditionally conducted by coupling a fluid solver and a linear reduced-order model for the structure. This reduces computation time and greatly facilitates the coupling. However, linear calculations and predictions of aeroelastic phenomena are no longer sufficient, and geometric non-linearities should be taken into account in aeroelastic calculations. In the literature, model reduction methods to capture geometric non-linearity have been proposed, but these generally address structural issues alone and are not always compatible with the particular nature of aerodynamic loads or adapted to a coupling with another solver. This is the reason for this study. The purpose of this PhD work is therefore to develop a nonlinear reduced order model (ROM) of the structure which can be coupled with a nonlinear fluid solver (CFD) in order to ease nonlinear aeroelastic analyses. The ROM must be independent of the full-order model (FOM) in the sense that it should not rely on any call to an external solver during the computations, but only requires knowledge of the reduced variables.

Organization of the manuscript

In **Chapter 1**, the formalism needed to build reduced models for rotating structures subject to geometric non-linearities is introduced. To this end, the equations of the vibratory dynamics of rotating structures are first introduced. Subsequently, time and frequency resolution methods for structural dynamics are presented. Finally, various model reduction methods for geometrically non-linear structures are described.

The aim of **Chapter 2** is to build and validate a reduced-order model characterizing the geometric non-linear displacements of a structure, which could be connected to an external fluid solver. An extensive literature review on reduced order models is conducted to base our developments on projection based reduced order models which could be coupled to a fluid solver, while still accounting for geometric non-linear deformations. We specifically develop a reduction method based on dual modes with an innovative way of calculating the coefficients of the projected non-linear forces. The aim is to set up a construction process enabling the model to be built systematically, so that the reduced order model is usable for different test cases. This is achieved by developing a methodology for constructing the reduction base, and by formatting the calculation of the internal non-linear forces in the form of a linear system solution to facilitate the resolution. Finally, we study the ability of the reduced model to characterize geometric non-linear deformations and compare the results with other reduction methods from the literature on the 2D case of an Euler-Bernoulli beam with von Kármán hypothesis. Different load cases are studied, in the configuration with and without centrifugal rotation.

The purpose of **Chapter 3** is to assess the ability of the proposed reduced model to handle 3D finite element cases for further use on complex geometries. To this end, we consider a structure analogous to the beam studied in Chapter 2, but this time meshed with 3D finite elements. The reduction method proposed in Chapter 2 is applied to this structure, and the results of the reduced model are in good agreement with those of the full finite element calculations for a vertical loading case, with and without considering centrifugal rotation.

Chapter 4 is dedicated to the introduction of the formalism needed to deal with cases of fluid-structure interaction. To this end, the fluid equations and the arbitrary Lagrangian-Eulerian formulation are first introduced to study fluid dynamics in a moving mesh. Coupling methods for dealing with coupled fluid-structure problems are then presented, along with transfer methods for communicating displacements and forces from one mesh to another.

The aim of **Chapter 5** is to demonstrate the ability of the non-linear ROM built in chapter 2 to perform fluid-structure coupling on a 2D case between this model and an external fluid solver. This is done by making the two solvers communicate with one another to achieve a partitioned coupling. The fluid-structure interaction consists of the beam studied in Chapter 2, excited by the von Kármán vortex wake downstream of a fixed cylinder. The ability of the reduced model to reproduce the high-fidelity solution is demonstrated, notably by accurately recovering the lock-in phenomenon observed for a certain range of Reynolds numbers.

The objective of **Chapter 6** is to consider an industrial application case in order to validate the reduction approach for realistic structures. To this end, we consider a turbomachinery blade for which we build our reduced model around a rotation speed corresponding to a nominal operating case. We first compare the results of the reduced model with those of full finite element calculations for arbitrarily chosen load cases. We then recover the unsteady loads acting on the blade from CFD calculations for the full 360° configuration of the nacelle and apply to the blade a load derived from the distribution of the unsteady forcing. The results obtained with the reduced model are compared to those of a high-fidelity calculation highlighting a very good agreement with a reduced order model of small size and negligible computational cost.

Chapter 1

Model order reduction for geometrical nonlinear structures in rotation

The purpose of the present chapter is first to present the equations of the dynamics relative to a structure in rotation subject to geometric nonlinearities. Then temporal and frequency methods of resolution of the latter equation are presented. The final section consists of a short introduction to various reduction techniques present in the literature to tackle geometrically nonlinear structures.

Contents

1.1 Dynamic equations of motion for geometrical nonlinear structures in rotation

In this section, the dynamic equation of motion for geometrically nonlinear structures in rotation is established. First, the kinematics of a deformable solid in rotation [67, 72] is presented, then the principle of virtual work is formulated in the moving frame and transposed to the reference configuration of the solid [42, 170]. Subsequently, the continuous equations are discretized with a Galerkin approximation and using Finite Elements (FE) to obtain the dynamic equation of motion in matrix form, with a focus at the end of the section on the case of a constant rotation speed.

1.1.1 Solid kinematics

A deformable solid $\mathcal{S}$ of volume Ω_0 and surface $\partial\Omega_0$ is considered. In this solid, a material point M of the reference undeformed configuration is defined in the frame $\mathcal{R}_{\mathrm{m}} = (\boldsymbol{e_x}, \boldsymbol{e_y}, \boldsymbol{e_z})$ by

$$\boldsymbol{OM} = \boldsymbol{X} = \begin{pmatrix} X_1 \\ X_2 \\ X_3 \end{pmatrix}_{\mathcal{R}_{\mathrm{m}}} . \tag{1.1}$$

The current position of the material point M is defined by $\boldsymbol{OM} = \boldsymbol{x} = \begin{pmatrix} x_1 & x_2 & x_3 \end{pmatrix}^T_{\mathcal{R}_{\mathrm{m}}}$ in the deformed configuration. The bijective function $\boldsymbol{\Phi}$ links the current position $\boldsymbol{x}$ of the material point to its position $\boldsymbol{X}$ in the reference undeformed configuration: $\boldsymbol{x} = \boldsymbol{\Phi}(\boldsymbol{X}, t)$. The vector $\boldsymbol{u}$ links the material point M in the reference configuration to the same material point M in the current configuration:

$$\boldsymbol{u}(\boldsymbol{X}, t) = \Phi(\boldsymbol{X}, t) - \boldsymbol{X} = \boldsymbol{x} - \boldsymbol{X}. \tag{1.2}$$

Figure 1.1 illustrates the aforementioned notations linking the solid in the reference configuration its the deformed configuration.

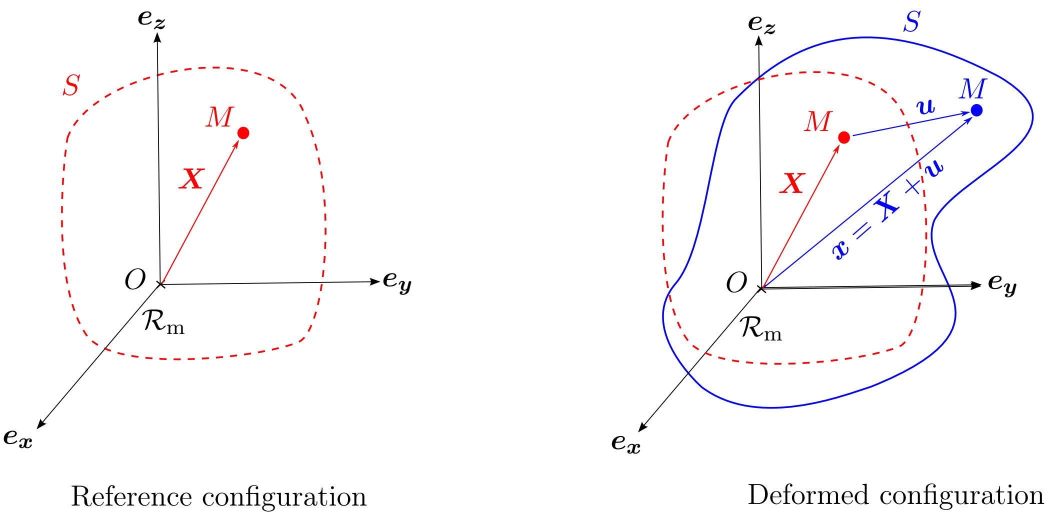

Reference configuration

Deformed configuration

Figure 1.1: Reference and deformed configurations of the solid.

A fixed inertial frame $\mathcal{R}_{\mathrm{g}} = (\hat{\boldsymbol{e}}_{\boldsymbol{x}}, \hat{\boldsymbol{e}}_{\boldsymbol{y}}, \hat{\boldsymbol{e}}_{\boldsymbol{z}})$ is introduced to distinguish it from the local moving frame linked to the solid $\mathcal{R}_{\mathrm{m}}$. The movement of the frame $\mathcal{R}_{\mathrm{m}}$ regarding the frame $\mathcal{R}_{\mathrm{g}}$ is composed of a translation (written $\hat{\boldsymbol{s}}(t)$ with coordinates expressed in $\mathcal{R}_{\mathrm{g}}$) and a rotation (written $\boldsymbol{\omega}(t)$ with coordinates expressed in $\mathcal{R}_{\mathrm{m}}$). Figure 1.2 illustrates the movement and deformation of the solid with time. As shown on the figure, the initial state at $t = 0$ may be different from the undeformed configuration of the solid. Indeed, the initial position can be a prestressed position of the solid. The position of the material point M is described in the moving frame $\mathcal{R}_{\mathrm{m}}$ by:

$$\boldsymbol{OM} = \boldsymbol{X} + \boldsymbol{u}(\boldsymbol{X}, t) = \boldsymbol{x}. \tag{1.3}$$

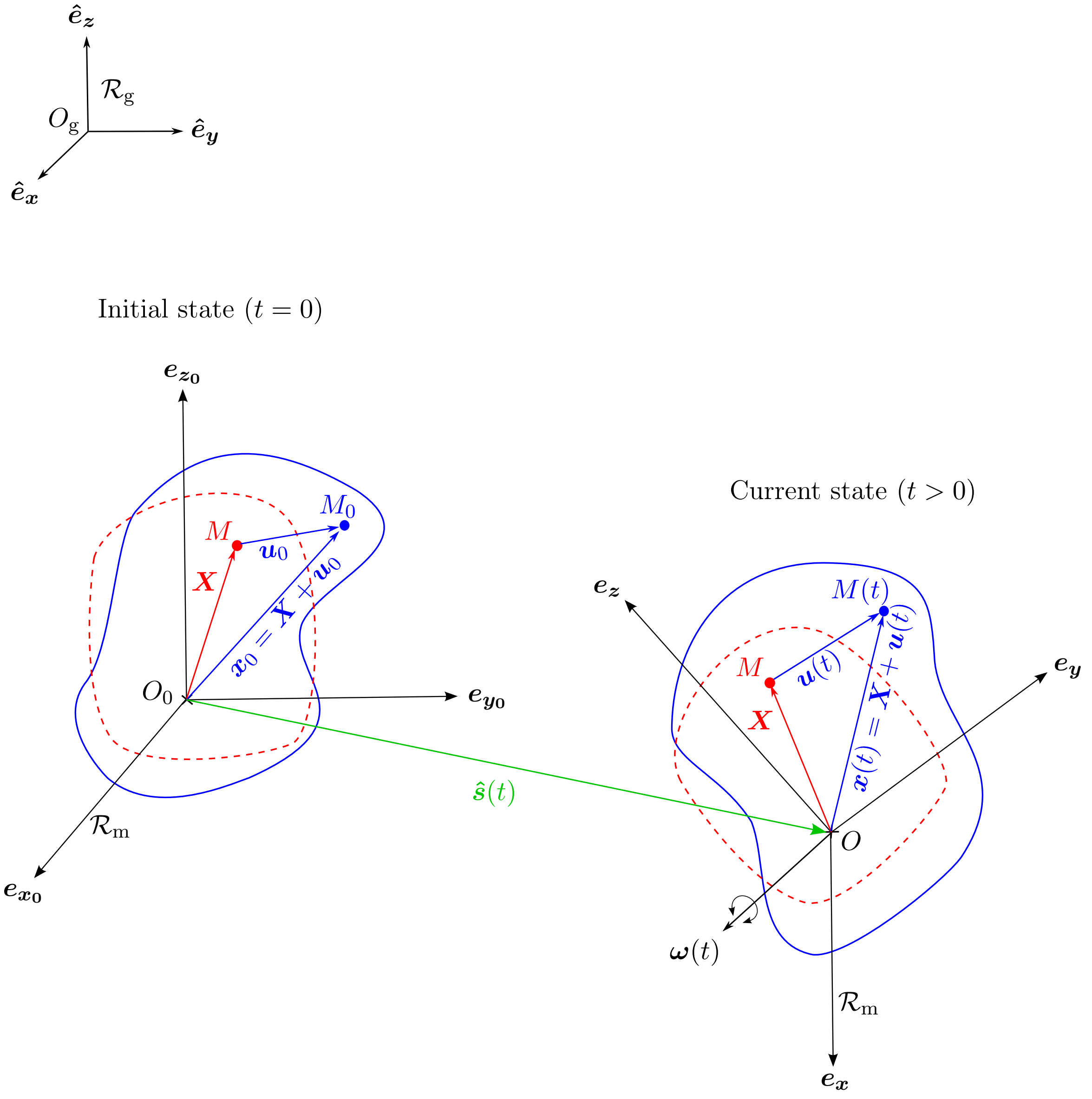

Figure 1.2: Kinematics of the solid.

The aim is to study the dynamics of the structure in the moving frame. However, the dynamics equation of motion derives from the local equation of conservation of momentum (Newton's law of motion) which is valid in an inertial frame, not in a moving frame. Therefore, the idea is to express the conservation of momentum in the inertial frame $\mathcal{R}_{\mathrm{g}}$, but with the displacements defined with respect to the moving frame $\mathcal{R}_{\mathrm{m}}$. The first step consists in writing the acceleration with respect to the inertial frame $\mathcal{R}_\mathrm{g}$ of a material point M of the solid. The relation of composition of the accelerations stipulates that:

$$\boldsymbol{a}(M,t)_{/\mathcal{R}_\mathrm{g}} = \underbrace{\boldsymbol{a}(M,t)_{/\mathcal{R}_\mathrm{m}}}_{\text{relative acceleration}} \tag{1.4}$$

$$+ \underbrace{\boldsymbol{a}(O,t)_{/\mathcal{R}_\mathrm{g}} + \boldsymbol{\omega} \times (\boldsymbol{\omega} \times \boldsymbol{OM}) + \frac{\mathrm{d}\boldsymbol{\omega}}{\mathrm{d}t} \times \boldsymbol{OM}}_{\text{drive acceleration}} \tag{1.5}$$

$$+ \underbrace{2\boldsymbol{\omega} \times \left.\frac{\mathrm{d}\boldsymbol{OM}}{\mathrm{d}t}\right|_{\mathcal{R}_\mathrm{m}}}_{\text{coriolis acceleration}}, \tag{1.6}$$

where the coordinates of the vectors are expressed in $\mathcal{R}_\mathrm{m}$. In this equation, the terms $\boldsymbol{a}(M,t)_{/\mathcal{R}_\mathrm{g}}$ and $\boldsymbol{a}(M,t)_{/\mathcal{R}_\mathrm{m}}$ are the acceleration of the material point M respectively in the frames $\mathcal{R}_\mathrm{g}$ and $\mathcal{R}_\mathrm{m}$, while $\boldsymbol{a}(O,t)_{/\mathcal{R}_\mathrm{g}}$ is the acceleration of the point O with respect to $\mathcal{R}_\mathrm{g}$. The relative velocity $\frac{\mathrm{d}\boldsymbol{OM}}{\mathrm{d}t}|_{\mathcal{R}_\mathrm{m}}$ is the velocity of the material point M with respect to the moving frame $\mathcal{R}_\mathrm{m}$. The frame is not specified in the time derivative of the vector of angular velocity $\mathrm{d}\boldsymbol{\omega}/\mathrm{d}t = \dot{\boldsymbol{\omega}}$ since it can be shown that it is independent from the referential of derivation.
In Equation (1.4), the expression of the relative velocity and acceleration are:

$$\left.\frac{\mathrm{d}\boldsymbol{OM}}{\mathrm{d}t}\right|_{\mathcal{R}_\mathrm{m}} = \dot{\boldsymbol{x}} = \dot{\boldsymbol{u}}, \tag{1.7}$$

$$\boldsymbol{a}(M,t)_{/\mathcal{R}_\mathrm{m}} = \left.\frac{\mathrm{d}^2\boldsymbol{OM}}{\mathrm{d}t^2}\right|_{\mathcal{R}_\mathrm{m}} = \ddot{\boldsymbol{x}} = \ddot{\boldsymbol{u}}. \tag{1.8}$$

Regarding the acceleration $\boldsymbol{a(O,t)}_{/\mathcal{R}_\mathrm{g}}$ of the point O, it is convenient to write its coordinates in $\mathcal{R}_\mathrm{g}$, then use a rotation matrix to obtain its coordinates in $\mathcal{R}_\mathrm{m}$. To describe in $\mathcal{R}_\mathrm{g}$ the movement of a vector whose coordinates are given the moving frame $\mathcal{R}_\mathrm{m}$, the following rotation matrix $\mathbf{R}$ is considered:

$$\mathbf{R} = \begin{pmatrix} \langle \boldsymbol{e_x}, \hat{\boldsymbol{e}}_{\boldsymbol{x}} \rangle & \langle \boldsymbol{e_y}, \hat{\boldsymbol{e}}_{\boldsymbol{x}} \rangle & \langle \boldsymbol{e_z}, \hat{\boldsymbol{e}}_{\boldsymbol{x}} \rangle \\ \langle \boldsymbol{e_x}, \hat{\boldsymbol{e}}_{\boldsymbol{y}} \rangle & \langle \boldsymbol{e_y}, \hat{\boldsymbol{e}}_{\boldsymbol{y}} \rangle & \langle \boldsymbol{e_z}, \hat{\boldsymbol{e}}_{\boldsymbol{y}} \rangle \\ \langle \boldsymbol{e_x}, \hat{\boldsymbol{e}}_{\boldsymbol{z}} \rangle & \langle \boldsymbol{e_y}, \hat{\boldsymbol{e}}_{\boldsymbol{z}} \rangle & \langle \boldsymbol{e_z}, \hat{\boldsymbol{e}}_{\boldsymbol{z}} \rangle \end{pmatrix}. \tag{1.9}$$

The rotation matrix is orthogonal: $\mathbf{R}^T\mathbf{R} = \mathbf{I} = \mathbf{R}\mathbf{R}^T$. Conversely, the rotation matrix $\mathbf{R}^T$ provides with a matrix product the coordinates in $\mathcal{R}_\mathrm{m}$ of a vector whose coordinates are initially given in $\mathcal{R}_\mathrm{g}$. Deriving the orthogonality relation, the matrix $\boldsymbol{\Omega} = \dot{\mathbf{R}}^T\mathbf{R}$ is introduced:

$$\frac{\partial \mathbf{R}^T\mathbf{R}}{\partial t} = \mathbf{0}, \tag{1.10}$$

$$\dot{\mathbf{R}}^T\mathbf{R} + \mathbf{R}^T\dot{\mathbf{R}} = \boldsymbol{\Omega} + \boldsymbol{\Omega}^T = \mathbf{0}. \tag{1.11}$$

The matrix $\boldsymbol{\Omega}$ is a skew-symmetric matrix of dimension three and has therefore only three independent components. These components are those of the unique angular velocity vector $\boldsymbol{\omega} = \begin{pmatrix}\omega_1(t) & \omega_2(t) & \omega_3(t)\end{pmatrix}^T_{\mathcal{R}_\mathrm{m}}$:

$$\boldsymbol{\Omega} = \begin{pmatrix} 0 & -\omega_3 & \omega_2 \\ \omega_3 & 0 & -\omega_1 \\ -\omega_2 & \omega_1 & 0 \end{pmatrix}. \tag{1.12}$$

The acceleration of the point O with respect to the inertial frame $\mathcal{R}_\mathrm{g}$ is written $\ddot{\boldsymbol{s}}$. Using the rotation matrix $\mathbf{R}^T$, the expression in the moving frame $\mathcal{R}_\mathrm{m}$ of such accelerations is:

$$\boldsymbol{a}(O,t)_{/\mathcal{R}_\mathrm{g}} = \mathbf{R}^T\ddot{\boldsymbol{s}}. \tag{1.13}$$

Hence, replacing in Equation (1.4), the expression of the acceleration of the material point M with respect to the inertial frame $\mathcal{R}_\mathrm{g}$, with coordinates expressed in the moving frame $\mathcal{R}_\mathrm{m}$ becomes:

$$\boldsymbol{a}(M,t)_{/\mathcal{R}_\mathrm{g}} = \ddot{\boldsymbol{u}} + \mathbf{R}^T\ddot{\boldsymbol{s}} + \boldsymbol{\omega}\times(\boldsymbol{\omega}\times(\boldsymbol{X}+\boldsymbol{u})) + \dot{\boldsymbol{\omega}}\times(\boldsymbol{X}+\boldsymbol{u}) + 2\boldsymbol{\omega}\times\dot{\boldsymbol{u}}. \tag{1.14}$$

In what follows, the notation $\ddot{\boldsymbol{y}}$ is used to describe, with coordinates defined in $\mathcal{R}_\mathrm{g}$, the acceleration of the material point M with respect to the aforementioned inertial frame $\mathcal{R}_\mathrm{g}$. Thus, the left member of Equation (1.14) becomes $\boldsymbol{a}(M,t)_{/\mathcal{R}_\mathrm{g}} = \mathbf{R}^T\ddot{\boldsymbol{y}}$. Besides, the matrix $\boldsymbol{\Omega}$ is used to replace the cross products by matrix products, leading to:

$$\boxed{\mathbf{R}^T\ddot{\boldsymbol{y}} = \ddot{\boldsymbol{u}} + \mathbf{R}^T\ddot{\boldsymbol{s}} + \boldsymbol{\Omega}^2(\boldsymbol{X}+\boldsymbol{u}) + \dot{\boldsymbol{\Omega}}(\boldsymbol{X}+\boldsymbol{u}) + 2\boldsymbol{\Omega}\dot{\boldsymbol{u}}.} \tag{1.15}$$

In this section, the kinematics of a deformable solid in rotation were detailed. The acceleration of a material point regarding the inertial frame was written according to its displacement expressed in the moving frame.

1.1.2 Strong and weak formulation of the principle of virtual work

The local equation of conservation of momentum is applied in the inertial frame $\mathcal{R}_\mathrm{g}$. The coordinates of the quantities involved are written in the current configuration as follows:

$$\mathbf{div}\,(\boldsymbol{\sigma}(\boldsymbol{x},t)) + \rho(\boldsymbol{x})\boldsymbol{b_v}(\boldsymbol{x},t) = \rho(\boldsymbol{x})\mathbf{R}^T\ddot{\boldsymbol{y}}, \tag{1.16}$$

with $\boldsymbol{\sigma}$ the Cauchy stress tensor and $\boldsymbol{b_v}$ the volume forces. The border $\partial\Omega$ of the solid $\mathcal{S}$ is partitioned into the sub-border S^d where Dirichlet boundary conditions are applied $\boldsymbol{u}(\boldsymbol{x},t) = \boldsymbol{u}^d(\boldsymbol{x},t)$ and the sub-border Γ where Neumann boundary conditions are applied $\boldsymbol{\sigma}(\boldsymbol{x},t)\boldsymbol{n}(\boldsymbol{x},t) = \boldsymbol{t}(\boldsymbol{x},t)$ with $\boldsymbol{n}$ is the normal vector pointing outwards of the solid domain and $\boldsymbol{t}$ the imposed surface force. The sub-borders satisfy the relations: $S^d \cup \Gamma = \partial\Omega$ and $S^d \cap \Gamma = \varnothing$. The strong formulation of the problem consists in searching the solution of the following system in the set of functions belonging to the second order differentiability class $\mathcal{C}^2(\Omega)$:

$$\left\{\begin{array}{l}
\text{Local conservation of momentum:} \\
\qquad \mathbf{div}\,(\boldsymbol{\sigma}(\boldsymbol{x},t)) + \rho(\boldsymbol{x})\boldsymbol{b_v}(\boldsymbol{x},t) = \rho(\boldsymbol{x})\mathbf{R}^T\ddot{\boldsymbol{y}} \\
\\
\qquad\qquad \text{Boundary conditions:} \\
\qquad\qquad\qquad \boldsymbol{u}(\boldsymbol{x},t) = \boldsymbol{u}^d(\boldsymbol{x},t) \quad \text{on } S^d \\
\qquad\qquad\qquad \boldsymbol{\sigma}(\boldsymbol{x},t)\mathbf{n}(\boldsymbol{x},t) = \boldsymbol{t}(\boldsymbol{x},t) \quad \text{on } \Gamma \\
\\
\qquad\qquad \text{Initial conditions:} \\
\qquad\qquad\qquad \mathbf{u}(\boldsymbol{x},0) = \boldsymbol{u}_0 \quad \forall \boldsymbol{x} \in \Omega(t) \\
\qquad\qquad\qquad \dot{\boldsymbol{u}}(\boldsymbol{x},0) = \dot{\boldsymbol{u}}_0 \quad \forall \boldsymbol{x} \in \Omega(t) \\
\\
\qquad\qquad \text{Constitutive equation:} \\
\qquad\qquad\qquad \boldsymbol{\sigma}(\varepsilon, \dot{\varepsilon})
\end{array}\right. \tag{1.17}$$

The strong formulation imposes restrictive derivability conditions. The aim of the weak formulation is to reduce the constraints on the derivability of the solution to a solution belonging to the

Sobolev $\mathcal{H}^1(\Omega)$ set of square-integrable functions and with derivatives also square-integrable. To do so, the equation of conservation of momentum is multiplied by a compatible virtual displacement $\boldsymbol{\delta u}(\boldsymbol{x})$ and integrated on the total volume $\Omega(t)$ to obtain the integral formulation:

$$\int\limits_{\Omega(t)} \left(\mathbf{div}\,(\boldsymbol{\sigma}) + \rho \boldsymbol{b_v} - \rho \mathbf{R}^T \ddot{\boldsymbol{y}}\right) \cdot \boldsymbol{\delta u} \;\mathrm{d}\Omega(t) = 0. \tag{1.18}$$

Rewritten in the form:

$$\int\limits_{\Omega(t)} \mathrm{div}\,(\boldsymbol{\sigma\delta u})\;\mathrm{d}\Omega(t) - \int\limits_{\Omega(t)} \boldsymbol{\sigma} : \boldsymbol{\nabla_x}\,(\boldsymbol{\delta u})\;\mathrm{d}\Omega(t) + \int\limits_{\Omega(t)} \rho \boldsymbol{b_v} \cdot \boldsymbol{\delta u}\;\mathrm{d}\Omega(t) - \int\limits_{\Omega(t)} \rho \mathbf{R}^T \ddot{\boldsymbol{y}} \cdot \boldsymbol{\delta u}\;\mathrm{d}\Omega(t) = 0, \tag{1.19}$$

using the relation: $\mathbf{div}\,(\boldsymbol{\sigma}) \cdot \boldsymbol{\delta u} = \mathrm{div}\,(\boldsymbol{\sigma\delta u}) - \boldsymbol{\sigma} : \boldsymbol{\nabla_x}\,(\boldsymbol{\delta u})$ where $\boldsymbol{\nabla_x}$ corresponds to the gradient in the current configuration. We remind the reader that the divergence and the gradient here derivate the quantities regarding the local coordinates.

The Green-Ostrogradsky theorem is applied in the first integral and the stress tensor $\boldsymbol{\sigma}$ is considered symmetrical:

$$\begin{aligned}\int\limits_{\Omega(t)} \mathrm{div}\,(\boldsymbol{\sigma\delta u})\,\mathrm{d}\Omega(t) &= \int\limits_{\partial\Omega} (\boldsymbol{\sigma\delta u}) \cdot \mathbf{n}\;\mathrm{d}\partial\Omega = \int\limits_{\partial\Omega} \boldsymbol{\delta u}^T \boldsymbol{\sigma}^T \mathbf{n}\;\mathrm{d}\partial\Omega = \int\limits_{\partial\Omega} \boldsymbol{\delta u}^T \boldsymbol{\sigma} \mathbf{n}\;\mathrm{d}\partial\Omega \\ &= \int\limits_{\partial\Omega} \boldsymbol{\delta u}^T \boldsymbol{t}\;\mathrm{d}\partial\Omega = \int\limits_{\partial\Omega} \boldsymbol{t} \cdot \boldsymbol{\delta u}\;\mathrm{d}\partial\Omega.\end{aligned} \tag{1.20}$$

Thus the integral form of the weak formulation of the virtual work principle in the current configuration becomes:

$$\boxed{\int\limits_{\Gamma} \boldsymbol{t} \cdot \boldsymbol{\delta u}\;\mathrm{d}\Gamma(t) - \int\limits_{\Omega(t)} \boldsymbol{\sigma} : \boldsymbol{\nabla_x}\,(\boldsymbol{\delta u})\;\mathrm{d}\Omega(t) + \int\limits_{\Omega(t)} \rho \boldsymbol{b_v} \cdot \boldsymbol{\delta u}\;\mathrm{d}\Omega(t) - \int\limits_{\Omega(t)} \rho \mathbf{R}^T \ddot{\boldsymbol{y}} \cdot \boldsymbol{\delta u}\;\mathrm{d}\Omega(t) = 0} \tag{1.21}$$

in which the virtual displacement is imposed to be null at the Dirichlet border, meaning that $\int_{\partial\Omega} \boldsymbol{t} \cdot \boldsymbol{\delta u}\;\mathrm{d}\partial\Omega = \int_{\Gamma} \boldsymbol{t} \cdot \boldsymbol{\delta u}\;\mathrm{d}\Gamma$. The solution $\boldsymbol{u}$ belongs to the set $\mathcal{U} = \left\{\boldsymbol{u} \mid \boldsymbol{u} \in \mathcal{H}^1(\Omega(t)),\;\; \boldsymbol{u} = \boldsymbol{u}^d \;\text{ on }\; S^d\right\}$ and the virtual displacement $\boldsymbol{\delta u}$ belongs to $\delta\mathcal{U} = \left\{\boldsymbol{\delta u} \mid \boldsymbol{\delta u} \in \mathcal{H}^1(\Omega(t)),\;\; \boldsymbol{\delta u} = 0 \;\text{ on }\; S^d\right\}$.

1.1.3 Transposition of the weak formulation of the virtual work principle in the reference configuration

In this section, the weak formulation of the virtual work principal is transposed in the reference configuration. The gradient $\boldsymbol{F}$ of the transformation $\boldsymbol{\Phi}$, linking a material point in the reference configuration to the same material point in the current configuration, is defined as:

$$\boldsymbol{F} = \frac{\mathrm{d}\boldsymbol{x}}{\mathrm{d}\boldsymbol{X}} = \frac{\mathrm{d}\boldsymbol{u}}{\mathrm{d}\boldsymbol{X}} + \boldsymbol{I} \qquad \text{(using } \boldsymbol{x} = \boldsymbol{X} + \boldsymbol{u}\text{)}, \tag{1.22}$$

and its determinant is written J: $J = \mathbf{det}(\boldsymbol{F})$.

Transposition of the acceleration and external volume forces:
Considering a volume $\mathrm{d}v$ and an oriented surface $\boldsymbol{n}\mathrm{d}a$ in the current configuration, the corresponding volume $\mathrm{d}V$ and oriented surface $\boldsymbol{N}\mathrm{d}A$ in the reference configuration verify:

$$\mathrm{d}v = J\mathrm{d}V \tag{1.23}$$

$$\boldsymbol{n}\mathrm{d}a = J\boldsymbol{F}^{-T}\boldsymbol{N}\mathrm{d}A. \tag{1.24}$$

Since $\mathrm{d}v = J\mathrm{d}V$ and $\rho(\boldsymbol{x}) = J\rho_0$, the transposition of the mass conservation in the reference configuration reads:

$$\int_{\Omega(t)} \rho(\boldsymbol{x},t)\mathrm{d}v = \int_{\Omega_0} \rho_0 \mathrm{d}V. \tag{1.25}$$

Therefore, the transposition of the acceleration term and the volume forces in the reference configuration are straightforward and become respectively:

$$\int\limits_{\Omega(t)} \rho(\boldsymbol{x})\mathbf{R}^T\ddot{\boldsymbol{y}}(t)\cdot\boldsymbol{\delta u}(\boldsymbol{x},t)\ \mathrm{d}\Omega(t) = \int\limits_{\Omega_0} \rho_0\mathbf{R}^T\ddot{\boldsymbol{y}}(\boldsymbol{X},t)\cdot\boldsymbol{\delta u}(\boldsymbol{X},t)\ \mathrm{d}\Omega_0 \tag{1.26}$$

and

$$\int\limits_{\Omega(t)} \rho(\boldsymbol{x})\boldsymbol{b_v}(\boldsymbol{x},t)\cdot\boldsymbol{\delta u}(\boldsymbol{x},t)\ \mathrm{d}\Omega(t) = \int\limits_{\Omega_0} \rho_0\boldsymbol{b_v}(\boldsymbol{X},t)\cdot\boldsymbol{\delta u}(\boldsymbol{X},t)\ \mathrm{d}\Omega_0 \tag{1.27}$$

Transposition of the surface forces:
In the weak formulation, the integral form of the surface forces is given by:

$$\int\limits_{\Gamma(t)} \boldsymbol{t}\cdot\boldsymbol{\delta u}\ \mathrm{d}\Gamma(t) = \int\limits_{\Gamma(t)} \boldsymbol{\delta u}^T\boldsymbol{\sigma}\mathbf{n}\ \mathrm{d}\Gamma(t) \tag{1.28}$$

The relation between the oriented surfaces (1.24) gives $\boldsymbol{n}\Gamma(\mathrm{t}) = J\boldsymbol{F}^{-T}\boldsymbol{N}\Gamma_0$. Thus, introducing the Boussinesq stress tensor (also called first Piola-Kirchhoff stress tensor) $\boldsymbol{\Pi} = J\boldsymbol{\sigma}\boldsymbol{F}^{-T}$, the following relation is obtained:

$$\boldsymbol{\sigma}\mathbf{n}\ \mathrm{d}\Gamma(t) = J\boldsymbol{\sigma}\boldsymbol{F}^{-T}\boldsymbol{N}\Gamma_0 = \boldsymbol{\Pi}\boldsymbol{N}\Gamma_0. \tag{1.29}$$

The scalar product with the virtual displacement and the integration over the surfaces lead to:

$$\int\limits_{\Gamma(t)} \boldsymbol{t}\cdot\boldsymbol{\delta u}\ \mathrm{d}\Gamma(t) = \int\limits_{\Gamma(t)} \boldsymbol{\delta u}^T\boldsymbol{\sigma}\mathbf{n}\ \mathrm{d}\Gamma(t) = \int\limits_{\Gamma_0} \boldsymbol{\delta u}^T\boldsymbol{\Pi}\boldsymbol{N}\mathrm{d}\Gamma_0. \tag{1.30}$$

Finally the transposition of the surface forces in the reference configuration reads:

$$\int\limits_{\Gamma(t)} \boldsymbol{t}(\boldsymbol{x},t)\cdot\boldsymbol{\delta u}(\boldsymbol{x},t)\ \mathrm{d}\Gamma(t) = \int\limits_{\Gamma_0} \boldsymbol{\Pi}\boldsymbol{N}\cdot\boldsymbol{\delta u}(\boldsymbol{X},t)\ \mathrm{d}\Gamma_0. \tag{1.31}$$

Transposition of the internal forces:
The weak formulation of the internal forces is the following:

$$\int_{\Omega(t)} \boldsymbol{\sigma} : \boldsymbol{\nabla_x}(\boldsymbol{\delta u})\mathrm{d}\Omega(t) = \int_{\Omega_0} \boldsymbol{\sigma} : \boldsymbol{\nabla_x}(\boldsymbol{\delta u})J\mathrm{d}\Omega_0, \tag{1.32}$$

where the gradient operator $\boldsymbol{\nabla_x}$ in the current configuration can be expressed according to its counterpart $\boldsymbol{\nabla_X}$ in the reference configuration by:

$$\boldsymbol{\nabla_x}(\boldsymbol{\delta u}) = \frac{\partial \boldsymbol{\delta u}}{\partial \boldsymbol{x}} = \frac{\partial \boldsymbol{\delta u}}{\partial \boldsymbol{X}}\frac{\partial \boldsymbol{X}}{\partial \boldsymbol{x}} = \boldsymbol{\nabla_X}(\boldsymbol{\delta u})\boldsymbol{F}^{-1}. \tag{1.33}$$

The transposition of the term $\boldsymbol{\sigma} : \boldsymbol{\nabla_x}(\boldsymbol{\delta u})J\mathrm{d}\Omega_0$ involves the properties of the trace operator:

$$J\boldsymbol{\sigma} : \boldsymbol{\nabla_x}(\boldsymbol{\delta u}) = J\mathbf{tr}\Big(\boldsymbol{\sigma}\boldsymbol{\nabla_x}(\boldsymbol{\delta u})^T\Big) = \mathbf{tr}\Big(\boldsymbol{\nabla_X}(\boldsymbol{\delta u})^T\boldsymbol{\Pi}\Big) = \boldsymbol{\Pi} : \boldsymbol{\nabla_X}(\boldsymbol{\delta u}), \tag{1.34}$$

leading to the transposition in the reference configuration of the internal forces:

$$-\int_{\Omega(t)} \boldsymbol{\sigma} : \boldsymbol{\nabla_x}(\boldsymbol{\delta u})\mathrm{d}\Omega(t) = -\int_{\Omega_0} \boldsymbol{\Pi} : \boldsymbol{\nabla_X}(\boldsymbol{\delta u})\mathrm{d}\Omega_0. \tag{1.35}$$

Hence the weak formulation of the virtual work in the reference configuration becomes:

$$\int\limits_{\Gamma_0} \boldsymbol{\Pi N} \cdot \boldsymbol{\delta u}\ \Gamma_0 - \int_{\Omega_0} \boldsymbol{\Pi} : \boldsymbol{\nabla_X}(\boldsymbol{\delta u})\mathrm{d}\Omega_0 + \int\limits_{\Omega_0} \rho_0 \boldsymbol{b_v} \cdot \boldsymbol{\delta u}\ \mathrm{d}\Omega_0 - \int\limits_{\Omega_0} \rho_0 \mathbf{R}^T \ddot{\boldsymbol{y}} \cdot \boldsymbol{\delta u}\ \mathrm{d}\Omega_0 = 0. \tag{1.36}$$

Nevertheless, the Boussinesq stress tensor $\boldsymbol{\Pi}$ is not symmetrical and is a hybrid tensor in the sense that $\boldsymbol{\Pi N}dA$ is equal to an elementary force $\boldsymbol{df}$ in the current configuration, meaning that the Boussinesq stress tensor does not fully satisfy the objective of expressing the stress in the reference configuration. We can introduce the symmetrical tensor $\boldsymbol{S}$ such that $\boldsymbol{\Pi} = \boldsymbol{FS}$ called the second Piola-Kirchhoff stress tensor. The weak formulation in the reference frame with the second Piola-Kirchhoff stress tensor is the following:

$$\int\limits_{\Gamma_0} \boldsymbol{FSN} \cdot \boldsymbol{\delta u}\ \Gamma_0 - \int_{\Omega_0} \boldsymbol{FS} : \boldsymbol{\nabla_X}(\boldsymbol{\delta u})\mathrm{d}\Omega_0 + \int\limits_{\Omega_0} \rho_0 \boldsymbol{b_v} \cdot \boldsymbol{\delta u}\ \mathrm{d}\Omega_0 - \int\limits_{\Omega_0} \rho_0 \mathbf{R}^T \ddot{\boldsymbol{y}} \cdot \boldsymbol{\delta u}\ \mathrm{d}\Omega_0 = 0. \tag{1.37}$$

Besides, the virtual work of the internal forces is usually written with the variation of the Green-Lagrange strain tensor as follows:

$$-\int_{\Omega_0} \boldsymbol{\Pi} : \boldsymbol{\nabla_X}(\boldsymbol{\delta u})\ \mathrm{d}\Omega_0 = -\int_{\Omega_0} \boldsymbol{S} : \boldsymbol{\delta E}\ \mathrm{d}\Omega_0. \tag{1.38}$$

Indeed, the Green-Lagrange strain tensor is defined by:

$$\boldsymbol{E} = \frac{1}{2}\left[\boldsymbol{\nabla_X u} + (\boldsymbol{\nabla_X u})^T + (\boldsymbol{\nabla_X u})^T\boldsymbol{\nabla_X u}\right], \tag{1.39}$$

its variation is therefore:

$$\boldsymbol{\delta E} = \frac{1}{2}\left[\boldsymbol{\nabla_X \delta u} + (\boldsymbol{\nabla_X \delta u})^T + (\boldsymbol{\nabla_X \delta u})^T(\boldsymbol{\nabla_X u}) + (\boldsymbol{\nabla_X u})^T(\boldsymbol{\nabla_X \delta u})\right]. \tag{1.40}$$

Thus, using the properties of the trace operator, the desired equality is obtained:

$$\begin{aligned}
\boldsymbol{S} : \boldsymbol{\delta E} &= \mathbf{tr}(\boldsymbol{S}^T\boldsymbol{\delta E}) = \mathbf{tr}(\boldsymbol{S}\ \boldsymbol{\delta E}) && (1.41)\\
&= \mathbf{tr}\Big(\boldsymbol{S}\Big[(\boldsymbol{\nabla_X \delta u})^T\underbrace{(\boldsymbol{I} + \boldsymbol{\nabla_X u})}_{\boldsymbol{F}}\Big]\Big) && (1.42)\\
&= \mathbf{tr}\Big(\boldsymbol{FS}(\boldsymbol{\nabla_X \delta u})^T\Big) = \mathbf{tr}\Big(\boldsymbol{\Pi}(\boldsymbol{\nabla_X \delta u})^T\Big) = \boldsymbol{\Pi} : (\boldsymbol{\nabla_X \delta u}). && (1.43)
\end{aligned}$$

Finally, the weak formulation of the virtual work in the reference configuration becomes:

$$\boxed{\int_{\Gamma_0} \boldsymbol{FSN} \cdot \boldsymbol{\delta u}\, \Gamma_0 - \int_{\Omega_0} \boldsymbol{S} : \boldsymbol{\delta E}\, \mathrm{d}\Omega_0 + \int_{\Omega_0} \rho_0 \boldsymbol{b_v} \cdot \boldsymbol{\delta u}\, \mathrm{d}\Omega_0 - \int_{\Omega_0} \rho_0 \mathbf{R}^T \ddot{\boldsymbol{y}} \cdot \boldsymbol{\delta u}\, \mathrm{d}\Omega_0 = 0} \tag{1.44}$$

The weak formulation of the virtual work principle in the reference configuration can be decomposed as the sum of the virtual work of the internal and external forces equal to the virtual work associated to the acceleration:

$$\boxed{\delta W_{\text{int}} + \delta W_{\text{ext}} = \delta W_{\text{acc}}} \tag{1.45}$$

with δW_{int} the virtual work of the internal forces:

$$\delta W_{\text{int}} = -\int_{\Omega_0} \boldsymbol{S} : \boldsymbol{\delta E}\, \mathrm{d}\Omega_0, \tag{1.46}$$

δW_{ext} the virtual work of the external forces:

$$\delta W_{\text{ext}} = \int_{\Gamma_0} \boldsymbol{FSN} \cdot \boldsymbol{\delta u}\, \Gamma_0 + \int_{\Omega_0} \rho_0 \boldsymbol{b_v} \cdot \boldsymbol{\delta u}\, \mathrm{d}\Omega_0, \tag{1.47}$$

and δW_{acc} the virtual work associated to the acceleration:

$$\delta W_{\text{acc}} = \int_{\Omega_0} \rho_0 \mathbf{R}^T \ddot{\boldsymbol{y}} \cdot \boldsymbol{\delta u}\, \mathrm{d}\Omega_0. \tag{1.48}$$

1.1.4 Virtual work of the internal forces in the frame of finite deformations

In the frame of finite deformations (small strains, large displacements and rotations), the second Piola-Kirchhoff stress-tensor verifies Hooke's-law of linear elastic deformations:

$$\boldsymbol{S} = \boldsymbol{\mathcal{H}} : \boldsymbol{E} \tag{1.49}$$

with $\boldsymbol{\mathcal{H}}$ a fourth order tensor called elasticity tensor and depending on the material properties, in our case only the Young's modulus E and Poisson's coefficient ν. It leads to the following development:

$$\begin{aligned}
\boldsymbol{S} : \boldsymbol{\delta E} &= \boldsymbol{E} : \boldsymbol{\mathcal{H}} : \boldsymbol{\delta E} && (1.50)\\
&= \frac{1}{4}\Big(\boldsymbol{\nabla_X u} + (\boldsymbol{\nabla_X u})^T\Big) : \boldsymbol{\mathcal{H}} : \Big(\boldsymbol{\nabla_X \delta u} + (\boldsymbol{\nabla_X \delta u})^T\Big)\\
&+ \frac{1}{4}\Big(\boldsymbol{\nabla_X u} + (\boldsymbol{\nabla_X u})^T\Big) : \boldsymbol{\mathcal{H}} : \Big((\boldsymbol{\nabla_X \delta u})^T(\boldsymbol{\nabla_X u}) + (\boldsymbol{\nabla_X u})^T(\boldsymbol{\nabla_X \delta u})\Big)\\
&+ \frac{1}{4}\Big((\boldsymbol{\nabla_X u})^T(\boldsymbol{\nabla_X u})\Big) : \boldsymbol{\mathcal{H}} : \Big(\boldsymbol{\nabla_X \delta u} + (\boldsymbol{\nabla_X \delta u})^T\Big)\\
&+ \frac{1}{4}\Big((\boldsymbol{\nabla_X u})^T(\boldsymbol{\nabla_X u})\Big) : \boldsymbol{\mathcal{H}} : \Big((\boldsymbol{\nabla_X \delta u})^T(\boldsymbol{\nabla_X u}) + (\boldsymbol{\nabla_X u})^T(\boldsymbol{\nabla_X \delta u})\Big) && (1.51)
\end{aligned}$$

The virtual work of the internal forces can therefore be decomposed in three terms that will lead to respectively linear, quadratic and cubic polynomials of the degrees of freedom in the Finite Element discretization:

$$\delta W_{\text{int}} = -\int_{\Omega_0} \boldsymbol{S} : \boldsymbol{\delta E}\, \mathrm{d}\Omega_0 = \delta W_1 + \delta W_2 + \delta W_3, \tag{1.52}$$

with

$$-\delta W_1 = \int_{\Omega_0} \frac{1}{4}\Big[(\boldsymbol{\nabla}_{\boldsymbol{X}}\boldsymbol{u}) + (\boldsymbol{\nabla}_{\boldsymbol{X}}\boldsymbol{u})^T\Big] : \boldsymbol{\mathcal{H}} : \Big[(\boldsymbol{\nabla}_{\boldsymbol{X}}\boldsymbol{\delta u}) + (\boldsymbol{\nabla}_{\boldsymbol{X}}\boldsymbol{\delta u})^T\Big] \,\mathrm{d}\Omega_0, \tag{1.53}$$

$$\begin{aligned}
-\delta W_2 = &\int_{\Omega_0} \frac{1}{4}\Big[(\boldsymbol{\nabla}_{\boldsymbol{X}}\boldsymbol{u}) + (\boldsymbol{\nabla}_{\boldsymbol{X}}\boldsymbol{u})^T\Big] : \boldsymbol{\mathcal{H}} : \Big[(\boldsymbol{\nabla}_{\boldsymbol{X}}\boldsymbol{\delta u})^T(\boldsymbol{\nabla}_{\boldsymbol{X}}\boldsymbol{u})^T\Big] \,\mathrm{d}\Omega_0 \\
&+ \int_{\Omega_0} \frac{1}{4}\Big[(\boldsymbol{\nabla}_{\boldsymbol{X}}\boldsymbol{u}) + (\boldsymbol{\nabla}_{\boldsymbol{X}}\boldsymbol{u})^T\Big] : \boldsymbol{\mathcal{H}} : \Big[(\boldsymbol{\nabla}_{\boldsymbol{X}}\boldsymbol{u})^T(\boldsymbol{\nabla}_{\boldsymbol{X}}\boldsymbol{\delta u})^T\Big] \,\mathrm{d}\Omega_0 \\
&+ \int_{\Omega_0} \frac{1}{4}\Big[(\boldsymbol{\nabla}_{\boldsymbol{X}}\boldsymbol{u})^T(\boldsymbol{\nabla}_{\boldsymbol{X}}\boldsymbol{u})\Big] : \boldsymbol{\mathcal{H}} : \Big[(\boldsymbol{\nabla}_{\boldsymbol{X}}\boldsymbol{\delta u}) + (\boldsymbol{\nabla}_{\boldsymbol{X}}\boldsymbol{\delta u})^T\Big] \,\mathrm{d}\Omega_0,
\end{aligned} \tag{1.54}$$

$$\begin{aligned}
-\delta W_3 = &\int_{\Omega_0} \frac{1}{4}\Big[(\boldsymbol{\nabla}_{\boldsymbol{X}}\boldsymbol{u})^T(\boldsymbol{\nabla}_{\boldsymbol{X}}\boldsymbol{u})\Big] : \boldsymbol{\mathcal{H}} : \Big[(\boldsymbol{\nabla}_{\boldsymbol{X}}\boldsymbol{\delta u})^T(\boldsymbol{\nabla}_{\boldsymbol{X}}\boldsymbol{u})\Big] \,\mathrm{d}\Omega_0 \\
&+ \int_{\Omega_0} \frac{1}{4}\Big[(\boldsymbol{\nabla}_{\boldsymbol{X}}\boldsymbol{u})^T(\boldsymbol{\nabla}_{\boldsymbol{X}}\boldsymbol{u})\Big] : \boldsymbol{\mathcal{H}} : \Big[(\boldsymbol{\nabla}_{\boldsymbol{X}}\boldsymbol{u})^T(\boldsymbol{\nabla}_{\boldsymbol{X}}\boldsymbol{\delta u})\Big] \,\mathrm{d}\Omega_0.
\end{aligned} \tag{1.55}$$

1.1.5 Galerkin approximation

The Galerkin method of Finite Element discretization [9, 209] consists in writing the displacement $\boldsymbol{u}$ as a linear combination of shape functions (interpolation functions) and the nodal values u_i $i \in [1, N]$. It is common to apply the same discretization to the virtual displacement:

$$\boldsymbol{u}(\boldsymbol{X}, t) = \sum_{i=1}^{N} \mathbf{N}(\boldsymbol{X})\; u_i(t) \tag{1.56}$$

$$\boldsymbol{\delta u}(\boldsymbol{X}, t) = \sum_{i=1}^{N} \mathbf{N}(\boldsymbol{X})\; \delta u_i(t) \tag{1.57}$$

Galerkin approximation applied to the virtual work of the internal forces:
Introducing the Galerkin decomposition in the components of the virtual work of the internal forces leads to:

$$-\delta W_{\text{int}} = -\delta W_1 - \delta W_2 - \delta W_3 = \boldsymbol{\delta}\mathbf{u}^T\Big(\mathbf{K_{mat}}\mathbf{u} + \mathbf{f_{nl2}}(\mathbf{u}) + \mathbf{f_{nl3}}(\mathbf{u})\Big), \tag{1.58}$$

with the degrees of freedom $\mathbf{u} = \begin{pmatrix} u_1 & \dots & u_N \end{pmatrix}^T$, the virtual degrees of freedom $\boldsymbol{\delta}\mathbf{u} = \begin{pmatrix} \delta u_1 & \dots & \delta u_N \end{pmatrix}^T$, the linear stiffness matrix $\mathbf{K_{mat}} = \left(K^{ij}_{\text{mat}}\right)_{(i,j)\in[1,N]^2}$ and respectively the quadratic and cubic internal forces $\mathbf{f_{nl2}}(\mathbf{u}) = \left(\overset{k}{\mathrm{f}_{\text{nl2}}}\right)_{k\in[1,N]}$, $\mathbf{f_{nl3}}(\mathbf{u}) = \left(\overset{k}{\mathrm{f}_{\text{nl3}}}\right)_{k\in[1,N]}$ defined by:

$$K_e^{ij} = \int_{\Omega_0} \frac{1}{4}\left[(\boldsymbol{\nabla_X}\mathbf{N}_j) + (\boldsymbol{\nabla_X}\mathbf{N}_j)^T\right] : \boldsymbol{\mathcal{H}} : \left[(\boldsymbol{\nabla_X}\mathbf{N}_i) + (\boldsymbol{\nabla_X}\mathbf{N}_i)^T\right] \,\mathrm{d}\Omega_0 \tag{1.59}$$

$$\begin{aligned}\mathrm{f_{nl2}}^k = \sum_{i,j} \Bigg[\frac{1}{4}\int_{\Omega_0} & \left[(\boldsymbol{\nabla_X}\mathbf{N}_i) + (\boldsymbol{\nabla_X}\mathbf{N}_i)^T\right] : \boldsymbol{\mathcal{H}} : \left[(\boldsymbol{\nabla_X}\mathbf{N}_k)^T(\boldsymbol{\nabla_X}\mathbf{N}_j)\right] \\ & + \left[(\boldsymbol{\nabla_X}\mathbf{N}_i) + (\boldsymbol{\nabla_X}\mathbf{N}_i)^T\right] : \boldsymbol{\mathcal{H}} : \left[(\boldsymbol{\nabla_X}\mathbf{N}_j)^T(\boldsymbol{\nabla_X}\mathbf{N}_k)\right] \\ & + \left[(\boldsymbol{\nabla_X}\mathbf{N}_i)^T(\boldsymbol{\nabla_X}\mathbf{N}_j)\right] : \boldsymbol{\mathcal{H}} : \left[(\boldsymbol{\nabla_X}\mathbf{N}_k) + (\boldsymbol{\nabla_X}\mathbf{N}_k)^T\right] \,\mathrm{d}\Omega_0\Bigg] u_i u_j\end{aligned} \tag{1.60}$$

$$\begin{aligned}\mathrm{f_{nl3}}^k = \sum_{i,j,p} \Bigg[\frac{1}{4}\int_{\Omega_0} & \left[(\boldsymbol{\nabla_X}\mathbf{N}_i)(\boldsymbol{\nabla_X}\mathbf{N}_j)^T\right] : \boldsymbol{\mathcal{H}} : \left[(\boldsymbol{\nabla_X}\mathbf{N}_k)^T(\boldsymbol{\nabla_X}\mathbf{N}_p)\right] \\ & + \left[(\boldsymbol{\nabla_X}\mathbf{N}_i)(\boldsymbol{\nabla_X}\mathbf{N}_j)^T\right] : \boldsymbol{\mathcal{H}} : \left[(\boldsymbol{\nabla_X}\mathbf{N}_p)^T(\boldsymbol{\nabla_X}\mathbf{N}_k)\right] \,\mathrm{d}\Omega_0\Bigg] u_i u_j u_p.\end{aligned} \tag{1.61}$$

Galerkin approximation applied to the virtual work of the external forces:
The Galerkin approximation in the virtual work of the external forces writes:

$$\delta W_{\mathrm{ext}} = \int\limits_{\Gamma_0} \left(\sum_{k=1}^{N} \mathbf{N}_k^T \delta u_k\right)(\boldsymbol{FSN})\;\Gamma_0 + \int\limits_{\Omega_0} \rho_0 \left(\sum_{k=1}^{N} \mathbf{N}_k^T \delta u_k\right) \boldsymbol{b_v} \,\mathrm{d}\Omega_0 \tag{1.62}$$

$$= \sum_{k=1}^{N} \delta u_k \left[\int\limits_{\Gamma_0} \mathbf{N}_k^T (\boldsymbol{FSN})\;\Gamma_0 + \int\limits_{\Omega_0} \rho_0 \mathbf{N}_k^T \boldsymbol{b_v} \,\mathrm{d}\Omega_0\right] \tag{1.63}$$

$$= \boldsymbol{\delta}\mathbf{u}^T \Big(\mathbf{f_c} + \mathbf{f_v}\Big), \tag{1.64}$$

with $\mathbf{f_c}$ the vector of the external surface forces: $\mathbf{f_c} = \left(\mathrm{f_c}^k\right)_{k\in[1,N]}$ and $\mathbf{f_v}$ the vector of the external volume forces, $\mathbf{f_v} = \left(\mathrm{f_v}^k\right)_{k\in[1,N]}$ verifying:

$$\mathrm{f_c}^k = \int\limits_{\Gamma_0} \mathbf{N}_k^T (\boldsymbol{FSN})\;\Gamma_0, \tag{1.65}$$

$$\mathrm{f_v}^k = \int\limits_{\Omega_0} \rho_0 \mathbf{N}_k^T \boldsymbol{b_v} \,\mathrm{d}\Omega_0. \tag{1.66}$$

Galerkin approximation applied to the virtual work associated to the acceleration:
Regarding the virtual work associated to the acceleration, the introduction of the Galerkin approximation leads to:

$$\delta W_{\mathrm{acc}} = \boldsymbol{\delta}\mathbf{u}^T \Big(\mathbf{M}\ddot{\mathbf{u}} + \mathbf{D_g}\dot{\mathbf{u}} - \mathbf{K_c}\mathbf{u} + \mathbf{K_a}\mathbf{u} - \mathbf{f}_{\boldsymbol{\omega}}\Big) \tag{1.67}$$

with

- The mass matrix:

$$\mathbf{M} = \Big(\mathrm{M}^{ij}\Big)_{(i,j)\in[1,N]^2} \qquad \text{with} \qquad \mathrm{M}^{ij} = \int\limits_{\Omega_0} \rho_0 \mathbf{N}_i^T \mathbf{N}_j \,\mathrm{d}\Omega_0$$

- The gyroscopic coupling matrix:

$$\mathbf{D_g} = \left(\mathrm{D_g}^{ij}\right)_{(i,j)\in[1,N]^2} \qquad \text{with} \qquad \mathrm{D_g}^{ij} = \int\limits_{\Omega_0} 2\rho_0 \mathbf{N}_i^T \boldsymbol{\Omega} \mathbf{N}_j \; \mathrm{d}\Omega_0$$

- The centrifugal softening matrix:

$$\mathbf{K_c} = \left(\mathrm{K_c}^{ij}\right)_{(i,j)\in[1,N]^2} \qquad \text{with} \qquad \mathrm{K_c}^{ij} = -\int\limits_{\Omega_0} \rho_0 \mathbf{N}_i^T \boldsymbol{\Omega}^2 \mathbf{N}_j \; \mathrm{d}\Omega_0$$

- The centrifugal acceleration matrix:

$$\mathbf{K_a} = \left(\mathrm{K_a}^{ij}\right)_{(i,j)\in[1,N]^2} \qquad \text{with} \qquad \mathrm{K_a}^{ij} = \int\limits_{\Omega_0} \rho_0 \mathbf{N}_i^T \dot{\boldsymbol{\Omega}} \mathbf{N}_j \; \mathrm{d}\Omega_0$$

- The vector of centrifugal forces:

$$\mathbf{f}_{\boldsymbol{\omega}} = \left(\mathrm{f}_\omega{}^{k}\right)_{k\in[1,N]} \qquad \text{with} \qquad \mathrm{f}_\omega{}^{k} = -\int\limits_{\Omega_0} \rho_0 \mathbf{N}_k^T \left(\mathbf{R}^T \ddot{\hat{\boldsymbol{s}}} + \boldsymbol{\Omega}^2 \boldsymbol{X} + \dot{\boldsymbol{\Omega}} \boldsymbol{X}\right) \; \mathrm{d}\Omega_0$$

The matrix $\mathbf{K_c}$ is named centrifugal softening matrix, because in the case where the rotation vector coincides with the axis of rotation of the moving frame $\mathcal{R}_\mathrm{m}$, for instance the axis $\boldsymbol{e_z}$: $\boldsymbol{\omega} = \begin{pmatrix} 0 & 0 & \omega_3 \end{pmatrix}^T$, the rotation matrix $\boldsymbol{\Omega}$ and its square become:

$$\boldsymbol{\Omega} = \begin{pmatrix} 0 & -\omega_3 & 0 \\ \omega_3 & 0 & 0 \\ 0 & 0 & 0 \end{pmatrix} \qquad \text{and} \qquad \boldsymbol{\Omega}^2 = -\begin{pmatrix} \omega_3^2 & 0 & 0 \\ 0 & \omega_3^2 & 0 \\ 0 & 0 & 0 \end{pmatrix} \tag{1.68}$$

Therefore the matrix $\mathbf{K_c}$ has a softening effect in the global stiffness $(\mathbf{K_{mat}} - \mathbf{K_c} + \mathbf{K_a})$. Previous developments lead us to write the principal of the virtual works in the following form:

$$\boldsymbol{\delta}\mathbf{u}^T \left[\mathbf{M}\ddot{\mathbf{u}} + \mathbf{D_g}\dot{\mathbf{u}} + \big(\mathbf{K_{mat}} - \mathbf{K_c} + \mathbf{K_a}\big)\mathbf{u} + \mathbf{f_{nl2}}(\mathbf{u}) + \mathbf{f_{nl3}}(\mathbf{u}) - \mathbf{f}_{\boldsymbol{\omega}} - \mathbf{f_c} - \mathbf{f_v}\right] = \mathbf{0} \tag{1.69}$$

The problem is therefore to find $\mathbf{u}$ verifying $\boldsymbol{u}(\boldsymbol{X},t) = \sum_{i=1}^{N} \mathbf{N}_i(\boldsymbol{X}) u_i(t) \;\in \mathcal{U}$ such that for any $\boldsymbol{\delta}\mathbf{u}$ such as $\boldsymbol{\delta u}(\boldsymbol{X},t) = \sum_{i=1}^{N} \mathbf{N}_i(\boldsymbol{X}) \delta u_i(t) \;\in \delta\mathcal{U}$ the system (1.69) is verified. It leads to solve the following system, governing the dynamics of the structure:

$$\boxed{\mathbf{M}\ddot{\mathbf{u}} + \mathbf{D_g}\dot{\mathbf{u}} + \big(\mathbf{K_{mat}} - \mathbf{K_c} + \mathbf{K_a}\big)\mathbf{u} + \mathbf{f_{nl2}}(\mathbf{u}) + \mathbf{f_{nl3}}(\mathbf{u}) = \mathbf{f_c} + \mathbf{f_v} + \mathbf{f}_{\boldsymbol{\omega}}} \tag{1.70}$$

1.1.6 Equation of the dynamics with constant rotation speed

When turbomachines or propellers are considered, the structure is in rotation around a fixed axis and centrifugal effects contribute to the dynamics. In this work, the rotation speed around its axis is considered constant. The centrifugal acceleration matrix $\mathbf{K_a}$ is therefore null and the total displacement degrees of freedom of the structure, defined as $\mathbf{u}$ in Equation (1.70), are now written $\mathbf{u_t}$. The total displacement is the sum of a static nonlinear displacement $\mathbf{u_s}$ due to the centrifugal external force, and of vibrations $\mathbf{u}$ around this prestressed position: $\mathbf{u_t} = \mathbf{u_s} + \mathbf{u}$. The prestressed position $\mathbf{u_s}$ is solution of:

$$(\mathbf{K_{mat}} - \mathbf{K_c})\mathbf{u_s} + \mathbf{f_{nl}}(\mathbf{u_s}) = \mathbf{f}_{\boldsymbol{\omega}}, \tag{1.71}$$

with $\mathbf{f_{nl}}(\mathbf{u})$ the sum of the quadratic $\mathbf{f_{nl2}}(\mathbf{u})$ and cubic $\mathbf{f_{nl3}}(\mathbf{u})$ nonlinear forces. Centrifugal effects are included in the softening matrix $\mathbf{K_c}$ and the constant centrifugal load $\mathbf{f}_{\boldsymbol{\omega}}$. The geometric nonlinearities $\mathbf{f_{nl}}$ are expanded around the prestressed solution $\mathbf{u_s}$:

$$\mathbf{f_{nl}}(\mathbf{u_s} + \mathbf{u}) = \mathbf{f_{nl}}(\mathbf{u_s}) + \mathbf{K_{nl}}(\mathbf{u_s})\mathbf{u} + \mathbf{g_{nl}}(\mathbf{u}), \tag{1.72}$$

where $\mathbf{K_{nl}}(\mathbf{u_s})$ is the tangent stiffness matrix, i.e. the Jacobian of $\mathbf{f_{nl}}(\mathbf{u_t})$ evaluated at the prestressed position $\mathbf{u_s}$ and $\mathbf{g_{nl}}(\mathbf{u})$ is the vector of the nonlinear forces with respect to the prestressed position as illustrated in Figure 1.3. In the rotating frame, the equation governing the vibrations of the structure around the centrifugally prestressed position is:

$$\mathbf{M}\ddot{\mathbf{u}} + \mathbf{C}\dot{\mathbf{u}} + \underbrace{\left[\mathbf{K_{mat}} - \mathbf{K_c} + \mathbf{K_{nl}}(\mathbf{u_s})\right]}_{\mathbf{K}(\Omega)} \mathbf{u} + \mathbf{g_{nl}}(\mathbf{u}) = \underbrace{\mathbf{f_c} + \mathbf{f_v}}_{\mathbf{f}_{\mathrm{ext}}}, \tag{1.73}$$

in which the gyroscopic effect was neglected and a Rayleigh structural damping $\mathbf{C}$ introduced. Due to the centrifugal and geometrical nonlinear effects, a hardening or softening behavior can be observed depending on the speed of rotation and the considered mode [187].

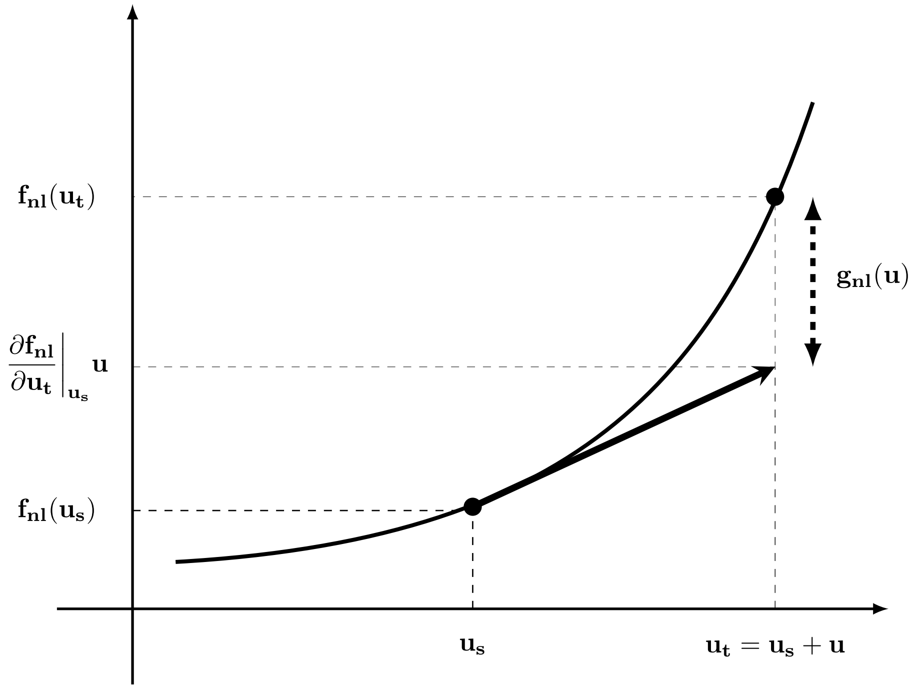

Figure 1.3: Nonlinear geometric forces at constant rotation speed.

1.2 Methods of resolution

In the previous section, the equation governing the dynamics of the structure was established. For the sake of simplicity, whether the structure is in rotation or not, the total internal forces including the stiffness are written $\mathbf{f}_{\mathbf{int}}(\mathbf{u})$. A simplified form of the equation of the dynamics can thus be written as follows:

$$\mathbf{M}\ddot{\mathbf{u}} + \mathbf{C}\dot{\mathbf{u}} + \mathbf{f}_{\mathbf{int}}(\mathbf{u}) = \mathbf{f}_{\text{ext}}. \tag{1.74}$$

There are two main types of resolution of such an equation. On one side the temporal integration of the equation relative to initial conditions and a time-dependent external load. On the other side frequency methods aim to compute directly the limit cycle associated with a harmonic external force.

1.2.1 Temporal methods

The dynamics of the structure can be solved with a temporal integration from an initial condition. Temporal resolutions compute the dynamics of the structure during the transient regime reaching a possible periodic regime also called a dynamic steady state. Numerous temporal solver schemes exist in the literature for the time integration of dynamical equations like backward differentiation, Runge-Kutta methods, multi-step methods like the Gear [62] scheme or the Bathe algorithm [9] and its variations Bathe-β_1/β_2, ρ_∞-Bathe. In structural dynamics, one-step methods of the Newmark's family are usually preferred, like the standard Newmark algorithm [134] and its variations HHT-α [78] and α-generalized [4, 27], briefly recalled in the next paragraph.

The Newmark scheme [157] is based on an acceleration averaged in the time step $\forall t \in [t_n, t_{n+1}]$: $\ddot{\mathbf{u}}(t) = (\ddot{\mathbf{u}}(t_n) + \ddot{\mathbf{u}}(t_{n+1}))/2$ (with the temporal discretization $t_{n+1} = t_n + \Delta t$) and two coefficients γ and β such that:

$$\mathbf{u}_{n+1} = \mathbf{u}_n + \Delta t\dot{\mathbf{u}}_n + \frac{\Delta t^2}{2}\left[(1-2\beta)\ddot{\mathbf{u}}_n + 2\beta\ddot{\mathbf{u}}_{n+1}\right] \tag{1.75}$$

$$\dot{\mathbf{u}}_{n+1} = \dot{\mathbf{u}}_n + \Delta t\left[(1-\gamma)\ddot{\mathbf{u}}_n + \gamma\ddot{\mathbf{u}}_{n+1}\right]. \tag{1.76}$$

The parameters γ, β control the numerical damping, accuracy and stability of the integration scheme. The values $\gamma = 0.5$, $\beta = 0.25$ are usually chosen to guarantee linear unconditional stability, no numerical damping and second-order accuracy. For geometrically nonlinear problems, Newmark's scheme is also unconditionally stable with the parameters $\gamma = 0.5$ and $\beta \geq 0.25$ [84]. The practical implementation of the nonlinear Newmark algorithm is based on a prediction step and a correction step, the latter including a Newton-Raphson iterative method for the convergence of the residual. Figure 1.4 explains in pseudo-code the implementation of the nonlinear Newmark algorithm.

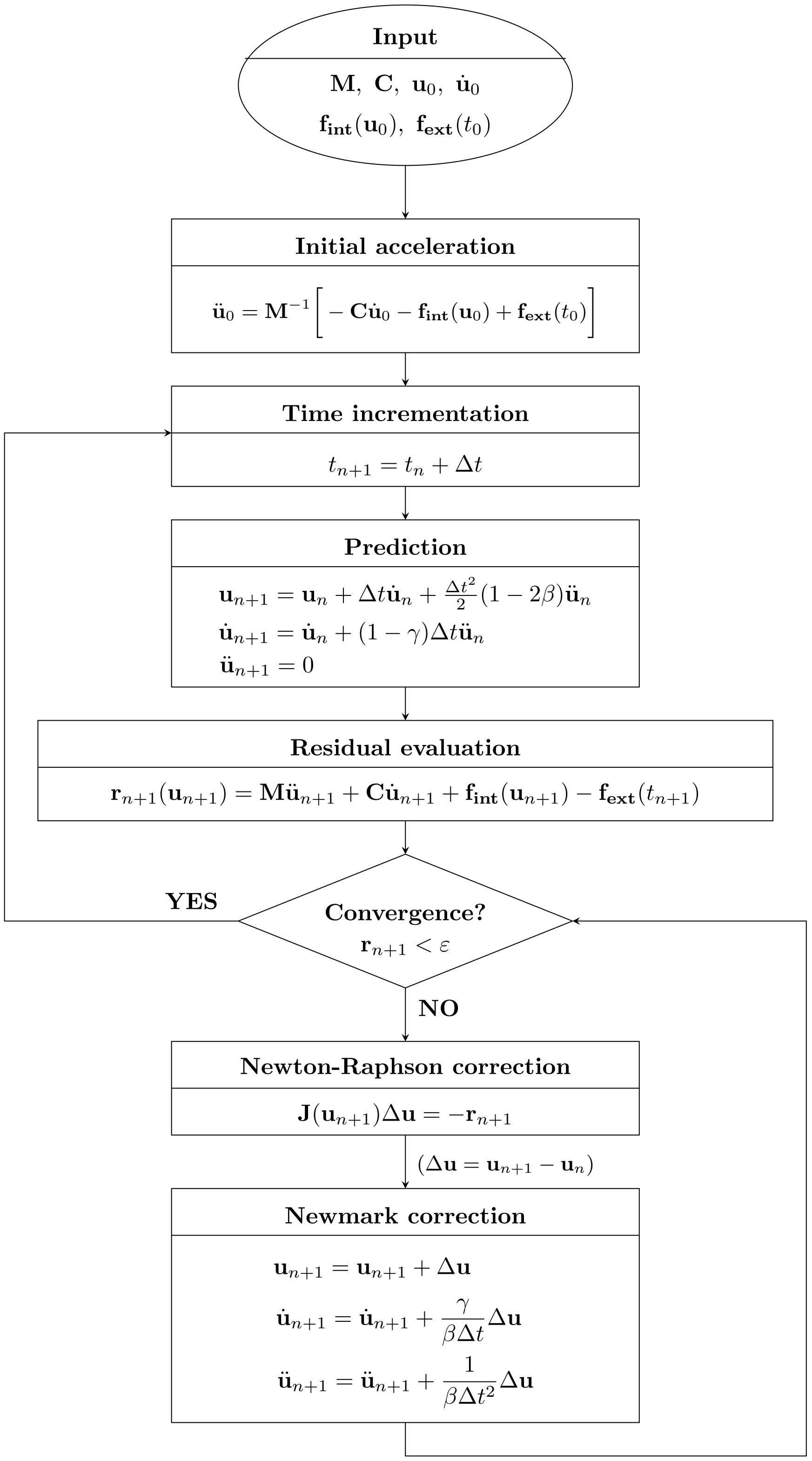

Figure 1.4: Nonlinear Newmark integration scheme as presented in [157].

In structural dynamics, a slight numerical damping is sometimes desired in order to mitigate the large frequencies that have a negligible contribution to the dynamics and that can lead to numerical instabilities. In Newmark's scheme, the numerical damping is controlled by the coefficient γ, when

$\gamma \geq 0.5$. The HHT-α integration scheme was proposed in [78] to introduce numerical damping while preserving unconditional stability. The Newmark coefficients γ, β are both defined regarding a single parameter $\alpha_{\text{HHT}} \in [0, \frac{1}{3}[$ introducing numerical damping by setting $\gamma \geq 0.5$ and preserving the unconditional stability:

$$\gamma = \frac{1}{2} + \alpha_{\text{HHT}} \tag{1.77}$$

$$\beta = \frac{1}{4}(1 + \alpha_{\text{HHT}})^2. \tag{1.78}$$

The coefficient α_{HHT} can be defined according to the asymptotic spectral radius $0.5 \leq \rho_\infty \leq 1$ such that $\rho_\infty = 1$ leads to no numerical damping. The coefficient α_{HHT} is determined from the asymptotic spectral radius as follows:

$$\alpha_{\text{HHT}} = \frac{1 - \rho_\infty}{1 + \rho_\infty}. \tag{1.79}$$

Nevertheless, with such a choice of parameters, the usual Newmark scheme loses its second-order accuracy to a first-order accuracy. The HHT-α integration scheme proposes to keep the second-order accuracy by modifying the equation of the dynamics in averaging the internal and external forces between the current and previous time steps via the parameter α_{HHT}:

$$\begin{aligned} \mathbf{M}\ddot{\mathbf{u}}_{n+1} + (1 - \alpha_{\text{HHT}}) \left[\mathbf{C}\dot{\mathbf{u}}_{n+1} + \mathbf{f_{int}}(\mathbf{u}_{n+1})\right] + \alpha_{\text{HHT}} \left[\mathbf{C}\dot{\mathbf{u}}_n + \mathbf{f_{int}}(\mathbf{u}_n)\right] \\ = (1 - \alpha_{\text{HHT}})\mathbf{f}_{\text{ext}}(t_{n+1}) + \alpha_{\text{HHT}}\mathbf{f}_{\text{ext}}(t_n). \end{aligned} \tag{1.80}$$

Similarly, Chung and Hulbert [27] proposed the α-generalized method, averaging the force terms in the dynamics equation like the HHT-α method with a coefficient α_f but also averaging the inertial term with a different coefficient α_m:

$$\begin{aligned} (1 - \alpha_m)\mathbf{M}\ddot{\mathbf{u}}_{n+1} + \alpha_m\mathbf{M}\ddot{\mathbf{u}}_n + (1 - \alpha_f) \left[\mathbf{C}\dot{\mathbf{u}}_{n+1} + \mathbf{f_{int}}(\mathbf{u}_{n+1})\right] + \alpha_f \left[\mathbf{C}\dot{\mathbf{u}}_n + \mathbf{f_{int}}(\mathbf{u}_n)\right] \\ = (1 - \alpha_f)\mathbf{f}_{\text{ext}}(t_{n+1}) + \alpha_f\mathbf{f}_{\text{ext}}(t_n). \end{aligned} \tag{1.81}$$

The Newmark coefficients γ, β are determined from the coefficients $0 \leq \alpha_m \leq \alpha_f \leq 0.5$ to keep the second-order accuracy and unconditional stability:

$$\gamma = \frac{1}{2} + \alpha_f + \alpha_m \tag{1.82}$$

$$\beta = \frac{1}{4}(1 + \alpha_f + \alpha_m)^2, \tag{1.83}$$

where the coefficients α_m and α_f can be expressed from the asymptotic spectral radius with:

$$\alpha_m = \frac{2\rho_\infty - 1}{\rho_\infty + 1} \tag{1.84}$$

$$\alpha_f = \frac{\rho_\infty}{\rho_\infty + 1}. \tag{1.85}$$

A study of the nonlinear properties of the α-generalized method is proposed in [4] along with a different nonlinear algorithm for the implementation.

1.2.2 Frequency methods

The integration of the dynamics of the structure under a periodic external load can result in a significant transient regime before reaching a periodic steady state. In some cases, the integration during the transient regime can be computationally expensive to compute for large structures and of no specific interest. Therefore, frequency methods of integration enable computing only the periodic steady-state resulting in faster computations. Besides, the computational time of a continuation method along one parameter such as the frequency of excitation for instance is greatly reduced and unstable regions are easier to capture than with temporal integrations.

A common frequency method is the *Harmonic Balance Method* (HBM) [6, 75, 103, 128]. It consists in searching the solution of the dynamics equation directly in the space of periodic functions and is usually combined with a continuation method with respect to a parameter (for instance the frequency) to capture the limit cycles. Common continuation methods are for instance the *arc-length* and *pseudo arc-length* methods, the *Shooting* method or the *Asymptotic-Numerical Method* (ANM). The *Shooting* continuation method [85, 129, 130, 172, 183] consists in starting from a periodic limit cycle then slightly modifying the continuation parameter and converging to the new limit cycle with Newton-Raphson iterations. The ANM [29, 31, 127] is a continuation method along nonlinear branches based on the perturbation method.

This paragraph illustrates the HBM continuation first on the test case of a Duffing oscillator, then on a Timoshenko beam. The equation governing the dynamics of the Duffing oscillator is the following:

$$m\ddot{x} + c\dot{x} + kx + \alpha_D x^3 = f. \tag{1.86}$$

In the case considered, the mass $m = 1$, damping $c = 0.05$, stiffness $k = 1$ and the influence of the nonlinear factor α_D and the external load f are illustrated. Figure 1.5 represents the HBM continuation of the Duffing oscillator with various levels of external force for a fixed nonlinear parameter $\alpha_D = 1$ compared to the linear case corresponding to $\alpha_D = 0$. The backbone curve representing the evolution of the maximal displacement and associated pulsation as a function of the external force is also represented in the figure and can be approximated as follows [208]:

$$A = \sqrt{\frac{4m(\omega^2 - \omega_0^2)}{3\alpha_D}}, \tag{1.87}$$

with A the amplitude of the displacement and $\omega_0 = \sqrt{k/m}$ the angular frequency of the associated linear system.

It can be noticed that the unstable region where two solutions exist for the same pulsation is captured by the HBM continuation. A continuation with temporal methods fails to capture such an unstable region resulting in a jump from one branch to the other at the bifurcation point.

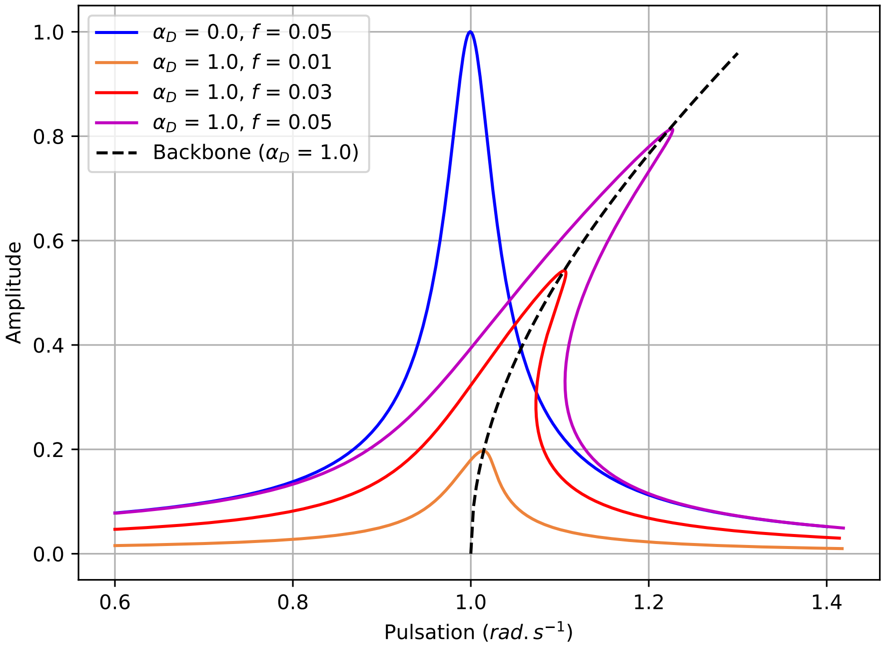

Figure 1.5: Frequency response of a Duffing oscillator with increasing external load obtained using the HBM continuation method.

Similarly, Figure 1.6 represents the HBM continuation for a fixed external force $f = 0.1$ N and different signs and amplitudes of the cubic nonlinear parameter α_D. The nonlinear behavior of the oscillator is hardening for positive values of α_D and softening for negative values.

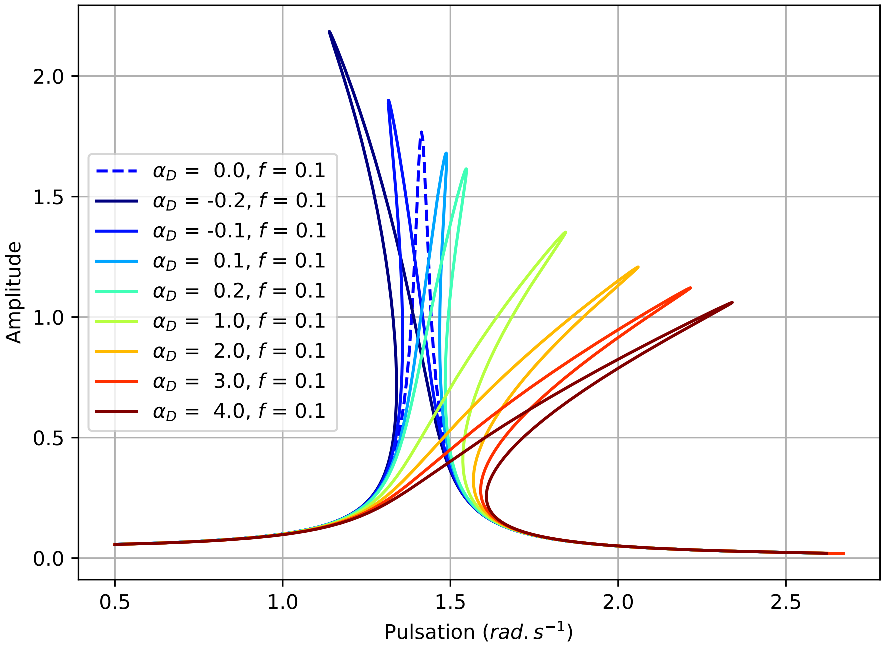

Figure 1.6: Frequency response of a Duffing oscillator using the HBM continuation method for several values of the nonlinear parameters α_D.

The second application illustrates the HBM continuation for the case of a 2D Timoshenko beam[1] reduced to its neutral axis. The beam is bi-clamped and loaded vertically in the middle with an external load of 1 N. The length of the beam is equal to 1 m, its thickness $h = 0.005$ m and its width 0.1 m. The Young's modulus is equal to $E = 104$ GPa and the density is $\rho = 4400$ kg.m^{-3}. The beam is discretized using 6 Finite Elements with linear shape functions and a reduced integration of the nonlinear terms to avoid shear locking [171]. The damping matrix is equal to $\mathbf{C} = 2\xi\mathbf{M}$ with a damping factor $\xi = 0.005$. Figure 1.7 depicts the vertical displacement at the beam centre divided by the thickness. For such a test case, the geometric nonlinearity is significant even for small amplitudes of displacement.

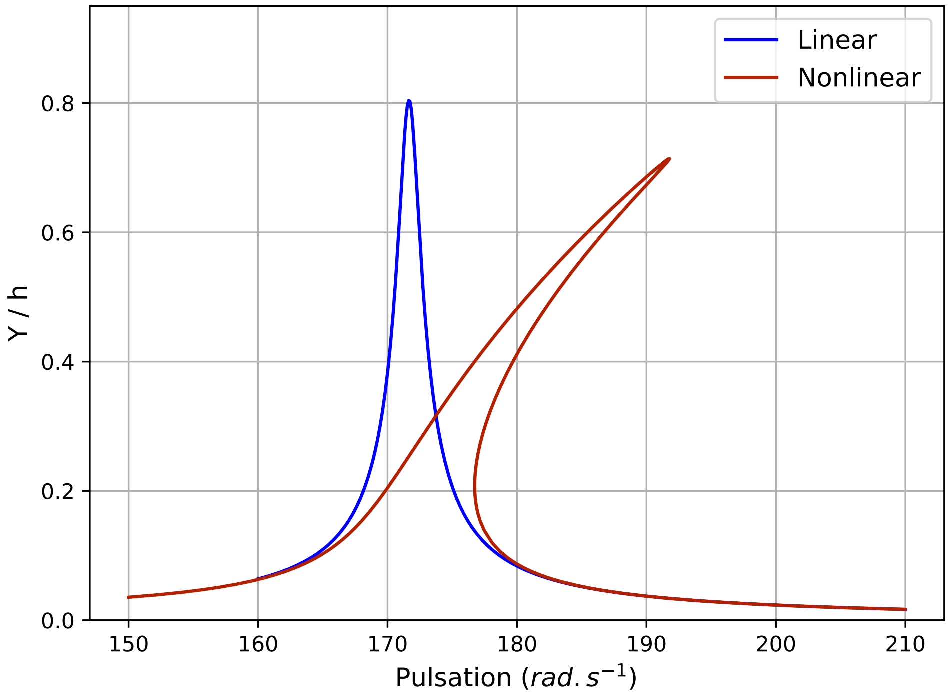

Figure 1.7: Frequency response obtained with HBM continuation of a Timoshenko beam loaded vertically at the center.

---

[1] This model has been developed during the thesis but is not presented here for the sake of brevity.

1.3 Reduction techniques for nonlinear structures

In the previous section, the structural dynamics equations were established and methods of resolution were introduced. The resolution of large FE systems is computationally expensive. The topic of the current section is to present some methods found in the literature to build reduced order models (ROMs) and thus reduce the size of the system to solve and the computational time. The focus is on projection-based reduced order models with the determination of the projection basis and the expression of the projected nonlinear forces. Then, other reduction methods are briefly introduced.

1.3.1 Projection-based reduced order models

The behavior of the structure is studied thanks to a classical finite element model, whose degrees of freedom in displacement, written $\mathbf{u}$, verify the equation of the dynamics:

$$\mathbf{M}\ddot{\mathbf{u}} + \mathbf{C}\dot{\mathbf{u}} + \mathbf{f_{int}}(\mathbf{u}) = \mathbf{f}_{\mathrm{a}}(\mathbf{u_t}, \dot{\mathbf{u}}_\mathbf{t}), \tag{1.88}$$

where $\mathbf{M}$,$\mathbf{C}$, $\mathbf{f_{int}}$, and $\mathbf{f}_{\mathrm{a}}$ are respectively the mass matrix, the damping matrix, the internal forces and the aerodynamic forces vector in the case of an aeroelastic problem. The internal forces can be decomposed as the sum of a linear component $\mathbf{Ku}$ with $\mathbf{K}$ the elastic stiffness matrix and a geometric nonlinear component $\mathbf{g_{nl}}(\mathbf{u})$.

Projection-based reduced order models consist in projecting the equations of the dynamics on a wisely-chosen basis of reduced dimension $\mathbf{V}$. The displacements degrees of freedom are approximated by $\mathbf{u} \approx \mathbf{Vq}$ where $\mathbf{q}$ are called the generalized coordinates. After projection, the equation of the dynamics becomes :

$$\underbrace{\mathbf{V}^T\mathbf{M}\mathbf{V}}_{\widetilde{\mathbf{M}}}\ddot{\mathbf{q}} + \underbrace{\mathbf{V}^T\mathbf{C}\mathbf{V}}_{\widetilde{\mathbf{C}}}\dot{\mathbf{q}} + \underbrace{\mathbf{V}^T\mathbf{K}\mathbf{V}}_{\widetilde{\mathbf{K}}}\mathbf{q} + \underbrace{\mathbf{V}^T\mathbf{g_{nl}}(\mathbf{Vq})}_{\widetilde{\mathbf{g}}_{\mathbf{nl}}(\mathbf{q})} = \underbrace{\mathbf{V}^T\mathbf{f}_{\mathrm{a}}}_{\widetilde{\mathbf{f}}_{\mathrm{a}}}. \tag{1.89}$$

The reduction matrix $\mathbf{V}$ contains only few vectors, therefore the projected matrices $\widetilde{\mathbf{M}}$, $\widetilde{\mathbf{C}}$ and $\widetilde{\mathbf{K}}$ have negligible dimensions compared to the initial problem.

1.3.1.1 Reduction on a linear basis

Mechanical vibrations can be characterized by linear normal modes $\mathbf{\Phi} = \{\boldsymbol{\phi}_1, \cdots, \boldsymbol{\phi}_n\}$, where n is the number of degrees of freedom of the structure. The linear normal modes are solution vectors of the eigenvalue equation :

$$\left(\mathbf{K} - \omega_i^2\mathbf{M}\right)\boldsymbol{\phi}_i = \mathbf{0} \ \ \forall i \in [1, n], \tag{1.90}$$

where ω_i are the angular eigenfrequencies.

When the amplitudes of displacement are small and the geometric nonlinearity can be neglected, the problem is linear. In such a case, a satisfactory choice to represent the dynamical behavior is a reduction basis containing only the first linear normal modes, computed around the prestressed position, and whose frequencies belong to the excitation band. On the contrary, when the geometric nonlinearity is significant, a coupling may appear between some low and high frequency modes. Consequently, the first linear modes are no longer sufficient to capture the whole dynamics and the reduction basis needs to be enriched by other modes in order to account for the coupling between the modes.

1.3.1.2 Proper-orthogonal decomposition, a simulation-based reduced order model

When the distribution of the external forces applied to the structure is fixed and known, nonlinear static solutions (also known as static modes) can be included in the reduction basis. Likewise, the reduction basis can be obtained from former simulation results using simulation-based methods such as the Proper-Orthogonal Decomposition (POD). The POD modes can for instance be determined by Singular Value Decomposition (SVD) from samples of high-fidelity computations and embrace relevant information characterizing the nonlinear deformation of the structure. The idea of the POD is to consider n_a "snapshots" of one or several solutions of the full order system. Each snapshot is a vector of the displacements of the degrees of freedom under external excitation. Several full-order model simulations with representative external loads are computed, from which snapshots of those solutions are extracted. The POD method is an optimization problem consisting in finding an optimal orthogonal base of a lower dimension that minimises the error of the orthogonal projection. Applications to structural and fluid dynamics are found for example in [11, 54, 98, 104, 111, 148, 149, 167, 203].

The snapshots are gathered in a matrix $\mathbf{A}$ (of size $(N \times n_a)$) in which columns are the snapshots. Considering the correlation matrix $\mathbf{R_{corr}} = \mathbf{A}\mathbf{A}^T$, the POD modes $\mathbf{\Phi}_{POD}$ (called Proper Orthogonal Modes) solutions of the POD optimization problem can be computed as the eigenvectors related to the non-zero eigenvalues of the correlation matrix $\mathbf{R_{corr}}$.

$$\mathbf{R_{corr}}\mathbf{\Phi}_{POD} = \mathbf{\Phi}_{POD}\mathbf{D}_{POD} \quad \text{with} \quad \mathbf{R_{corr}} = \mathbf{A}\mathbf{A}^T \tag{1.91}$$

where $\mathbf{D}_{POD}$ is a diagonal matrix containing the associated eigenvalues (called Proper Orthogonal Values). Those eigenvalues are real and positive since the matrix $\mathbf{R_{corr}} = \mathbf{A}\mathbf{A}^T$ is symmetrical and positively defined. The POD modes are orthogonal, and verify $\mathbf{\Phi}_{POD}^T\mathbf{\Phi}_{POD} = \mathbf{I}$ when appropriately normalized. This way of calculating the POD modes is used when the dimension of the matrix $\mathbf{R_{corr}}$ is small. It is called the *direct method.* A second method for the computing of the POD modes is the Singular Value Decomposition of the matrix $\mathbf{A}$:

$$\mathbf{A} = \mathbf{U}\mathbf{\Sigma}\mathbf{W}^T \quad \text{with} \quad \mathbf{U}\mathbf{U}^T = \mathbf{I} \quad \text{and} \quad \mathbf{W}\mathbf{W}^T = \mathbf{I} \tag{1.92}$$

$$\mathbf{\Sigma} = \begin{pmatrix} \mathbf{\Sigma}_r & 0 \\ 0 & 0 \end{pmatrix} \quad \text{with} \quad \mathbf{\Sigma}_r = \operatorname{diag}(\lambda_1, \lambda_2, \cdots, \lambda_r) \tag{1.93}$$

The matrices $\mathbf{U}$ $(N \times N)$ and $\mathbf{W}$ $(n_a \times n_a)$ are orthogonal. $\mathbf{\Sigma}$ is a matrix $(N \times n_a)$ and $\lambda_1, \lambda_2, \cdots, \lambda_r$ are singular values of the matrix $\mathbf{A}$ with r the rank of the matrix $\mathbf{A}$. Writing $\mathbf{U}_r$ and $\mathbf{W}_r$ the r first columns of $\mathbf{U}$ and $\mathbf{W}$, the snapshot matrix is given by $\mathbf{A} = \mathbf{U}_r\mathbf{\Sigma}_r\mathbf{W}_r{}^T$ with $\mathbf{U}_r\mathbf{U}_r^T = \mathbf{I}$ and $\mathbf{W}_r\mathbf{W}_r^T = \mathbf{I}$. The eigenvectors of the correlation matrix can easily be computed using the singular value decomposition considering the following relation:

$$\mathbf{R_{corr}}\mathbf{U}_r = \mathbf{A}\mathbf{A}^T\mathbf{U}_r = \mathbf{U}_r\mathbf{\Sigma}_r^2. \tag{1.94}$$

Henceforth, the vectors of the matrix $\mathbf{U}_r$ are the POD modes and the associated eigenvalues are $\mathbf{D}_{POD} = \mathbf{\Sigma}^2$.

Another way to compute the POD modes is based on the observation that the eigenvalues (the diagonal terms of $\mathbf{D}_{POD}$) of $\mathbf{A}^T\mathbf{A}$ are the sames as the eigenvalues of $\mathbf{A}\mathbf{A}^T$:

$$\mathbf{A}^T\mathbf{A}\ \mathbf{W}_r = \mathbf{W}_r\mathbf{\Sigma}^2 = \mathbf{W}_r\mathbf{D}_{POD}. \tag{1.95}$$

However the POD modes are the eigenvectors of $\mathbf{A}\mathbf{A}^T$ not the eigenvectors of $\mathbf{A}^T\mathbf{A}$. Nevertheless the eigenvectors of $\mathbf{A}\mathbf{A}^T$ are linked to the eigenvectors of $\mathbf{A}^T\mathbf{A}$ by the following relation:

$$\mathbf{U}_r\mathbf{\Sigma}_r\mathbf{W}_r^T = \mathbf{A} \implies \mathbf{U}_r = \mathbf{A}(\mathbf{\Sigma}_r\mathbf{W}_r)^{-1} = \mathbf{A}\mathbf{W}_r\mathbf{\Sigma}_r^{-1}, \tag{1.96}$$

where $\mathbf{\Sigma}_r^{-1}$ is a diagonal matrix that is a normalisation of the eigenvectors $\mathbf{W}_r$ of $\mathbf{A}^T\mathbf{A}$. The idea of the *snapshot method* presented by Sirovich in 1987 is to compute the eigenvectors $\mathbf{x_a}$ of the matrix $\mathbf{A}^T\mathbf{A}$ and to determine the POD modes (eigenvectors of $\mathbf{A}\mathbf{A}^T$) by multiplicating those eigenvectors by the matrix of the snapshots $\mathbf{A}$: $\mathbf{\Phi}_{POD} = \mathbf{A}\mathbf{x_a}$. The advantage is that the size of the matrix $\mathbf{A}^T\mathbf{A}$ is $(n_a \times n_a)$ which is usually smaller than the size $(N \times N)$ of the matrix $\mathbf{A}\mathbf{A}^T$. Most of the time, not all those modes are necessary but only the ones with the highest eigenvalues λ_k, representing the most significant percentage of the sum of all the eigenvalues. The POD eigenvalues are ranked from the highest to the lowest $\lambda_1, \lambda_2, \cdots, \lambda_r$. Writing $\mathcal{E}_{cu}$ the relative information criteria of the snapshots captured by the first k POD vectors: $\mathcal{E}_{cu} = \sum_{i=1}^{k} \lambda_i / \sum_{i=1}^{r} \lambda_i$, an arbitrary way to select the POD modes is to take the ones for which the sum of the respective eigenvalues represent 99% of the sum of all the eigenvalues (ie $\mathcal{E}_{cu} = 0.99$). Nevertheless, this method is arbitrary and biased since the eigenvalues λ_i span different orders of magnitude and the criteria of $\mathcal{E}_{cu} = 0.99$ may be reached with only the first or two first eigenvalues λ_i while more are necessary for a satisfactory accuracy. A more accurate selection of them is to observe the distribution of the eigenvalues with a log scale and see if there is a distinct gap between the significant and the negligible modes.

The POD modes are optimal compared to the linear modes because they are determined from snapshots of solutions and are the result of a minimisation problem. Nevertheless, the POD modes are particularly dependent on the load case, making them inadequate for the various load cases such as those encountered in aerodynamics. Besides, POD modes require a database of high-fidelity nonlinear solutions, whose generation involves expensive calculations for industrial applications.

1.3.1.3 Modal derivatives

As explained previously, the truncation of the linear normal modes to build the reduced basis does not accurately capture the nonlinear phenomena. Specific modes have to be added to the reduction basis to give a precise account of the nonlinearity. However, the modes added to the reduction basis should contain information on the coupling between several linear normal modes and should not depend on specific loading cases. One idea is the extension to the nonlinearity of the linear normal modes, introducing modal derivatives. Modal derivatives are second-order Taylor decompositions of the equilibrium position of the structure. Considering a displacement $\mathbf{u}$ around the equilibrium/prestressed position $\mathbf{u_s}$, the total displacement with respect to the undeformed position is written: $\mathbf{u_t} = \mathbf{u_s} + \mathbf{u}$. The modal truncation of the linear normal modes consists in approximating the displacement $\mathbf{u}$ at the first order using the linear normal modes computed on the position $\mathbf{u_s}$:

$$\mathbf{u} \simeq \sum_{i=1}^{n_\mathrm{b}} \boldsymbol{\phi}_i(\mathbf{u_s}) q_i. \tag{1.97}$$

Nevertheless, this approximation is valid in the linear range, when $\mathbf{u}$ is small, meaning that the displacement is close to the equilibrium position where the linear normal modes are computed. Therefore, when the displacement around $\mathbf{u_s}$ is larger, the linear normal modes on the current position $\boldsymbol{\phi}_i(\mathbf{u_s} + \mathbf{u})$ are different than those computed at the equilibrium position $\boldsymbol{\phi}_i(\mathbf{u_s})$. The idea of modal derivatives is to consider the evolution of the effective linear normal modes as a function of the generalized coordinates from the decomposition (1.97): $\boldsymbol{\phi}_i(\mathbf{u_s}+\mathbf{u}) = \boldsymbol{\phi}_i(\mathbf{q})$. Therefore $\mathbf{u} \simeq \sum_{i=1}^{n_\mathrm{b}} \boldsymbol{\phi}_i(\mathbf{q}) q_i$ and the displacement $\mathbf{u}$ is approximated with a second order Taylor decomposition:

$$\mathbf{u} \approx \sum_{i=1}^{n_\mathrm{b}} \left.\frac{\partial \mathbf{u}}{\partial q_i}\right|_{\mathbf{q}=0} q_i + \sum_{i=1}^{n_\mathrm{b}}\sum_{j=1}^{n_\mathrm{b}} \frac{1}{2}\left(\left.\frac{\partial^2 \mathbf{u}}{\partial q_i \partial q_j}\right|_{\mathbf{q}=0} + \left.\frac{\partial^2 \mathbf{u}}{\partial q_i \partial q_j}\right|_{\mathbf{q}=0}\right) q_i q_j. \tag{1.98}$$

Evaluating the derivatives of the displacement regarding the generalized coordinates using equation (1.97) gives:

$$\frac{\partial \mathbf{u}}{\partial q_i} = \boldsymbol{\phi}_i(\mathbf{q}) + \sum_{j=1}^{n_\mathrm{b}} \frac{\partial \boldsymbol{\phi}_i(\mathbf{q})}{\partial q_i} q_j \tag{1.99}$$

$$\frac{\partial^2 \mathbf{u}}{\partial q_i \partial q_j} = \frac{\partial \boldsymbol{\phi}_i(\mathbf{q})}{\partial q_j} + \frac{\partial \boldsymbol{\phi}_j(\mathbf{q})}{\partial q_i} + \sum_{k=1}^{n_\mathrm{b}} \frac{\partial^2 \boldsymbol{\phi}_k(\mathbf{q})}{\partial q_i \partial q_j} q_k \tag{1.100}$$

The evaluation of the derivatives at the prestressed position are thus:

$$\left.\frac{\partial \mathbf{u}}{\partial q_i}\right|_{\mathbf{q}=0} = \boldsymbol{\phi}_i(\mathbf{u_s}) \tag{1.101}$$

$$\left.\frac{\partial^2 \mathbf{u}}{\partial q_i \partial q_j}\right|_{\mathbf{q}=0} = \frac{\partial \boldsymbol{\phi}_i}{\partial q_j}(\mathbf{u_s}) + \frac{\partial \boldsymbol{\phi}_j}{\partial q_i}(\mathbf{u_s}), \tag{1.102}$$

and the Taylor expansion of the displacement is finally expressed with the derivative of the linear normal modes:

$$\mathbf{u} \approx \sum_{i=1}^{n_\mathrm{b}} \boldsymbol{\phi}_i(\mathbf{u_s})\, q_i + \sum_{i=1}^{n_\mathrm{b}}\sum_{j=1}^{n_\mathrm{b}} \frac{1}{2}\left(\underbrace{\frac{\partial \boldsymbol{\phi}_i}{\partial q_j}(\mathbf{u_s})}_{\boldsymbol{\theta}_{ij}} + \underbrace{\frac{\partial \boldsymbol{\phi}_j}{\partial q_i}(\mathbf{u_s})}_{\boldsymbol{\theta}_{ji}} \right) q_i q_j, \tag{1.103}$$

where the first term is the linear mode computed on the equilibrium position and $\boldsymbol{\theta}_{ij}, \boldsymbol{\theta}_{ji}$ are the modal derivatives. They represent the evolution of the mode $\boldsymbol{\phi}_i(\mathbf{u_s})$ for a displacement in the direction of the mode $\boldsymbol{\phi}_j(\mathbf{u_s})$ and vice versa. In what follows the notation $\boldsymbol{\phi}_i$ replaces the notation $\boldsymbol{\phi}_i(\mathbf{u_s})$ for the sake of simplicity. Since the linear modes are computed on the equilibrium position there is no ambiguity. The reduction basis chosen for the projection is finally:

$$\mathbf{V} = \Big[\underbrace{\boldsymbol{\phi}_1, \cdots, \boldsymbol{\phi}_{n_\mathrm{b}}}_{\text{linear modes}}, \underbrace{\boldsymbol{\theta}_{11}, \cdots, \frac{1}{2}(\boldsymbol{\theta}_{ij}+\boldsymbol{\theta}_{ji}), \cdots, \boldsymbol{\theta}_{n_\mathrm{b} n_\mathrm{b}}}_{\text{modal derivatives}} \Big] \tag{1.104}$$

Numerical computation of the modal derivatives: There are several ways to compute modal derivatives using a FE solver [86, 88, 114, 133, 166, 178]. In [86, 88, 133], the authors suggest an exact computation of the modal derivatives by differentiating regarding the generalized coordinates q_j the eigenvalue equation $(\mathbf{K} - \omega_i^2 \mathbf{M})\boldsymbol{\phi}_i = 0$ verified by the linear normal mode $\boldsymbol{\phi}_i$:

$$(\mathbf{K} - \omega_i^2 \mathbf{M}) \frac{\partial \boldsymbol{\phi}_i}{\partial q_j} + \left(\frac{\partial \mathbf{K}}{\partial q_j} - \frac{\partial \omega_i^2}{\partial q_j}\mathbf{M} \right) \boldsymbol{\phi}_i = 0, \tag{1.105}$$

where $\mathbf{K}$ is the stiffness evaluated at the position $\mathbf{u_s}$, it corresponds to the tangent stiffness matrix evaluated at the prestressed displacement: $\mathbf{K_{tan}}(\mathbf{u_s})$. As a reminder, the tangent stiffness matrix is the derivation of the internal forces $\mathbf{f_{int}}$ regarding the displacement: for a total displacement $\mathbf{u_t}$, $\mathbf{K_{tan}}(\mathbf{u_t}) = \partial \mathbf{f_{int}}(\mathbf{u_t})/\partial \mathbf{u_t}$. When the structure is undeformed, the tangent stiffness matrix corresponds to the elastic stiffness $\mathbf{K_{mat}}$. In Equation (1.105), the derivative $\partial \mathbf{K}/\partial q_j$ is the evolution of the tangent stiffness under a displacement in the direction of the mode $\boldsymbol{\phi}_j$:

$$\frac{\partial \mathbf{K}}{\partial q_j} = \frac{\partial \mathbf{K_{tan}}(\mathbf{u_s} + q_j \boldsymbol{\phi}_j)}{\partial q_j}. \tag{1.106}$$

From a numerical point of view, it can be computed in a non-intrusive way using a FE solver with finite differences, for instance a centered derivation:

$$\frac{\partial \mathbf{K_{tan}}}{\partial q_j} = \frac{\mathbf{K_{tan}}(\mathbf{u_s} + h\boldsymbol{\phi}_j) - \mathbf{K_{tan}}(\mathbf{u_s} - h\boldsymbol{\phi}_j)}{2h} \tag{1.107}$$

where h is a small displacement in the direction of the mode j. At this point, the unknowns are the modal derivative and the derivative of the associated eigenvalue. A second relation is provided by the derivation regarding the generalized coordinate q_j of the M-orthogonality relation: $\boldsymbol{\phi}_i^T \mathbf{M} \boldsymbol{\phi}_i = 1$ verified by the linear normal modes $\boldsymbol{\phi}_i$:

$$\boldsymbol{\phi}_i^T \mathbf{M} \frac{\partial \boldsymbol{\phi}_i}{\partial q_j} + \boldsymbol{\phi}_i^T \mathbf{M}^T \frac{\partial \boldsymbol{\phi}_i}{\partial q_j} = 0 \tag{1.108}$$

$$\implies \boldsymbol{\phi}_i^T \mathbf{M} \frac{\partial \boldsymbol{\phi}_i}{\partial q_j} = 0, \tag{1.109}$$

using the symmetry of the mass matrix: $\mathbf{M} = \mathbf{M}^T$. Hence, the modal derivative $\partial \boldsymbol{\phi}_i/\partial q_j$ is solution of the system:

$$\begin{bmatrix} \mathbf{K} - \omega_i^2 \mathbf{M} & \mathbf{M}\boldsymbol{\phi}_i \\ (\mathbf{M}\boldsymbol{\phi}_i)^T & 0 \end{bmatrix} \begin{bmatrix} \dfrac{\partial \boldsymbol{\phi}_i}{\partial q_j} \\ \dfrac{\partial \omega_i^2}{\partial q_j} \end{bmatrix} = \begin{bmatrix} -\dfrac{\partial \mathbf{K}}{\partial q_j} \boldsymbol{\phi}_i \\ 0 \end{bmatrix}. \tag{1.110}$$

The previous method is nevertheless computationally expensive, the latter can be reduced by neglecting the inertia [86, 88] in Equation (1.105):

$$\mathbf{K} \frac{\partial \boldsymbol{\phi}_i}{\partial q_j} = -\frac{\partial \mathbf{K}}{\partial q_j} \boldsymbol{\phi}_i. \tag{1.111}$$

Such modal derivatives are referred to as static modal derivatives in [178]. The paper also suggests to compute them with a finite difference derivation:

$$\frac{\partial \boldsymbol{\phi}_i}{\partial q_j} = \frac{\boldsymbol{\phi}_i(\mathbf{u_s} + \Delta h \boldsymbol{\phi}_j) - \boldsymbol{\phi}_i(\mathbf{u_s})}{\Delta h}, \tag{1.112}$$

where $\boldsymbol{\phi}_i(\mathbf{u_s} + \Delta h \boldsymbol{\phi}_j)$ is the i^{th} linear normal modes computed on the prestressed position $\mathbf{u_s} + \Delta h \boldsymbol{\phi}_j$. In [114] the authors suggest the computation of the static modal derivatives using the internal forces in case the tangent stiffness matrix is not available in the FE solver. Since $\mathbf{K_{tan}} = \partial \mathbf{f_{int}}/\partial \mathbf{u}$ and $\mathbf{u} = \sum_i q_i \boldsymbol{\phi}_i$, the derivation of the displacement regarding the generalized coordinate q_i becomes: $\partial \mathbf{u}/q_i = \boldsymbol{\phi}_i$, it can be observed that:

$$\frac{\partial \mathbf{K_{tan}}}{\partial \mathbf{q}_j} \boldsymbol{\phi}_i = \frac{\partial}{\partial \mathbf{q}_j} \left(\frac{\partial \mathbf{f_{int}}}{\partial \mathbf{u}} \right) \frac{\partial \mathbf{u}}{\partial \mathbf{q}_i} = \frac{\partial^2 \mathbf{f_{int}}}{\partial \mathbf{q}_i \partial \mathbf{q}_j}. \tag{1.113}$$

Replacing in Equation (1.111), the static modal derivatives can thus be computed using the internal forces. The latter are determined numerically using Taylor expansions, for instance:

$$\begin{aligned}\frac{\partial^2 \mathbf{f_{int}}}{\partial \mathbf{q}_i \partial \mathbf{q}_j} = \frac{1}{4h_ih_j}\Big[&\mathbf{f_{int}}\left(\mathbf{u_s} + h_i\boldsymbol{\phi}_i + h_j\boldsymbol{\phi}_j\right) - \mathbf{f_{int}}\left(\mathbf{u_s} + h_i\boldsymbol{\phi}_i - h_j\boldsymbol{\phi}_j\right)\\ &-\mathbf{f_{int}}\left(\mathbf{u_s} - h_i\boldsymbol{\phi}_i + h_j\boldsymbol{\phi}_j\right) + \mathbf{f_{int}}\left(\mathbf{u_s} - h_i\boldsymbol{\phi}_i - h_j\boldsymbol{\phi}_j\right)\Big]\end{aligned} \tag{1.114}$$

Enhancing the reduction basis with modal derivatives helps to capture the nonlinearity. Nevertheless, their theory is based on small displacements around an equilibrium position and therefore the efficiency of the modal derivatives on strongly nonlinear displacements is reduced. Besides, a major limitation of modal derivatives is their plurality. The number of modal derivatives drastically increases with the number of linear normal modes considered. In a basis containing n_b linear normal modes, $n_\mathrm{b}(n_\mathrm{b}+1)/2$ modal derivatives exist. Although a criterion to reduce their number is proposed in [114], it is a serious limitation since the goal is to obtain a reduction basis with the smallest possible dimension. A selection of the most relevant modal derivatives is thus necessary. This can be achieved with for example the Maximal Modal Interaction described in [190] or the Modal Virtual Work proposed in [91]. Applications to industrial fan blade structures are for instance found in [36–38].

1.3.1.4 Dual modes

Another possibility to enrich the reduction basis is the use of dual modes [100, 124, 142, 204, 205]. The latter are computed from nonlinear static solutions obtained by imposing external loads to the structure, whose distribution involves the first linear normal modes so that the loads are not case-dependent. Those nonlinear static solutions contain information on the geometric nonlinearity that is missing from the linear normal modes. Such information is extracted and a SVD is performed. Eventually, the SVD modes with the highest singular values as well as the modes associated to a significant linearized strain energy are the dual modes selected to enrich the reduction basis.

This section details the determination of dual modes which are added to the projection basis in order to capture the geometric nonlinearity. A set of external forces are first applied to the structure as a combination of the first linear normal modes $(\boldsymbol{\phi})_{i\in[1,n_\mathrm{b}]}$ of the structure:

$$\forall \ell \in [1, n_\mathrm{L}] \qquad \mathbf{f}_\mathrm{ext}^{(\ell)} = \mathbf{K}\left(\sum_{i=1}^{n_\mathrm{b}} \alpha_i^{(\ell)}\boldsymbol{\phi}_i\right), \tag{1.115}$$

where $\alpha_i^{(\ell)}$ are weighting coefficients selected to generate different levels of load cases. The associated nonlinear static solutions $\mathbf{u_s}^{(\ell)}$ are computed from the equation:

$$\mathbf{K}\mathbf{u_s}^{(\ell)} + \mathbf{g_{nl}}(\mathbf{u}^{(\ell)}) = \mathbf{f}_\mathrm{ext}^{(\ell)}. \tag{1.116}$$

From those nonlinear static solutions, generalized coordinates $\mathbf{q}^{(\ell)}$ on the modes of the reduction basis are extracted by least-squares approximations since $\mathbf{u}^{(\ell)} \approx \mathbf{\Phi}\mathbf{q}^{(\ell)}$. The residual of the approximation is written $\mathbf{r}^{(\ell)}$. For each nonlinear static solution, the following relation is verified:

$$\mathbf{u}^{(\ell)} = \mathbf{\Phi}\mathbf{q}^{(\ell)} + \mathbf{r}^{(\ell)}, \tag{1.117}$$

and all the residuals $\mathbf{r}^{(\ell)}$ are gathered in a matrix, from which a singular value decomposition (SVD) is computed:

$$\left[\mathbf{r}^{(1)}, \quad \cdots, \quad \mathbf{r}^{(n_\mathrm{L})}\right] = \left[\mathbf{d}_1, \quad \cdots, \quad \mathbf{d}_{n_\mathrm{p}}\right] \operatorname{diag}(\sigma_1, \sigma_2, \cdots, \sigma_{n_\mathrm{p}}) \mathbf{W}^T, \tag{1.118}$$

where $(\sigma_i)_{i \in [1, n_\mathrm{p}]}$ are the non-null singular values ordered from the largest to the smallest, $(\mathbf{d}_i)_{i \in [1, n_\mathrm{p}]}$ the left singular vectors of the decomposition and $\mathbf{W}^T$ containing the right singular vectors, of shape $(n_\mathrm{p} \times n_\mathrm{L})$. The projection of the residual vectors $\mathbf{r}^{(\ell)}$ on the SVD basis vectors is the following:

$$\mathbf{r}^{(\ell)} = \sum_{k=1}^{n_\mathrm{p}} \beta_k^\ell \mathbf{d}_k, \tag{1.119}$$

with $\beta_k^\ell = \sigma_k \mathbf{W}_{\ell k}$. The sum $\mathcal{E}_r$ of the linearized strain energy of all the nonlinear residual displacements $\mathbf{r}^{(\ell)}$ is defined in [100] by:

$$\mathcal{E}_r = \sum_{\ell=1}^{n_\mathrm{L}} \mathbf{r}^{(\ell)^T} \mathbf{K} \mathbf{r}^{(\ell)} = \sum_{k=1}^{n_\mathrm{p}} \underbrace{\left(\sum_{\ell=1}^{n_\mathrm{L}} {\beta_k^\ell}^2 \mathbf{d}_k^T \mathbf{K} \mathbf{d}_k \right)}_{E_k}, \tag{1.120}$$

since $\forall (k, j) \in [1, n_\mathrm{p}]^2, \mathbf{d}_k^T \mathbf{d}_j = \delta_{kj}$.

As explained in [100], the dual modes selected for inclusion in the reduction basis are the vectors $\left(\mathbf{d}_i\right)_{i \in [1, n_\mathrm{p}]}$ with the largest singular values σ_i and those contributing the most to the linearized strain energy, i.e. those leading to the largest values of E_i.

The vectors $\left(\mathbf{d}_i\right)_{i \in [1, n_\mathrm{p}]}$ ranked by decreasing singular values are selected until the desired precision is obtained. To do so, the reduction basis $\mathbf{\Phi}$ is supplemented by the vectors $\left(\mathbf{d}_1, \mathbf{d}_2, ..., \mathbf{d}_k\right)$ to form the matrix $\mathbf{V}^{(k)} = [\mathbf{\Phi}, \mathbf{d}_1, \cdots, \mathbf{d}_k]$. Then the matrix $\mathbf{U}_s$ collecting all static displacements $\mathbf{u}^{(\ell)}$ is approximated as $\mathbf{V}^{(k)} \mathbf{Q}^{(k)}$ by a least-squares method. The dual modes are first selected with respect to the following criterion to ensure that the static solutions are properly approximated when adequate linear and dual modes are included in the basis:

$$\frac{\max(|\mathbf{U_s} - \mathbf{V}^{(k)} \mathbf{Q}^{(k)}|)}{\max(|\mathbf{U_s}|)} < \varepsilon_\sigma \tag{1.121}$$

The second step is to satisfy a sufficient contribution to the linearized strain energy. The remaining dual modes candidates are ordered by decreasing linearized strain energy contributions and are added to the reduction basis until the following error is below the threshold ε_E:

$$\frac{\left(\mathcal{E}_r - \sum_{i=1}^{k} E_i \right)}{\mathcal{E}_r} < \varepsilon_E \tag{1.122}$$

with E_i the contribution to the total linearized strain energy defined in (1.120). The new reduction basis is finally the concatenation $\mathbf{V} = [\mathbf{\Phi}, \mathbf{\Phi}_\mathrm{dual}]$ of the first linear normal modes $\mathbf{\Phi}$ and the selection of dual modes $\mathbf{\Phi}_\mathrm{dual}$ satisfying both criteria.

1.3.2 Computation of the nonlinear forces coefficients

When a partitioned fluid-structure coupling is considered, the fluid solver interacts with an external FE solver to compute the displacement of the structure at every sub-iteration of coupling. The transfer of data between the fluid and the structure solvers is not an easy task and a significant advantage is to use a *non-intrusive* ROM, independent from any FE solver during the online stage.

However, since the evaluation of the projected nonlinear forces $\widetilde{\mathbf{g}}_{\mathbf{nl}}(\mathbf{q}) = \mathbf{V}^T\mathbf{g}_{\mathbf{nl}}(\mathbf{V}\mathbf{q})$ requires back-and-forth exchanges between the ROM and the FEM variables, the ROM resulting from Equation (1.89) is therefore intrusive. More precisely, the physical displacements $\mathbf{u} \approx \mathbf{V}\mathbf{q}$ have first to be assembled before the evaluation of the nonlinear forces $\mathbf{g}_{\mathbf{nl}}(\mathbf{V}\mathbf{q})$ by the FE solver, which are finally projected again in the reduced space. It would be of great interest to know the explicit expression of the projected nonlinear forces $\widetilde{\mathbf{g}}_{\mathbf{nl}}(\mathbf{q})$ as a function of the generalized coordinates. Thus the structural problem could be solved directly in the reduced space:

$$\widetilde{\mathbf{M}}\ddot{\mathbf{q}} + \widetilde{\mathbf{C}}\dot{\mathbf{q}} + \widetilde{\mathbf{K}}\mathbf{q} + \widetilde{\mathbf{g}}_{\mathbf{nl}}(\mathbf{q}) = \widetilde{\mathbf{f}}_{\mathrm{a}}. \tag{1.123}$$

Considering geometric nonlinearities in the frame of finite displacements (small strains, large displacements and large rotations) and the Saint Venant-Kirchhoff constitutive model, the projected nonlinear forces resulting from geometric nonlinearities is a third-order polynomial function of the generalized coordinates [125, 126]. Indeed, the internal nonlinear forces $\mathbf{f}_{\mathbf{nl}}(\mathbf{u})$ are cubic in the degrees of freedom $\mathbf{u}$ as shown in Equation (1.59) and so are $\mathbf{g}_{\mathbf{nl}}(\mathbf{u})$ from Equation (1.72). Introducing the projection $\mathbf{u} = \mathbf{V}\mathbf{q}$ in their expression leads to the cubic polynomial expression of $\widetilde{\mathbf{g}}_{\mathbf{nl}}(\mathbf{q})$. Writing $\widetilde{g}^k_{\mathrm{nl}}(\mathbf{q})$ the k^{th} coordinate of the projected nonlinear force, its expression can be written explicitly from the generalized coordinates:

$$\widetilde{g}^k_{\mathrm{nl}}(\mathbf{q}) = \sum_{i=1}^{n}\sum_{j=i}^{n}\beta^k_{ij}q_iq_j + \sum_{i=1}^{n}\sum_{j=i}^{n}\sum_{m=j}^{n}\gamma^k_{ijm}q_iq_jq_m, \tag{1.124}$$

with n the number of modes in the reduction basis, while β^k_{ij} and γ^k_{ijm} are respectively the quadratic and cubic coefficients of the polynomial approximation of the nonlinear forces. Appendix C provides a formulation of the Jacobian of the projected nonlinear forces that will be exploited for the resolution of the nonlinear systems. Nevertheless, the coefficients β^k_{ij} and γ^k_{ijm} have yet to be determined. Two methods are found in the literature. The first one involves the determination of the coefficients with imposed displacements, called STEP [126] and its necessary corrections for 3D cases [8], [199]. In this method, the coefficients of the polynomial are determined specifically by imposing to the structure various displacements with the shape of well-chosen linear combinations of the linear normal modes. The second method relies on prescribed loads to the structure to determine the coefficients. Such a method is called *Implicit Condensation* [122], and an *Expansion* step has been proposed [79]. Prescribed loads instead of displacements are imposed to the structure, with load distributions derived from the linear normal modes. Both the nonlinear static solutions and the nonlinear forces are computed. The generalized coordinates on the reduction basis are extracted from the nonlinear static solutions by means of a least-squares approximation. The coefficients β^k_{ij} and γ^k_{ijm} are finally obtained by identification between the formula (1.124) and the nonlinear forces computed with the FE solver.

1.3.2.1 STEP method

The STEP method is a non-intrusive method introduced by Muravyov and Rizzi [126, 158] to build an autonomous reduced order model with respect to the computation of the nonlinear forces. The latter are indeed expressed as an explicit function of the generalized coordinates.

The STEP method consists in writing each component $k = (1, \cdots, n)$ of $\widetilde{\mathbf{g}}_{\mathbf{nl}}(\mathbf{q})$ as a third order polynomial as shown in Equation (1.124). The coefficients β^k_{ij} and γ^k_{ijm} can be identified in a non-intrusive way using a finite element software by evaluating the nonlinear forces $\mathbf{g}_{\mathbf{nl}}(\mathbf{u})$ and its projection on the k^{th} mode $\mathbf{V}_k$:

$$\widetilde{g}^k_{\text{nl}}(\mathbf{u}) = \mathbf{V}_k^T \mathbf{g}_{\mathbf{nl}}(\mathbf{u}). \tag{1.125}$$

The coefficients of the polynomial expression (1.124) are computed one by one by imposing to the structure wisely-chosen combinations of the linear normal modes. The following paragraphs detail the procedure to compute the coefficients associated with the projection on the k^{th} mode of the nonlinear internal forces.

Computation of the coefficients β^k_{ii} and γ^k_{iii}:

The quadratic and cubic coefficients of one repeated index $i \in \{1, \cdots, n\}$ are evaluated by imposing to the structure two opposite displacements along the mode $\mathbf{V}_i$ with a chosen amplitude q_i:

$$\mathbf{u}_1 = \mathbf{V}_i q_i \tag{1.126}$$

$$\mathbf{u}_2 = -\mathbf{V}_i q_i. \tag{1.127}$$

The projected nonlinear forces associated with such displacements are given by Equation (1.124):

$$\widetilde{g}^k_{\text{nl}}(\mathbf{u}_1) = \beta^k_{ii}\ q_i^2 + \gamma^k_{iii}\ q_i^3 \tag{1.128}$$

$$\widetilde{g}^k_{\text{nl}}(\mathbf{u}_2) = \beta^k_{ii}\ q_i^2 - \gamma^k_{iii}\ q_i^3, \tag{1.129}$$

from which the coefficients $\beta^k_{ii}, \gamma^k_{iii}$ are deduced:

$$\beta^k_{ii} = \frac{1}{2q_i^2}\left[\widetilde{g}^k_{\text{nl}}(\mathbf{u}_1) + \widetilde{g}^k_{\text{nl}}(\mathbf{u}_2)\right] \tag{1.130}$$

$$\gamma^k_{iii} = \frac{1}{2q_i^3}\left[\widetilde{g}^k_{\text{nl}}(\mathbf{u}_1) - \widetilde{g}^k_{\text{nl}}(\mathbf{u}_2)\right]. \tag{1.131}$$

Since two solutions are necessary to determine the coefficients $\beta^k_{ii}, \gamma^k_{iii}$ for a given k, the number of static calculations to perform in order to compute those coefficients for all $k \in \{1, \cdots, n\}$ is $2n$.

Computation of the coefficients β^k_{ij},γ^k_{iij} and γ^k_{ijj}:

The next step is the computation of the coefficients involving two indices $i \in \{1, \cdots, n\}$ and $j \in \{1, \cdots, n\}$ with $i < j$. The coefficients computed in the previous paragraph are reused in this step to determine the coefficients β^k_{ij},γ^k_{iij} and γ^k_{ijj}. Three combinations of the linear normal modes $\mathbf{V}_i$ and $\mathbf{V}_j$ are imposed to the structure with respective amplitude q_i and q_j:

$$\mathbf{u}_3 = \mathbf{V}_i q_i + \mathbf{V}_j q_j \tag{1.132}$$

$$\mathbf{u}_4 = -\mathbf{V}_i q_i - \mathbf{V}_j q_j \tag{1.133}$$

$$\mathbf{u}_5 = \mathbf{V}_i q_i - \mathbf{V}_j q_j. \tag{1.134}$$

The expression of the projected nonlinear forces (Equation (1.124)) associated with those displacements are:

$$\widetilde{g}^k_{\text{nl}}(\mathbf{u}_3) = \beta^k_{ii}\ q_i^2 + \beta^k_{ij}\ q_i q_j + \beta^k_{jj}\ q_j^2 + \gamma^k_{iii}\ q_i^3 + \gamma^k_{iij}\ q_i^2 q_j + \gamma^k_{ijj}\ q_i q_j^2 + \gamma^k_{jjj}\ q_j^3 \tag{1.135}$$

$$\widetilde{g}^k_{\text{nl}}(\mathbf{u}_4) = \beta^k_{ii}\ q_i^2 + \beta^k_{ij}\ q_i q_j + \beta^k_{jj}\ q_j^2 - \gamma^k_{iii}\ q_i^3 - \gamma^k_{iij}\ q_i^2 q_j - \gamma^k_{ijj}\ q_i q_j^2 - \gamma^k_{jjj}\ q_j^3 \tag{1.136}$$

$$\widetilde{g}^k_{\text{nl}}(\mathbf{u}_5) = \beta^k_{ii}\ q_i^2 - \beta^k_{ij}\ q_i q_j + \beta^k_{jj}\ q_j^2 + \gamma^k_{iii}\ q_i^3 - \gamma^k_{iij}\ q_i^2 q_j + \gamma^k_{ijj}\ q_i q_j^2 - \gamma^k_{jjj}\ q_j^3, \tag{1.137}$$

from which the coefficients β^k_{ij}, γ^k_{ijj} and γ^k_{iij} are obtained as:

$$\beta^k_{ij} = \frac{1}{2q_iq_j}\left[\widetilde{g}^k_{\text{nl}}(\mathbf{u}_3) + \widetilde{g}^k_{\text{nl}}(\mathbf{u}_4) - 2\beta^k_{ii}q_i^2 - 2\beta^k_{jj}q_j^2\right] \tag{1.138}$$

$$\gamma^k_{ijj} = \frac{1}{2q_iq_j^2}\left[\widetilde{g}^k_{\text{nl}}(\mathbf{u}_3) + \widetilde{g}^k_{\text{nl}}(\mathbf{u}_5) - 2\beta^k_{ii}q_i^2 - 2\beta^k_{jj}q_j^2 - 2\gamma^k_{iii}q_i^3\right] \tag{1.139}$$

$$\gamma^k_{iij} = \frac{1}{2q_i^2q_j}\left[-\widetilde{g}^k_{\text{nl}}(\mathbf{u}_4) - \widetilde{g}^k_{\text{nl}}(\mathbf{u}_5) + 2\beta^k_{ii}q_i^2 + 2\beta^k_{jj}q_j^2 - 2\gamma^k_{jjj}q_j^3\right]. \tag{1.140}$$

The determination of the coefficients of this second step for all $k \in \{1, \cdots, n\}$ requires the computation of $\frac{3}{2}n(n-1)$ static nonlinear solutions.

Computation of the coefficients γ^k_{ijm}:

The last step of the method consists in the determination of the coefficients γ^k_{ijm} for $i \in \{1, \cdots, n\}$, $j \in \{1, \cdots, n\}$ and $m \in \{1, \cdots, n\}$ with $i < j < m$. Only one displacement is required, defined as the sum of the three linear normal modes $\mathbf{V}_i, \mathbf{V}_j$ and $\mathbf{V}_m$ with the respective amplitudes q_i, q_j and q_m:

$$\mathbf{u}_6 = \mathbf{V}_iq_i + \mathbf{V}_jq_j + \mathbf{V}_mq_m. \tag{1.141}$$

The projected internal forces resulting from the displacements $\mathbf{u}_6$ involve all combinations of the generalized coordinates q_i, q_j and q_m:

$$\begin{aligned}\widetilde{g}^k_{\text{nl}}(\mathbf{u}_6) = \beta^k_{ii}q_i^2 + \beta^k_{ij}q_iq_j + \beta^k_{im}q_iq_m + \beta^k_{jj}q_j^2 + \beta^k_{jm}q_jq_m + \beta^k_{mm}q_m^2 + \gamma^k_{iii}q_i^3 \\ +\gamma^k_{iij}q_i^2q_j + \gamma^k_{iim}q_i^2q_m + \gamma^k_{ijj}q_iq_j^2 + \gamma^k_{ijm}q_iq_jq_m + \gamma^k_{imm}q_iq_m^2 \\ +\gamma^k_{jjj}q_j^3 + \gamma^k_{jjm}q_j^2q_m + \gamma^k_{jmm}q_jq_m^2 + \gamma^k_{mmm}q_m^3,\end{aligned} \tag{1.142}$$

from which the coefficient γ^k_{ijm} is determined, taking advantage of the coefficients already known from the previous steps:

$$\begin{aligned}\gamma^k_{ijm} = \frac{1}{q_iq_jq_m}\Big[\widetilde{g}^k_{\text{nl}}(\mathbf{u}_6) - \beta^k_{ii}q_i^2 - \beta^k_{ij}q_iq_j - \beta^k_{im}q_iq_m - \beta^k_{jj}q_j^2 - \beta^k_{jm}q_jq_m - \beta^k_{mm}q_m^2 \\ -\gamma^k_{iii}q_i^3 - \gamma^k_{iij}q_i^2q_j - \gamma^k_{iim}q_i^2q_m - \gamma^k_{ijj}q_iq_j^2 - \gamma^k_{imm}q_iq_m^2 \\ -\gamma^k_{jjj}q_j^3 - \gamma^k_{jjm}q_j^2q_m - \gamma^k_{jmm}q_jq_m^2 - \gamma^k_{mmm}q_m^3\Big].\end{aligned} \tag{1.143}$$

The number of static nonlinear computations necessary to compute all the coefficients γ^k_{ijm} is equal to $= \frac{1}{6}n(n-1)(n-2)$. Hence, the total number of nonlinear finite element static computations needed to determine all the coefficients of the STEP method is equal to $2n + \frac{3}{2}n(n-1) + \frac{1}{6}n(n-1)(n-2) = \frac{1}{6}(n^3 + 6n^2 + 5n)$. Consequently, the number of STEP coefficients grow significantly with the size of the reduced basis.

The identification of the coefficients with the STEP method is particularly efficient for von Kármán beams and plates applications where the expression of the nonlinear forces is cubic [65, 118]. Nevertheless, for 3D structures, the determination of the coefficients with the STEP method in its original form has limitations due to imposed displacements that constrain the natural Poisson volume deformations, resulting in imposing significant local internal forces polluting the numerical resolution with large numbers leading to numerical inaccuracies. Thus the STEP coefficients depends strongly on the amplitudes q_i, q_j, q_m of the imposed displacements for 3D cases. For each problem there is a range of adequate amplitudes q_i, q_j, q_m where the coefficients are well determined and independent of the imposed amplitude. Improvements of the STEP method for 3D structures are found in the literature such as a POD correction of the coefficients called StepC [8] and a modified STEP [199] where the displacements are imposed only on specific degrees of freedom in order to let the Poisson volume deformation free. Another approach consisting in computing the nonlinear forces element-wise is proposed in [99] and hyper reduction techniques are suggested to reduce its computational cost.

1.3.2.2 Implicit Condensation and Expansion

The idea of the *Implicit Condensation* method [122] is to select in the reduction basis the first n_b linear normal modes: $\mathbf{\Phi} = [\boldsymbol{\phi}_1, \cdots, \boldsymbol{\phi}_{n_\mathrm{b}}]$ corresponding usually to bending modes for slender structures. Then the nonlinear forces coefficients of Equation (1.124) are identified thanks to static nonlinear displacements obtained under load cases. A set of n_L loading cases $\mathbf{f}_\mathrm{ext}^{(1)}$, $\mathbf{f}_\mathrm{ext}^{(2)}$, $\cdots$, $\mathbf{f}_\mathrm{ext}^{(n_\mathrm{L})}$ are introduced. The distribution of each load case $\ell \in [1, n_\mathrm{L}]$ is defined as a linear combination of the linear normal modes:

$$\mathbf{f}_\mathrm{ext}^{(\ell)} = \lambda_1^{(\ell)}\boldsymbol{\phi}_1 + \lambda_2^{(\ell)}\boldsymbol{\phi}_2 + \cdots + \lambda_{n_\mathrm{b}}^{(\ell)}\boldsymbol{\phi}_{n_\mathrm{b}}. \tag{1.144}$$

The determination of the quadratic and cubic coefficients of the reduced nonlinear forces is carried out by identification between Equation (1.124) and the projection of the internal nonlinear forces obtained with the nonlinear static computations under the loads (1.144): $\mathbf{K}\mathbf{u}^{(\ell)} + \mathbf{g_{nl}}(\mathbf{u}^{(\ell)}) = \mathbf{f}_\mathrm{ext}^{(\ell)}$. In the original IC method, the reduction basis comprises exclusively bending modes. Therefore, the contribution of the other modes, for instance the membrane modes of beam or shells, is omitted in the result. The specificity of the ICE method is to improve the solution obtained with the IC method by adding a post-processing step whose aim is to enrich the displacement solution with information on the membrane displacement that is not contained in the few linear normal modes selected. The assumption is that the total displacement $\mathbf{u}$ is the sum of the approximated solution obtained with the first linear normal modes selected $\mathbf{u}_\mathrm{b}$ and a set of *Expansion* modes $\mathbf{\Psi}$ multiplied by generalized coordinates $\boldsymbol{\eta}$. Such generalized coordinates are defined as quadratic functions of the generalized coordinates associated to the selected modes $\mathbf{\Phi}$:

$$\mathbf{u}_\mathrm{ICE} = \mathbf{u}_\mathrm{b} + \mathbf{u}_\mathrm{m} = \sum_{k=1}^{n_\mathrm{b}} \boldsymbol{\phi}_k q_k + \sum_{k=1}^{n_\mathrm{m}} \boldsymbol{\psi}_k \eta_k = \mathbf{\Phi}\mathbf{q} + \mathbf{\Psi}\boldsymbol{\eta}. \tag{1.145}$$

The first linear bending modes $(\boldsymbol{\phi}_k)_{k\in[1,n_\mathrm{b}]}$ are known as well as the corresponding generalized coordinates q_k. On the contrary, the modal amplitudes of the *Expansion* modes $\mathbf{\Psi}$ are obtained as quadratic combinations of the modal amplitudes relative to the first linear normal modes q_k:

$$\boldsymbol{\eta} = \begin{bmatrix} q_1^2 & q_1q_2 & \cdots & q_1q_{n_\mathrm{b}} & q_2^2 & q_2q_3 & \cdots & q_2q_{n_\mathrm{b}} & \cdots & q_{n_\mathrm{b}}^2 \end{bmatrix}^T. \tag{1.146}$$

Nevertheless, the $n_\mathrm{m} = n_\mathrm{b}(n_\mathrm{b}+1)/2$ *Expansion* modes $\left(\boldsymbol{\psi}_q\right)_{q\in[1,n_\mathrm{m}]}$ are not known and have to be determined during the construction of the reduced order model. To this end, a matrix $(\mathbf{Q}_\mathrm{m})_{(n_\mathrm{m}\times n_\mathrm{L})}$ (respectively $(\mathbf{Q}_\mathrm{b})_{(n_\mathrm{b}\times n_\mathrm{L})}$) is built, whose lines are the generalized amplitudes $(\eta_q)_{q\in[1,n_\mathrm{m}]}$ (respectively $(q_k)_{k\in[1,n_\mathrm{b}]}$) and the columns their values for each static solutions associated to a loading $\mathbf{f}_\mathrm{ext}^{(\ell)}$. Introducing the matrix $(\mathbf{U}_\mathrm{t})_{(n_\mathrm{b}\times n_\mathrm{L})}$ whose columns are the nonlinear static solutions $\mathbf{u}_\mathrm{ICE}^{(\ell)} = \mathbf{u}_\mathrm{b}^{(\ell)} + \mathbf{u}_\mathrm{m}^{(\ell)}$ leads to the matrix system:

$$\mathbf{U}_\mathrm{t} = \mathbf{\Phi}\mathbf{Q}_\mathrm{b} + \mathbf{\Psi}\mathbf{Q}_\mathrm{m}. \tag{1.147}$$

The *Expansion* modes used for the ICE reconstruction of the displacement are then obtained by:

$$\mathbf{\Psi} = \left[\mathbf{U}_{\mathrm{t}} - \mathbf{\Phi}\mathbf{Q}_{\mathrm{b}}\right]\mathbf{Q}_{\mathrm{m}}^{+}, \tag{1.148}$$

where $\mathbf{Q}_{\mathrm{m}}^{+}$ is the pseudo-inverse of $\mathbf{Q}_{\mathrm{m}}$. In [79], the authors suggest using the first bending modes in the reduction basis, therefore the *Expansion* modes are mostly modes with a predominant membrane contribution. During the temporal resolution of the dynamics equations of motion, the structural response in terms of modal bending amplitudes $\mathbf{u}_{\mathrm{b}}$ is determined. The corresponding membrane displacements η_k are then computed with Equation (1.146) and the total displacement is finally rebuilt as $\mathbf{u} = \mathbf{u}_{\mathrm{b}} + \mathbf{u}_{\mathrm{m}}$. Equation (1.146) is a quadratic mapping or quadratic modal condensation [80] and is valid for von Kármán beams but is *a priori* an approximation for more complex structures. Besides, for cantilever structures, the IC method with bending modes and its expansion ICE becomes inaccurate in dynamic cases with large axial displacements, which will be shown in section 2.3. Indeed, since only bending modes are included in the reduced basis, there is no equation relative to the membrane dynamics in the reduced system and the static reconstruction of the *Expansion* may be inaccurate.

1.3.3 Reduction methods based on different approaches

The previous section was dedicated to projection-based reduced order models with the determination of the reduction basis capable of capturing geometric nonlinearities as well as the determination of an explicit expression of the internal nonlinear forces projected in such a basis. Different approaches exist in the literature. For instance, an adaptation of the Koiter–Newton method is proposed in [177] to accurately compute large deflections. Hyper-reduction methods are also relevant; they are also projection-based but the computation of the internal forces is different in the sense that they are computed in a subset, not at all degrees of freedom. In contrast to projection-based methods, nonlinear normal modes are based on the reduction in the normal form of the equations governing the dynamics thus introducing a change of variable between the physical degrees of freedom and the normal coordinates. The reduced dynamics is computed in an invariant manifold of small dimension, then rebuilt in the physical space via the change of variable.

1.3.3.1 Hyper-reduction techniques

The issue raised by the classical projection $\mathbf{V}^T\mathbf{f}_{\mathbf{int}}(\mathbf{Vq})$ of the internal forces in the reduced space is that the internal forces are known in the physical space, not the reduced space. It means that the online cost of such a projection is very expensive. Indeed, at each evaluation of the internal force $\mathbf{f}_{\mathbf{int}}$, but also tangent stiffness $\partial\mathbf{f}_{\mathbf{int}}/\partial\mathbf{u}$, such evaluation should be carried out in the physical space. The displacement $\mathbf{u}$ is first approximated by $\mathbf{Vq}$, then the internal forces $\mathbf{f}_{\mathbf{int}}(\mathbf{Vq})$ are computed in each element and assembled. The result is finally projected in the reduced space. The computational cost of such a procedure is very significant. Considering geometric nonlinearities, an explicit expression of the projected nonlinear forces as a cubic polynomial of the generalized coordinates is proposed in section 1.3.2. Such expression is valid only for geometrical nonlinearities and not for other complex types of nonlinearities. The idea of hyper-reduction methods is different in the sense that the internal forces are still computed in the physical space but only at some carefully chosen points and interpolated at the others.

The Direct Empirical Interpolation Method (DEIM), introduced by S. Chaturantabut and D. C. Sorensen [26], is based on the approximation of the internal forces by a product between a subspace matrix $\mathbf{D} \in \mathbb{R}^{N\times m_D}$ and a coefficients vector $\mathbf{c}$:

$$\mathbf{f}_{\mathbf{int}}(\mathbf{u}(t)) \approx \mathbf{Dc}(t). \tag{1.149}$$

The system is over-determined, the coefficients vector $\mathbf{c}$ is chosen with a boolean matrix $\mathbf{E} = \left[\boldsymbol{e}_{\rho_1}, \boldsymbol{e}_{\rho_2}, \cdots, \boldsymbol{e}_{\rho_{m_D}}\right] \in \mathbb{R}^{N \times m_D}$ where $\boldsymbol{e}_{\rho_j}$ is the ρ_j^{th} column of the identity matrix $\mathbf{I}_N$ such that:

$$\mathbf{E}^T \mathbf{f_{int}}(\mathbf{u}(t)) = (\mathbf{E}^T \mathbf{D})\mathbf{c}(t). \tag{1.150}$$

The coefficients vector $\mathbf{c}$ is uniquely defined by $\mathbf{c}(t) = (\mathbf{E}^T \mathbf{D})^{-1} \mathbf{E}^T \mathbf{f_{int}}(\mathbf{u}(t))$ supposing $\mathbf{E}^T \mathbf{D}$ nonsingular. The approximation of the internal forces is finally:

$$\mathbf{f_{int}}(\mathbf{u}) \approx \mathbf{D}\mathbf{c}(t) = \mathbf{D}(\mathbf{E}^T \mathbf{D})^{-1} \ \ \mathbf{E}^T \mathbf{f_{int}}(\mathbf{u}(t)). \tag{1.151}$$

During the online stage of the computation, the nonlinear forces are evaluated only at the degrees of freedom specified by the interpolation indices constituting the matrix $\mathbf{E}$. It is what is meant by the matrix product between the transpose of the boolean matrix and the assembled internal force: $\mathbf{E}^T \mathbf{f_{int}}(\mathbf{u}(t))$ but not what is performed numerically since such assembling is precisely what the method aims to avoid. It is also the difficulty of the method. Indeed, to be efficient the FE code should be able to compute the internal forces only at the desired dofs, which is cumbersome to implement in industrial FE codes. The DEIM approximation of the internal forces in Equation (1.151) requires the determination of the reduction basis $\mathbf{D}$ and the $m_D \ll N$ interpolation indices $\{\rho_1, \cdots, \rho_{m_D}\}$. The matrix $\mathbf{D}$ for the projection into a subspace is usually a POD basis obtained with a SVD of snapshots of internal forces $\left[\mathbf{f_{int}}(\mathbf{u}(t_1)), \ \ \mathbf{f_{int}}(\mathbf{u}(t_2)), \ \ \cdots, \ \ \mathbf{f_{int}}(\mathbf{u}(t_n))\right]$ and the interpolation indices required to build the matrix $\mathbf{E}$ are obtained with a greedy algorithm based on the projection basis. Therefore the accuracy of the DEIM method is solely depending on the quality of the reduction basis. Besides, the method has a major drawback which is the loss of symmetry of the system as well as the loss of consistency and stability [49]. Applying the DEIM to only the purely nonlinear internal forces $\mathbf{g_{nl}}(\mathbf{u})$ reduces the possible impact of the loss of these properties.

In finite elements in general and more particularly in 3D meshes, nodes have several neighbouring elements. The evaluation of the internal force at one dof needs the evaluation of all the neighbouring elements of the selected dof. Thus more evaluations than only the collocation dofs are needed. To counter that issue, P. Tiso and D.J.Rixen suggested the unassembled DEIM (UDEIM) method [191]. This method is the use of the DEIM method on the unassembled system to avoid the previously mentioned necessity to evaluate all neighbouring elements of the collocation dofs. However, the matrix $\mathbf{D}$ has to be built with POD on unassembled internal force snapshots. Besides DEIM and UDEIM collocation processes being equivalent, the major drawback of the DEIM method in terms of loss of symmetry, consistency and stability are also affecting the UDEIM method.

While the DEIM method approximates the internal forces in the physical space and then projects them into a reduced basis, the Energy Conserving Mesh Sampling and Weighting (ECSW) method computes an approximation of the reduced internal forces, preserving the symmetry, stability and consistency. Introduced in the field of computer graphics [3], this method was then transposed to nonlinear dynamic problems [25, 49, 50]. The ECSW method consists in finding a relevant approximation of the virtual work of the reduced internal forces by restricting the computation to a subset of fewer elements and introducing weighting factors to characterise the energy of the full system as well as make sure of the positiveness of the virtual work. The elements of the subset and the associated weighting factors are the solutions to an optimization problem aiming to find the maximum of weighting factors equal to zero (meaning the lowest number of elements to consider in the subset) while respecting the equation with a given tolerance. Such an optimization problem is solved by a Non-Negative Least Square solver, requiring a significant computational time. A reduction of the computational time is proposed in [25] and an approximate solution is often selected. The advantage of the ECSW method over the DEIM and the UDEIM is that it is based on the virtual work principle and maintains properties such as symmetry, stability and consistency.

1.3.3.2 Nonlinear Normal Modes and invariant manifolds

Nonlinear normal modes are adapted to polynomial nonlinearities and consist in searching periodic solutions in the vicinity of the resonating frequency. In its original form, the first step is the projection of the equations of the dynamics in the space of all the linear modes $\boldsymbol{\Phi}$ consisting of N coupled oscillators. For instance, the homogeneous equation relative to the oscillator k is the following:

$$\ddot{x}_k + 2\xi_p \dot{x}_k + \omega_k^2 x_k + \sum_{i,j}^{N} g_{ij}^k x_i x_j + \sum_{i,j,m}^{N} h_{ijm}^k x_i x_j x_m = 0, \tag{1.152}$$

with x_k the degrees of freedom of the oscillators. In this equation the external forces are not considered, they are added in the second member afterwards during the computation of the solution. In the linear case, without the nonlinear terms, the projection results in N uncoupled oscillators, represented by hyperplanes in the phase space as illustrated in Figure 1.8a. It means that a motion initiated along one mode does not trigger the motion of other modes. However, when nonlinear terms are present, the oscillators are coupled and a motion along one mode triggers a motion along other modes. The first definition of the nonlinear modes is a family of periodic orbits around the equilibrium. The existence of such orbits is proved by the Lyapunov theorem [112]. This concept was taken up by Rosenberg [160–164] as the periodic orbits of a nonlinear mode. It is an analytic approach based on an energetic formulation of the conservative system (without damping). The analytical approach inspired several studies [154, 196, 197] and a numerical approach for the computation of such nonlinear modes was proposed in [179].

Another definition of nonlinear modes was proposed by Shaw & Pierre [173–175]. They introduced the nonlinear modes as invariant manifolds in the phase space, tangent to the corresponding linear modes at the origin as illustrated in Figure 1.8b. With such a definition, the nonlinear modes can be seen as an extension of the linear mode to the nonlinearity. A generalization to damped systems is possible in contradiction with the definition of Rosenberg. Shaw & Pierre's definition of the nonlinear modes is based on the center manifold theory [22, 68, 97]. A separation between lightly damped "master modes" and strongly damped "slave modes". The reduced dynamics is governed by the master modes while the movement of the slave modes is defined as a function of the master modes. Several methods of computation were proposed such as the multiple-scale method [106, 107, 195] and complex formulations [93, 131, 132, 175]. A reformulation of the method using polar coordinates to compute the geometry of the manifold was proposed in [144]. The computation of nonlinear normal modes was also performed in the conservative case with continuation methods like Shooting [141] and Harmonic Balance [66]. To treat nonconservative systems, a pseudo-periodic variation of the nonlinear modes called complex nonlinear modes was proposed in [108, 109] and contact applications were treated in [94, 95, 101, 102]. Besides, it is worth mentioning that the invariant manifold satisfying the definition of Shaw & Pierre is not unique: Haller proved the existence of a unique manifold (called spectral submanifold) under appropriate nonresonance and spectral quotient conditions [73].

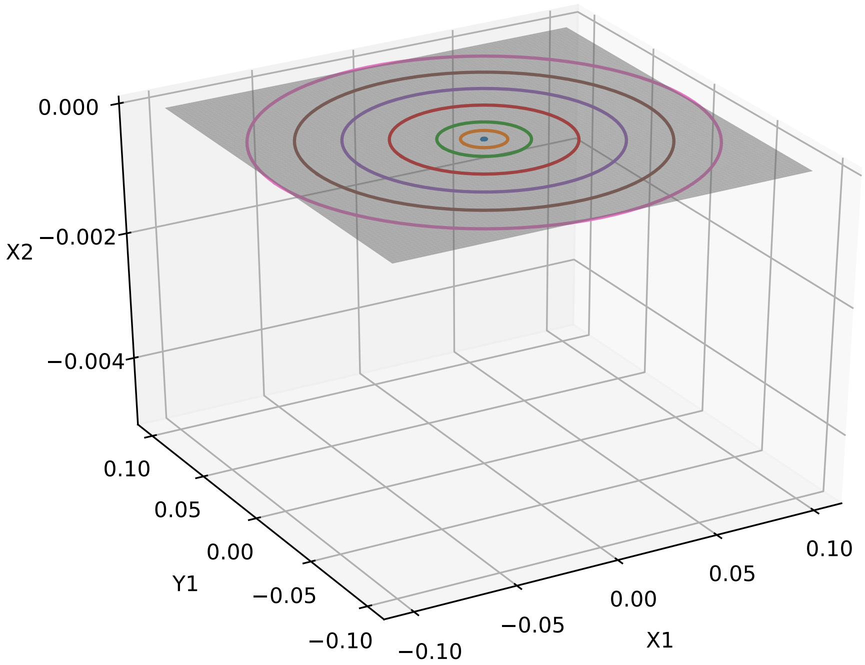

(a) Linear

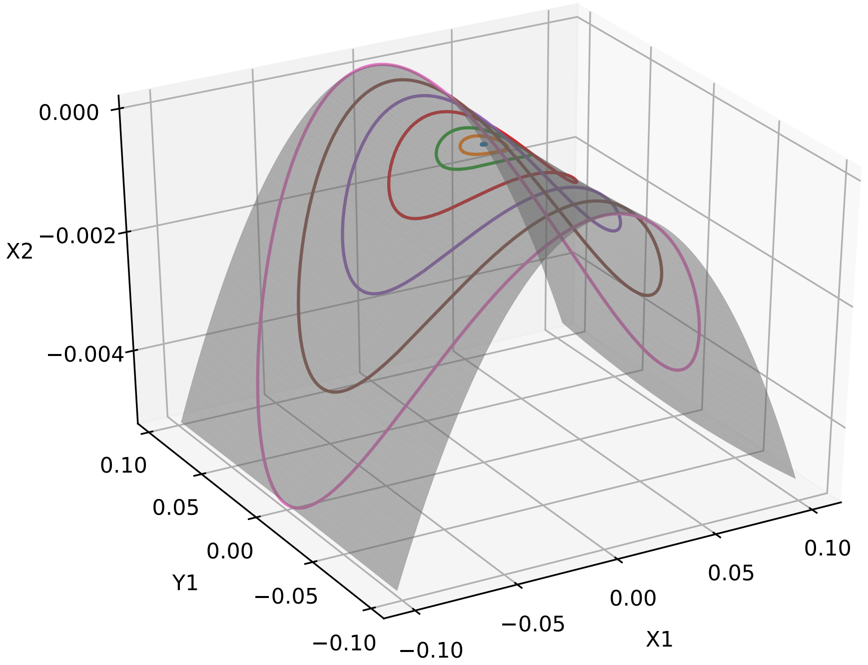

(b) Nonlinear

Figure 1.8: Linear (a) and nonlinear (b) invariant manifolds containing the periodic orbits of the linear/nonlinear problem with two degrees of freedom proposed in [176].

The limitation of such a formulation is that the variables used to compute the dynamics in the manifold are the master modes. The problem is that a fold in the manifold cannot be captured. The Normal Form approach overcomes such a limitation by introducing a nonlinear change of variable between the master modes and the normal coordinates by transposing the equation of the dynamics to its normal form. This transposition to the normal form derives from the Poincaré and Poincaré-Dulac theorems [46, 150]. The theorems are based on a first-order dynamical formalism. Thus, the velocities are added as variables in the equations of motion (1.152) of the N oscillators. The vector $\mathbf{X} = [x_1, y_1, \cdots, x_k, y_k, \cdots, x_N, y_N]$ of size $2N$ is considered and the oscillators' equations are transformed into a first-order system:

$$\dot{\mathbf{X}} = \mathbf{F}(\mathbf{X}) = \mathbf{\Lambda X} + \mathbf{N_2}(\mathbf{X}) + \mathbf{N_3}(\mathbf{X}), \tag{1.153}$$

in which the equations relative to the k^{th} oscillator are:

$$\dot{x}_k = y_k \tag{1.154}$$

$$\dot{y}_k = -2\xi_k \dot{x}_k - \omega_k^2 x_k - \sum_{i,j}^{N} g_{ij}^k x_i x_j - \sum_{i,j,m}^{N} h_{ijm}^k x_i x_j x_m, \tag{1.155}$$

where $\mathbf{\Lambda}$ is the diagonal matrix containing the eigenvalues $(\lambda_i)_{i=1,N}$ of the associated linear system while $\mathbf{N_2}(\mathbf{X}), \mathbf{N_3}(\mathbf{X})$ are respectively the quadratic and cubic nonlinearities. According to Poincaré's theorem, a nonlinear change of variable $\mathbf{Z}(\mathbf{X})$ exists such that the system (1.153) becomes linear in the absence of internal resonances:

$$\dot{\mathbf{Z}} = \Lambda \mathbf{X}. \tag{1.156}$$

Internal resonances are relations between the eigenvalues. An internal resonance of order p is a relation: $\lambda_i = \sum_{j=1}^{N} m_j \lambda_j$ with $m_j \geq 0$ and $\sum_{j=1}^{N} m_j = p$. Poincaré-Dulac's theorem demonstrates that in the case of internal resonances, the linear relation cannot be obtained and nonlinear terms relative to the internal resonances are kept. The equation in the normal form is thus:

$$\dot{\mathbf{Z}} = \Lambda \mathbf{X} + \mathbf{M_2}(\mathbf{X}) + \mathbf{M_3}(\mathbf{X}) + \cdots, \tag{1.157}$$

where $\mathbf{M_2}(\mathbf{X}), \mathbf{M_3}(\mathbf{X})$ and the higher orders contain only the resonating monomials. However, in the dynamical system (1.153), the eigenvalues are complex conjugates: $\mathbf{\Lambda} = \text{diag}\{\pm i\omega_k\}$ leading to trivial internal resonances of the form: $+i\omega_j = +i\omega_j + i\omega_k - i\omega_k$ for any $j, k \in [1, N]^2$. To implement the reduction to the normal form, [192] suggested a change of variable of the third order in the entire system between the physical and normal coordinates:

$$x_k = R_k + \mathcal{P}_1(R_i, S_i) \tag{1.158}$$

$$y_k = S_k + \mathcal{P}_2(R_i, S_i), \tag{1.159}$$

with $\mathcal{P}_1, \mathcal{P}_2$ polynomial functions of the normal coordinates $(R_i, S_i)_{i\in[1,N]}$, which expressions are detailed in the article [192]. With such a change of variable, all non-resonating monomials are eliminated leading to fewer nonlinear terms in the expression. The dynamics is computed in the space of the normal coordinates R_k, S_k and then rebuilt in the physical space x_k, y_k. To study the vibrations along one or several master modes, the number of equations in the reduced dynamics is considerably reduced since only a few nonlinear couplings remain leading to a significant truncation of the system. An explicit development up to the third order is provided, both for the conservative and damped systems. The expressions are given in the absence of non-trivial internal resonances, the latter requiring keeping additional terms in the normal form. A method of parametrisation of the change of variable was proposed in [16–18, 74] introducing polynomial developments in the change of variable and equations leading to an under-determined system. The determination of the system links the Shaw & Pierre approach referred to as *graph style* and the normal form approach called *normal form style*. The graph style approach consists in keeping linear relations between the normal coordinates and the master coordinates, while the normal form style is based on nonlinear change of variables. A non-intrusive implementation of the parametrisation method regarding an external FE solver is proposed in [202] under the name *direct normal form* (DNF). The parametrisation is there restricted to the second and third orders. To allow developments to arbitrary orders of parametrisation, an intrusive approach is detailed in [200]. In the previous methods, the construction of the nonlinear modes is based on the homogeneous equation, the external load is omitted and applied afterwards. Including a polynomial decomposition of the periodic external load is possible and results in time-dependent manifolds [138, 151].

1.4 Conclusion of the chapter

This first chapter introduced the dynamics of a structure in rotation around a fixed axis at constant rotation speed along with a description of temporal and frequency resolution methods of such equations. Then some common reduction methods were presented to reduce the dimension of the system to solve. The focus was first made on projection-based reduction methods for which the difficulty resides in the determination of the reduction basis capturing the nonlinearity and the determination of an explicit expression of the projected nonlinear forces. Finally, reduction methods based on other approaches were summarized. First hyper-reduction methods, computing the nonlinear forces only at some degrees of freedom are mentioned, then nonlinear normal modes are introduced. Such an approach is based on the computation of the dynamics in an invariant manifold instead of a projection on a linear basis. In the next chapter, the requirements of the structural ROM to tackle fluid-structure interaction problems are explained. A new reduced order model is proposed and tested on a simple test case of a beam model.

Chapter 2

Development of a non-intrusive ROM for aeroelastic coupling

In this chapter, the specificity of the fluid-structure coupling in the construction of reduced order models is first explained. Then, taking those considerations into account, a new reduced order model based on the implicit condensation and dual modes is introduced and further referred to as ICDual. Finally, the efficiency of such a ROM is evaluated thanks to a 2D Euler-Bernoulli/von Kármán beam model, first without, then with centrifugal rotation around a fixed axis. The interest of such a beam model is that the nonlinearity is cubic in the degrees of freedom. Therefore, the proposed ROM is directly transposable to 3D finite element applications with Saint Venant-Kirchhoff models where the geometric nonlinearity is known to be cubic in the degrees of freedom.

Contents

2.1 Reduction techniques for FSI

In the classical context of aeroelasticity, it is sufficient to consider linear structures when assessing stability. However, the need to reduce fuel consumption in the aeronautical industry has led to the development of higher-performance, lighter structures, resulting in geometric non-linearities induced by large displacements, modifying their static and dynamic behaviors. In this thesis, we focus on "high-fidelity" calculations to take into account non-linearities on both the structure and fluid sides. In the present chapter, the purpose is to build a non-linear reduced model only for the structure. Fluid dynamics is not reduced and is calculated using a CFD solver. Chapter 4 describes the fluid part and the coupling in more detail. To treat fluid-structure interaction problems of large dimensions, a linear reduced order model is often considered [23, 69–71, 116]. Besides, via forced-response of small amplitude, an aerodynamic damping and stiffness can be identified, and aeroelastic phenomena investigated [30, 44]. However, such method cannot be applied to large amplitude vibrations where both the fluid and the structure undergo a nonlinear behavior. The context of this work is to capture with high-fidelity the behavior of the fluid and to build a nonlinear ROM for the structure. A weak coupling approach between the fluid solver elsA [19] and a nonlinear reduced order model using complex nonlinear modes was proposed in [136] to treat friction at blade roots. Regarding geometric nonlinearities, [123] coupled a fluid solver with an ICE ROM to replace the structural solver and compute the aeroelastic response of a wing. The specificity of the aerodynamic forces is that those are follower forces leading to a dependency of the load to the position. Considering a reduction method based on invariant manifolds, the load has to be either explicitly known leading to time dependent invariant manifolds, or is not considered in the construction of the model but is applied afterwards. Examples of such methods for fluid-structure interaction problems are found in [2, 110, 193]. In the present work, a projection-based ROM is considered, with a reduction basis consisting of both linear normal modes and a pertinent set of dual modes. The nonlinear forces in the reduced space are approximated as a third-order polynomial of the generalized coordinates whose coefficients are identified via imposed loads.

2.2 A new reduced order model combining dual modes and the implicit condensation (ICDual)

In this section, an original reduction method using dual modes and determining the coefficients of the projected nonlinear forces with imposed loads is detailed. Such method will be referred to as ICDual. First, the determination of the dual modes to improve the reduction basis is detailed. Then, two methods to determine the coefficients of the projected nonlinear forces using prescribed loads are proposed. The originality of the method lies in the determination of the projected nonlinear forces. The coefficients associated to both the linear normal modes and the dual modes in the reduction basis are obtained from imposed loads generated with the linear normal modes shapes only. Thus the same loads cases can be used to determine the dual modes and the projected nonlinear forces coefficients. This first method is similar to the Implicit Condensation method in the sense that it exploits the FE nonlinear forces while a second is based on the tangent stiffness matrices and is detailed further.

2.2.1 Computation of the nonlinear forces coefficients

The coefficients of the nonlinear forces approximation are computed similarly to the IC method in the sense that prescribed loads are applied to the structure. However, the reduction basis considered in the present work does not only contain linear normal modes, but also dual modes. Here, the loads are not imposed on the entire basis containing both linear normal modes and dual modes as suggested in [122, 143], but only on the linear normal modes. Indeed, applying loads to the dual modes produces internal forces whose amplitudes differ by several orders of magnitude from those associated to linear modes. The choice of the weighting coefficients to impose those loads becomes tricky and strongly alters the results.

In this thesis, external loads are therefore prescribed only from a combination of linear modes, but displacements associated to dual modes are also included in the static solutions because of the nonlinear coupling. The same loads as those used for the determination of the dual modes Equation (1.115) can thus be reused and possibly supplemented by additional load cases. With such distribution of loads based on the linear modes, the ROM can be used for different load cases, such as aerodynamic forces for instance since the prescribed loads in Equation (1.115) are rather generic. Besides, the product with the stiffness matrix provides an estimation of the amplitude of the real physical displacement. Indeed, if the geometric nonlinearity was neglected, the displacement obtained by such a load case would exactly be the distribution imposed by the linear combination of modes $\sum_{i=1}^{n_\mathrm{b}} \alpha_i^{(\ell)} \boldsymbol{\phi}_i$. Since geometrical nonlinearities affect the static displacement and generally result in smaller displacements or with similar order of magnitude than linear ones, the previous remark gives an upper limit to the order of magnitude of the displacement. This observation provides a strategy to select the coefficients $\alpha_i^{(\ell)}$ so that the loads imposed are large enough to trigger geometric nonlinearities, and not too large to remain below the yields stresses of the materials. From this set of n_L external loadings, the n_L nonlinear static displacements are obtained by solving, with a Newton-Raphson algorithm, the nonlinear static equations:

$$\mathbf{K}\mathbf{u}_\mathbf{s}^{(\ell)} + \mathbf{f_{nl}}(\mathbf{u}_\mathbf{s}^{(\ell)}) = \mathbf{f}_\mathrm{ext}^{(\ell)}, \tag{2.1}$$

Then the associated generalized coordinates $\mathbf{q}^{(\ell)}$ are computed by a least-squares approximation using the pseudo-inverse of $\mathbf{V}$ from the equation:

$$\mathbf{q}^{(\ell)} = (\mathbf{V}^T\mathbf{V})^{-1}\mathbf{V}^T\mathbf{u}_\mathbf{s}^{(\ell)}. \tag{2.2}$$

At this point n_L couples $\left(\mathbf{q}^{(\ell)}, \mathbf{f_{nl}}(\mathbf{u}_\mathbf{s}^{(\ell)})\right)$ are determined and satisfy the following system for the unknowns β_{ij}^k and γ_{ijm}^k:

$$\widetilde{f}_\mathrm{nl}^k(\mathbf{q}^{(\ell)}) = \mathbf{V}_k^T\mathbf{f_{nl}}(\mathbf{V}\mathbf{q}^{(\ell)}) = \sum_{i=1}^{n}\sum_{j=i}^{n} \beta_{ij}^k q_i^{(\ell)} q_j^{(\ell)} + \sum_{i=1}^{n}\sum_{j=i}^{n}\sum_{m=j}^{n} \gamma_{ijm}^k q_i^{(\ell)} q_j^{(\ell)} q_m^{(\ell)}. \tag{2.3}$$

The previous system of equations for each $k \in [1, n]$ can be written in the matrix form as follows:

$$\begin{bmatrix} \mathbf{q}_\mathrm{quad}^T(\mathbf{q}^{(1)}) \\ \mathbf{q}_\mathrm{quad}^T(\mathbf{q}^{(2)}) \\ \vdots \\ \mathbf{q}_\mathrm{quad}^T(\mathbf{q}^{(n_\mathrm{L})}) \end{bmatrix} \begin{pmatrix} \beta_{11}^k \\ \beta_{12}^k \\ \vdots \\ \beta_{nn}^k \end{pmatrix} + \begin{bmatrix} \mathbf{q}_\mathrm{cub}^T(\mathbf{q}^{(1)}) \\ \mathbf{q}_\mathrm{cub}^T(\mathbf{q}^{(2)}) \\ \vdots \\ \mathbf{q}_\mathrm{cub}^T(\mathbf{q}^{(n_\mathrm{L})}) \end{bmatrix} \begin{pmatrix} \gamma_{111}^k \\ \gamma_{112}^k \\ \vdots \\ \gamma_{nnn}^k \end{pmatrix} \approx \begin{bmatrix} \mathbf{f_{nl}}^T(\mathbf{u}_\mathbf{s}^{(1)}) \\ \mathbf{f_{nl}}^T(\mathbf{u}_\mathbf{s}^{(2)}) \\ \vdots \\ \mathbf{f_{nl}}^T(\mathbf{u}_\mathbf{s}^{(n_\mathrm{L})}) \end{bmatrix} \mathbf{V}_k \tag{2.4}$$

with:

$$\begin{cases} \mathbf{q}_\mathrm{quad}(\mathbf{q}) &= \left[(q_1)^2 \quad q_1q_2 \quad q_2q_2 \quad q_2q_3 \quad q_3q_3 \quad \cdots \quad (q_n)^2\right]^T \\ \mathbf{q}_\mathrm{cub}(\mathbf{q}) &= \left[(q_1)^3 \quad q_1q_1q_2 \quad q_1q_2q_2 \quad q_1q_2q_3 \quad q_1q_3q_3 \quad \cdots \quad (q_n)^3\right]^T. \end{cases} \tag{2.5}$$

If the FE code provides the quadratic and cubic components of $\mathbf{f_{nl}}$ separately, the nonlinear coefficients can be identified individually by solving two different systems. Otherwise, the coefficients have to be identified simultaneously by solving the system (2.4) that can be written as follows:

$$\begin{bmatrix}\mathbf{Q}_\mathrm{quad} & \mathbf{Q}_\mathrm{cub}\end{bmatrix} \begin{bmatrix} \boldsymbol{\beta}^k \\ \boldsymbol{\gamma}^k \end{bmatrix} \approx \begin{bmatrix} \mathbf{f_{nl}}^T(\mathbf{u}_\mathbf{s}^{(1)}) \\ \vdots \\ \mathbf{f_{nl}}^T(\mathbf{u}_\mathbf{s}^{(n_\mathrm{L})}) \end{bmatrix} \mathbf{V}_k \tag{2.6}$$

For each k and $n \geq 3$, the system includes $n(n+1)/2$ unknowns for the coefficients β_{ij}^k and $(n^3 + 3n^2 + 2n)/6$ for the coefficients γ_{ijm}^k. The system is thus well determined when the number of loads n_L is equal to the number of coefficients; otherwise the system is over- or under-determined and a least-squares approximation is necessary. Note that when the problem presents symmetries, a significant number of coefficients are null and less load cases are required. When the quadratic and cubic coefficients cannot be computed separately, penalized regression methods such as Ridge, Lasso [189] or Elastic Net [210] can be preferred to the usual least-squares due to the possibly large condition number of the system. Two advantages of the proposed procedure over the identification of coefficients based on prescribed displacements can be mentioned. Firstly, for 3D structures, no correction is required unlike the case where displacements are imposed [7, 199]. Secondly, the load cases and the associated solutions, computed to determine the dual modes, are reused here in the determination of the force coefficients. It is worth mentioning that more load cases may be necessary to identify the coefficients according to the number of unknowns in the system to solve, especially when the quadratic and cubic nonlinear forces cannot be identified separately.

2.2.2 Variant using the tangent stiffness matrix

When available as an output of the FE code, the use of the tangent stiffness matrix is suggested in [143] to compute the coefficients. Indeed, considering the Jacobian of the projected nonlinear forces, the system writes:

$$\begin{bmatrix} \delta\mathbf{Q}_{\text{quad}}(\mathbf{q}^{(1)}) \\ \delta\mathbf{Q}_{\text{quad}}(\mathbf{q}^{(2)}) \\ \vdots \\ \delta\mathbf{Q}_{\text{quad}}(\mathbf{q}^{(n_{\text{L}})}) \end{bmatrix} \begin{pmatrix} \beta^k_{11} \\ \beta^k_{12} \\ \vdots \\ \beta^k_{nn} \end{pmatrix} + \begin{bmatrix} \delta\mathbf{Q}_{\text{cub}}(\mathbf{q}^{(1)}) \\ \delta\mathbf{Q}_{\text{cub}}(\mathbf{q}^{(2)}) \\ \vdots \\ \delta\mathbf{Q}_{\text{cub}}(\mathbf{q}^{(n_{\text{L}})}) \end{bmatrix} \begin{pmatrix} \gamma^k_{111} \\ \gamma^k_{112} \\ \vdots \\ \gamma^k_{nnn} \end{pmatrix} \approx \begin{bmatrix} \widetilde{\mathbf{K}}^{(1)}_{\text{nl},k} \\ \widetilde{\mathbf{K}}^{(2)}_{\text{nl},k} \\ \vdots \\ \widetilde{\mathbf{K}}^{(n_{\text{L}})}_{\text{nl},k} \end{bmatrix}, \tag{2.7}$$

where

$$\delta\mathbf{Q}_{\text{quad}}(\mathbf{q}) = \begin{bmatrix} \dfrac{\partial\mathbf{q}_{\text{quad}}(\mathbf{q})}{\partial q_1} \\ \vdots \\ \dfrac{\partial\mathbf{q}_{\text{quad}}(\mathbf{q})}{\partial q_n} \end{bmatrix}, \quad \delta\mathbf{Q}_{\text{cub}}(\mathbf{q}) = \begin{bmatrix} \dfrac{\partial\mathbf{q}_{\text{cub}}(\mathbf{q})}{\partial q_1} \\ \vdots \\ \dfrac{\partial\mathbf{q}_{\text{cub}}(\mathbf{q})}{\partial q_n} \end{bmatrix}, \tag{2.8}$$

and where the notation $\widetilde{\mathbf{K}}^{(\ell)}_{\text{nl},k}$ corresponds to the transpose of the k^{th} row of the matrix $\mathbf{K_{nl}}^{(\ell)} = \mathbf{V}^T\mathbf{K_{nl}}(\mathbf{u}_\mathbf{s}^{(\ell)})\mathbf{V}$. As in the case with the nonlinear forces $\mathbf{f_{nl}}$, when the quadratic and cubic components of $\mathbf{K_{nl}}$ can be treated separately, the nonlinear coefficients $\boldsymbol{\beta}^k$ and $\boldsymbol{\gamma}^k$ can be identified individually by solving two different systems, otherwise the full system can be solved. In [142], the tangent stiffness matrix is evaluated with imposed displacements. Here, the tangent stiffness matrix $\mathbf{K_{nl}}(\mathbf{u}_\mathbf{s}^{(\ell)})$ is evaluated for the nonlinear static solutions $\mathbf{u}^{(\ell)}$ ($\ell \in [1, n_{\text{L}}]$) computed under the loads $\mathbf{f}^{(\ell)}_{\text{ext}}$. Each nonlinear static solution $\mathbf{u}^{(\ell)}$ gives a set of n equations, compared to only one equation with the nonlinear force $\mathbf{f_{nl}}(\mathbf{u}^{(\ell)})$. Thus, the number of static solutions necessary to compute the coefficients is much lower than with the method based on nonlinear forces in section 2.2.1.

Once the reduction basis and the coefficients of the nonlinear internal forces have been calculated, the coupling between this ROM and a fluid solver can be performed. The fluid-structure coupling procedure used in this work is discussed in the chapter 4 and applied in chapter 5.

2.3 Application to a one-dimensional Euler-Bernoulli beam with von Kármán hypothesis

This section provides details on an Euler-Bernoulli beam model, the shear deformation of the sections is thus neglected. In each element of the discretized beam, the von Kármán hypothesis of small axial strain/ moderate rotations is assumed. Such beam formulation is then used in section 2.3.2 to evaluate the efficiency of the ROMs under several load cases.

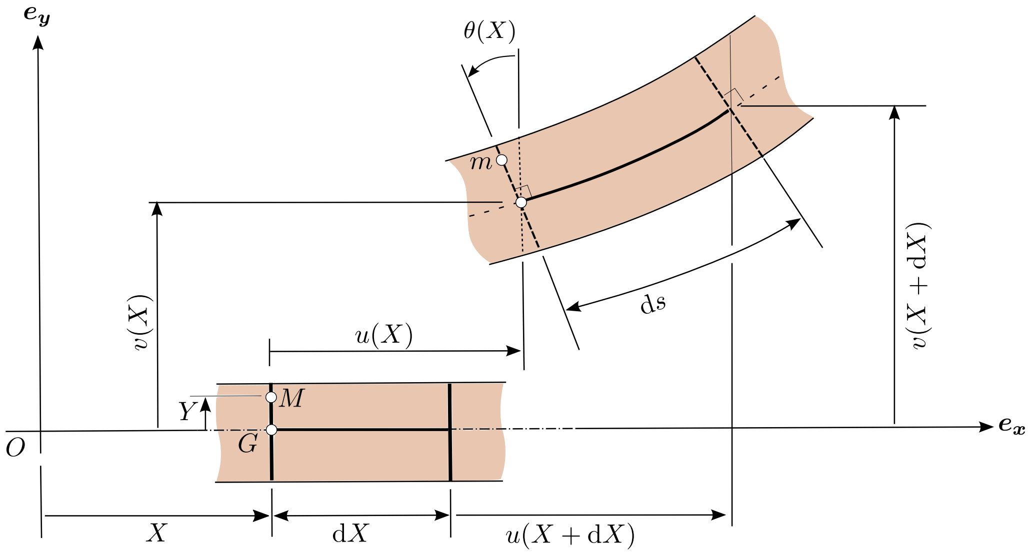

Figure 2.1: Lagrangian kinematics of the beam.

A material point M in the initial geometry is described in the reference frame $(\boldsymbol{e_x}, \boldsymbol{e_y})$ by its lagrangian coordinates (X, Y). The same material point is written m in the deformed geometry. Figure 2.1 illustrates the notations used in the beam formulation. The position vector of the material point M in the initial and deformed configurations are:

$$\boldsymbol{OM} = X\boldsymbol{e_x} + Y\boldsymbol{e_y} \tag{2.9}$$

$$\boldsymbol{Om} = \boldsymbol{OM} + \boldsymbol{u}(M). \tag{2.10}$$

The position of the material point M is defined by a solid rotation $\boldsymbol{R}(\theta)$ of the section around the associated point G on the neutral axis. The displacements vector $\boldsymbol{u}(M)$ is therefore:

$$\boldsymbol{u}(M) = \boldsymbol{u}(G) + [\boldsymbol{R}(\theta) - \mathbf{I}]\,\boldsymbol{GM} \quad \text{with} \quad \boldsymbol{R}(\theta) = \begin{pmatrix} \cos\theta & -\sin\theta \\ \sin\theta & \cos\theta \end{pmatrix}_{(e_x, e_y)} \tag{2.11}$$

Writing $\boldsymbol{u}(G) = u\boldsymbol{e_x} + v\boldsymbol{e_y}$ the coordinates of the point G on the neutral axis and noting that $\boldsymbol{GM} = Y\boldsymbol{e_y}$, then the displacement $\boldsymbol{u}(M)$ writes:

$$\boldsymbol{u}(M) = \underbrace{[u - Y\sin\theta]}_{u_x}\,\boldsymbol{e_x} + \underbrace{[v - Y(\cos\theta - 1)]}_{u_y}\,\boldsymbol{e_y}, \tag{2.12}$$

where $u_x(X, Y, t)$ and $u_y(X, Y, t)$ are respectively the axial and transverse components of the displacement $\boldsymbol{u} = \boldsymbol{u}(X, Y, t)$ of the point M. The position of the point m is therefore:

$$\boldsymbol{Om} = \boldsymbol{OM} + \boldsymbol{u}(M) = (X + u - Y\sin\theta)\boldsymbol{e_x} + (v + Y\cos\theta)\boldsymbol{e_y}. \tag{2.13}$$

Engineering strain

Supposing first that the shear deformation is allowed in the beam formulation, the extension/compression of an infinitesimal distance $\mathrm{d}X$ on the neutral axis of the beam is measured by the engineering strain $\tilde{e}$. The angle θ is the rotation of the section with shear deformation and φ the angle of rotation of the section without shear strain, the difference is written $\tilde{\gamma} = \theta - \varphi$.

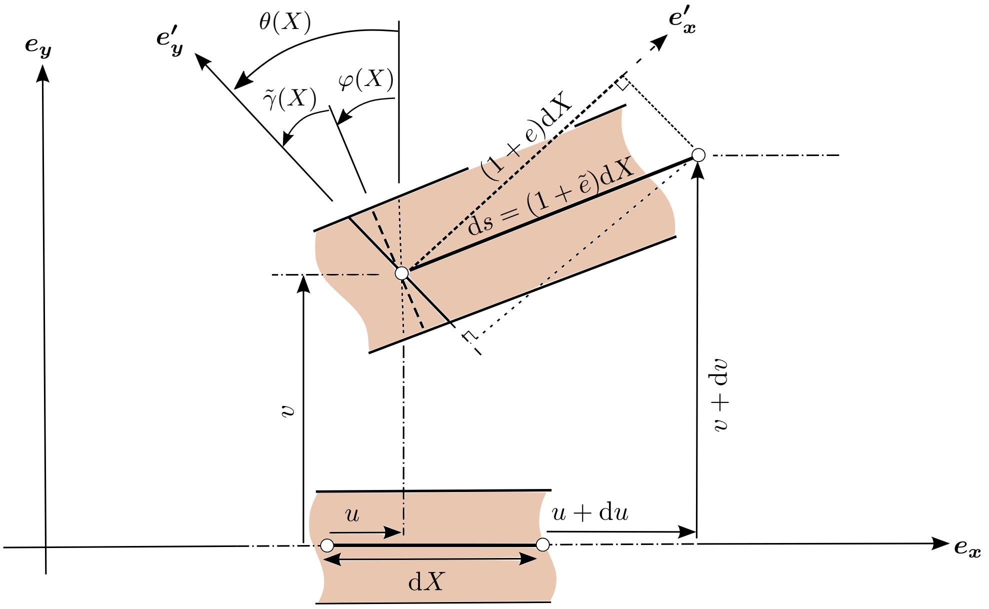

Figure 2.2: Definition of the engineering strain.

Figure 2.2 represents the engineering strain and the rotation of the section when shear deformation is allowed. The following relations are obtained:

$$\sin\varphi = \frac{\mathrm{d}v}{\mathrm{d}s} = \frac{v'}{1+\tilde{e}}, \tag{2.14}$$

$$\cos\varphi = \frac{\mathrm{d}u + \mathrm{d}X}{\mathrm{d}s} = \frac{1+u'}{1+\tilde{e}}, \tag{2.15}$$

$$\tag{2.16}$$

in which the notations u' and v' are introduced respectively for $\mathrm{d}u/\mathrm{d}X$ and $\mathrm{d}v/\mathrm{d}X$. The strain of the neutral axis in the direction perpendicular to the section is written e and its expression according to the variables u, v, θ is:

$$\begin{aligned}
(1+e) &= (1+\tilde{e})\cos\tilde{\gamma} = (1+\tilde{e})\cos(\theta-\varphi) && (2.17)\\
&= (1+\tilde{e})\big[\cos\theta\cos\varphi + \sin\theta\sin\varphi\big] && (2.18)\\
&= (1+\tilde{e})\big[\cos\theta\left(\frac{1+u'}{1+\tilde{e}}\right) + \sin\theta\left(\frac{v'}{1+\tilde{e}}\right)\big] && (2.19)\\
&= (1+u')\cos\theta + v'\sin\theta, && (2.20)
\end{aligned}$$

while the expression of the shear deformation is:

$$\begin{aligned}\gamma &= -(1+\tilde{e})\sin\tilde{\gamma} = -(1+\tilde{e})\sin(\theta-\varphi) && (2.21)\\ &= -(1+\tilde{e})\big[\sin\theta\cos\varphi - \sin\varphi\cos\theta\big] && (2.22)\\ &= -(1+\tilde{e})\big[\sin\theta\left(\frac{1+u'}{1+\tilde{e}}\right) - \left(\frac{v'}{1+\tilde{e}}\right)\cos\theta\big] && (2.23)\\ &= -(1+u')\sin\theta + v'\cos\theta. && (2.24)\end{aligned}$$

The Bernoulli beam formulation stipulates that the shear deformation is neglected ($\gamma = 0$), it implies that the rotation of the section is perpendicular to the neutral axis: $\tilde{\gamma} = 0$ thus $\varphi = \theta$ and $\tilde{e} = e$.

The von Kármán beam model

The gradient of the displacement of the point M is given by the following expression:

$$\nabla\boldsymbol{u} = \begin{pmatrix} \dfrac{\partial u_x}{\partial X} & \dfrac{\partial u_x}{\partial Y} \\ \dfrac{\partial u_y}{\partial X} & \dfrac{\partial u_y}{\partial Y} \end{pmatrix} = \begin{pmatrix} u' - Y\theta'\cos\theta & -\sin\theta \\ v' - Y\theta'\sin\theta & \cos\theta - 1 \end{pmatrix}, \tag{2.25}$$

from which an expression of the Green-Lagrange strain tensor can be derived:

$$\boldsymbol{E} = \frac{1}{2}\left[\nabla\boldsymbol{u} + \nabla\boldsymbol{u}^T + \nabla\boldsymbol{u}^T\nabla\boldsymbol{u}\right]. \tag{2.26}$$

The individual components of the Green-Lagrange strain tensor are thus:

$$\begin{aligned} E_{xx} &= \frac{1}{2}\big[(1+u')^2 + v'^2 - 1\big] - Y\theta'\big[(1+u')\cos\theta + v'\sin\theta\big] + \frac{1}{2}Y^2\theta'^2, && (2.27)\\ E_{xy} &= E_{yx} = \frac{1}{2}\big[-(1+u')\sin\theta + v'\cos\theta\big] = \frac{\gamma}{2} = 0, && (2.28)\\ E_{yy} &= 0. && (2.29)\end{aligned}$$

Therefore, the only non-null component of the Green-Lagrange strain tensor is the axial component. Its evaluation on the neutral axis ($Y = 0$) is written E_{xx}^0 and has the following expression:

$$E_{xx}^0 = \frac{1}{2}\big[(1+u')^2 + v'^2 - 1\big] = \frac{1}{2}\big[(1+e)^2 - 1\big]. \tag{2.30}$$

The von Kármán hypothesis of small axial deformation and moderate rotations for Bernoulli beams translates into small e and u', but moderate $\theta = v'$. Since the engineering strain is small,

$$e \approx E_{xx}^0 = \frac{1}{2}\big[(1+u')^2 + v'^2 - 1\big] = u' + \frac{1}{2}u'^2 + \frac{1}{2}v'^2, \tag{2.31}$$

and as u' is small, the von Kármán hypothesis takes the following form for the engineering strain:

$$e \approx E_{xx}^0 \approx u' + \frac{1}{2}v'^2 = u' + \frac{1}{2}\theta^2. \tag{2.32}$$

Approximation of the Green-Lagrange strain tensor for small strains

In the von Kármán hypothesis of small strain detailed above, the link between the engineering strain e and the axial component on the neutral axis of the Green-Lagrange strain tensor is provided. In this paragraph, an expression of the Green-Lagrange strain tensor in the entire section as a function of the engineering strain e and the curvature κ is detailed. The idea of the small strain approximation of the Green-Lagrange strain tensor is to allow large rotations while neglecting the quadratic part of the pure deformation. The gradient of the transformation is defined by:

$$\boldsymbol{F} = \nabla(\boldsymbol{Om}) = \mathbf{I} + \nabla \boldsymbol{u} = \begin{pmatrix} 1 + u' - Y\theta' \cos\theta & -\sin\theta \\ v' - Y\theta' \sin\theta & \cos\theta \end{pmatrix} \tag{2.33}$$

$$= \begin{pmatrix} 1 + u' & 0 \\ v' & 0 \end{pmatrix} + \boldsymbol{R}(\theta) \begin{pmatrix} -Y\theta' & 0 \\ 0 & 1 \end{pmatrix} \tag{2.34}$$

The transformation is decomposed into a rotation and a pure deformation, it is the polar decomposition of the gradient of the transformation:

$$\boldsymbol{F} = \boldsymbol{R}(\theta)\boldsymbol{U} \tag{2.35}$$

with $\boldsymbol{R}(\theta)$ the rotation operator, an orthogonal matrix, and $\boldsymbol{U}$ the pure deformation:

$$\boldsymbol{U} = \boldsymbol{R}(\theta)^{-1}\boldsymbol{F} = \boldsymbol{R}(\theta)^T\boldsymbol{F} = \boldsymbol{R}(-\theta)\boldsymbol{F} \tag{2.36}$$

$$= \begin{pmatrix} (1 + u')\cos\theta + v'\cos\theta - Y\theta' & 0 \\ -(1 + u')\sin\theta + v'\cos\theta & 1 \end{pmatrix}. \tag{2.37}$$

Since $\gamma = -(1 + u')\sin\theta + v'\cos\theta = 0$, the pure deformation $\boldsymbol{U}$ becomes:

$$\boldsymbol{U} = \underbrace{\begin{pmatrix} 1 & 0 \\ 0 & 1 \end{pmatrix}}_{\mathbf{I}} + \underbrace{\begin{pmatrix} e - Y\theta' & 0 \\ 0 & 0 \end{pmatrix}}_{\text{written } \boldsymbol{L}}. \tag{2.38}$$

With such decomposition, the Green-Lagrange strain tensor becomes:

$$\boldsymbol{E} = \frac{1}{2}\left(\boldsymbol{F}^T\boldsymbol{F} - \mathbf{I}\right) = \frac{1}{2}\big(\boldsymbol{U}^T \underbrace{\boldsymbol{R}(\theta)^T\boldsymbol{R}(\theta)}_{\mathbf{I}} \boldsymbol{U} - \mathbf{I}\big) = \frac{1}{2}\left(\boldsymbol{U}^T\boldsymbol{U} - \mathbf{I}\right) = \frac{1}{2}\left(\boldsymbol{L} + \boldsymbol{L}^T + \boldsymbol{L}^T\boldsymbol{L}\right), \tag{2.39}$$

with:

$$\boldsymbol{L}^T\boldsymbol{L} = \begin{pmatrix} (e - Y\theta')^2 & 0 \\ 0 & 0 \end{pmatrix} \tag{2.40}$$

The quadratic part of the pure deformation, $\boldsymbol{L}^T\boldsymbol{L}$, is neglected since it is a product of small terms. First, the strain deformation e is small because the axial strains are considered small. Second, the term $Y\theta'$ is small since $\kappa = \theta'$ is of the order of magnitude of $\frac{1}{R}$ with R the radius of curvature which is much larger than $|Y|$ ($|R| >> |Y|$). Therefore the Green-Lagrange strain tensor becomes:

$$\boldsymbol{E} \approx \frac{1}{2}\left(\boldsymbol{L} + \boldsymbol{L}^T\right) = \begin{pmatrix} e - Y\kappa & 0 \\ 0 & 0 \end{pmatrix} \tag{2.41}$$

2.3.1 Virtual work principle

The virtual work principle stipulates that for any virtual displacement $\delta\boldsymbol{u}$ applied to the structure, the sum of the virtual work of the internal forces δW_{int} and the virtual work of the external forces δW_{ext} is equal to the virtual work associated with the acceleration δW_{acc}:

$$\delta W_{\text{int}} + \delta W_{\text{acc}} = \delta W_{\text{acc}} \tag{2.42}$$

with

$$\delta W_{\text{acc}} = \iiint_V \rho \boldsymbol{a}_{/\mathcal{R}_{\text{g}}} \cdot \delta\boldsymbol{u} \, \text{d}V \tag{2.43}$$

$$\delta W_{\text{int}} = -\iiint_V \boldsymbol{S} : \boldsymbol{\delta E} \cdot \delta\boldsymbol{u} \, \text{d}V \tag{2.44}$$

$$\delta W_{\text{acc}} = \iiint_V \boldsymbol{f}_{\text{ext}}^{\text{volume}} \cdot \delta\boldsymbol{u} \, \text{d}V + \iint_S \boldsymbol{f}_{\text{ext}}^{\text{surface}} \cdot \delta\boldsymbol{u} \, \text{d}S \tag{2.45}$$

$$\tag{2.46}$$

Virtual work of the internal forces
Considering a linear isotropic elastic material of Young's modulus E and following the Saint Venant-Kirchhoff constitutive law, the relation between the Piola-Kirchhoff stress tensor and the Green-Lagrange strain tensor is the following:

$$\mathbf{E} = \frac{1+\nu}{E}\mathbf{S} - \frac{\nu}{E}\text{trace}(\mathbf{S})\mathbf{I}. \tag{2.47}$$

Therefore, in the case of the present beam, the only non-zero component of the Piola-Kirchhoff stress tensor is the axial component and is equal to $\text{S}_{xx} = E\text{E}_{xx} = E(e - Y\kappa)$. The virtual work of the internal forces is thus

$$\delta W_{\text{int}} = -\iiint_V S_{xx}\delta E_{xx} \, \text{d}V \tag{2.48}$$

$$= -\iiint_V E(e - Y\kappa)(\delta e - Y\delta\kappa) \, \text{d}V. \tag{2.49}$$

After integration in the section of the beam, the virtual work of the internal forces of the beam is obtained:

$$\delta W_{\text{int}} = -\int_0^L \big(EAe\delta e + EI\kappa\delta\kappa\big) \, \text{d}X, \tag{2.50}$$

where A is the area of the section and I the inertia, and using the relations:

$$\int_Y \int_Z \text{d}Y\text{d}Z = A \tag{2.51}$$

$$\int_Y Y^2 \text{d}Y = I \tag{2.52}$$

$$\int_Y Y \, \text{d}Y = 0. \tag{2.53}$$

In the current case of the Bernoulli beam with von Kármán hypothesis, the membrane strain, the curvature and their variations are:

$$e = u' + \frac{1}{2}\theta^2 \qquad \Longrightarrow \quad \delta e = \delta u' + \theta\delta\theta \tag{2.54}$$

$$\kappa = \frac{\partial\theta}{\partial X} = \theta' \qquad \Longrightarrow \quad \delta\kappa = \delta\theta' \tag{2.55}$$

and the virtual work of the internal forces becomes:

$$\begin{aligned}
\delta W_{\text{int}} &= -\int_0^L \big(EAe\delta e + EI\kappa\delta\kappa\big)\,\mathrm{d}X && (2.56)\\
&= -\int_0^L \big[EA(u' + \frac{2}{2}\theta^2)(\delta u' + \theta\delta\theta) + EI\theta'\delta\theta'\big]\,\mathrm{d}X && (2.57)\\
&= -\int_0^L \Big[\underbrace{\big(EAu'\delta u' + EI\theta'\delta\theta'\big)}_{\text{linear contribution}} + \underbrace{EA(u'\theta\delta\theta + \frac{1}{2}\theta^2\delta u') +}_{\text{quadratic contribution}} \underbrace{\frac{1}{2}EA\theta^3\delta\theta}_{\text{cubic contribution}}\Big]\,\mathrm{d}X && (2.58)
\end{aligned}$$

Finite elements discretization in an element

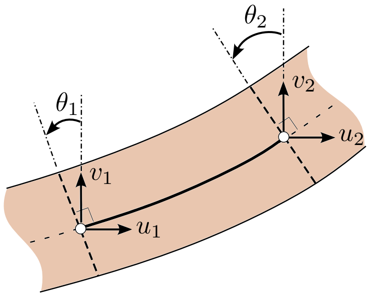

Figure 2.3: Degrees of freedom in one element of the beam.

In this paragraph, the FE discretization of the beam is introduced and will be later used in the virtual work principle. The FE discretization of Euler-Bernoulli beams is based on linear shape functions for the axial degrees of freedom and cubic Hermitian shape functions for the vertical and rotation degrees of freedom. Considering one element, the associated nodal values written $u_1, v_1, \theta_1, u_2, v_2, \theta_2$ are represented in Figure 2.3. Let $x \in [0, L_e]$ with L_e the length of the element e; the horizontal and vertical displacement in the element write:

$$\begin{aligned}
u(x) &= N_1(x)u_1 + N_2(x)u_2 && (2.59)\\
v(x) &= H_1(x)v_1 + H_2(x)\theta_1 + H_3(x)v_2 + H_4(x)\theta_2 && (2.60)
\end{aligned}$$

or under matrix form for the vector of unknowns $\mathbf{u}_{\text{e}} = \begin{bmatrix} u_1 & v_1 & \theta_1 & u_2 & v_2 & \theta_2 \end{bmatrix}^T$:

$$\begin{bmatrix} u_e(x) \\ v_e(x) \end{bmatrix} = \mathbf{N}\mathbf{u}_{\text{e}} \quad \text{with} \quad \mathbf{N} = \begin{pmatrix} \mathbf{N}_{\text{u}} \\ \mathbf{N}_{\text{v}} \end{pmatrix} = \begin{pmatrix} N_1 & 0 & 0 & N_2 & 0 & 0 \\ 0 & H_1 & H_2 & 0 & H_3 & H_4 \end{pmatrix} \qquad (2.61)$$

The shape functions N_1 and N_2 are linear while the shape functions H_1, H_2, H_3 and H_3 are 3rd order Hermite functions:

$$\begin{cases} N_1(x) = 1 - \dfrac{x}{L_e} \\ N_2(x) = \dfrac{x}{L_e} \\ H_1(x) = \left(1 + \dfrac{2x}{L_e}\right)\left(1 - \dfrac{x}{L_e}\right)^2 \\ H_2(x) = x\left(1 - \dfrac{x}{L_e}\right)^2 \\ H_3(x) = \dfrac{x^2}{L_e}\left(3 - \dfrac{2x}{L_e}\right) \\ H_4(x) = \dfrac{x^2}{L_e}\left(\dfrac{x}{L_e} - 1\right) \end{cases} \tag{2.62}$$

Besides, the rotation of the section is given by:

$$\theta_e(x) = \frac{\mathrm{d}v_e(x)}{\mathrm{d}x} = \frac{\mathrm{d}\mathbf{N}_\mathrm{v}(x)}{\mathrm{d}x}\mathbf{u}_\mathrm{e} \equiv {\mathbf{N}_\mathrm{v}}'\,\mathbf{u}_\mathrm{e} \tag{2.63}$$

with

$${\mathbf{N}_\mathrm{v}}' = \begin{bmatrix} 0 & \dfrac{\mathrm{d}H_1(x)}{\mathrm{d}x} & \dfrac{\mathrm{d}H_2(x)}{\mathrm{d}x} & 0 & \dfrac{\mathrm{d}H_3(x)}{\mathrm{d}x} & \dfrac{\mathrm{d}H_4(x)}{\mathrm{d}x} \end{bmatrix} \tag{2.64}$$

Finite elements discretization introduced in the virtual work of the internal forces

As explained previously, the virtual work of the internal forces is the sum of a linear, quadratic and cubic contributions, written respectively $-\delta W_\mathrm{int}^{(1)}$, $-\delta W_\mathrm{int}^{(2)}$ and $-\delta W_\mathrm{int}^{(3)}$:

$$-\delta W_\mathrm{int}^{(1)} = \int_0^{L_e} \left(EAu'\delta u' + EI\theta'\delta\theta'\right)\,\mathrm{d}X \tag{2.65}$$

$$-\delta W_\mathrm{int}^{(2)} = \int_0^{L_e} EA(u'\theta\delta\theta + \frac{1}{2}\delta u'\theta^2)\,\mathrm{d}X \tag{2.66}$$

$$-\delta W_\mathrm{int}^{(3)} = \int_0^{L_e} \frac{1}{2}EA\theta^3\delta\theta\,\mathrm{d}X \tag{2.67}$$

The FE discretization is then introduced in these expressions. Considering first the linear contribution, the FE discretization leads to:

$$\begin{aligned} -\delta W_\mathrm{int}^{(1)} &= \int_0^{L_e} \left(EAu'\delta u' + EI\theta'\delta\theta'\right)\,\mathrm{d}X && (2.68)\\ &= \int_0^{L_e} \left[EA(\mathbf{N}_\mathrm{u}^{'}\boldsymbol{\delta}\mathbf{u}_\mathrm{e})^T(\mathbf{N}_\mathrm{u}^{'}\mathbf{u}_\mathrm{e}) + EI(\mathbf{N}_\mathrm{v}^{''}\boldsymbol{\delta}\mathbf{u}_\mathrm{e})^T(\mathbf{N}_\mathrm{v}^{''}\mathbf{u}_\mathrm{e})\right]\,\mathrm{d}X && (2.69)\\ &= \boldsymbol{\delta}\mathbf{u}_\mathrm{e}^T\left(\int_0^{L_e}\left[EA({\mathbf{N}_\mathrm{u}^{'}}^T)(\mathbf{N}_\mathrm{u}^{'}) + EI({\mathbf{N}_\mathrm{v}^{''}}^T)(\mathbf{N}_\mathrm{v}^{''})\right]\,\mathrm{d}X\right)\mathbf{u}_\mathrm{e} && (2.70)\\ &= \boldsymbol{\delta}\mathbf{u}_\mathrm{e}^T\;\mathbf{K}_\mathrm{e}\;\mathbf{u}_\mathrm{e} && (2.71) \end{aligned}$$

with $\mathbf{K}_\mathrm{e}$ the elastic stiffness matrix of the element:

$$\mathbf{K}_\mathrm{e} = \int_0^{L_e} \left[EA(\mathbf{N}_\mathrm{u}'^{\,T})(\mathbf{N}_\mathrm{u}') + EI(\mathbf{N}_\mathrm{v}''^{\,T})(\mathbf{N}_\mathrm{v}'') \right] \mathrm{d}X \tag{2.72}$$

$$= \frac{EA}{L_e} \begin{pmatrix} 1 & 0 & 0 & -1 & 0 & 0 \\ 0 & 0 & 0 & 0 & 0 & 0 \\ 0 & 0 & 0 & 0 & 0 & 0 \\ -1 & 0 & 0 & 1 & 0 & 0 \\ 0 & 0 & 0 & 0 & 0 & 0 \\ 0 & 0 & 0 & 0 & 0 & 0 \end{pmatrix} + \frac{EI}{L_e^3} \begin{pmatrix} 0 & 0 & 0 & 0 & 0 & 0 \\ 0 & 12 & 6L_e & 0 & -12 & 6L_e \\ 0 & 6L_e & 4L_e^2 & 0 & -6L_e & 2L_e^2 \\ 0 & 0 & 0 & 0 & 0 & 0 \\ 0 & -12 & -6L_e & 0 & 12 & -6L_e \\ 0 & 6L_e & 2L_e^2 & 0 & -6L_e & 4L_e^2 \end{pmatrix} \tag{2.73}$$

The integration of the quadratic and cubic contributions of the internal nonlinear forces is slightly different. In fact, using an exact integration of the shape functions with the von Kármán hypothesis may lead to membrane locking, especially for a free boundary condition [155]. Indeed, at a free end (here at $x = L$ for a cantilever beam), the membrane strain is null for any position X in the last element:

$$e = 0 = \frac{\partial u}{\partial X} + \frac{1}{2}\left(\frac{\partial v}{\partial X}\right)^2 . \tag{2.74}$$

It means that the degrees of the polynomial approximations of $\partial u/\partial X$ and $(\partial v/\partial X)^2$ have to be the same. However, the shape functions for u are linear and those for v are cubic. Therefore, the above-mentioned constraint is not satisfied and leads to excessively stiff elements. This membrane-locking phenomenon is significantly accentuated when the lengths of the discretization elements are large. As explained in [155], a numerical way to prevent such a locking is to perform a reduced-integration with a single Gauss point of the nonlinear terms in the FE discretization of $-\delta W_\mathrm{int}^{(2)}$ and $-\delta W_\mathrm{int}^{(3)}$. After integration, the quadratic and cubic contributions of the virtual work of the internal forces are the following:

$$-\delta W_\mathrm{int}^{(2)} = \int_0^{L_e} EA(u'\theta\delta\theta + \frac{1}{2}\delta u'\theta^2)\ \mathrm{d}X = \boldsymbol{\delta}\mathbf{u}_\mathrm{e}^T \mathbf{f}_\mathrm{nl}^\mathrm{quad}(\mathbf{u}_\mathrm{e}) \tag{2.75}$$

$$-\delta W_\mathrm{int}^{(3)} = \int_0^{L_e} \frac{1}{2} EA\theta^3\delta\theta\ \mathrm{d}X = \boldsymbol{\delta}\mathbf{u}_\mathrm{e}^T \mathbf{f}_\mathrm{nl}^\mathrm{cub}(\mathbf{u}_\mathrm{e}), \tag{2.76}$$

where $\mathbf{f}_\mathrm{nl}^\mathrm{quad}(\mathbf{u}_\mathrm{e})$ and $\mathbf{f}_\mathrm{nl}^\mathrm{cub}(\mathbf{u}_\mathrm{e})$ are respectively the vectors of the quadratic and cubic nonlinear forces. Their computation with the symbolic Python library *Sympy* leads to the following expressions:

$$\mathbf{f}_\mathrm{nl}^\mathrm{quad} = \frac{EA}{32L_e^2} \begin{bmatrix} -\mathbf{f}_\mathrm{nl}^a & -12\mathbf{f}_\mathrm{nl}^b & -2L_e\mathbf{f}_\mathrm{nl}^b & \mathbf{f}_\mathrm{nl}^a & 12\mathbf{f}_\mathrm{nl}^b & -2L_e\mathbf{f}_\mathrm{nl}^b \end{bmatrix}^T \tag{2.77}$$

$$\mathbf{f}_\mathrm{nl}^\mathrm{cub} = \frac{EA}{512L_e^3} \begin{bmatrix} 0 & 6\mathbf{f}_\mathrm{nl}^c & L_e\mathbf{f}_\mathrm{nl}^c & 0 & -6\mathbf{f}_\mathrm{nl}^c & L_e\mathbf{f}_\mathrm{nl}^c \end{bmatrix}^T \tag{2.78}$$

with

$$\begin{cases} \mathbf{f}_\mathrm{nl}^a = L_e^2(\theta_1+\theta_2)^2 + 12L_e(\theta_1+\theta_2)(v_1-v_2) + 36(v_1-v_2)^2 \\ \mathbf{f}_\mathrm{nl}^b = (u_1-u_2)[L_e(\theta_1+\theta_2) + 6(v_1-v_2)] \\ \mathbf{f}_\mathrm{nl}^c = L_e^2(\theta_1+\theta_2)^2\big[L_e(\theta_1+\theta_2) + 18(v_1-v_2)\big] \\ \qquad + 108(v_1-v_2)^2\big[L_e(\theta_1+\theta_2) + 2(v_1-v_2)\big] \end{cases} \tag{2.79}$$

Finally, the virtual work in an element of the internal forces verifies

$$\boxed{-\delta W_\mathrm{int} = \boldsymbol{\delta}\mathbf{u}_\mathrm{e}^T \Big[\mathbf{K}_\mathrm{e}\mathbf{u}_\mathrm{e} + \mathbf{f}_\mathrm{nl}^\mathrm{quad}(\mathbf{u}_\mathrm{e}) + \mathbf{f}_\mathrm{nl}^\mathrm{cub}(\mathbf{u}_\mathrm{e})\Big]} \tag{2.80}$$

Finite elements discretization introduced in the virtual work of the external forces
The expression of the virtual work of the external forces is:

$$\delta W_{\text{acc}} = \iiint_V \boldsymbol{f}_{\text{ext}}^{\text{volume}} \cdot \boldsymbol{\delta u} \,\mathrm{d}V + \iint_S \boldsymbol{f}_{\text{ext}}^{\text{surface}} \cdot \boldsymbol{\delta u} \,\mathrm{d}S. \tag{2.81}$$

Introducing the FE discretization in the expression for one element leads to:

$$\delta W_{\text{acc}} = \boldsymbol{\delta} \mathbf{u}_{\text{e}}^T \mathbf{f}_{\text{ext}}, \tag{2.82}$$

where $\mathbf{f}_{\text{ext}}$ is the vector of the external forces.

Virtual work associated to the acceleration
The expression of the virtual work associated to the acceleration is the following:

$$\delta W_{\text{acc}} = \iiint_V \rho \boldsymbol{a}_{/\mathcal{R}_{\text{g}}} \cdot \boldsymbol{\delta u} \,\mathrm{d}V \tag{2.83}$$

The acceleration of a material point M is obtained by deriving twice Equation (2.13) with respect to time , leading to:

$$\boldsymbol{a(M)}_{/\mathcal{R}_{\text{g}}} = \left[\ddot{u} - Y(\ddot{\theta}\text{cos}\theta - \dot{\theta}^2\text{sin}\theta)\right]\boldsymbol{e_x} + \left[\ddot{v} - Y(\ddot{\theta}\text{sin}\theta + \dot{\theta}^2\text{cos}\theta)\right]\boldsymbol{e_y} \tag{2.84}$$

Regarding the virtual displacement, it is obtained from the expression of the continuous displacement field:

$$\boldsymbol{u} = \left[u - Y \sin\theta\right] \boldsymbol{e_x} + \left[v - Y(\cos\theta - 1)\right] \boldsymbol{e_y} \tag{2.85}$$

$$\boldsymbol{\delta u} = \left[\delta u - Y \cos\theta\delta\theta\right] \boldsymbol{e_x} + \left[\delta v - Y \sin\theta\delta\theta\right] \boldsymbol{e_y} \tag{2.86}$$

Therefore

$$\begin{aligned} \boldsymbol{a(M)}_{/\mathcal{R}_{\text{g}}} \cdot \boldsymbol{\delta u} = {} & \left[\ddot{u} - Y(\ddot{\theta}\text{cos}\theta - \dot{\theta}^2\text{sin}\theta)\right]\left[\delta u - Y\cos\theta\delta\theta\right] \\ & + \left[\ddot{v} - Y(\ddot{\theta}\text{sin}\theta + \dot{\theta}^2\text{cos}\theta)\right]\left[\delta v - Y\sin\theta\delta\theta\right] \end{aligned} \tag{2.87}$$

Developing and simplifying the expressions, we obtain:

$$\boldsymbol{a(M)}_{/\mathcal{R}_{\text{g}}} \cdot \boldsymbol{\delta u} = \ddot{u}\delta u + \ddot{v}\delta v + Y^2\ddot{\theta}\delta\theta + Y\left[\cdots\right] \tag{2.88}$$

where the expression $Y\left[\cdots\right]$ is not developed because it will be canceled by the integration of an odd function between opposed limits.
Considering the previous developments, the expression of the virtual work associated to the acceleration becomes:

$$\delta W_{\text{acc}} = \iiint_V \rho \boldsymbol{a(M)}_{/\mathcal{R}_{\text{g}}} \cdot \boldsymbol{\delta u} \,\mathrm{d}V = \int_0^L \rho A\left[\ddot{u}\delta u + \ddot{v}\delta v\delta u\right] + \rho I\ddot{\theta}\delta\theta \,\mathrm{d}X \tag{2.89}$$

Therefore, the FE discretization in an element of the contribution independent of the rotation, written δW_{acc} becomes:

$$\delta W_{\text{acc}} = \boldsymbol{\delta}\mathbf{u}_{\text{e}}^T \underbrace{\left(\int_0^L \rho A \begin{bmatrix}\mathbf{N}_{\text{u}} & \mathbf{N}_{\text{v}}\end{bmatrix} \begin{bmatrix}\mathbf{N}_{\text{u}} \\ \mathbf{N}_{\text{v}}\end{bmatrix} \mathrm{d}X + \int_0^L \rho I\left(\mathbf{N}_{\text{v}}^{\prime\,T}\mathbf{N}_{\text{v}}^{\prime}\right) \mathrm{d}X\right)}_{\text{written }\ \mathbf{M}_{\text{e}}} \ddot{\mathbf{u}}_{\text{e}} = \boldsymbol{\delta}\mathbf{u}_{\text{e}}^T \mathbf{M}_{\text{e}} \ddot{\mathbf{u}}_{\text{e}} \tag{2.90}$$

with $\mathbf{M}_{\mathrm{e}}$ the elementary mass matrix. Generally, the contribution of the rotational inertia is negligible. In this work, the mass matrix of one element is computed under the assumption that the local rotational inertia of the section is neglected and has the following expression:

$$\mathbf{M}_{\mathrm{e}} = \frac{\rho A}{2} \int_0^{L_e} \mathbf{N}^T \mathbf{N} \;\; \mathrm{d}x \tag{2.91}$$

$$= \rho A \frac{L_e}{420} \begin{pmatrix} 140 & 0 & 0 & 70 & 0 & 0 \\ 0 & 156 & 22L_e & 0 & 54 & -13L_e \\ 0 & 22L_e & 4L_e^2 & 0 & 13L_e & -3L_e^2 \\ 70 & 0 & 0 & 140 & 0 & 0 \\ 0 & 54 & 13L_e & 0 & 156 & -22L_e \\ 0 & -13L_e & -3L_e^2 & 0 & -22L_e & 4L_e^2 \end{pmatrix} \tag{2.92}$$

Finally the virtual work principle in an element of the beam leads to the equation:

$$\delta W_{\mathrm{acc}} - \delta W_{\mathrm{int}} - \delta W_{\mathrm{acc}} = 0 \tag{2.93}$$

$$\boldsymbol{\delta}\mathbf{u}_{\mathrm{e}}^T \left[\mathbf{M}_{\mathrm{e}} \ddot{\mathbf{u}}_{\mathrm{e}} + \mathbf{K}_{\mathrm{e}} \mathbf{u}_{\mathrm{e}} + \mathbf{f}_{\mathrm{nl}}^{\mathrm{quad}}(\mathbf{u}_{\mathrm{e}}) + \mathbf{f}_{\mathrm{nl}}^{\mathrm{cub}}(\mathbf{u}_{\mathrm{e}}) - \mathbf{f}_{\mathrm{ext}} \right] = 0 \tag{2.94}$$

Since this equation is verified for all admissible virtual displacements, the equation of the dynamics after assembling on all the elements is thus:

$$\boxed{\mathbf{M}\ddot{\mathbf{u}} + \mathbf{K}\mathbf{u} + \mathbf{f}_{\mathbf{nl2}}(\mathbf{u}) + \mathbf{f}_{\mathbf{nl3}}(\mathbf{u}) = \mathbf{f}_{\mathrm{ext}}}, \tag{2.95}$$

where $\mathbf{u}$ is the vector of all the degrees of freedom, $\mathbf{M}$ and $\mathbf{K}$ the mass and stiffness matrices, $\mathbf{f}_{\mathbf{nl2}}(\mathbf{u})$ and $\mathbf{f}_{\mathbf{nl3}}(\mathbf{u})$ the quadratic and cubic internal forces and $\mathbf{f}_{\mathrm{ext}}$ the vector of external forces.

Particular case of static solution under external loads with no axial contribution

When no axial load is applied, the linear and non-linear components of the vertical displacement and the rotation are identical since the nonlinearity is restricted to the axial displacement. This behavior is explained by the following developments. The static nonlinear equation in one element is considered and writes as follows:

$$\mathbf{K}_{\mathrm{e}} \mathbf{u}_{\mathrm{e}} + \mathbf{f}_{\mathrm{nl}}^{\mathrm{quad}}(\mathbf{u}_{\mathrm{e}}) + \mathbf{f}_{\mathrm{nl}}^{\mathrm{cub}}(\mathbf{u}_{\mathrm{e}}) = \mathbf{f}_{\mathrm{ext}}. \tag{2.96}$$

The six equations of the above system are:

$$\begin{cases} \dfrac{EA}{L_e}(u_1 - u_2) & + \dfrac{EA}{32L_e^2}\mathbf{f}_{\mathrm{nl}}^a & = F_{x_1} \\ \dfrac{EI}{L_e^3}(12v_1 + 6L_e\theta_1 - 12v_2 + 6L_e\theta_2) & + \dfrac{EA}{32L_e^2}12\mathbf{f}_{\mathrm{nl}}^b + \dfrac{EA}{512L_e^3}6\mathbf{f}_{\mathrm{nl}}^c & = F_{y_1} \\ \dfrac{EI}{L_e^3}(6L_e v_1 + 4L_e^2\theta_1 - 6L_e v_2 + 2L_e^2\theta_2) & + \dfrac{EA}{32L_e^2}2L_e\mathbf{f}_{\mathrm{nl}}^b + \dfrac{EA}{512L_e^3}L_e\mathbf{f}_{\mathrm{nl}}^c & = F_{\theta_1} \\ \dfrac{EA}{L_e}(u_2 - u_1) & - \dfrac{EA}{32L_e^2}\mathbf{f}_{\mathrm{nl}}^a & = F_{x_2} \\ \dfrac{EI}{L_e^3}(-12v_1 - 6L_e\theta_1 + 12v_2 - 6L_e\theta_2) & - \dfrac{EA}{32L_e^2}12\mathbf{f}_{\mathrm{nl}}^b - \dfrac{EA}{512L_e^3}6\mathbf{f}_{\mathrm{nl}}^c & = F_{y_2} \\ \dfrac{EI}{L_e^3}(6L_e v_1 + 2L_e^2\theta_1 - 6L_e v_2 + 4L_e^2\theta_2) & + \dfrac{EA}{32L_e^2}2L_e\mathbf{f}_{\mathrm{nl}}^b + \dfrac{EA}{512L_e^3}L_e\mathbf{f}_{\mathrm{nl}}^c & = F_{\theta_2} \end{cases} \tag{2.97}$$

When no external axial load is applied ($F_{x_1} = 0 = F_{x_2}$), the associated equations lead to the equation:

$$32L_e(u_2 - u_1) = \mathbf{f}^a_{\mathrm{nl}}(v_1, \theta_1, v_2, \theta_2). \tag{2.98}$$

Since $\mathbf{f}^a_{\mathrm{nl}}$ is independent of the axial displacements u_1 and u_2, the above equation provides a relation between the displacement $u_2 - u_1$ and the other degrees of freedom $v_1, \theta_1, v_2, \theta_2$. Regarding the equations relative to $F_{y_1}, F_{\theta_1}, F_{v_2}, F_{\theta_2}$, the linear and nonlinear solutions are the same if the nonlinear terms in $\mathbf{f}^b_{\mathrm{nl}}$ and $\mathbf{f}^c_{\mathrm{nl}}$ cancel one another, which is the case if the relation: $32L_e\mathbf{f}^b_{\mathrm{nl}}(u_1, v_1, \theta_1, u_2, v_2, \theta_2) + \mathbf{f}^c_{\mathrm{nl}}(v_1, \theta_1, v_2, \theta_2) = 0$ is verified. The nonlinear forces $\mathbf{f}^c_{\mathrm{nl}}$ are independent of the axial degrees of freedom, however, $\mathbf{f}^b_{\mathrm{nl}}$ can be expressed using the difference $u_2 - u_1$ as follows:

$$\mathbf{f}^b_{\mathrm{nl}} = (u_2 - u_1)\big[L_e(\theta_1 + \theta_2) + 6(v_1 - v_2)\big]. \tag{2.99}$$

Therefore, when no axial load is applied, using relation (2.98) in the expression of $\mathbf{f}^b_{\mathrm{nl}}$ gives:

$$\mathbf{f}^b_{\mathrm{nl}} = \big[L_e(\theta_1 + \theta_2) + 6(v_1 - v_2)\big]\mathbf{f}^a_{\mathrm{nl}}, \tag{2.100}$$

and the relation $32L_e\mathbf{f}^b_{\mathrm{nl}}(u_1, v_1, \theta_1, u_2, v_2, \theta_2) + \mathbf{f}^c_{\mathrm{nl}}(v_1, \theta_1, v_2, \theta_2) = 0$ is verified. Thus, the terms in $\mathbf{f}^b_{\mathrm{nl}}$ and $\mathbf{f}^c_{\mathrm{nl}}$ in the system (2.97) cancel one another in the equations relative to $F_{y_1}, F_{\theta_1}, F_{y_2}$ and F_{θ_2}. Consequently, the vertical displacement and the rotations are equivalent in the linear and nonlinear cases when no axial load is applied. The previous development was carried out at the scale of a single element. After the assembling on all the elements, it remains true in the clamped-free configuration, where the nonlinearity in vertical displacements and rotations cancel one another by telescoping from one element to the next, starting from the free end. It is however not true for clamped-clamped configurations for instance.

Despite what has just been described, this von Kármán beam model will still be used in the following for a clamped-free configuration under vertical and follower static loads. In the first case, there will still be axial non-linear effects generated by the imposed transverse force and, in the case of follower forces, there is a coupling between axial and transverse displacement.

2.3.2 Application of the reduced order model to the beam case

A clamped-free beam of rectangular cross-section is considered for the application. The beam is discretized with 50 elements in which the von Kármán hypothesis is considered. The dimensions and properties of the beam are presented in Table 2.1. It is well known that the Euler-Bernoulli beam model with von Kármán hypothesis has a limited range of validity, as shown for example in [187]. Indeed, under external loads with no axial contribution, the nonlinear vertical and rotational components vanish, leading to purely axial nonlinearity (see paragraph 2.3.1). This model is however considered here because geometric nonlinearities in such a case are cubic in the degrees of freedom (see Equation (2.58)). The proposed ROM is therefore directly transposable to 3D finite element applications with Saint Venant-Kirchhoff model where the geometric nonlinearity is known to be cubic in the degrees of freedom (as shown in Equation 1.58).

Beam dimensions	
L (length)	4 m
h (thickness)	7.10^{-2} m
b (width)	$3h$

Material properties	
E	100 GPa
ρ	$4,400$ kg.m^{-3}

Table 2.1: Dimensions and material properties of the beam

In the beam model, the linear bending and membrane linear normal modes are uncoupled due to the independence of the contribution along u and v, θ in the mass and stiffness matrices. Figure 2.4 represents the shape of the first three linear modes and Figure 2.5 shows the modal frequencies of the linear bending and membrane modes. It is observed that the first linear modes in terms of frequency are bending modes while the modal frequencies of the first membrane modes are significantly higher. As far as linear computations are concerned, the dynamics is well captured by the linear normal modes whose associated frequencies are included in the span of excitation frequencies. However, when geometric nonlinearities are at stake, a nonlinear coupling appears between the linear normal modes. Consequently, the excitation of low-frequency bending modes triggers the movement of high-frequency membrane modes. Thus, to obtain accurate results, all the modes that are excited should be added to the reduction basis which would lead to a large reduction basis. In the beam case, almost all the membrane modes should be considered in addition to the first linear bending modes. On the other hand, dual modes contain the nonlinear coupling due to the geometric nonlinearities and enable to capture the nonlinearity with few modes in the reduction basis.

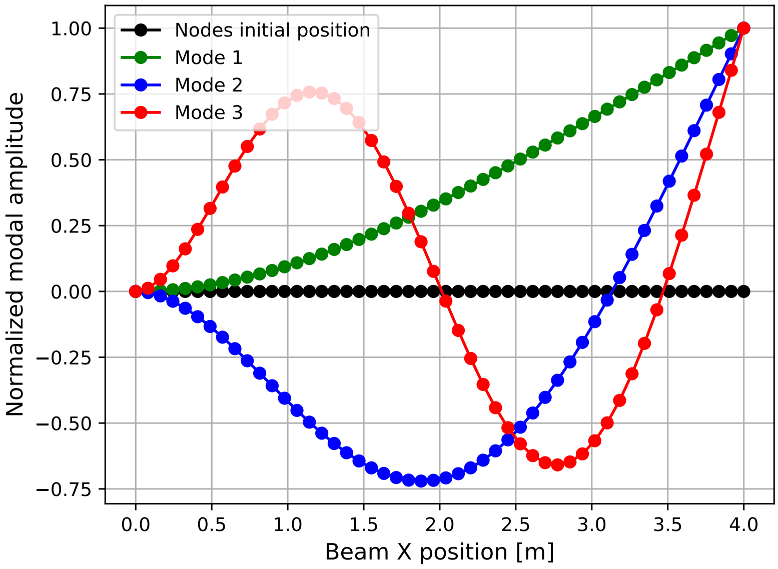

Figure 2.4: First three linear mode shapes of the beam.

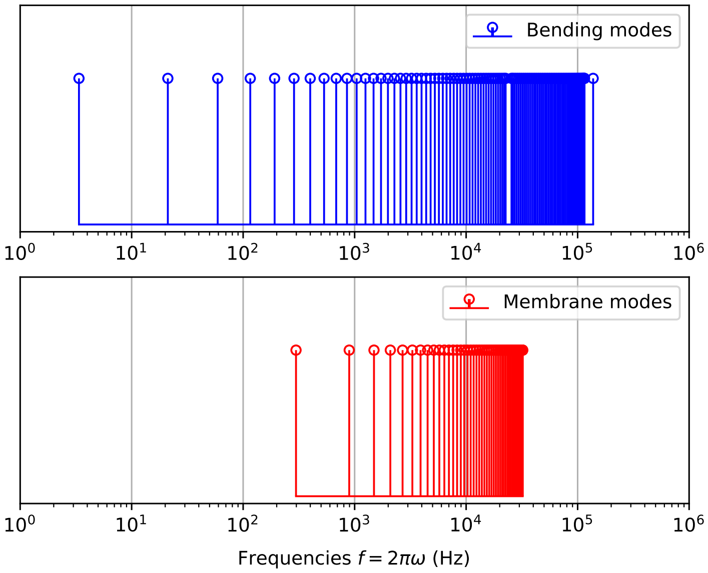

Figure 2.5: Frequencies of the bending and membrane linear normal modes.

2.3.2.1 Reduced order beam model with dual modes

The first three linear normal modes are initially considered in order to build the reduction basis. Those modes are bending modes that do not capture the in-plane dynamics. As explained in the previous section, the basis is completed with dual modes determined by imposing loads to the structure, with the distribution defined in Equation (1.144) as the combination of the first three linear modes:

$$\mathbf{f}_{\text{ext}}^{(\ell)} = \mathbf{K}\left(\pm \alpha_1^{(\ell)} \boldsymbol{\phi}_1 \pm \alpha_2^{(\ell)} \boldsymbol{\phi}_2 \pm \alpha_3^{(\ell)} \boldsymbol{\phi}_3 \right), \tag{2.101}$$

with the modes $\boldsymbol{\phi}_1, \boldsymbol{\phi}_2, \boldsymbol{\phi}_3$ normalized by their maximal vertical value and $\alpha_1^{(\ell)} \in \{10h, 0\}$, $\alpha_2^{(\ell)} \in \{1h, 0\}$, $\alpha_3^{(\ell)} \in \{1h, 0\}$. Such coefficients for the loads are chosen to promote nonlinearity along the first linear modes and include a smaller contribution along the second and third modes. The values of $10h$ and $1h$ are arbitrarily chosen since we expect to observe a significant nonlinearity in the test cases when the linear displacement is greater than 10 times the beam's thickness, but the nonlinear displacements along the other modes are expected to be rather small. Other loading amplitudes were tested and the same coefficients were obtained, except when the amplitudes chosen were excessively large or too small to trigger nonlinearities, which is the same problem as when displacements are imposed. With this range of amplitudes $\alpha_i^{(\ell)}$, the first linear mode is considered as a dominant mode undergoing large deformations and is slightly perturbed in the direction of the other linear normal modes. The loads are imposed positively and negatively so that no side is favored in the construction of the database of nonlinear static solutions for the $n_{\mathrm{L}} = 26$ different load cases corresponding to all the possible combinations with three modes.

A singular value decomposition of the static solution residuals $\mathbf{r}^{(\ell)}$ is then performed according to the process of selection of the dual modes detailed in section 1.3.1.4. The singular values and the linearized strain energies of the dual mode candidates are plotted in Figure 2.6. In the present case, the SVD modes with the highest singular values are also those with the highest linearized strain energy contribution. The dual modes appended to the initial basis of linear modes are thus the vectors $\mathbf{d}_{\{1,2,3,4,5\}}$. In cases such as the present configuration, it could be argued that only the criterion of the singular values can be retained. However, the criterion based on the energy highlights, among the dual mode candidates with large singular value, those with a significant membrane contribution. When there is no clear drop in the singular values, it was observed on other configurations that some dual modes candidates with a small contribution to the linearized energy may contribute less to the dynamics and are not necessary in the reduction basis. The new reduction basis considered is therefore the concatenation of the first 3 linear normal modes and the 5 dual modes: $\mathbf{V} = [\boldsymbol{\Phi}, \mathbf{d}_{\{1,2,3,4,5\}}]$. It is worth mentioning that for beam applications, the dual modes leading to a high linearized strain energy have a negligible bending contribution compared to their axial contribution. Indeed, the axial stiffness of a beam is larger than the bending stiffness. Thus, the linearized strain energy associated to vectors with dominant membrane contribution is usually larger than the one of modes with dominant bending contribution. With this selection of dual modes, the relative error in precision defined in Equation (1.121) is $\varepsilon_\sigma = \mathcal{O}(10^{-6})$ and the relative error in linearized strain energy contribution defined in Equation (1.122) is $\varepsilon_E = \mathcal{O}(10^{-8})$.

Once the reduction basis $\mathbf{V}$ is obtained, the next step in the construction of the model is the determination of the projected nonlinear forces from the expression (2.3). The coefficients of the polynomial are identified with the *Implicit Condensation* method by imposing load cases defined as in Equation (2.101). The loads and associated nonlinear static solutions defined previously for the selection of the dual modes are reused here. Besides, due to symmetry considerations on the geometry and the linear normal modes, many nonlinear coefficients are vanishing. Some coefficients are also vanishing because the dual modes have only axial contributions, leading to null coefficients in the expression of the internal forces for the von Kármán beam detailed in Equation (2.79). Since the expression of the nonlinear forces $\mathbf{f_{nl}}$ is explicitly known for our beam problem, the internal nonlinear forces can be decomposed in their quadratic $\mathbf{f}_{\mathrm{nl}}^{\mathrm{quad}}$ and their cubic $\mathbf{f}_{\mathrm{nl}}^{\mathrm{cub}}$ contributions. The quadratic and cubic coefficients introduced in Equation (2.4) can therefore be splitted in two different matrices. The nonlinear force coefficients are then identified from two independent systems which are better conditioned when considered separately. It has been verified on this test case, that the nonlinear coefficients obtained using the nonlinear forces as well as those using the tangent stiffness matrices (method detailed in section 2.2.2) match exactly with a symbolic

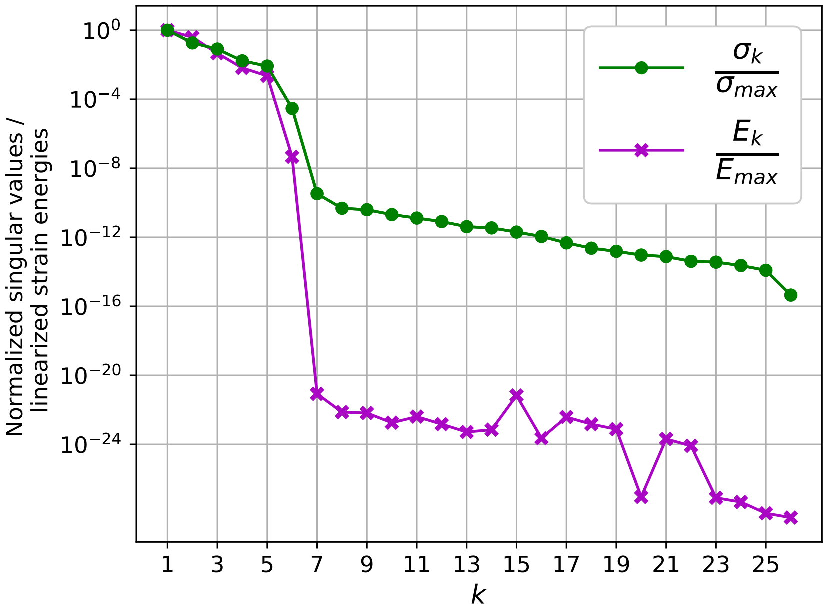

Figure 2.6: Singular values and linearized strain energies of the static solution residuals.

computation of the coefficients. A method based on imposed displacements [126, 143] also resulted in the same coefficients. In the rest of the document, the *Implicit Condensation* method with dual modes will be called ICDual, to differentiate the method from the classical IC method including only bending modes and from the ICE method with the expansion step.

2.3.2.2 Structural response under different load cases

In this section, the efficiency of the ROM will be evaluated on two different load cases illustrated in Figure 2.7: a vertically distributed load along the beam and a follower load at the tip. The ICDual ROM will be compared to the ICE solution and to the solution obtained with the nonlinear full-order model (FOM), firstly on a static load case, then under a dynamic load case at the resonance of the first linear normal mode.

(a) Load case 1 (b) Load case 2

Figure 2.7: Load cases considered: (a) Distributed vertical load; (b) Follower load at tip.

Load case 1: Vertical distributed load along the beam

The first loading case consists of a vertical uniformly distributed load on the beam. The total load applied to the beam is 80,000 N, meaning a uniformly distributed load density of 20,000 N/m. The geometric nonlinearity alters the vertical amplitude of the displacement and produces a significant axial shortening due to the coupling between the axial and vertical displacements. On the contrary, the linear computation does not lead to any axial shortening since bending and traction-compression are not coupled.

The classical *Implicit Condensation* method (IC) and its *Expansion* (ICE) are compared to the ICDual ROM and to the linear and nonlinear reference solutions in Figure 2.8. Regarding the IC/ICE ROMs, the first 3 linear normal modes are used in the reduction basis. The vertical displacement of the beam is well captured by the IC method. However, the axial displacement is not captured at all. The reason is that the reduction basis contains only bending modes, thus no equation solves the axial displacement in the reduced system. Nonetheless, the *Expansion* step (ICE) enables to rebuild the axial displacement in post-processing and matches with the FOM solution. With the ICE method, the nonlinear static solution was obtained with only 3 linear normal modes. The solution is first computed with the IC method and then post-processed with the *Expansion* step. The ICE method is very accurate on this static case since the reconstruction step of the Expansion phase is based on a static correction which is adapted here to capture the missing membrane effect.

The ICDual ROM contains the same linear bending modes as the ICE method, completed with the five dual modes determined previously. Such a ROM perfectly captures the nonlinear FE solution as a result of the computation, while the same result was obtained with the ICE method only after the *Expansion* step.

Table 2.2 represents the relative cumulative error for to the axial u_i and vertical v_i degrees of freedom:

$$\varepsilon_{\text{cumul}} = \frac{\displaystyle\sum_{i=1}^{N} \sqrt{\left(u_i - u_i^{\text{FOM}}\right)^2 + \left(v_i - v_i^{\text{FOM}}\right)^2}}{\displaystyle\sum_{i=1}^{N} \sqrt{\left(u_i^{\text{FOM}}\right)^2 + \left(v_i^{\text{FOM}}\right)^2}} \tag{2.102}$$

Table 2.2: Error between the nonlinear FOM and ROM solutions of the beam displacement for several amplitudes of static distributed load.

	Relative cumulative error $\varepsilon_{\text{cumul}}$ (%)		
Total load integrated (N)	40,000	60,000	80,000
Linear FOM	6.67	9.98	13.25
ICE ROM	2.28×10^{-2}	2.32×10^{-2}	2.38×10^{-2}
ICDual ROM	2.29×10^{-2}	2.34×10^{-2}	2.41×10^{-2}

The error is computed on the norm of the displacement. Since the ICE and ICDual ROMs are both very close to the FOM result, the error component by component gives the same conclusions. This validates the approach followed here with a reduction basis enriched with dual modes in pre-processing. Nevertheless, the ICDual method solves the coupled dynamics of the system in bending and traction-compression, instead of restricting the dynamics to the bending and rebuilding the coupling with the ICE afterwards. This will be of paramount importance for the following dynamic application.

The ICDual method is now evaluated on a dynamic case and compared to the result of the ICE method. The load distribution is the same as the static case, but its amplitude is reduced to 1,400 N/m to obtain displacements with the same order of magnitude as the fluid-structure interaction case of section 5. A sinusoidal time dependency is applied to the loading with a

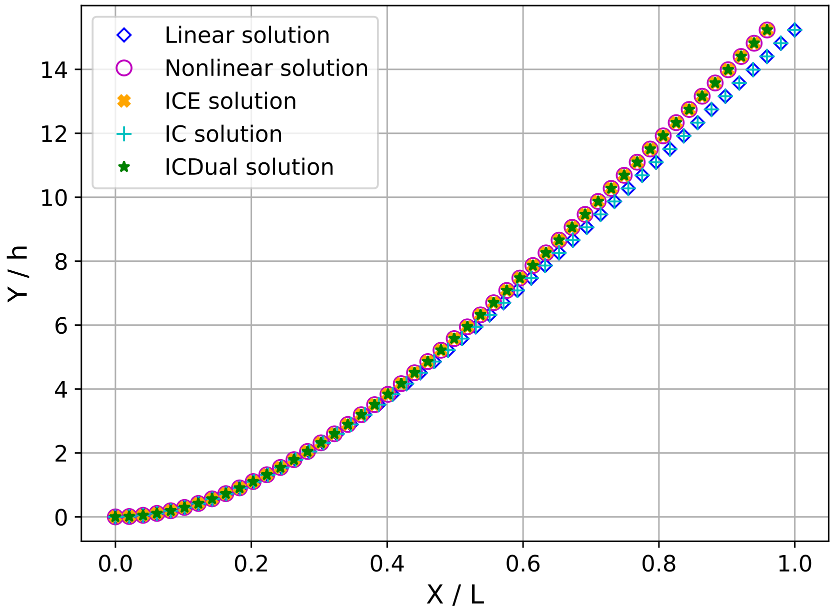

(a) Beam deformation

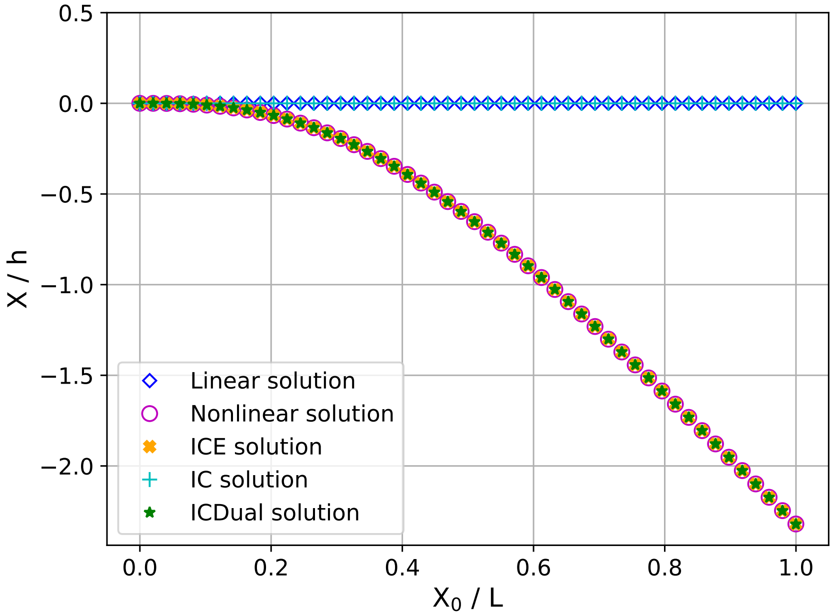

(b) Axial displacement

Figure 2.8: Nonlinear static displacement of the clamped-free von Kármán beam, loaded with a vertical uniformly distributed load along the beam of 20,000 N/m. Comparison between the linear FOM, nonlinear FOM, the IC/ICE and ICDual solutions.

frequency $f_0 = 3.37$ Hz (frequency of the first mode) and the time step for the temporal integration is equal to 2×10^{-3} s. A Rayleigh damping $\mathbf{C} = 2\xi\omega_0\mathbf{M}$ is considered, with $\xi = 5 \times 10^{-2}$ and $\omega_0 = 2\pi f_0$ the pulsation of the first linear normal mode. Figure 2.9 displays the vertical and axial displacements at the tip of the beam once the periodic regime is established. The time integration is carried out using a classical nonlinear Newmark algorithm with Newton-Raphson iterations.

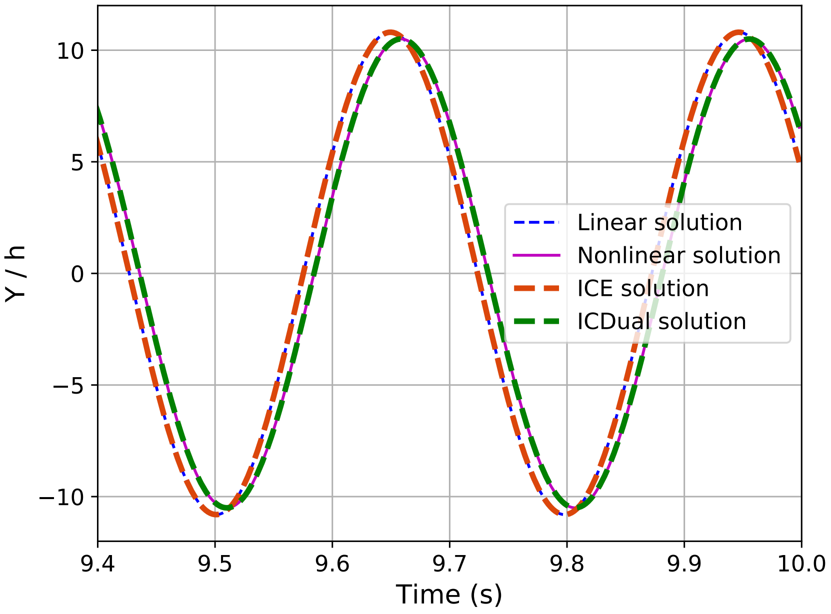

(a) Vertical displacement

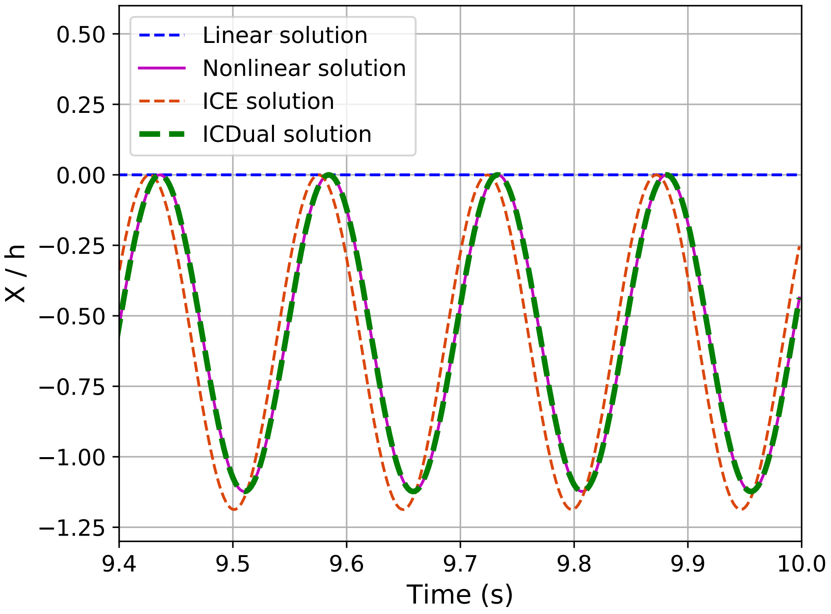

(b) Axial displacement

Figure 2.9: Nonlinear dynamic displacement of the clamped-free Euler-Bernoulli/von Kármán beam, loaded vertically with a uniformly distributed load of 1,400 N/m and of frequency $f_0 = 3.37$Hz. Comparison of the vertical (a) and axial (b) displacements at the tip of the beam between the nonlinear FE solution, the ICE and the ICDual computations.

The vertical displacement plotted in Figure 2.9(a) is very close in terms of amplitude for both the ICE and the ICDual methods. The ICE vertical displacement is however exactly the linear solution as shown in Table 2.3, while the ICDual solution captures exactly the nonlinear coupling affecting the vertical amplitude. Besides there is a slight phase shift of 9.70° between the reference nonlinear solution and the ICE and linear solutions.

Table 2.3: Relative error of the maximal displacement of the beam tip in periodic regime between the reference nonlinear FOM model and the linear FOM, ICE ROM and ICDual ROM models.

	Relative error of the tip displacement (%)	
	Y component	X component
Linear FOM	2.63	100
ICE ROM	2.63	5.18
ICDual ROM	2.02×10^{-4}	6.27×10^{-4}

Table 2.3 contains the relative axial ($|x_{\max} - x_{\max}^{\text{FOM}}|/|x_{\max}^{\text{FOM}}|$) and vertical ($|y_{\max} - y_{\max}^{\text{FOM}}|/|y_{\max}^{\text{FOM}}|$) errors of the maximal displacements of the beam tip in periodic regime between the reference nonlinear FOM model and the different reduced order models. The ICDual ROM captures perfectly the axial dynamics, both in terms of amplitude and phase (Figure 2.9(b)), whereas the ICE method is inaccurate. This result highlights the drawback of the ICE method where the dynamics of the system in traction-compression is not computed by the projected equation of the dynamics but rebuilt a posteriori with limited information. Besides, the *Expansion* step of the ICE method is a static reconstruction which depends only on the generalized coordinates of the bending modes, not on the velocity or the acceleration. With the ICE method, the axial displacement is therefore governed only by the projection of the beam on the bending modes, whatever the dynamics of it, whether it is static, quasi-static or strongly dynamic. Moreover, increasing the number of modes in the reduction basis to 8 or 10 modes does not improve the axial ICE solution since the dynamics in traction-compression is missing in the reduced equation of the dynamics Equation (1.89). On the contrary, with only 5 dual modes added to the reduction basis, the dynamics, both in traction-compression and in bending is perfectly captured.

Load case 2: Follower force at the tip

The second load case considered is a punctual follower load applied at the tip of the beam. In this case, the solution is inherently nonlinear since the external loads depends on the beam's position which undergoes large nonlinear displacements. The amplitude of the load is equal to 30,000 N. Figure 2.10 represents the classical IC and ICE solutions compared to the ICDual solution. Contrary to the previous static load case, the ICE solution no longer matches the nonlinear reference solution. Indeed, the projection of the follower force on the reduction basis filters out the axial components since the basis includes only bending modes with vertical contributions. Finally, the ICE method behaves as if the external load case was a purely vertical load since the *Expansion* step is not able to retrieve a correction adapted to the follower load. Increasing the number of linear normal modes in the reduction basis for the ICE method to 8 and even 10 did not improve the solution since the additional modes are still bending modes. The solution may be improved by introducing membrane modes, or, as suggested in the literature, to treat follower forces as an extension of the ICE method [135].

Unlike the ICE solution, the ICDual ROM perfectly captures the nonlinear FOM solution as shown in Figure 2.10 and its precision is quantified in Table 2.4. Indeed, with the dual modes in the reduction basis, the external forces are well represented in the reduction basis and the solution of the reduced system gives the correct nonlinear static solution.

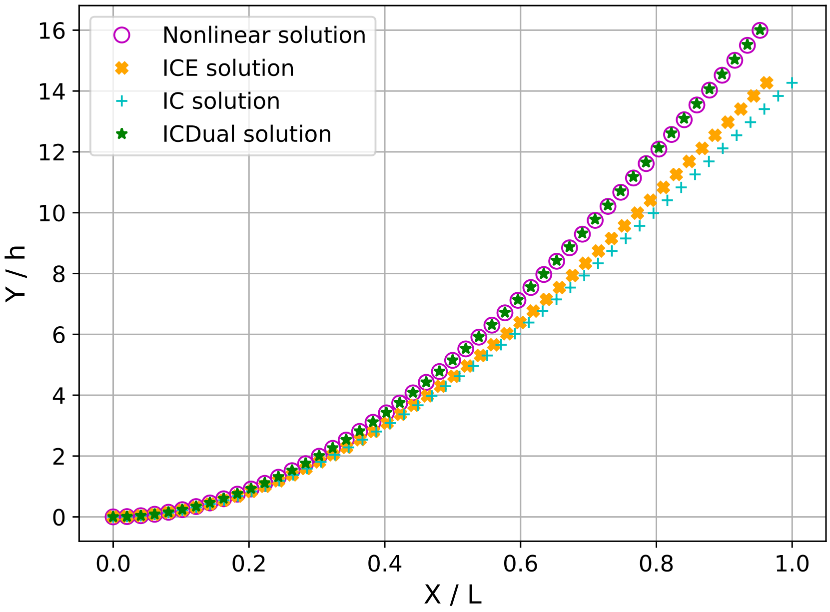

(a) Beam deformation

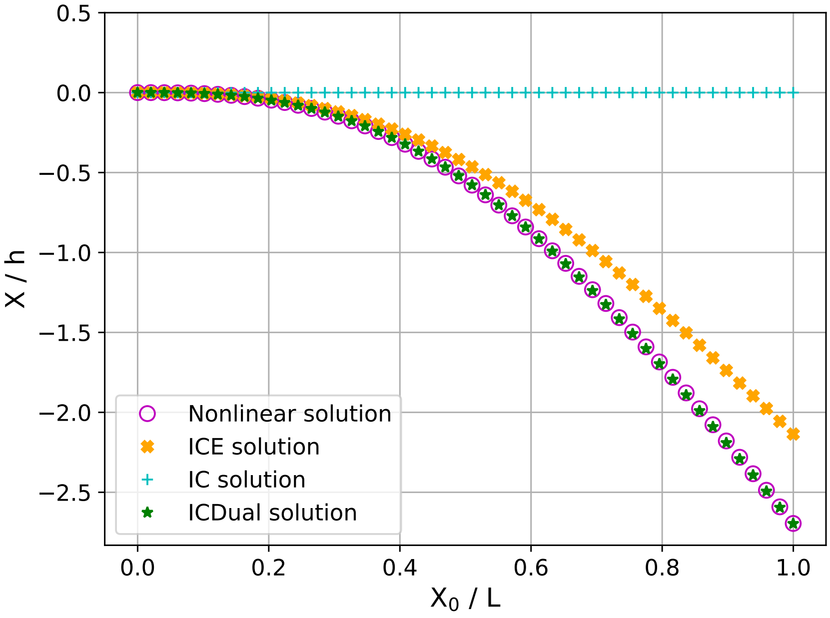

(b) Axial displacement

Figure 2.10: Nonlinear static displacement of the clamped-free Bernoullli/von Kármán beam, loaded at the tip with a follower load of 30,000 N. Comparison between the nonlinear, the IC, ICE and ICDual solutions.

The dynamics of the structure is then studied with a sinusoidal follower load, with the same frequency as the previous load case and an amplitude of 2,500 N. The Rayleigh damping and time step are also unchanged from the previous test case. Figure 2.11 shows the evolution in the periodic regime of the axial displacement at the tip of the beam and Table 2.5 summarizes the relative errors of the models compared to the nonlinear FOM solution.

The ICDual solution matches the FOM solution like for the other test case, while the ICE

Table 2.4: Error regarding the nonlinear FOM solution of the beam displacement for several amplitudes of static follower load at tip.

	Relative cumulative error $\varepsilon_{\text{cumul}}$ (%)		
Load (N)	10,000	20,000	30,000
ICE ROM	1.25	4.91	10.60
ICDual ROM	1.039×10^{-1}	1.288×10^{-1}	2.814×10^{-1}

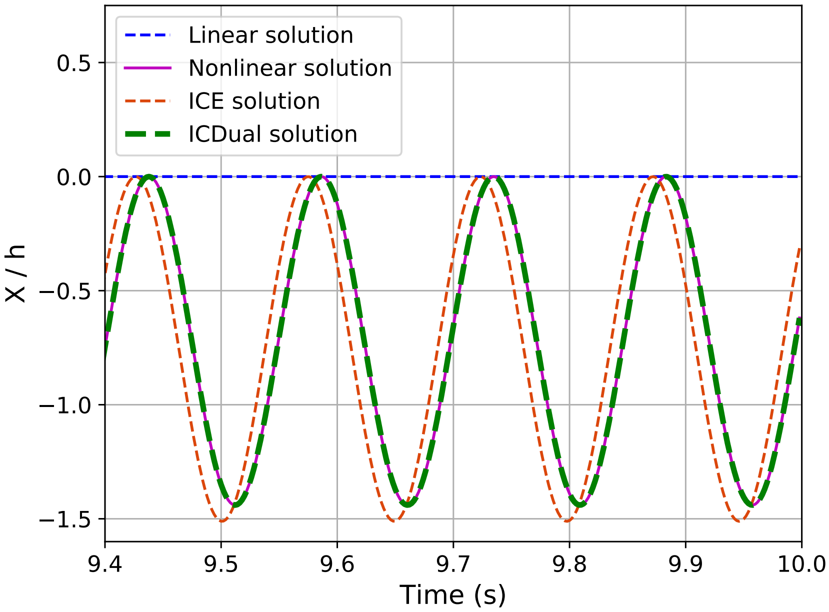

Figure 2.11: Nonlinear dynamic displacement of the clamped-free Euler-Bernoulli/von Kármán beam loaded at the tip with a dynamic follower load of amplitude 2,500 N and of frequency $f_0 = 3.37$ Hz. Comparison of the axial displacement at the tip of the beam between the nonlinear FE solution, the ICE and the ICDual computations.

solution presents a phase shift of 12° and does not render the axial displacement accurately. Other test cases were also considered such as a purely vertical load at the tip and a follower distributed load. The results under such load cases are not presented here for the sake of brevity but similar conclusions were obtained. Both the ICE and ICDual ROMs were accurate for the static vertical load at the tip but only the ICDual ROM was accurate in the dynamic case. Regarding the distributed follower load, only the ICDual ROM was accurate for both the static and dynamic cases.

In this section, the ICDual ROM was built for an Euler-Bernoulli/von Kármán beam and compared on different load configurations to solutions obtained with the IC and ICE methods. For all cases, both the static and dynamic nonlinear responses were precisely captured. The limitations of the classical ICE method have been highlighted, especially when dealing with follower forces or dynamic loads. Since the dual modes added in the reduction basis have only membrane contribution, it could be argued that linear membrane modes could be used instead. However, to obtain similar results with pure membrane modes it has been verified that for this configuration it is necessary to include all the membrane modes. This would lead to a tremendous number of

Table 2.5: Relative error of the maximal displacement of the beam tip in periodic regime between the reference nonlinear FOM model and the ICE and ICDual ROM models.

	Relative error of the tip displacement (%)	
	Y component	X component
ICE ROM	2.472	4.919
ICDual ROM	3.643×10^{-3}	8.175×10^{-3}

coefficients ($\mathcal{O}(10^5)$) to identify for the additional 49 membrane modes, whereas similar results are obtained with only 5 dual modes. The reader will find the previous results in the following journal paper [58].

2.3.3 Beam in rotation around a fixed axis

In this section, the beam is subject to centrifugal rotation. It is clamped on a disk at a distance $R = 10$ cm from the axis of rotation $\boldsymbol{e_y}$ and is turning around this axis $\boldsymbol{e_y}$ at the constant rotation speed $\omega = 500$ rpm. First, the theoretical aspects of the beam formulation in rotation are presented, then applications on similar load cases as for the case without rotation are treated.

2.3.3.1 Theoretical aspects

The inertial fixed frame is written $\mathcal{R}_\mathrm{g}(O, \hat{\boldsymbol{e}}_{\boldsymbol{x}}, \hat{\boldsymbol{e}}_{\boldsymbol{y}}, \hat{\boldsymbol{e}}_{\boldsymbol{z}})$ and the moving frame $\mathcal{R}_\mathrm{m}(O, \boldsymbol{e_x}, \boldsymbol{e_y}, \boldsymbol{e_z})$. Figure 2.12 provides an illustration of the study case with the notations used.

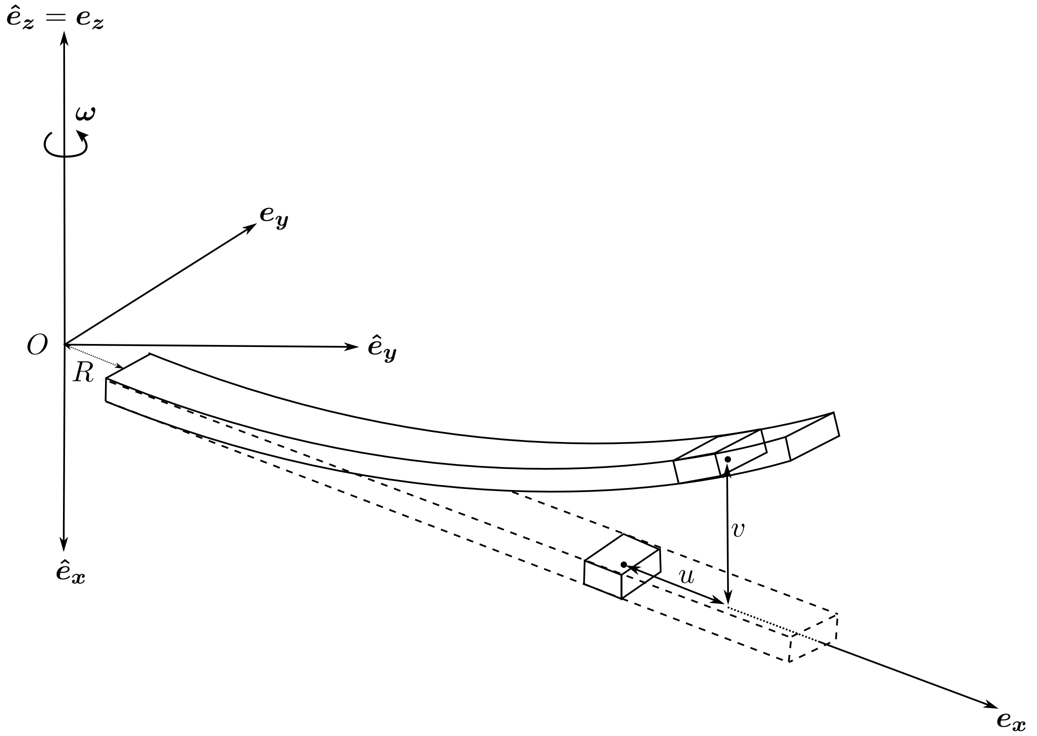

Figure 2.12: Beam in rotation around a fixed axis. Diagram inspired from [171].

The distance R of the clamped condition to the rotation axis is added in the expression of the vector $\boldsymbol{Om}$ that becomes:

$$\boldsymbol{Om} = [R + X + u - Y\text{sin}\theta]\boldsymbol{e_x} + [v + Y\text{cos}\theta]\boldsymbol{e_y} \tag{2.103}$$

The velocity and acceleration of the point M in the inertial frame are expressed via the combination of accelerations:

$$\begin{aligned} \boldsymbol{V(M)}_{/\mathcal{R}_\text{g}} &= \boldsymbol{V(M)}_{/\mathcal{R}_\text{m}} + \Omega\boldsymbol{e_y} \times \boldsymbol{Om} & (2.104)\\ \boldsymbol{a(M)}_{/\mathcal{R}_\text{g}} &= \underbrace{\boldsymbol{a(M)}_{/\mathcal{R}_\text{m}}}_{\text{relative acc.}} + \underbrace{2\Omega\boldsymbol{e_y} \times \boldsymbol{V(M)}_{/\mathcal{R}_\text{m}}}_{\text{coriolis acc.}} + \underbrace{\Omega\boldsymbol{e_y} \times \big(\Omega\boldsymbol{e_y} \times \boldsymbol{Om}\big)}_{\text{drive acc.}}, & (2.105) \end{aligned}$$

where the velocity and acceleration in the rotating frame $\mathcal{R}_\text{m}$ are given by::

$$\begin{aligned} \boldsymbol{V(M)}_{/\mathcal{R}_\text{m}} &= \big[\dot{u} - Y\dot{\theta}\text{cos}\theta\big]\boldsymbol{e_x} + \big[\dot{v} - Y\dot{\theta}\text{sin}\theta\big]\boldsymbol{e_y} & (2.106)\\ \boldsymbol{a(M)}_{/\mathcal{R}_\text{m}} &= \big[\ddot{u} - Y(\ddot{\theta}\text{cos}\theta - \dot{\theta}^2\text{sin}\theta)\big]\boldsymbol{e_x} + \big[\ddot{v} - Y(\ddot{\theta}\text{sin}\theta + \dot{\theta}^2\text{cos}\theta)\big]\boldsymbol{e_y} & (2.107) \end{aligned}$$

Therefore, the acceleration of the material point M in the inertial frame $\mathcal{R}_\text{g}$ becomes:

$$\begin{aligned} \boldsymbol{a(M)}_{/\mathcal{R}_\text{g}} &= \boldsymbol{a(M)}_{/\mathcal{R}_\text{m}} + 2\Omega\boldsymbol{e_y} \times \boldsymbol{V(M)}_{/\mathcal{R}_\text{m}} + \Omega\boldsymbol{e_y} \times \big(\Omega\boldsymbol{e_y} \times \boldsymbol{Om}\big)\\ &= \big[\ddot{u} - Y(\ddot{\theta}\text{cos}\theta - \dot{\theta}^2\text{sin}\theta) - \Omega^2(R + X + u - Y\text{sin}\theta)\big]\boldsymbol{e_x}\\ &\quad + \big[\ddot{v} - Y(\ddot{\theta}\text{sin}\theta + \dot{\theta}^2\text{cos}\theta)\big]\boldsymbol{e_y}\\ &\quad - 2\Omega(\dot{u} - Y\dot{\theta}\text{cos}\theta)\boldsymbol{e_z} \end{aligned} \tag{2.108}$$

Virtual work principle

In order to obtain the equation of the dynamics for the beam case in rotation, the virtual work principle is applied. The virtual work of the internal and external forces remain unchanged from the case without rotation, however, new contributions are added to the virtual work associated to the acceleration. The expression of the virtual work associated to the acceleration is the following:

$$\delta W_\text{acc} = \iiint_V \rho\boldsymbol{a}_{/\mathcal{R}_\text{g}} \cdot \boldsymbol{\delta u}\ \text{d}V, \tag{2.109}$$

with the virtual displacement: $\boldsymbol{\delta u} = [\delta u - Y\cos\theta\delta\theta]\,\boldsymbol{e_x} + [\delta v - Y\sin\theta\delta\theta]\,\boldsymbol{e_y}$. The scalar product of the virtual displacement with the acceleration leads to the expression:

$$\boldsymbol{a(M)}_{/\mathcal{R}_\text{g}} \cdot \boldsymbol{\delta u} = \big[\ddot{u} - \Omega^2(R + X + u)\big]\delta u + \ddot{v}\delta v + Y^2\big[\ddot{\theta} - \Omega^2\sin\theta\cos\theta\big]\delta\theta + Y\big[\cdots\big] \tag{2.110}$$

where the expression $Y\big[\cdots\big]$ is not developed since it will be cancelled by the integration for symmetry reasons. Considering the previous developments, the expression of the virtual work associated to the acceleration becomes:

$$\begin{aligned} \delta W_\text{acc} &= \iiint_V \rho\boldsymbol{a}_{/\mathcal{R}_\text{g}} \cdot \boldsymbol{\delta u}\ \text{d}V\\ &= \underbrace{\int_0^L \big[\rho A\ddot{u}\delta u + \rho A\ddot{v}\delta v + \rho I\ddot{\theta}\big]\ \text{d}X}_{\text{contribution already present without rotation}}\\ &\quad \underbrace{- \int_0^L \big[\rho A\Omega^2(R + X + u)\delta u + \rho I\Omega^2\sin\theta\cos\theta\delta\theta\big]\ \text{d}X}_{\text{contribution added by the rotation}} \end{aligned} \tag{2.111}$$

The contribution to the virtual work of the acceleration is decomposed in a contribution independent of the rotation $\delta W_{\text{acc}}^{0}$ and a contribution depending on the centrifugal rotation $\delta W_{\text{acc}}^{\Omega}$: $\delta W_{\text{acc}} = \delta W_{\text{acc}}^{0} + \delta W_{\text{acc}}^{\Omega}$. The contribution added by the rotation can be decomposed in three terms as follows:

$$\delta W_{\text{acc}}^{\Omega} = \delta W_{\text{acc}}^{\Omega(1)} + \delta W_{\text{acc}}^{\Omega(2)} + \delta W_{\text{acc}}^{\Omega(3)} \tag{2.112}$$

with

$$\delta W_{\text{acc}}^{\Omega(1)} = -\rho A \Omega^2 \int_0^L (R+X)\delta u \,\mathrm{d}X \tag{2.113}$$

$$\delta W_{\text{acc}}^{\Omega(2)} = -\rho A \Omega^2 \int_0^L u\delta u \,\mathrm{d}X \tag{2.114}$$

$$\delta W_{\text{acc}}^{\Omega(3)} = -\rho I \Omega^2 \int_0^L \sin\theta\cos\theta\delta\theta \,\mathrm{d}X \tag{2.115}$$

$$\approx -\rho I \Omega^2 \int_0^L \theta\delta\theta \,\mathrm{d}X \tag{2.116}$$

The last term is linearized with the approximation $\sin\theta\cos\theta = \theta$ to define later a centrifugal softening matrix in the FE discretization. It is worth mentioning that the choice made here is a stronger approximation than the von Kármán hypothesis, thus limiting the validity of the model to small rotations. Nevertheless, the term ρI being much smaller than ρA in our applications, and the associated term contributing only partially to the total stiffness, the approximation made above has a negligible effect and the beam model used remains valid for moderate rotations.

The Finite Element discretization is then introduced in the different contributions of the virtual work associated to the acceleration. The FE discretization in one element of the contribution independent of the rotation was already detailed in the case without centrifugal rotation and takes the following form: $\delta W_{\text{acc}}^{0} = \boldsymbol{\delta}\mathbf{u}_{\text{e}}^{T}\mathbf{M}_{\text{e}}\ddot{\mathbf{u}}_{\text{e}}$, see Equation (2.90). A constant vector $\mathbf{f}_{\omega}^{e}$ is introduced in the FE discretization of the contribution $\delta W_{\text{acc}}^{\Omega(1)}$:

$$\delta W_{\text{acc}}^{\Omega(1)} = -\rho A \Omega^2 \int_0^L (R+X)\, \underbrace{\mathbf{N}_{\text{u}}\boldsymbol{\delta}\mathbf{u}_{\text{e}}}_{=\boldsymbol{\delta}\mathbf{u}_{\text{e}}^{T}{\mathbf{N}_{\text{u}}}^{T}} \,\mathrm{d}X = \boldsymbol{\delta}\mathbf{u}_{\text{e}}^{T} \underbrace{\left(-\rho A \Omega^2 \int_0^L (R+X){\mathbf{N}_{\text{u}}}^{T} \,\mathrm{d}X\right)}_{\mathbf{f}_{\omega}^{e}}, \tag{2.117}$$

and the centrifugal softening matrix $\mathbf{K}_{\text{c}}^{e}$ arises from the FE discretization of $\delta W_{\text{acc}}^{\Omega(2)}$ and $\delta W_{\text{acc}}^{\Omega(3)}$:

$$\delta W_{\text{acc}}^{\Omega(2)} + \delta W_{\text{acc}}^{\Omega(3)} = -\int_0^L \rho A \Omega^2 \underbrace{[u][\delta u]}_{=[\delta u]^T[u]} + \rho I \Omega^2 \underbrace{[\theta][\delta\theta]}_{=[\delta\theta]^T[\theta]} \,\mathrm{d}X \tag{2.118}$$

$$= \boldsymbol{\delta}\mathbf{u}_{\text{e}}^{T} \underbrace{\left(-\int_0^L \rho A \Omega^2 \left({\mathbf{N}_{\text{u}}}^{T}\mathbf{N}_{\text{u}}\right) + \rho I \Omega^2 \left({\mathbf{N}_{\text{v}}^{'}}^{T}\right)\left(\mathbf{N}_{\text{v}}^{'}\right) \,\mathrm{d}X\right)}_{\mathbf{K}_{\text{c}}^{e}} \mathbf{u}_{\text{e}}. \tag{2.119}$$

Finally the virtual work in one element associated to the acceleration writes:

$$\boxed{\delta W_{\text{acc}} = \boldsymbol{\delta}\mathbf{u}_{\text{e}}^{T}\left(\mathbf{M}_{\text{e}}\ddot{\mathbf{u}}_{\text{e}} - \mathbf{K}_{\text{c}}^{e}\mathbf{u}_{\text{e}} - \mathbf{f}_{\omega}^{e}\right)} \tag{2.120}$$

with

$$\mathbf{K}_{\mathrm{c}}^{e} = \rho A \Omega^2 \int_0^L \left(\mathbf{N}_{\mathrm{u}}{}^T \mathbf{N}_{\mathrm{u}}\right) \, \mathrm{d}X + \rho I \Omega^2 \int_0^L \left(\mathbf{N}_{\mathrm{v}}'{}^T \mathbf{N}_{\mathrm{v}}'\right) \, \mathrm{d}X \tag{2.121}$$

$$= \frac{\rho A \Omega^2 L_e}{6} \begin{bmatrix} 2 & 0 & 0 & 1 & 0 & 0 \\ & 0 & 0 & 0 & 0 & 0 \\ & & 0 & 0 & 0 & 0 \\ & & & 2 & 0 & 0 \\ & \mathit{sym} & & & 0 & 0 \\ & & & & & 0 \end{bmatrix} + \frac{\rho I \Omega^2}{30 L_e} \begin{bmatrix} 0 & 0 & 0 & 0 & 0 & 0 \\ & 36 & 3L_e & 0 & -36 & 3L_e \\ & & 4L_e^2 & 0 & -3L_e & -L_e^2 \\ & & & 0 & 0 & 0 \\ & \mathit{sym} & & & 36 & -3L_e \\ & & & & & 4L_e^2 \end{bmatrix} \tag{2.122}$$

$$\mathbf{f}_{\omega}^{e} = \rho A \Omega^2 \int_0^L (R + X) \mathbf{N}_{\mathrm{u}}{}^T \, \mathrm{d}X \tag{2.123}$$

$$= \frac{\rho A \Omega^2 L_e}{6} \begin{bmatrix} L_e + 3R \\ 0 \\ 0 \\ 2L_e + 3R \\ 0 \\ 0 \end{bmatrix} \tag{2.124}$$

The virtual work principle in one element ($\delta W_{\text{acc}} - \delta W_{\text{int}} - \delta W_{\text{acc}} = 0$) applied to the beam in rotation around the fixed axis at constant rotation speed becomes:

$$\boldsymbol{\delta} \mathbf{u}_{\mathrm{e}}^{T} \left[\mathbf{M}_{\mathrm{e}} \ddot{\mathbf{u}}_{\mathrm{e}} - \mathbf{K}_{\mathrm{c}}^{e} \mathbf{u}_{\mathrm{e}} - \mathbf{f}_{\omega}^{e} + \mathbf{K}_{\mathrm{e}} \mathbf{u}_{\mathrm{e}} + \mathbf{f}_{\mathrm{nl}}^{\mathrm{quad}}(\mathbf{u}_{\mathrm{e}}) + \mathbf{f}_{\mathrm{nl}}^{\mathrm{cub}}(\mathbf{u}_{\mathrm{e}}) - \mathbf{f}_{\mathrm{ext}} \right] = 0. \tag{2.125}$$

This equation being verified for all admissible virtual displacements, after assembling with all the elements, the equation of the dynamics of the beam in rotation is deduced:

$$\mathbf{M} \ddot{\mathbf{u}} + \big(\mathbf{K} - \mathbf{K_c}\big) \mathbf{u} + \mathbf{f_{nl2}}(\mathbf{u_t}) + \mathbf{f_{nl3}}(\mathbf{u_t}) = \mathbf{f}_{\mathrm{ext}} + \mathbf{f}_{\boldsymbol{\omega}}, \tag{2.126}$$

with $\mathbf{u_t}$ the total displacement defined regarding the undeformed geometry of the beam. The total displacement $\mathbf{u_t}$ is the sum of a static nonlinear displacement $\mathbf{u_s}$ due to the centrifugal external force, and of vibrations $\mathbf{u}$ around this prestressed position. With a similar development as in section 1.1.6 and introducing a structural Rayleigh damping matrix $\mathbf{C}$, the equation of the dynamics around the prestressed position writes:

$$\boxed{\mathbf{M} \ddot{\mathbf{u}} + \mathbf{C} \dot{\mathbf{u}} + \big(\mathbf{K} - \mathbf{K_c} + \mathbf{K_{nl}}(\mathbf{u}_s)\big) \mathbf{u} + \mathbf{g_{nl2}}(\mathbf{u}) + \mathbf{g_{nl3}}(\mathbf{u}) = \mathbf{f}_{\mathrm{ext}}} \tag{2.127}$$

2.3.3.2 Applications

Due to the centrifugal rotation, the total stiffness of the system is changed and the linear modes cannot be separated into pure bending and membrane modes. The shape of the first three linear normal modes remains however similar to those in the case without rotation but with less curvature due to centrifugal effects as illustrated in Figure 2.13. The associated frequencies are respectively 9.54, 29.97 and 68.80 Hz. Besides, the observation made in paragraph 2.3.1 where a purely vertical load induced only axial nonlinearity is no longer true when the structure rotates because the total stiffness and the expressions of the purely nonlinear forces have changed.

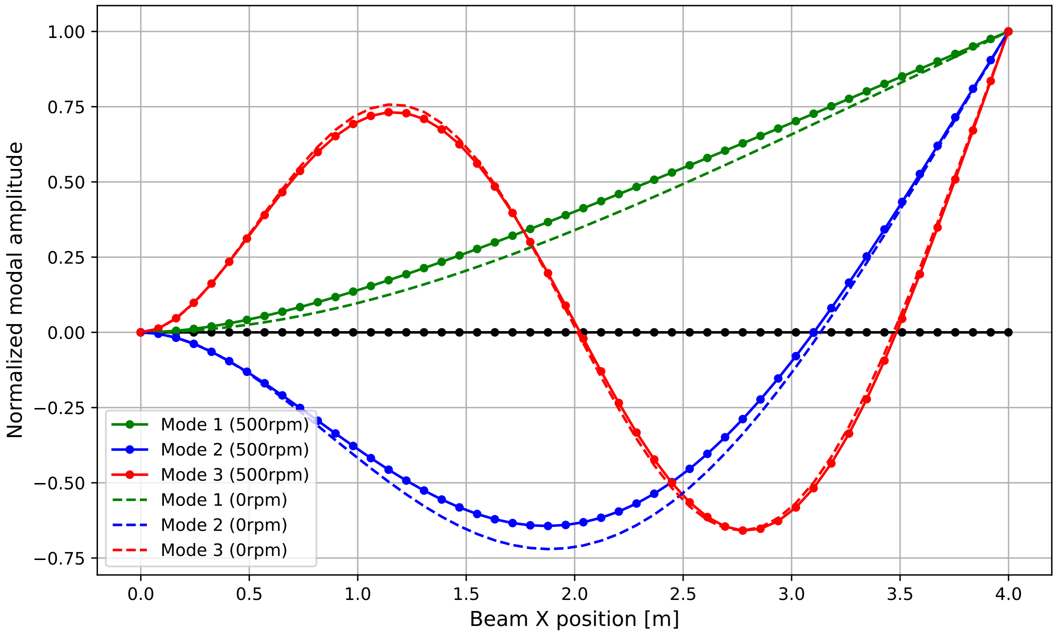

Figure 2.13: First three linear normal modes of the von Kármán beam in rotation at 500 rpm (-●-) compared to their counterpart at 0 rpm (−−).

ICDual ROM for the beam model in rotation:
Similarly to the case without rotation, the first three linear modes are first considered in the reduction basis and the loads imposed to determine the dual modes have the same shape as in Equation (2.101) with the same weighting coefficients. The only difference lies in the mode shapes plotted above in Figure 2.13. Figure 2.14 represents the singular values associated and the linearized strain energies of the dual mode candidates. Compared to the case without rotation (Figure 2.6), there is no clear drop in the singular values. It means that with the first five singular modes, the precision of the residual is lower since the other singular modes have a larger contribution than for the non-rotating case. Those five first dual mode candidates have a negligible vertical contribution and are considered to be modes with membrane contribution. Even though no particular drop is observed for the singular values, a clear one is observed for the complement linearized strain energy. The first five singular modes are chosen as dual modes to enrich the reduction basis.

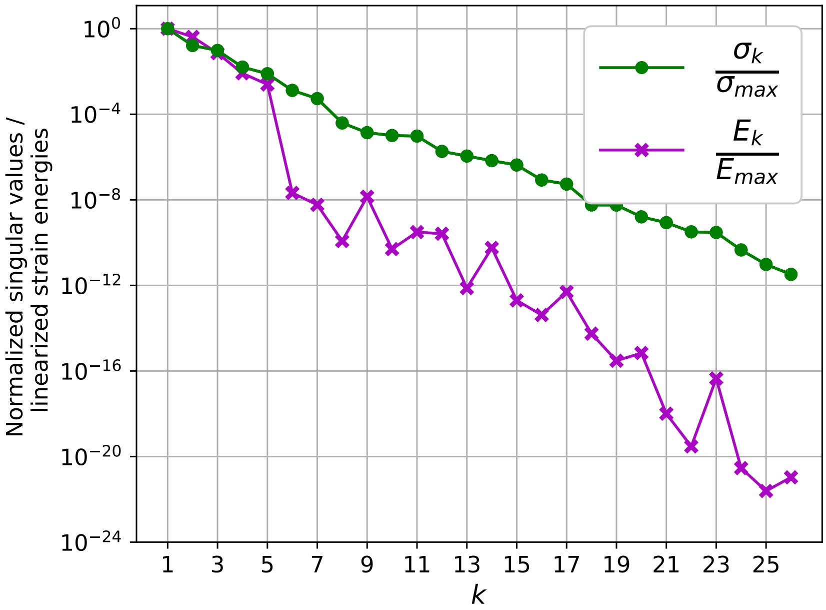

Figure 2.14: Singular values and linearized strain energies of the static solution residuals for the beam case in rotation at 500 rpm.

Static load cases:

In this paragraph, the beam in rotation is subject to three different static load cases. Their amplitude is larger than for the non-rotating case to reach significant transverse displacements despite the centrifugal load:

- S1: a vertical load uniformly distributed along the beam of 140,000 N/m.
- S2: a vertical load of amplitude 210,000 N at the tip of the beam.
- S3: a follower load of amplitude 210,000 N at the tip of the beam.

Figure 2.15 presents the comparison between the nonlinear static displacement, the linear one and the displacements obtained with the ICE/ICDual ROMs under the static distributed load S1. Figure 2.16 illustrates a similar comparison under the vertical load at the tip S2, and Figure 2.17 under the follower load at the tip S3. The errors with respect to the full-order model are presented in Table 2.6. Similar conclusions as those without rotation can be drawn. Under static non-follower loads, both the ICE and ICDual capture accurately the FOM solution. However, only the ICDual ROM captures accurately the static deflection due to a better projection of the follower load. It is worth mentioning that under centrifugal rotation and a load at the tip, the curvature of the beam is accentuated compared to the case without rotation, while the curvature of the linear normal modes is on the contrary reduced (see Figure 2.13).

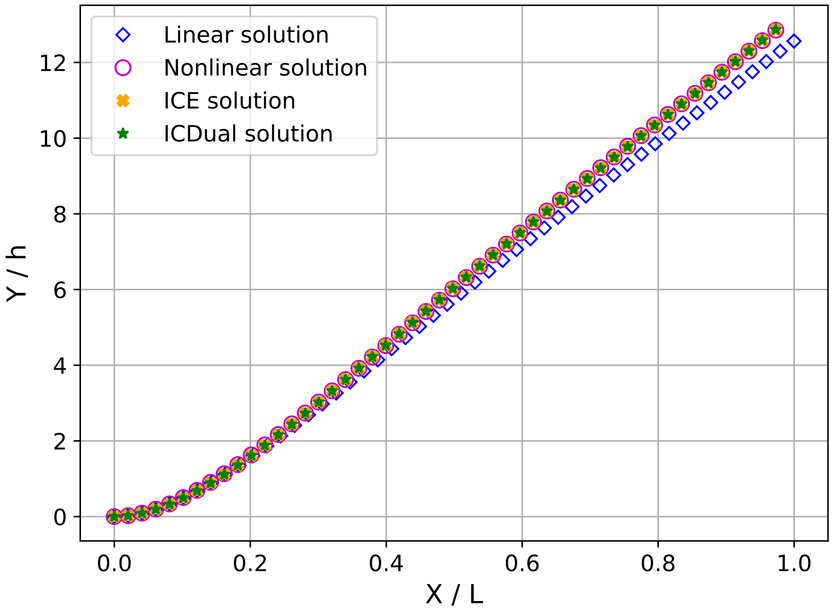

Figure 2.15: Nonlinear static displacement of the clamped-free von Kármán beam subject to the static load case S1. Comparison between the linear FOM, nonlinear FOM, the ICE and ICDual solutions.

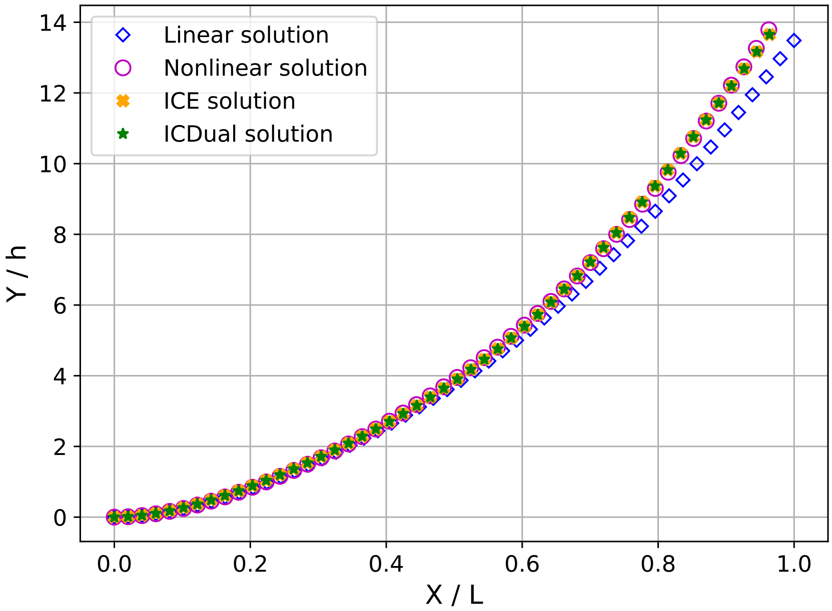

Figure 2.16: Nonlinear static displacement of the clamped-free von Kármán beam subject to the static load case S2. Comparison between the linear FOM, nonlinear FOM, ICE and ICDual solutions.

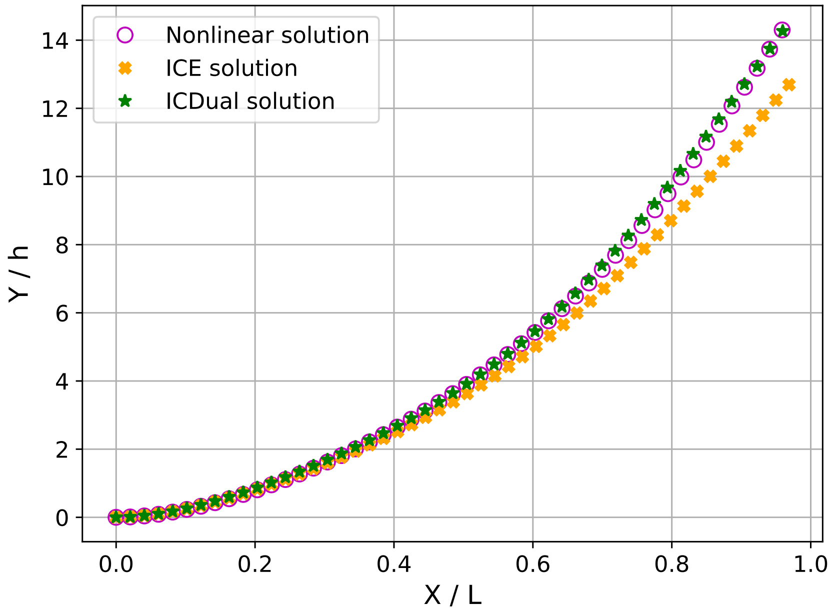

Figure 2.17: Nonlinear static displacement of the clamped-free von Kármán beam subject to the static load case S3. Comparison between the nonlinear, the IC, ICE and ICDual solutions.

Table 2.6: Error regarding the nonlinear FOM solution of the beam displacement for the different load cases in rotation.

	Relative cumulative error $\varepsilon_{\text{cumul}}$ (%)		
Load case	S1	S2	S3
Linear FOM	11.58	11.67	16.39
ICE ROM	0.14	0.75	8.48
ICDual ROM	0.13	0.75	1.37

Dynamic load cases:
In this paragraph, the beam in rotation is subject to three different dynamic load cases. The frequency of excitation corresponds to the resonance frequency of the first mode in rotation f_0^{500} Hz, the time step is 1×10^{-3}s and a Rayleigh damping is added: $\mathbf{C} = 2\xi\omega_0^{500}\mathbf{M}$ with $\xi = 5 \times 10^{-2}$. The external load distributions D1, D2 and D3 of the sinusoidal dynamic load are the following, their amplitude is 3.5% the amplitude of the static cases S1, S2 and S3 respectively:

- D1: a vertical load uniformly distributed along the beam of 4,900 N/m.
- D2: a vertical load of amplitude 7,350 N at the tip of the beam.
- D3: a follower load of amplitude 7,350 N at the tip of the beam.

Figure 2.18 represents the vertical and axial temporal displacements of the beam tip in the periodic regime computed with the different models under the load D1. While the ICDual ROM perfectly captures the nonlinear dynamics, the ICE ROM presents a slight phase shift and strongly overestimates the axial displacement. The same conclusion is observed with the test cases D2 and D3. It is also interesting to notice that unlike the non-rotating case, the vertical displacement of the ICE solution is not superimposed to the linear solution.

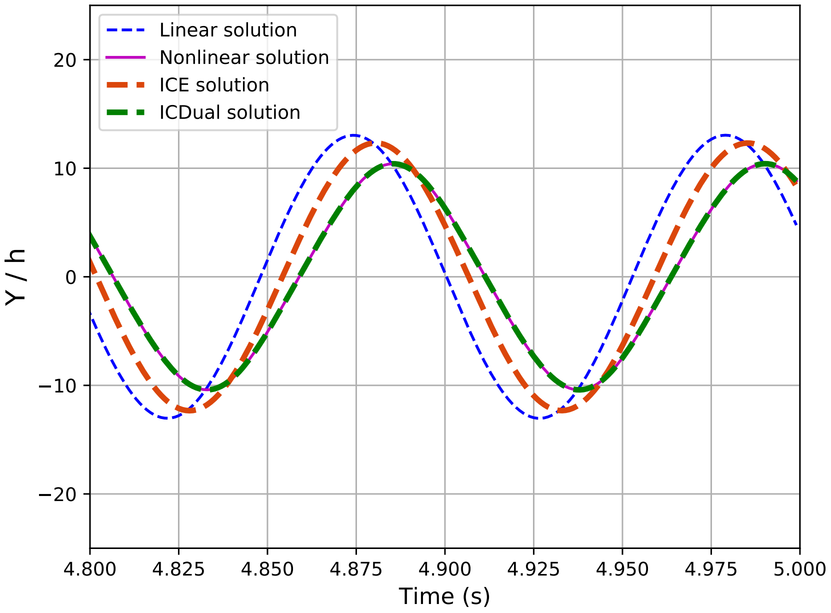

(a) Vertical displacement

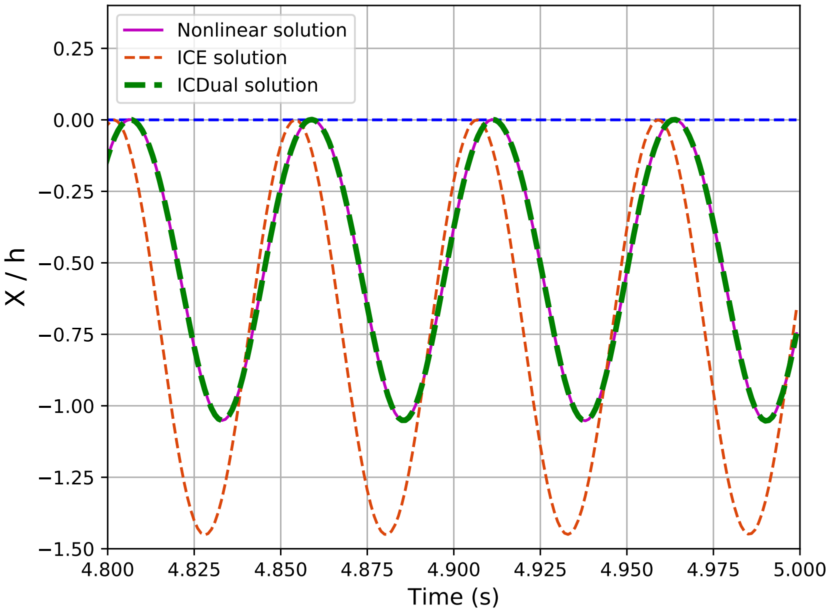

(b) Axial displacement

Figure 2.18: Nonlinear dynamic displacement of the clamped-free von Kármán beam in rotation at 500 rpm, under the dynamic load case D1. Comparison of the vertical (a) and axial (b) displacements at the tip of the beam between the nonlinear FE solution, the ICE and the ICDual computations.

The linear solution presents a phase shift of 38° for the test case D1 and of 34° for the test cases D2 and D3 while the ICDual ROM solution is perfectly in phase with the FOM solution. The phase shift of the ICE ROM is equal to 17° for all load cases. The relative errors of the models on the maximal Y and X tip displacements for the test cases considered are presented respectively in Tables 2.7 and 2.8.

Table 2.7: Relative error, for the different dynamic load cases, of the maximal vertical displacement of the beam tip in periodic regime between the reference nonlinear FOM model and the linear FOM, ICE ROM and ICDual ROM models.

	Relative error of the tip Y displacement (%)		
Load case	D1	D2	D3
Linear FOM	25.22	19.10	17.80
ICE ROM (3 modes)	18.41	14.96	13.78
ICE ROM (8 modes)	18.41	14.95	13.78
ICDual ROM	2.99×10^{-3}	2.48×10^{-2}	2.53×10^{-2}

Table 2.8: Relative error, for the different dynamic load cases, of the maximal axial displacement of the beam tip in periodic regime between the reference nonlinear FOM model and the linear FOM, ICE ROM and ICDual ROM models.

	Relative error of the tip X displacement (%)		
Load case	D1	D2	D3
Linear FOM	100	100	100
ICE ROM (3 modes)	37.93	30.81	28.20
ICE ROM (8 modes)	37.94	30.79	28.18
ICDual ROM	2.15×10^{-2}	3.90×10^{-2}	4.05×10^{-2}

The drawback of the ICE method is accentuated in the case of the beam in rotation. The ICE method computes the dynamics only for the first bending modes and the membrane dynamics is not computed in the reduced equation of the dynamics. For this reason, the axial dynamics is inaccurately rebuilt during the *Expansion* step. A difference in terms of amplitude and phase shift is also observed in the vertical displacement. Indeed, the ICE method assumes that the nonlinear forces coefficients present in the equation of the linear modes "implicitly" contain information about the membrane/bending coupling and somehow translate the effect of the axial nonlinearity in the vertical displacement. Nevertheless, it is observed in the test cases that both the vertical and axial displacements are imprecise and not improved with the ICE ROM built with 8 linear normal modes. This highlights the necessity to precisely compute the membrane/bending coupling, which is what the ICDual ROM does. The dual modes included in the reduction basis better capture the nonlinear coupling and result in more accurate solutions.

2.4 Conclusion of the chapter

In this chapter, the reduced order model ICDual was presented and evaluated on academic test cases for various load cases and the results were compared to other projection-based ROMs. This model is based on completing the linear normal modes basis with dual modes and identifying the projected nonlinear forces via imposed loads. The ICDual ROM is non-intrusive and not affected by the fact that aerodynamic forces are follower forces depending on the deformed position. Such a ROM is built and evaluated in this chapter for a one-dimensional Euler-Bernoulli beam with the von Kármán hypothesis, first without rotation, then subject to a centrifugal rotation at constant speed around a fixed axis. The accuracy of such a ROM was exhaustively tested on different load cases, local or distributed, follower or not, static and dynamic. The comparison with the classical ICE method highlighted that for static cases, both the ICDual and ICE models precisely capture the static deformation, except for follower forces where the ICE ROM does not take properly into account the component of the external load that is orthogonal to the linear modes included in the basis. Regarding dynamic vibrations, the comparison with the ICE method illustrated the necessity to accurately compute the nonlinear dynamical membrane/bending coupling, which is what the ICDual ROM does, while the ICE ROM rebuilds it poorly. The von Kármán beam model and 3D finite element applications with the Saint Venant-Kirchhoff model have in common that the internal nonlinear forces are cubic in the degrees of freedom. The ICDual ROM is therefore directly transposable to such applications, as demonstrated in chapters 3 and 6.

CHAPTER 3

Application to 3D finite elements models using an external FE solver

---

The purpose of this chapter is to apply the ICDual ROM to 3D finite element structures using an external solver. Indeed, such a ROM is non-intrusive and adapted to FE models where the internal nonlinear forces have a cubic dependence to the degrees of freedom. A simple test case of a 3D cantilever beam-like structure equivalent to the one studied in the previous chapter is thus considered in this chapter, first without, then subject to centrifugal rotation.

Contents

3.1 Vibrations of a 3D cantilever beam-like structure without rotation

The case considered has the same geometry as the beam studied in the previous chapter (same dimensions), but is discretized with 3D HEX20 finite elements (360 elements, 2181 nodes). As a reminder, the length of the beam is equal to 4 m, its thickness 7.10^{-2} m and its width 21.10^{-2} m. The Young's modulus is equal to 100 GPa, the density 4,400 kg.m^{-3} and the Poisson's ratio is equal to 0.3. Reference full-order computations are performed using the FE solver *Code_ Aster* [47]. In this section, we first investigate the case of the cantilever beam without rotation. The first three linear normal modes of the structure are shown in Figure 3.1. Their frequencies are respectively 3.38 Hz, 10.11 Hz and 21.17 Hz. In the 2D beam case, the first two linear modes correspond to the first and the third ones of the present case and their frequencies are respectively 3.37 Hz and 21.11 Hz.

Construction of the ROM

The linear normal modes basis is enriched with dual modes according to the process presented in section 1.3.1.4. A set of loads are applied to the beam; the residuals of the nonlinear static solutions are extracted and a SVD is performed on the matrix gathering these residuals. Figure 3.2 shows the first singular values of the SVD as well as the linearized strain energies of the SVD modes. On this graph, we notice that the first two SVD modes with the largest linearized strain energies correspond also to those with the highest singular values. We limit ourselves to those two modes to enhance the linear normal modes basis. With only two additional dual modes, the number of coefficients for the projected nonlinear forces is reasonable and no additional nonlinear

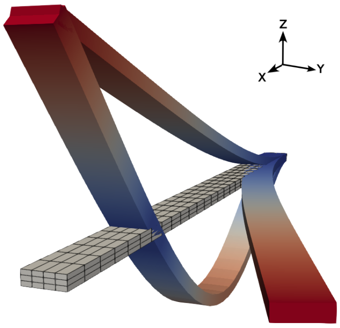

Figure 3.1: Visualization of the first 3 linear normal modes of the beam at 0 rpm. The mesh is the initial geometry.

static solutions are needed to compute the coefficients than those used for the determination of the dual modes. The shape of those dual modes is illustrated in Figure 3.3 showing that those modes are characterized by a purely axial deformation. Indeed, the first linear normal modes correspond to bending movements, triggering membrane displacements due to geometric nonlinearity.

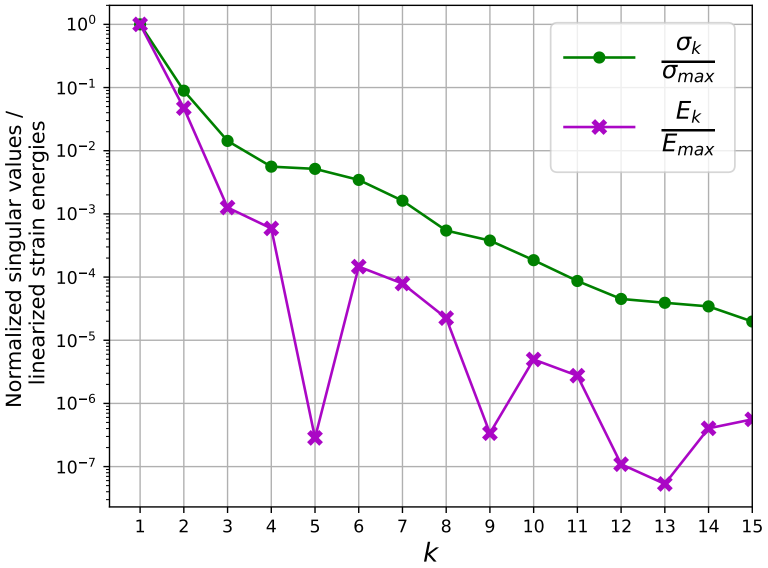

Figure 3.2: Normalized singular values (green) and linearized strain energies (purple) of the modes obtained by the SVD of the matrix of residuals.

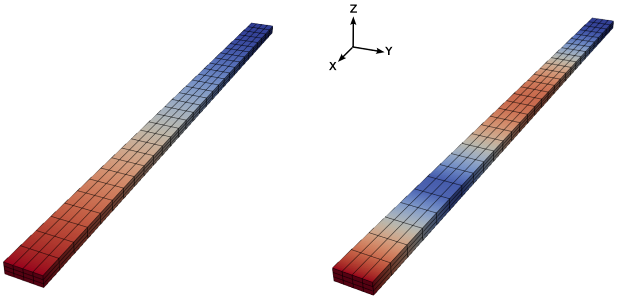

Figure 3.3: Two first dual modes added to the linear basis.

Nonlinear response under a static load

First, a static external load of amplitude 30,000 N is applied vertically at the tip of the beam. Figure 3.4 presents a comparison of the static deflections between the nonlinear FOM and the ROMs. For such a case, the ICE and ICDual reduced order models are superimposed with the nonlinear FOM solution. Both the static nonlinear solutions obtained with the ICE method and the ICDual method capture the nonlinear behavior of the structure. Nevertheless, the nonlinear static solution of the ICE method matches with the FOM solution after the expansion postprocessing step, while with the ICDual approach, the nonlinear solution is captured directly from the resolution of the reduced system. The relative cumulative errors defined in Equation (2.102) are 0.38% for the ICE and ICDual ROM, and 14% for the linear ROM.

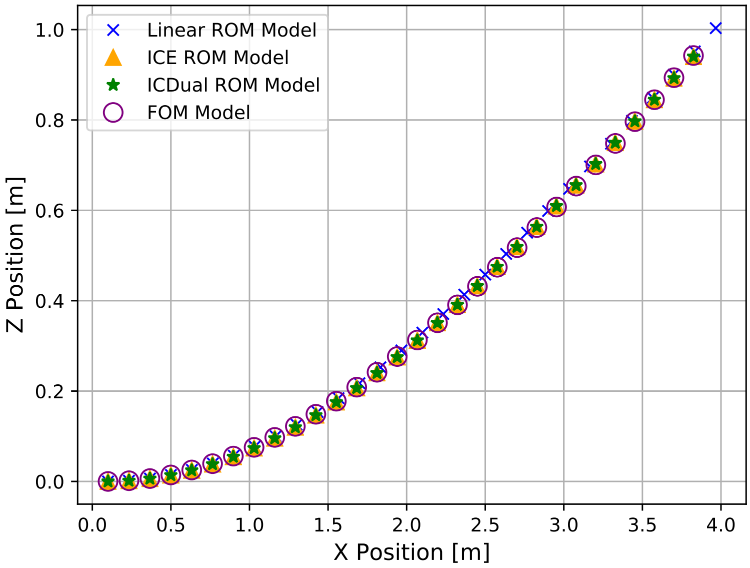

Figure 3.4: Comparison of the nonlinear static solution between the nonlinear FOM and the different ROMs.

Nonlinear response under a dynamic load

A dynamic sinusoidal load is then applied vertically at the tip of the beam, with an amplitude of 2,500 N, and a forcing frequency equal to the one of the first linear normal mode (3.38 Hz). The time integration is performed using an HHT-α scheme with $\alpha_{\text{HHT}} = 0.05$ and a time step of 2.10^{-3}s. Besides, a Rayleigh viscous damping is considered: $\mathbf{C} = 2\xi\omega_0\mathbf{M}$ with a damping ratio $\xi = 0.05$ and ω_0 the pulsation of the first linear normal mode. Figure 3.5 depicts the nonlinear displacement of the FOM over one period and Figure 3.6 represents the axial and vertical temporal displacements of the node in the center of the tip of the beam.

For such levels of deformation, the geometric nonlinearity of the structure is significant. Figure 3.7 represents the vertical and axial displacements of the node at the tip middle of the beam. Phase shifts of 14.5° and 9.7° are observed with respect to the FOM for respectively the ICE and ICDual ROMs.

Figure 3.8 compares the maximal displacements in the periodic regime of the FOM solution, the linear ROM solution and the solutions obtained with the reduced order models ICE and ICDual. The errors on the maximal axial and vertical displacements are quantified in Table 3.1. The

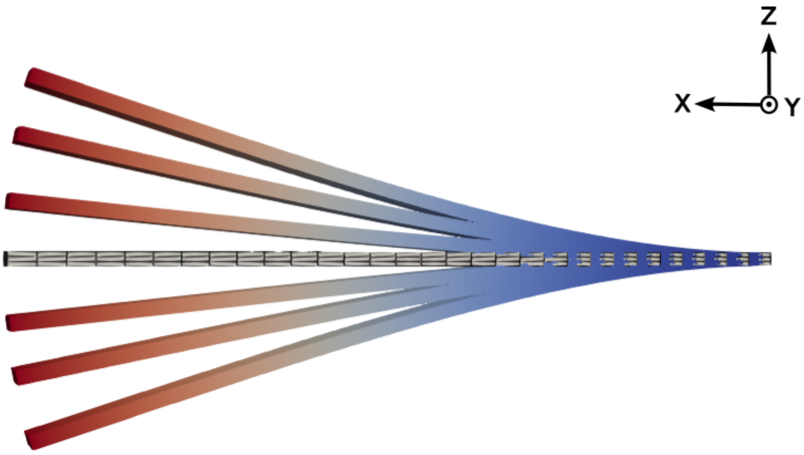

Figure 3.5: Nonlinear FOM displacements over a period.

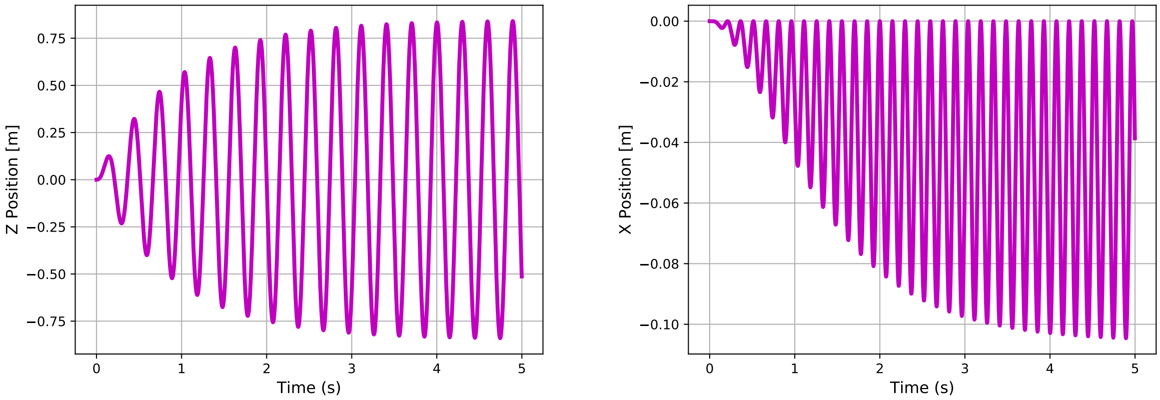

(a) Vertical displacement

(b) Axial displacement

Figure 3.6: Temporal vertical (a) and axial (b) displacements of the tip of the beam.

linear ROM solution does not capture at all the axial shortening of the beam resulting from the nonlinearity. The axial shortening is captured by the *Expansion* step of the ICE method but slightly differs from the FOM solution, which was not the case for the previous test case with a static load. This difference results from the *Expansion* step of the ICE method which is based on a static reconstruction of the solution from the bending dynamics, but the membrane dynamics itself is not solved in the reduced equation of the dynamics. On the contrary, the addition of dual modes to the reduction basis leads to the resolution of the dynamics in traction-compression directly in the reduced equation of the dynamics. Therefore, no reconstruction is needed and the dynamics is more accurately captured.

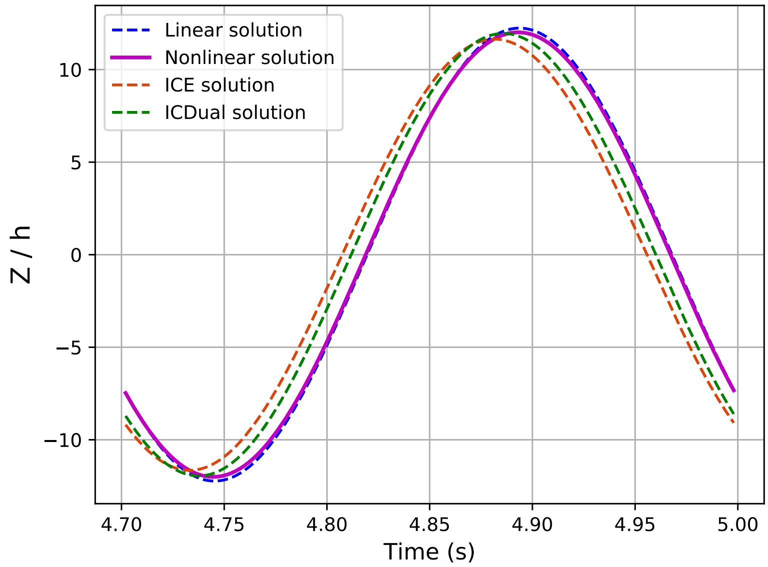

(a) Vertical displacement

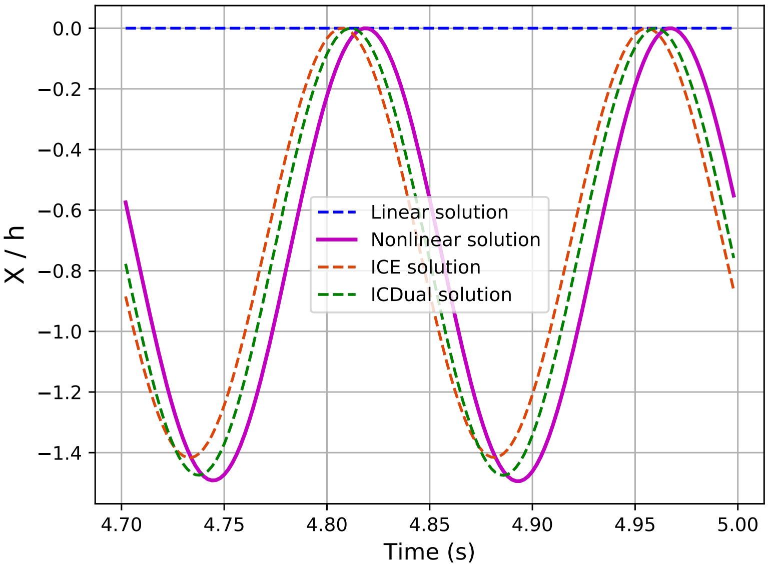

(b) Axial displacement

Figure 3.7: Temporal vertical (a) and axial (b) displacements of the tip of the beam. Comparison between the FOM and the linear, ICE and ICDual ROMs.

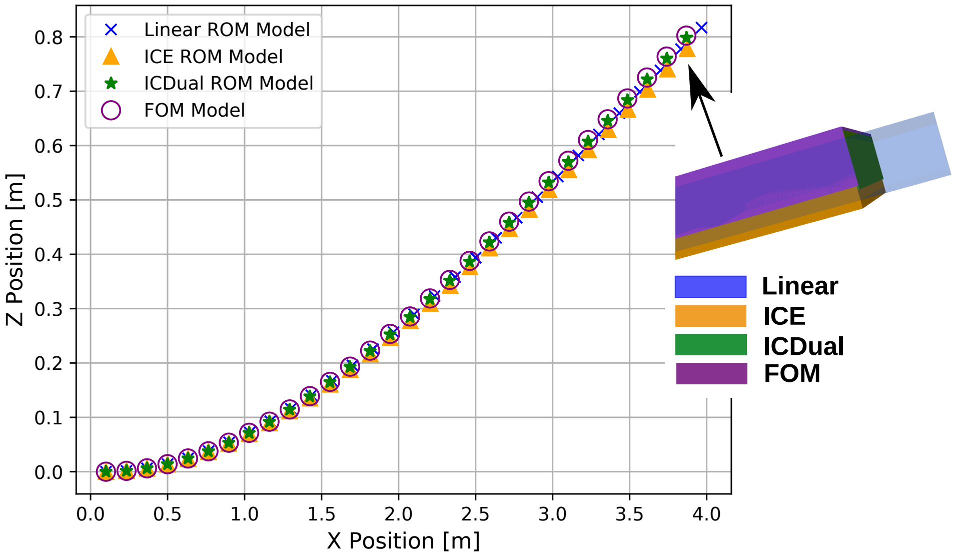

Figure 3.8: Comparison of the maximal displacements in periodic regime between the FOM and the different ROM solutions. The beam is subjected to a vertical sinusoidal load at the tip of amplitude 2,500 N and frequency 3.38 Hz.

Table 3.1: Relative error of the maximal displacement of the beam tip in periodic regime between the reference nonlinear FOM model and the linear FOM, ICE ROM and ICDual ROM models.

	Relative error of the tip displacement (%)	
	Y component	X component
Linear FOM	1.91	100
ICE ROM	3.05	5.20
ICDual ROM	0.48	1.27

3.2 Rotation at a constant speed

In this section, the beam is shifted by 10 cm from the vertical axis and rotates around the latter at a constant speed of 500 rpm. Centrifugal effects arise and the equilibrium position of the structure is the prestressed position due to the centrifugal forces, around which the linear normal modes are computed. The shape of the first three linear normal modes are very similar to those without rotation (see Figure 3.9) but their respective modal frequencies become 9.67 Hz, 10.86 Hz and 30.22 Hz. Then the process of determining the dual modes is applied. Figure 3.10 represents the singular values and the linearized strain energies of the SVD modes. The dual modes selected are the first two SVD modes, which have a similar shape as those of the case without rotation illustrated in Figure 3.3. The relative cumulative errors defined in Equation (2.102) are 2.3% for the ICE, 2.8% for the ICDual ROM, and 11.8% for the linear ROM.

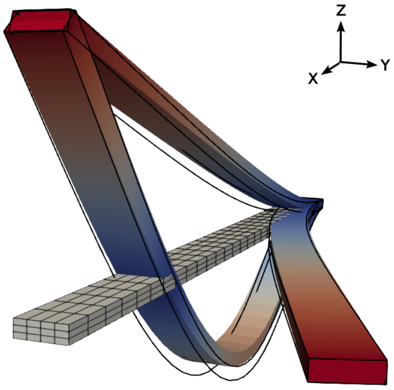

Figure 3.9: Visualization of the first 3 linear normal modes of the beam at 500 rpm. The mesh is the initial geometry and the feature edges their counterpart at 0 rpm.

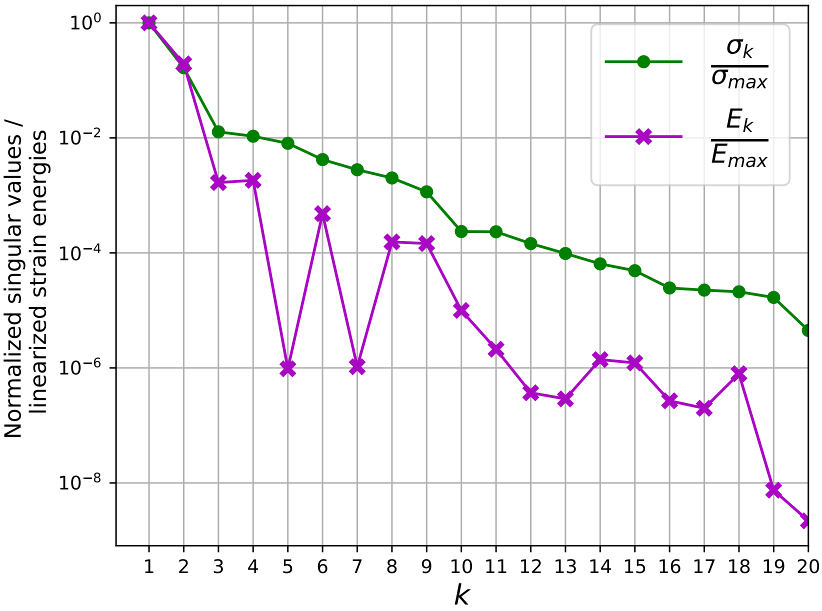

Figure 3.10: Normalized singular values (green) and linearized strain energies (purple) of the SVD modes of the beam in rotation at 500 rpm.

Similarly to the non-rotating analysis of the beam, a static load is applied vertically at the tip. In order to reach a comparable level of displacement, the applied load amplitude (210,000 N) is seven times larger than in the case without rotation. Figure 3.11 illustrates the linear and nonlinear static deflections under such a load case and Figure 3.12 compares the static deflection in the middle line between the nonlinear FOM and the ROM solutions. As in the non-rotating case, the linear ROM solution does not capture the bending/membrane displacement coupling resulting from the geometric nonlinearity. Both the ICE and ICDual models capture the nonlinear coupling leading to axial shortening. Nevertheless, due to the axial centrifugal forces and the vertical loading at the tip, the curvature of the beam is larger than the case without rotation. Such curvature is not perfectly captured by the ROMs. Regarding the position of the tip, the ICDual solution matches with the FOM solution, while the ICE solution underestimates the vertical displacement.

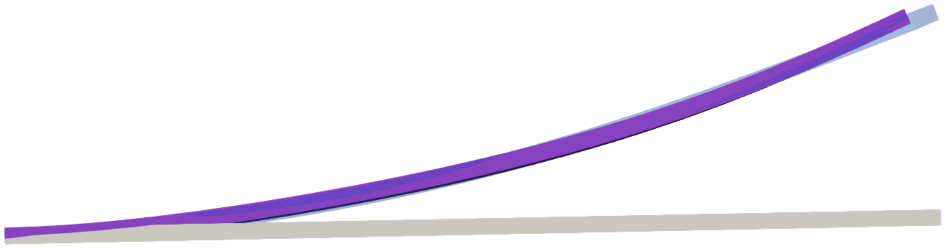

Figure 3.11: Comparison of the nonlinear and linear static deflections. The beam is in rotation at 500 rpm subject to a vertical static load at the tip of 210,000 N.

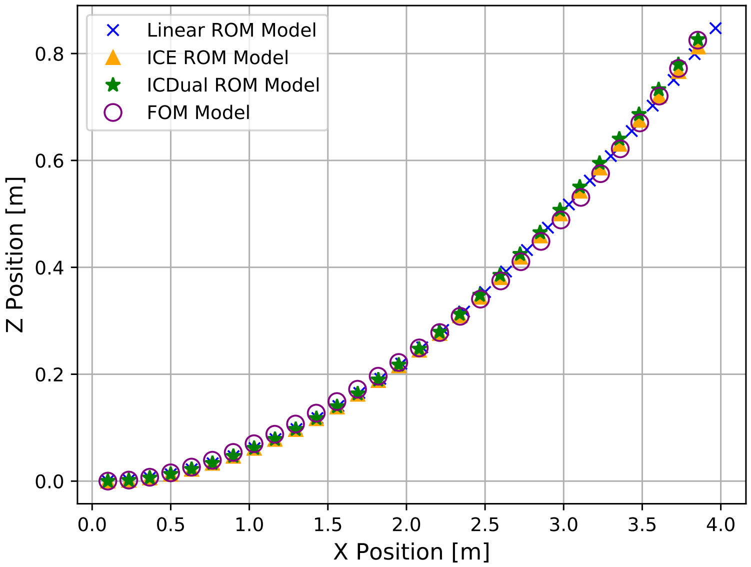

Figure 3.12: Comparison of the static deflections between the FOM and the different ROMs. The beam is in rotation at 500 rpm subject to a vertical static load at the tip of 210000 N.

To echo the beam test case without rotation, this second study deals with a dynamic loading applied vertically at the tip. The frequency of excitation is the one of the first linear normal mode in rotation (9.67 Hz) and its amplitude is 7,350 N, about three times the load of the non-rotating case in order to reach a similar magnitude of displacements. The same integration scheme as for the case without rotation is used but the time step is reduced by half. The Rayleigh damping is kept unchanged. The nonlinear solutions with the ICE and ICDual reduced order models are also computed. Figure 3.14 represents the vertical and axial displacements of the node at the tip middle of the beam. Phase shifts of 27.8° and 17.4° with respect to the FOM are observed for respectively the ICE and ICDual ROMs. The maximal amplitudes in the periodic regime of the different models are illustrated in Figure 3.13 and the errors on the maximal axial and vertical displacements are quantified in Table 3.2. While the solution with dual modes has a negligible error with respect to the nonlinear FOM solution, the ICE method slightly underestimates the amplitude of displacement; more linear normal modes would be needed in the reduction basis for the ICE method.

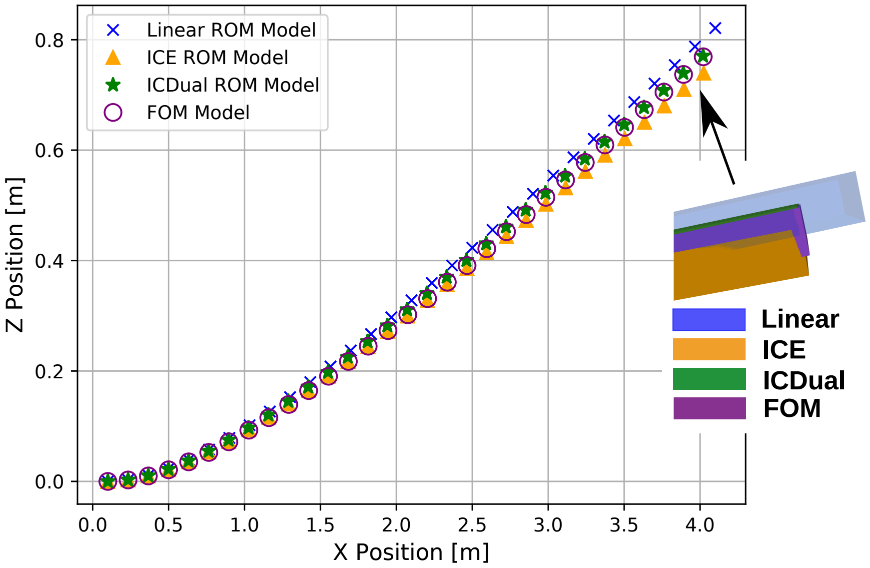

Figure 3.13: Comparison of the maximal displacement in periodic regime between the FOM and the different ROM solutions. The beam is subject to a vertical sinusoidal load at the tip, of amplitude 7350 N and frequency 9.67 Hz.

Table 3.2: Relative error in the rotating case of the maximal displacement of the beam tip in periodic regime between the reference nonlinear FOM model and the linear FOM, ICE ROM and ICDual ROM models.

	Relative error of the tip displacement (%)	
	Y component	X component
Linear FOM	6.41	100
ICE ROM	4.15	7.77
ICDual ROM	0.14	2.34

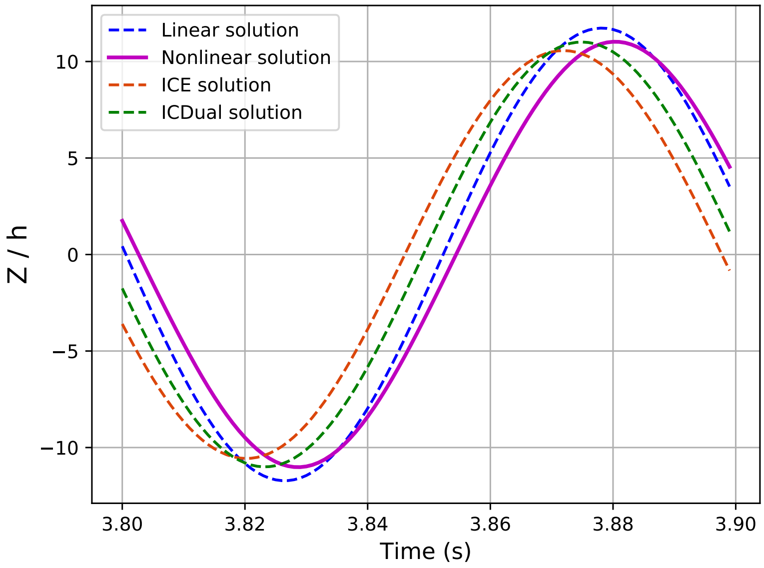

(a) Vertical displacement

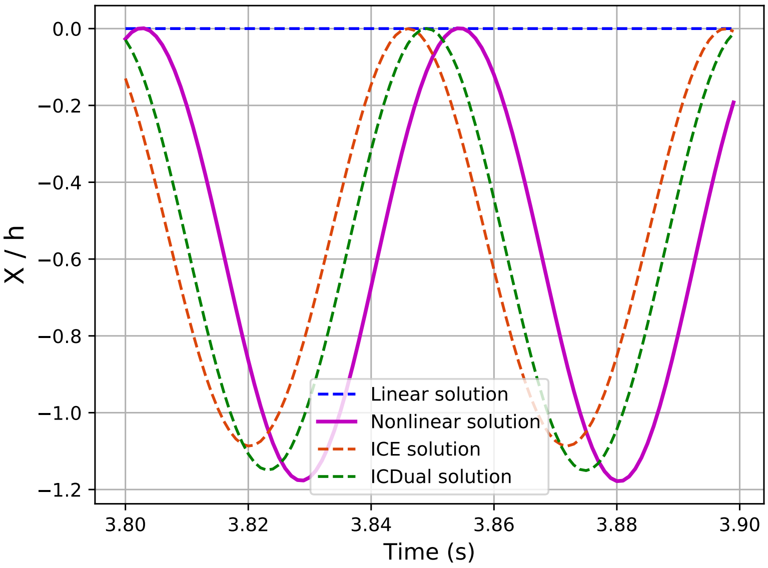

(b) Axial displacement

Figure 3.14: Temporal axial and vertical displacements of the tip of the beam. Comparison between the FOM and the linear, ICE and ICDual ROMs.

The same static solutions were used to build both the ICE and ICDual ROMs, meaning that the offline costs of the construction of the reduced order models are the same. By adding two dual modes to the reduction basis, the ICDual ROM improves the dynamic solution compared to the ICE ROM. Besides, building an ICE ROM with the first five linear normal modes does not improve the dynamic solution. However, it slightly improves the static solution thanks to the 15 postprocessing modes. In the test cases, the choice was made to remain general in the sense that the first three linear modes are used. However, since the external load is vertical along z and the beam is symmetrical and isotropic, no movement in the y direction is triggered and the second linear normal mode does not contribute. The solutions can be improved by considering the first three linear normal modes in the (x, z) plane, which means considering the first, third and fifth linear normal modes illustrated in Figure 3.15. Indeed, the second and fourth linear normal modes are the first and second bending modes in the y direction shown in Figure 3.16.

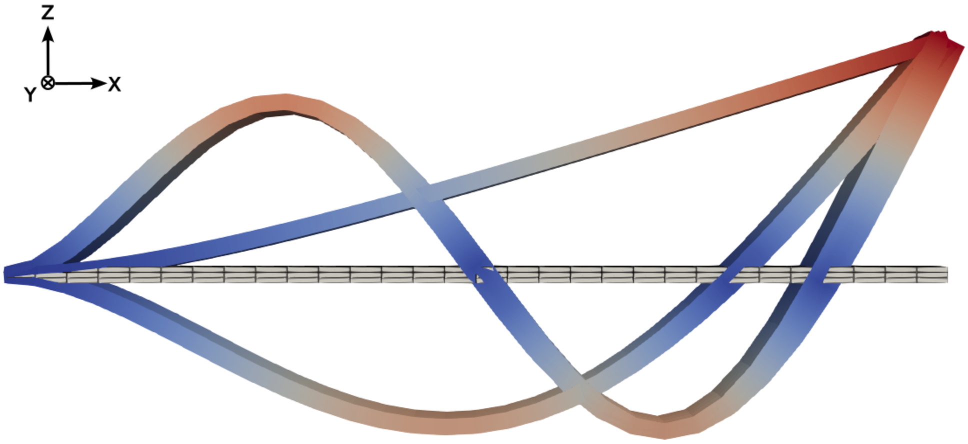

Figure 3.15: First three linear modes in the (x, z) plane of the beam in rotation at 500 rpm around the axis z.

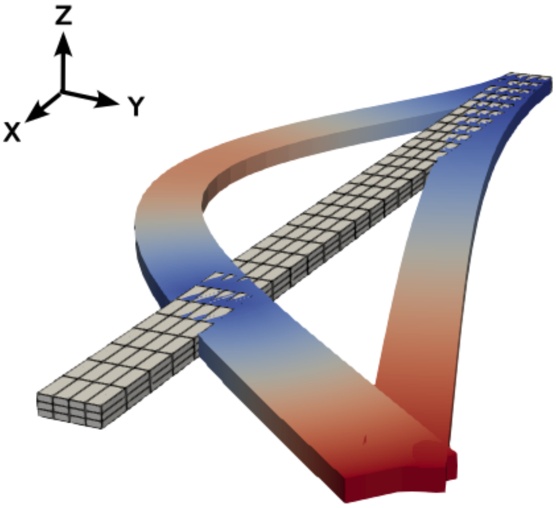

Figure 3.16: Second and fourth linear modes of the beam in rotation at 500 rpm around the axis z.

The dual modes built from the new reduction basis of the three first linear normal modes in the plane (x, z) are represented in Figure 3.17. Similarly to the previous reduction basis of linear normal modes, those dual modes are characterized by a membrane contribution. The solutions of the different ROMs for the static load case are represented in Figure 3.18. Both the ICE and ICDual are improved compared to the previous case with the reduction basis containing the transverse mode. The relative cumulative errors are here 0.70% for the ICE ROM and 1.52% for the ICDual ROM whereas the errors where respectively 2.3% and 2.8% when taking into account the transverse modes. As noted before, the combination of the vertical load at the tip of the beam and the centrifugal rotation leads to a stronger curvature of the beam than for the case without

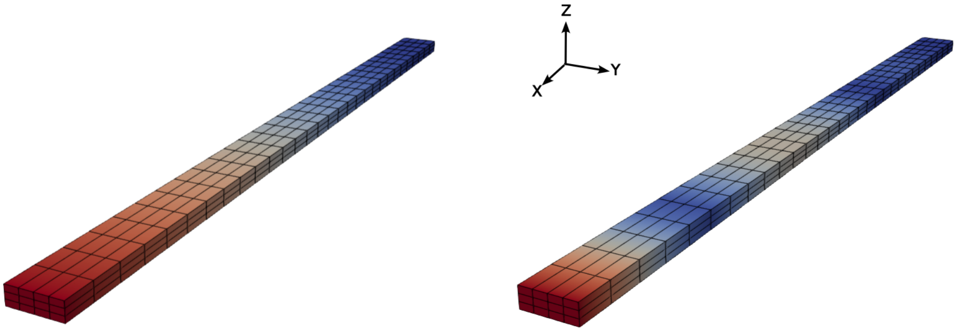

Figure 3.17: First two dual modes based on the first three linear normal modes in the (x, z) plane illustrated in Figure 3.15.

rotation. The third linear normal mode in the (x, z) plane helps capture such a curvature. The improvement of the ICE ROM is significant thanks to the six postprocessing modes and the ICE ROM is thus particularly accurate for this static case. The ICDual ROM is also improved and accurate, representing the nonlinear FOM static solution with an error of the order of magnitude of one percent.

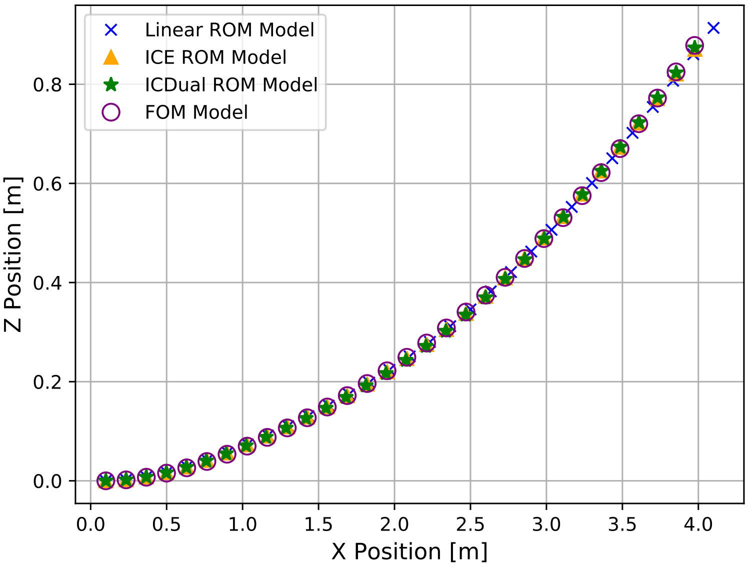

Figure 3.18: Comparison of the static deflections between the FOM and the different ROMs with reduction basis based on the first three linear modes in the (x, z) plane. The beam is in rotation at 500 rpm subject to a vertical static load at the tip of 210,000 N.

The fact that the ICDual ROM computes the nonlinear solution during the resolution and not in postprocessing will make a difference in the dynamic case. The solutions of the ROMs under the dynamic sinusoidal load case are shown in Figure 3.19. The phase shift of the ICE method remains 27° while the phase shift of the ICDual method is reduced to only 7°. Besides, the vertical and axial displacements in the periodic regime are slightly improved for the ICE ROM and the axial displacement of the ICDual ROM is greatly enhanced as shown in Table 3.3.

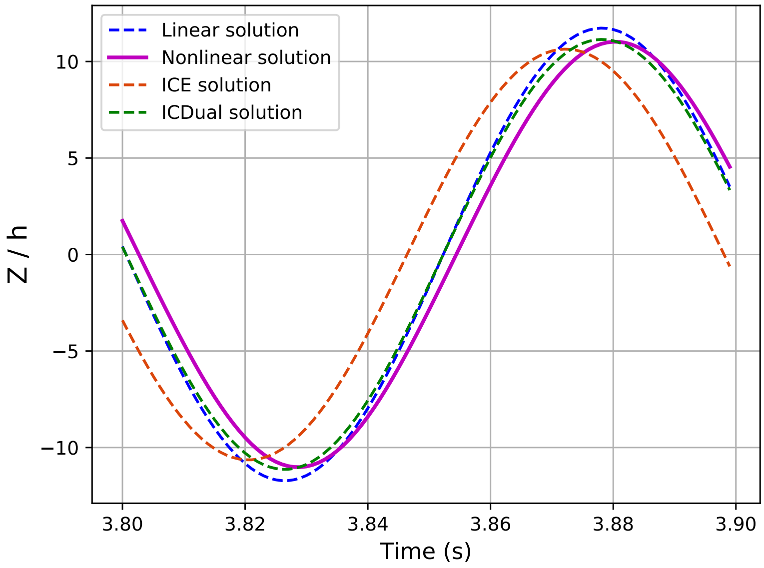

(a) Vertical displacement

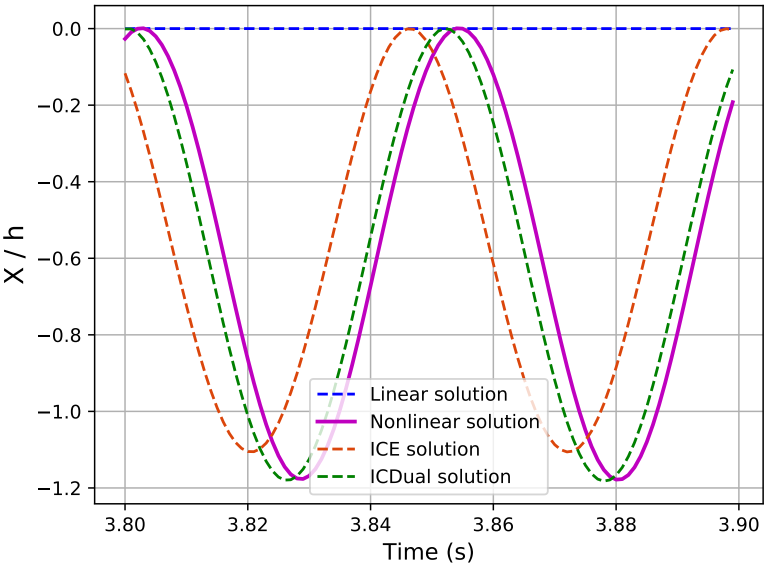

(b) Axial displacement

Figure 3.19: Temporal axial and vertical displacements of the tip of the beam. Comparison between the FOM and the linear, ICE and ICDual ROMs built with reduction basis based on the first three linear modes in the (x, z) plane.

Table 3.3: Relative error in the rotating case of the maximal displacement of the beam tip in periodic regime between the reference nonlinear FOM model and the linear FOM, ICE ROM and ICDual ROM models built with reduction basis based on the first three linear modes in the (x, z) plane.

	Relative error of the tip displacement (%)	
	Y component	X component
Linear FOM	6.41	100
ICE ROM	3.48	6.15
ICDual ROM	1.08	0.34

3.3 Notes on the non-intrusive computation of the projected nonlinear forces coefficients for 3D structures

In this section, we give some advice for the non-intrusive computation of the projected nonlinear forces coefficients using an external FE solver. The non-intrusive characteristic of the computation of the coefficients is considered necessary for industrial applications. An intrusive determination of the coefficients would be easier and more accurate, but it means that we need to have access to the code sources, which is not the case for commercial FE codes. The other possibility is to build our own FE solver with all the beam, shell, 3D volume, and composite elements necessary to tackle complex industrial geometries where locally added masses are also sometimes present. This goes beyond the context of this work. For this reason, one of the constraints for the ROM is the non-intrusiveness regarding an external FE solver.

Nonlinear coefficients may be determined with non-intrusive approaches either by imposed displacements or by imposed loads. The advantage of imposing displacements is to determine the coefficients one by one with pertinent combinations of displacements such as the STEP method. It works well for 1D structures with polynomial nonlinearities. However, for 3D structures, we already mentioned that it leads to numerical artifacts linked to the prescription of volume deformation [199]. Indeed, huge non-desired local efforts are introduced to impose the volume, polluting the numerical computation of the coefficients. The use of imposed loads instead of imposed displacements in the ICDual method prevents such inaccuracies. On the contrary, the nonlinear forces coefficients cannot be determined one by one but through the resolution of the linear system of Equation (2.4). Nevertheless, some precautions may be necessary to avoid numerical inaccuracies due to a possibly large condition number. First, the quadratic and cubic contributions of the nonlinear forces are usually not provided separately by the FE solvers so the determination of the coefficients cannot be splitted into two smaller systems instead of a single one. Second, the normalization of the linear normal modes and their contribution may lead to generalized coordinates of different orders of magnitude. The result is that the system to solve in Equation (2.4) has a condition number that may be large, affecting the robustness of the determination of the coefficients. One idea to circumvent such a problem is to deal with normalized generalized coordinates. Indeed, we remind the reader that generalized coordinates $(\mathbf{q}^{(\ell)})_{\ell\in[1,n_\mathrm{L}]}$ are obtained from the nonlinear static solutions $(\mathbf{u}_\mathbf{s}^{(\ell)})_{\ell\in[1,n_\mathrm{L}]}$. To normalize the computation of the coefficients, we divide all the components $q_k^{(\ell)}$ of the vectors of generalized coordinates $\mathbf{q}^{(\ell)}$ by the maximal absolute value of q_k for all the load cases: $\tilde{q}_k^{(\ell)} = q_k^{(\ell)}/\max(|q_k^{(\ell)}|)_{\ell\in[1,n_\mathrm{L}]}$. Such a normalization limits the discrepancies in the orders of magnitude of the monomials $\tilde{q}_i\tilde{q}_j$ and $\tilde{q}_i\tilde{q}_j\tilde{q}_m$ of generalized coordinates in the system to solve. The coefficients obtained are normalized and have to be then multiplied afterwards by the normalizations of the generalized coordinates to obtain their physical value.

A second point is linked to the number of static solutions available. As mentioned in section 2.2.1, the static solutions are built by imposing external forces using the shape of the linear normal modes and not the dual modes. However, the number of coefficients to determine when dual modes are included in the reduction basis is larger than the number of coefficients to determine with only the linear normal modes in the reduction basis. Consequently, the number of static solutions for a square system (Equation 2.2.1) in the resolution of the coefficients is $(n^3 + 6n^2 + 5n)/6$ with n the number of modes in the reduction basis. However, depending on the geometries and the symmetries, a lot of coefficients are usually null or negligible. For this reason, it is sometimes interesting to prefer a penalized least-squares approximation such as Ridge, Lasso [189] or Elastic-net [210] to the standard least-squares approximation. The advantage of such regression methods is double. First, the resolution of ill-posed systems is improved. Second, it avoids excessively large coefficients and sets negligible coefficients close to or equal to zero, especially the Lasso regression. In his work, penalized regressions with cross-validation were used thanks to the Python library *Scikit-learn* [140].

When the number of available static solutions is very low, it is interesting to get rid of negligible coefficients to gain precision in the computation of the others. To do so, a first computation of the nonlinear forces coefficients is performed. Considering the mode k, for each static solutions $(\mathbf{u}_\mathbf{s}^{(\ell)})_{\ell\in[1,n_\mathrm{L}]}$, the projected nonlinear forces along the mode k is considered:

$$\tilde{g}^k_{\mathrm{nl}}(\mathbf{q}^{(\ell)}) = \mathbf{V}_k^T \mathbf{g}_{\mathbf{nl}}(\mathbf{V}\mathbf{q}^{(\ell)}) = \sum_{i=1}^{n}\sum_{j=i}^{n} \beta^k_{ij} q_i^{(\ell)} q_j^{(\ell)} + \sum_{i=1}^{n}\sum_{j=i}^{n}\sum_{m=j}^{n} \gamma^k_{ijm} q_i^{(\ell)} q_j^{(\ell)} q_m^{(\ell)}. \tag{3.1}$$

This projected nonlinear force is the sum of quadratic and cubic contributions $\beta^k_{ij} q_i^{(\ell)} q_j^{(\ell)}$ and $\gamma^k_{ijm} q_i^{(\ell)} q_j^{(\ell)} q_m^{(\ell)}$. In this decomposition, some contributions may be negligible compared to others. For example, if the maximal absolute contribution is $\beta^k_{11} q_1^{(\ell)} q_1^{(\ell)}$ and $|\beta^k_{13} q_1^{(\ell)} q_3^{(\ell)}|/|\beta^k_{11} q_1^{(\ell)} q_1^{(\ell)}| < 10^{-5}$, then the contribution $\beta^k_{13} q_1^{(\ell)} q_3^{(\ell)}$ is negligible for the load case ℓ. If a contribution is negligible for all load cases, the associated coefficient can be set to zero. A new computation of the system with fewer unknowns is therefore more precise. This process can be repeated as a fixed-point procedure until no new negligible coefficients are found. Performing this process for all the modes and considering the previous point about the normalization improves the robustness of the method when only a few static solutions are available. For instance, the static solutions used to determine the dual modes can be reused without the need for further nonlinear static computations. It also means that the number of static solutions necessary is lower than for a determination of the coefficients by imposed displacements. Indeed, when dual modes are considered and the projected nonlinear forces coefficients are computed by imposed displacements, a first set of nonlinear static solutions are necessary to determine the dual modes, and another larger set is necessary to compute the coefficient. With the ICDual method, only the static solutions are necessary to determine the dual modes with potentially a few additional solutions when a lot of dual modes are included in the basis.

3.4 Conclusion of the chapter

In this chapter, the ICDual method was applied to a 3D FE cantilever beam-like structure. One case without centrifugal rotation and one with were studied. Both were subjected to a vertical load at the tip. The results are similar to those of the previous study of the Euler-Bernoulli/von

Kármán beam presented the previous chapter. Indeed, the eigenfrequencies and amplitudes of displacement are close and it was observed with both models that the differences in vertical amplitude between the linear and nonlinear solutions are more pronounced for the rotating case than for the non-rotating case. The conclusions of the reduction methods are also similar in the sense that both the ICE and ICDual ROM were accurate considering static loads, while the dynamic loads showed the limit of the ICE postprocessing reconstruction although the ICDual ROM remained particularly accurate. The ICDual ROM is built in a non-intrusive way from the FE solver *Code_Aster* [47], both for the determination of the dual modes and the computation of the projected nonlinear coefficients, thus validating the approach for 3D structures. An application to the complex geometry of a fan blade is found in chapter 6.

Chapter 4

Partitioned fluid-structure coupling procedure between the fluid solver and the structural ROM

In this chapter, the fluid equations of the coupled problem are introduced. The Navier-Stokes equations are considered to depict the fluid dynamics. Since the fluid mesh is deformed by the displacement of the structure, an Arbitrary Lagrangian-Eulerian (ALE) formulation is used for the CFD computations. Common mesh deformations techniques are then presented and illustrated with simple test cases. To compute fluid-structure interaction problems, two approaches are found in the literature: a monolithic and a partitioned coupling. A paragraph is dedicated to both approaches but it is the partitioned approach that will be used in this work. Finally, transfer methods for the loads and displacements between the fluid and structure meshes are explained.

Contents

4.1 Arbitrary Lagrangian-Eulerian formulation to consider the moving structure in the fluid

In the frame of fluid-structure interaction, the displacements of the structure due to aerodynamic loads change the position of the fluid boundary. A moving mesh is therefore considered and the Arbitrary Lagrangian-Eulerian formulation for the fluid equations is commonly used. In this section, the Navier-Stokes equations in Eulerian formulation are first reminded along with common constitutive equations. Then those equations in the Arbitrary Lagrangian-Eulerian formulation are provided.

4.1.1 Navier-Stokes equations in Eulerian formulation

In the field of computational fluid dynamics, the Eulerian description of the flow field is the way of observing the fluid motion by focusing on a specific location in space, which the fluid flow passes through as time passes. In the Eulerian description, the local equations of conservation for the fluid take the following form:

- Mass conservation equation:

$$\frac{\partial \rho}{\partial t} + \nabla \cdot (\rho \boldsymbol{v}) = 0. \tag{4.1}$$

- Momentum conservation equation:

$$\frac{\partial (\rho \boldsymbol{v})}{\partial t} + \nabla \cdot (\rho \boldsymbol{v} \otimes \boldsymbol{v} - \boldsymbol{\tau} + p\mathbf{I}) = 0, \tag{4.2}$$

where the source term due to the gravity is ignored and $\boldsymbol{\tau}$ is the viscous stress tensor of the fluid.

- Conservation of the total specific energy E:

$$\frac{\partial (\rho E)}{\partial t} + \nabla \cdot (\rho E \boldsymbol{v} + p\boldsymbol{v} - \boldsymbol{\tau}\boldsymbol{v} + \boldsymbol{q}) = 0. \tag{4.3}$$

The term "specific" means per unit of mass. The total specific energy is defined by $E = e + v^2/2$ with e the specific internal energy. The equations (4.1), (4.2) and (4.3) are the Navier-Stokes equations. It is common to introduce the vector of the conservative variables $\boldsymbol{W}$ and the fluxes $\boldsymbol{\mathcal{F}}$, sum of the convective and diffusive fluxes:

$$\boldsymbol{W} = \begin{bmatrix} \rho \\ \rho \boldsymbol{v} \\ \rho E \end{bmatrix}, \qquad \boldsymbol{\mathcal{F}} = \begin{bmatrix} \rho \boldsymbol{v} \\ \rho \boldsymbol{v} \otimes \boldsymbol{v} + p\mathbf{I} - \boldsymbol{\tau} \\ \rho E \boldsymbol{v} + p\boldsymbol{v} - \boldsymbol{\tau}\boldsymbol{v} + \boldsymbol{q} \end{bmatrix}. \tag{4.4}$$

The Navier-Stokes equations thus take the following form representing the temporal variation of the conservative variables $\boldsymbol{W}$ due to the losses by the diffusive and convective fluxes and by the creation through a source term. The source terms are not written here but are for instance due to the rotation[1], gravity or electromagnetism:

$$\frac{\partial \boldsymbol{W}}{\partial t} + \nabla \cdot \boldsymbol{\mathcal{F}}(\boldsymbol{W}) = 0. \tag{4.5}$$

4.1.2 Constitutive equations

The aforementioned equations of conservation are valid for all types of fluids. As such, the Navier-Stokes equations cannot be solved since there are too many unknowns. Constitutive equations describing the interdependency of the variables have to be added to the system such as Fourier's law of heat conduction and the hypothesis of Newtonian fluids for the viscous tensor for instance. Besides, the density and viscosity of compressible fluids depend on the temperature. Regarding gases, the perfect gas equation and Sutherland's law for the dynamic viscosity are commonly considered for the constitutive equations.

---

[1] For the turbomachine case treated in chapter 6, the equations are formulated in the relative frame and source terms are thus present due to the Coriolis and centrifugal effects.

Thermal conduction

Fourier's law of heat conduction is the constitutive equation expressing the diffusive flux resulting from the variation in temperature: $\boldsymbol{q} = -\kappa_T \nabla T$ with κ_T (in W.m^{-1}.K^{-1}) the thermal conductivity of the fluid.

Newtonian fluids

A Newtonian fluid is a fluid for which the viscous stresses depend linearly on the local deformation rate. The deformation rate tensor of the fluid is the sum of two contributions: the shear with constant volume $\left[\nabla \boldsymbol{v} + (\nabla \boldsymbol{v})^T\right]/2 - (\nabla \cdot \boldsymbol{v})\mathbf{I}/3$ and the isotropic expansion $(\nabla \cdot \boldsymbol{v})\mathbf{I}/3$. Likewise, the viscous stress tensor can also be seen as the sum of the two contributions : $\boldsymbol{\tau} = \boldsymbol{\tau}_{\text{shear}} + \boldsymbol{\tau}_{\text{exp}}$. A fluid is Newtonian when there is proportionality respectively between $\boldsymbol{\tau}_{\text{shear}}$ and the shear with constant volume and between $\boldsymbol{\tau}_{\text{exp}}$ and the isotropic expansion:

$$\boldsymbol{\tau}_{\text{shear}} = 2\mu \left[\nabla \boldsymbol{v} + (\nabla \boldsymbol{v})^T\right], \tag{4.6}$$

$$\boldsymbol{\tau}_{\text{exp}} = \lambda \frac{(\nabla \cdot \boldsymbol{v})\mathbf{I}}{3}, \tag{4.7}$$

with λ the second viscosity coefficient and μ the shear viscosity or first viscosity coefficient. The hypothesis of Stokes consists in neglecting the second viscosity coefficient $\lambda = 0$, leading to:

$$\boldsymbol{\tau} = \mu \left[\nabla \boldsymbol{v} + (\nabla \boldsymbol{v})^T - \frac{2}{3}(\nabla \cdot \boldsymbol{v})\mathbf{I}\right]. \tag{4.8}$$

Perfect gas equation

The perfect gas is a common model in which the intermolecular forces are neglected. The perfect gas equation links the pressure to the density and the temperature:

$$p = p(\rho, T) = \rho r T, \tag{4.9}$$

with $r = R/M$ the specific gas constant, in which R is the universal gas constant: $R = 8.314$ J.K^{-1}.mol^{-1} and M is the molar mass of the gas.

Sutherland's law

Sutherland's law is a semi-empirical relation specific for gases, expressing the dynamic viscosity of the fluid as a function of the temperature:

$$\mu(T) = \mu_{ref} \left(\frac{T}{T_{ref}}\right)^{3/2} \frac{T_{ref} + S}{T + S}, \tag{4.10}$$

where T_{ref} is the temperature of reference 273.15 K, S is a constant depending on the fluid and μ_{ref} is the dynamic viscosity of the fluid at the temperature T_{ref}.

4.1.3 Navier-Stokes equations in ALE formulation

In the Lagrangian approach, the computational mesh follows the particle motion and the grid nodes are permanently connected to the same material points. The principle of the Eulerian formulation is that the mesh is fixed in space and the particles move with respect to the mesh grid. A significant drawback for both methods is that the refinement of the mesh is fixed in space and fails to capture flow details that might occur out of the refined places. The Lagrangian approach is the classical formulation to treat mechanical structures undergoing large amplitude displacements while the

Eulerian formalism is common for fluid dynamics. In the frame of fluid-structure interaction, the displacement of the structure imposes a movement to the fluid mesh. Thus, it is common to adopt the Arbitrary Lagrangian-Eulerian (ALE) framework [43] to compute the fluid equations with respect to a moving mesh. The aim of the ALE formulation is indeed to allow freedom of moving the mesh, which can be moved arbitrarily as desired. Thus the ALE formulation enables to handle large distortions that were problematic in a purely Lagrangian approach and with a better accuracy than with only an Eulerian approach.

In a fluid-structure framework, the fluid mesh is deformed by the movement of the fluid-structure boundary. Figure 4.1 presents schematically the movement of a mesh $\boldsymbol{\xi}$ due to the displacement and deformation of the solid Ω_S in the fluid domain Ω_F. The moving fluid-structure interface is represented by Γ.

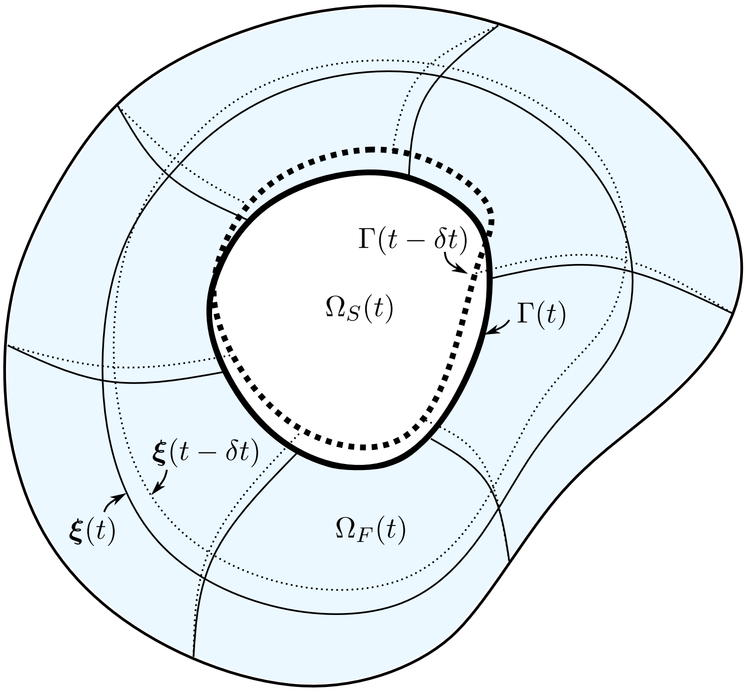

Figure 4.1: Simplified representation of the mesh movement justifying the ALE formulation for the fluid equations.

Writing Ω_F a control volume in the fluid domain and $S_F(t)$ its surface, the Reynolds transport theorem applied to the conservative variables $\boldsymbol{W}$ in the control volume Ω_F stipulates that:

$$\frac{\mathrm{d}}{\mathrm{d}t}\int_{\Omega_F}\boldsymbol{W}\,\mathrm{d}\Omega_F=\int_{\Omega_F}\frac{\partial\boldsymbol{W}}{\partial t}\,\mathrm{d}\Omega_F+\int_{S_F(t)}(\boldsymbol{W}\hat{\boldsymbol{v}})\cdot\boldsymbol{n}\,\mathrm{d}S_F(t),\tag{4.11}$$

with $\hat{\boldsymbol{v}}$ the velocity at the interface $S_F(t)$ of the control volume and $\boldsymbol{W}\hat{\boldsymbol{v}}=\begin{bmatrix}\rho\hat{\boldsymbol{v}} & \rho\boldsymbol{v}\otimes\hat{\boldsymbol{v}} & \rho E\hat{\boldsymbol{v}}\end{bmatrix}^T$ the flux exiting the control volume through the normal vector $\boldsymbol{n}$ pointing outwards. The integration over the control volume Ω_F of the local Equation (4.5) writes:

$$\int_{\Omega_F}\left[\frac{\partial\boldsymbol{W}}{\partial t}+\nabla\cdot\boldsymbol{\mathcal{F}}(\boldsymbol{W})\right]\,\mathrm{d}\Omega_F=0.\tag{4.12}$$

The application of the Green-Ostrogradsky theorem provides the relation:

$$\int_{\Omega_F}\left[\frac{\partial\boldsymbol{W}}{\partial t}+\nabla\cdot\boldsymbol{\mathcal{F}}(\boldsymbol{W})\right]\,\mathrm{d}\Omega_F=\int_{\Omega_F}\frac{\partial\boldsymbol{W}}{\partial t}\,\mathrm{d}\Omega_F+\int_{S_F(t)}\boldsymbol{\mathcal{F}}(\boldsymbol{W})\cdot\boldsymbol{n}\,\mathrm{d}S_F(t).\tag{4.13}$$

Thus, the second integral in (4.11) can be replaced by the integral of the flux of the conservative variables $\boldsymbol{W}$:

$$\int_{\Omega_F} \frac{\partial \boldsymbol{W}}{\partial t} \, \mathrm{d}\Omega_F = - \int_{S_F(t)} \boldsymbol{\mathcal{F}}(\boldsymbol{W}) \cdot \boldsymbol{n} \, \mathrm{d}S_F(t). \tag{4.14}$$

Finally, the integral formulation of the Navier-Stokes equations in ALE formulation is:

$$\frac{\mathrm{d}}{\mathrm{d}t} \int_{\Omega_F} \boldsymbol{W} \, \mathrm{d}\Omega_F + \int_{S_F(t)} \boldsymbol{\mathcal{F}}(\boldsymbol{W}, \hat{\boldsymbol{v}}) \cdot \boldsymbol{n} \, \mathrm{d}S_F(t) = 0, \tag{4.15}$$

with

$$\boldsymbol{\mathcal{F}}(\boldsymbol{W}, \hat{\boldsymbol{v}}) = \begin{bmatrix} \rho(\boldsymbol{v} - \hat{\boldsymbol{v}}) \\ \rho \boldsymbol{v} \otimes (\boldsymbol{v} - \hat{\boldsymbol{v}}) + p\mathbf{I} - \boldsymbol{\tau} \\ \rho E(\boldsymbol{v} - \hat{\boldsymbol{v}}) + p\boldsymbol{v} - \boldsymbol{\tau}\boldsymbol{v} + \boldsymbol{q} \end{bmatrix}. \tag{4.16}$$

4.2 Mesh deformation techniques

The structural deformation at the interface $\mathbf{u}_\Gamma$ has to be propagated inside the fluid computational domain to accommodate with the deformed position of the interface. The fluid mesh coordinates are denoted $\boldsymbol{\xi} = [\boldsymbol{\xi}_\mathrm{I}, \boldsymbol{\xi}_\Gamma]$ with $\boldsymbol{\xi}_\mathrm{I}$ the internal grid coordinates and $\boldsymbol{\xi}_\Gamma$ the fluid mesh coordinates on Γ, these latter satisfy $\boldsymbol{\xi}_\Gamma = \mathbf{u}_\Gamma$.

One approach to perform a mesh deformation is based on a structural analogy to propagate the deformation in the whole fluid domain [45]. The fluid domain is assimilated to a linear elastic material where prescribed displacements are imposed on the interface Γ. The analogous elastic material is characterized by a Young's modulus E and a Poisson's coefficient ν. The problem is formulated with a classical FE formulation as $\mathbf{K}_\mathrm{mesh}\boldsymbol{\xi} = \mathbf{0}$ in Ω_F with $\mathbf{K}_\mathrm{mesh}$ a stiffness matrix resulting from the assembly of all the local stiffness matrices, along with the constraint $\boldsymbol{\xi}_\Gamma = \mathbf{u}_\Gamma$. The stiffness in a fluid mesh cell $\mathbf{K}_k$ is defined by:

$$\mathbf{K}_k = \int_{\Omega_k} \mathbf{N}^T \mathbf{C} \mathbf{N} \, \mathrm{d}\Omega_k, \tag{4.17}$$

with $\mathbf{C}$ the linear isotropic elastic tensor. For 3D cases and using the Voigt notation, the tensor $\mathbf{C}$ is defined by:

$$\mathbf{C} = \frac{E}{(1+\nu)(1-2\nu)} \begin{pmatrix} 1-\nu & \nu & \nu & 0 & 0 & 0 \\ & 1-\nu & \nu & 0 & 0 & 0 \\ & & 1-\nu & 0 & 0 & 0 \\ & & & 1/2-\nu & 0 & 0 \\ & sym. & & & 1/2-\nu & 0 \\ & & & & & 1/2-\nu \end{pmatrix}. \tag{4.18}$$

The Young's modulus considered to build the stiffness matrix is however not uniform in the fluid domain but depends on the mesh metrics. It is a function of the cell volume, the idea is to increase the stiffness in the regions where the mesh is strongly refined, for instance in the fluid boundary layers at the walls. A common approach is to consider a Young's modulus inversely proportional to a power function of the mesh size. The total finite element problem is decomposed as:

$$\begin{bmatrix} \mathbf{K}_\mathrm{mesh}^\mathrm{II} & \mathbf{K}_\mathrm{mesh}^{\mathrm{I}\Gamma} \\ \mathbf{K}_\mathrm{mesh}^{\Gamma\mathrm{I}} & \mathbf{K}_\mathrm{mesh}^{\Gamma\Gamma} \end{bmatrix} \begin{bmatrix} \boldsymbol{\xi}_\mathrm{I} \\ \boldsymbol{\xi}_\Gamma \end{bmatrix} = \begin{bmatrix} \mathbf{0} \\ \mathbf{R}_\Gamma \end{bmatrix}, \tag{4.19}$$

with $\mathbf{R}_\Gamma$ the reaction on the fluid-structure interface Γ. Therefore, the internal displacements of the fluid mesh $\boldsymbol{\xi}_\mathrm{I}$ are obtained as the solution of the linear problem:

$$\mathbf{K}^{\mathrm{II}}_{\mathrm{mesh}}\boldsymbol{\xi}_\mathrm{I} = -\mathbf{K}^{\mathrm{I}\Gamma}_{\mathrm{mesh}}\boldsymbol{\xi}_\Gamma \tag{4.20}$$

To illustrate the method, Figure 4.2 shows the mesh deformation with structural analogy of a simple configuration meshed with tetrahedral elements. The white square representing the solid is subject to a translation, a rotation and a deformation. The mesh deformation with structural analogy is computed with the FEniCSx Finite Elements Python library.

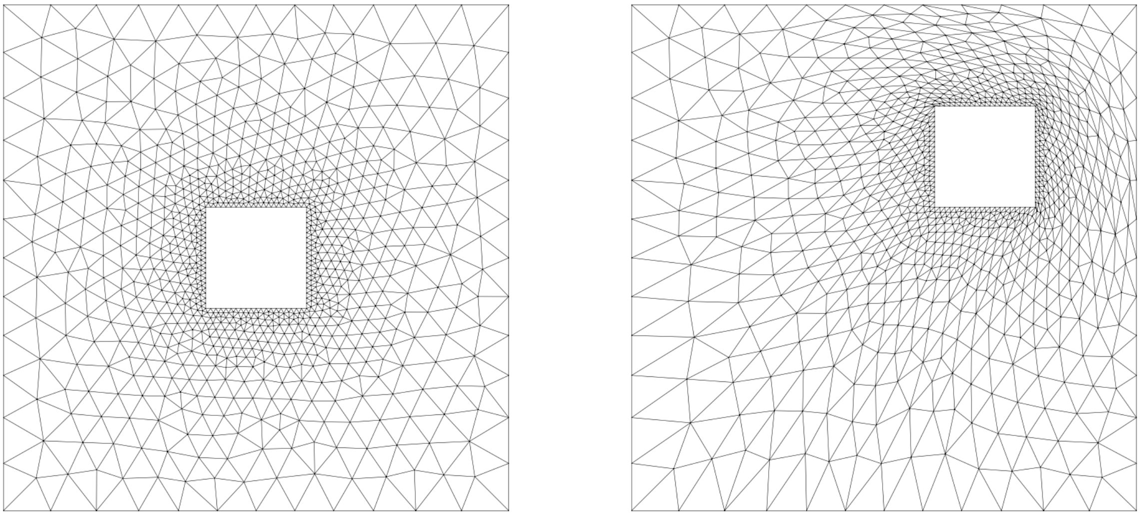

(a) Initial configuration

(b) Translation

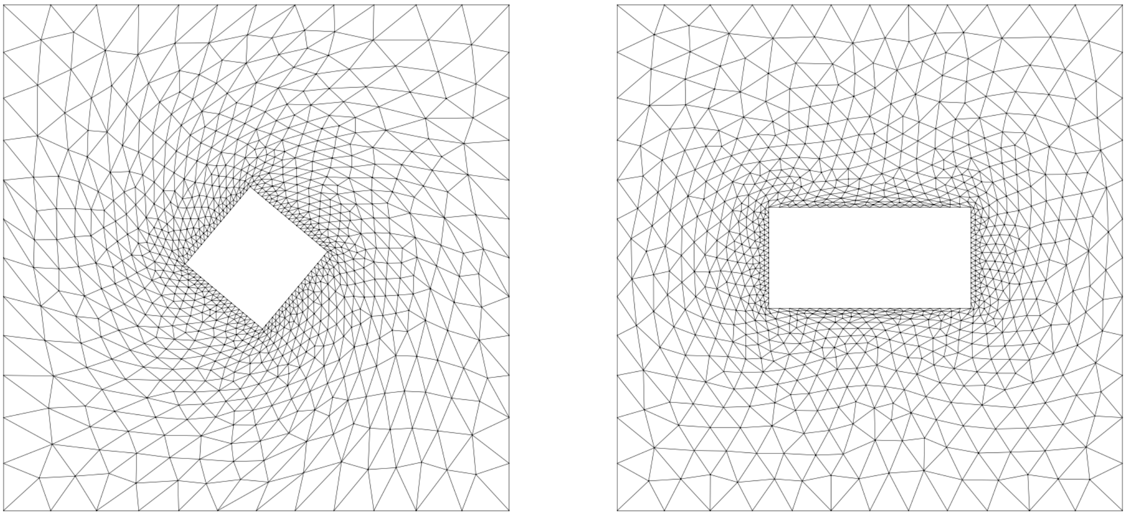

(c) Anti-clockwise rotation

(d) Axial stretching

Figure 4.2: Mesh deformation examples on a simple 2D configuration.

The mesh deformation with structural analogy of a more applicative case is represented in Figure 4.3. The case corresponds to a flexible beam attached to a fixed cylinder. The fluid domain is meshed with a structured grid. The mesh deformation displayed corresponds to a structural displacement with the shape of the 5th mode of the beam.

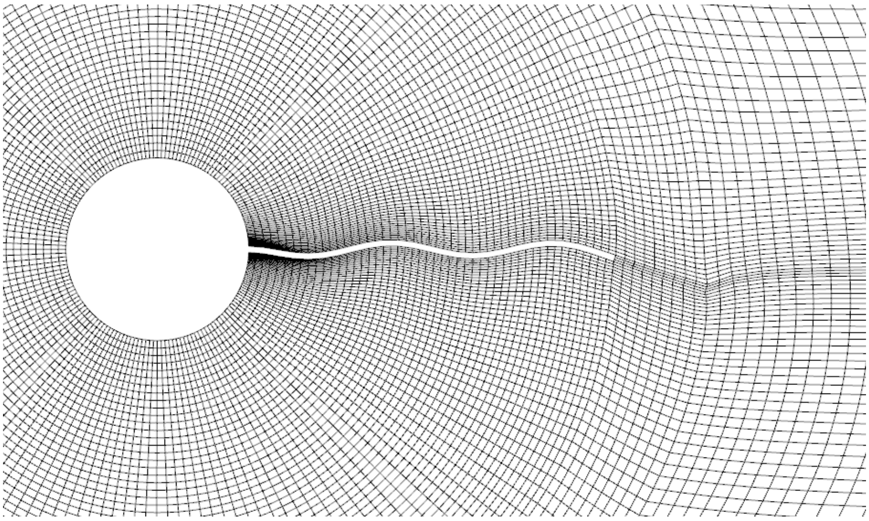

Figure 4.3: Fluid mesh deformation for the case of a beam attached to a fixed cylinder. The shape of the structural deformation corresponds to the 5th mode of the beam.

Other mesh deformation approaches are found in the literature. For instance, the TransFinite Interpolation (TFI) method [60] is an analytical method for the deformation of structured meshes using interpolation functions depending on the curvilinear coordinates of the mesh and matching exactly the displacements at the interface. Since the method is analytical, the computational time of the mesh deformation is minimal. Radial Basis Functions (RBF) are also relevant for mesh deformation [32]. The mesh deformation $\boldsymbol{\xi}(\boldsymbol{x})$ for a point $\boldsymbol{x}$ in space is given by:

$$\boldsymbol{\xi}(\boldsymbol{x}) = \sum_{i=1}^{N} \alpha_i \phi(||\boldsymbol{x} - \boldsymbol{x}_{\Gamma,i}||) + p(\boldsymbol{x}), \tag{4.21}$$

with $\phi(\boldsymbol{x})$ the radial basis kernel functions with a compact support, $p(\boldsymbol{x})$ a polynomial function and α_i weighting coefficients determined from the N known displacements $\boldsymbol{\xi}(\boldsymbol{x}_{\Gamma,i})$ at the interface (additional control points can also be considered). The mesh deformation can also be computed based on a distance metric d with the Inverse Distance Weighting (IDW) method [207]. In such method, the mesh deformation is evaluated as follows:

$$\boldsymbol{\xi}(\boldsymbol{x}) = \begin{cases} \dfrac{\sum_{i=1}^{N} w_i(\boldsymbol{x}) \boldsymbol{\xi}_{\Gamma,i}}{\sum_{i=1}^{N} w_i(\boldsymbol{x})} & \text{if } \ \forall i \ \ d(\boldsymbol{x}, \boldsymbol{x}_{\Gamma,i}) \neq 0 \\ \\ \boldsymbol{\xi}_{\Gamma,i} & \text{else} \end{cases} \tag{4.22}$$

with $\boldsymbol{\xi}_{\Gamma,i} = \boldsymbol{\xi}(\boldsymbol{x}_{\Gamma,i})$ and $w_i(\boldsymbol{x}) = 1/d(\boldsymbol{x}, \boldsymbol{x}_{\Gamma,i})^p$ where p is a positive integer power monitoring the influence of the distance on the weighting coefficient. To handle large displacements and rotations, a mesh deformation method based on quaternions is also proposed in [119].

4.3 Coupling procedures to couple the solvers

The numerical computation of fluid-structure interaction problems is challenging since the dynamics of the structure and of the fluid are intertwined. The boundary condition for the fluid is the structural displacement and the boundary conditions for the structure are the fluid loads. Besides, in the ALE formulation, the mesh deformation in the fluid domain due to the structural displacement should also be computed. In the literature, two fundamentally different approaches are implemented to solve a fluid-structure interaction problem [82]. On the one hand, the idea is to compute all the physics simultaneously in one large system. This approach is called the monolithic approach. The equations for the fluid, the structure, the mesh deformation and the transfers of loads and displacements are all gathered in one single system. On the other hand, the partitioned approach consists of two different solvers for the fluid and the structure. The two solvers exchange the necessary boundary conditions to one another in a specific integration sequence for each time increment. Figure 4.4 illustrates both approaches with simplified diagrams.

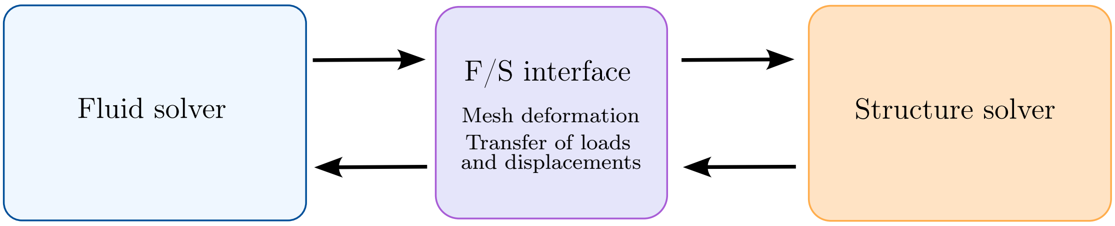

(a) Partitioned coupling

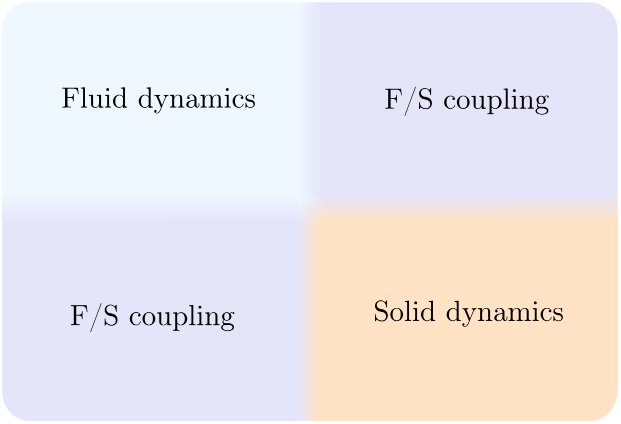

(b) Monolithic coupling

Figure 4.4: Schematic representation of the monolithic and partitioned coupling approaches.

The following paragraphs provide a short introduction to both methods with their respective advantages and drawbacks.

Monolithic approach

As mentioned above, the monolithic approach consists of the implicit resolution of a single system gathering the equations for the fluid, the structure, the mesh deformation and the transfers. Thus, all the components of the coupling are solved simultaneously in a single time increment loop, ensuring the stability and convergence of the coupling. The implicit formulation of the system also allows time steps that are not excessively small. Examples of fluid-structure interaction problems solved with the monolithic approach can be found in [76, 82, 83, 194]. The drawback of monolithic approaches is that it leads to nonlinear systems of large dimensions with values spanning several orders of magnitude corresponding to the different physics, at the expense of the condition number of the system. It is common to normalize the equations to obtain non-dimensional quantities to help the numerical resolution and to highlight physical phenomena according to the mass ratios. Nonetheless, the computation of the large linear systems in the nonlinear resolution loop is a challenge for monolithic approaches [40, 63, 76, 156]. Iterative methods such as GMRES (Generalized Minimal Residual) algorithms are commonly used along with specific preconditioners adapted to the particular shape of the matrix of the system.

Partitioned approach

In a partitioned coupling, different solvers are considered for the fluid and the structure. This allows for more modularity between the solvers. Besides, another advantage is that there is a dedicated solver for each physics, in which all the desired complexity can be easier integrated, which is cumbersome with a monolithic solver. The easiest partitioned coupling consists in alternating the fluid and the structure computations once per time step. This approach is called weak coupling or loosely-coupled approach. Two examples of loosely-coupled algorithms are illustrated in Figure 4.5.

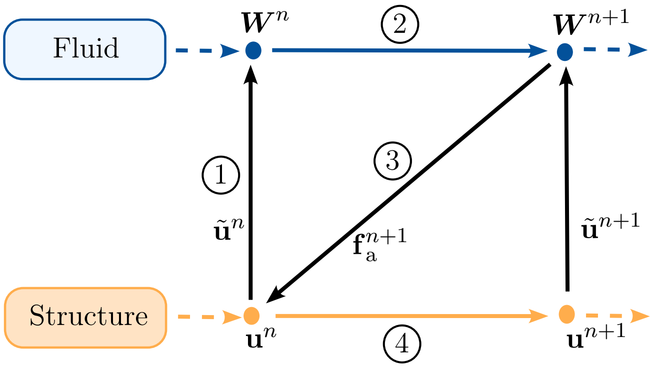

(a) Conventional serial weak coupling procedure

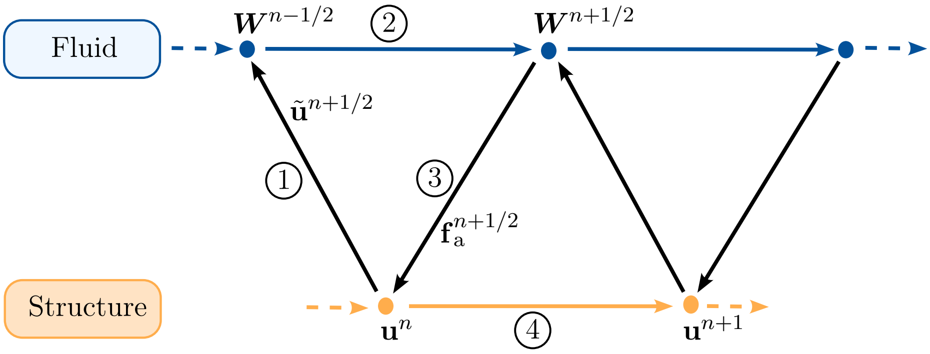

(b) Non-collocated weak coupling procedure with offset of half-a-time-step

Figure 4.5: Examples of weak coupling algorithms. The serial weak coupling (a) and the non-collocated weak coupling (b) procedures.

The fluid solver receives a prediction $\tilde{\mathbf{u}}$ of the structural displacement, computes the new conservative variables $\boldsymbol{W}$ and returns the actualized aerodynamic forces $\mathbf{f}_\mathrm{a}$ to the structural solver. A relaxation for the aerodynamic forces is sometimes suggested in the literature. Several choices for the prediction $\tilde{\mathbf{u}}$ are available in the literature. In [53], the author demonstrates that with proper integration schemes and expressions for the prediction, the loosely-coupled algorithms can satisfy second-order temporal accuracy without additional sub-iterations. Examples of weak coupling algorithms are for instance found in [55, 82] and in [51, 53, 147] with applications to aeroelastic configurations in the latters. A FSI application with large structural displacements is tackled in [184]. The weak coupling schemes presented in Figure 4.5 result in a temporal shift between the two solvers [147]. The fluid-structure interface conditions in velocity, displacement and stresses do not match exactly between the two solvers at each time step of the coupling. The convergence of the total fluid-structure problem is not guaranteed, which may lead to a loss of stability, of accuracy and the numerical solution to diverge from the physical solution. Besides, the temporal shift between the solvers can result in a purely numeric addition of energy to the system since the work exchanged between the two solvers is not perfectly balanced [147], which leads to added-mass instabilities [24, 59].

Parallel partitioned algorithms are also proposed in the literature. Figure 4.6 illustrates a simple parallel coupling algorithm. The fluid and structural solvers do not wait for their counterpart to actualize their variables according to the information they just provided, both solvers run at the same time. The two solvers only communicate with one another at given time intervals. Such coupling methods reduce significantly the computational time at the expense of a slight loss of accuracy. Variants of the parallel coupling shown in Figure 4.6 are for instance described in [51, 55], including sub-cycling to improve the accuracy.

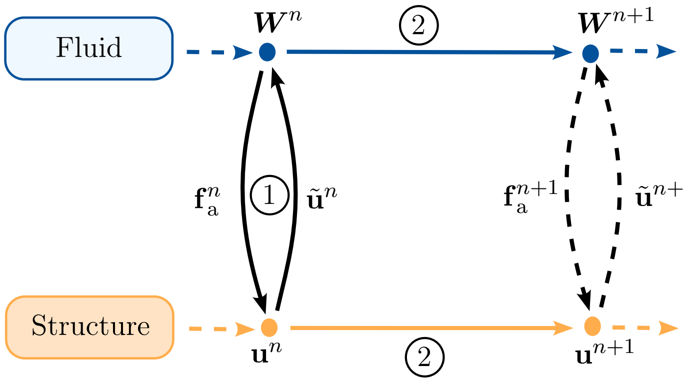

Figure 4.6: Example of parallel coupling between the fluid and structural solvers.

To satisfy the conditions at the fluid-structure interface and control the convergence of the global fluid-structure problem, an implicit partitioned coupling (also called strong coupling) is common. The approach consists of adding coupling sub-iterations within the same time step. Figure 4.7 illustrates the principle of a strong coupling with coupling sub-iterations before computing the next time step.

It is convenient for those sub-iterations to be fixed-point iterations between the solvers such as in [5, 13, 41, 121]. Nevertheless, other methods are possible such as a Gauss-Seidel procedure [96] or, as described in [5], the use of Robin-Neumann conditions with semi-implicit or implicit coupling. Another possibility is Newton-Raphson iterations on the global fluid-structure problem [56] where each physics is also converged independently before the Newton correction. It is less common since the cross jacobian operators are either not available or approximated by finite differences or simplified expressions. The paper ([56]) provides a strategy to better evaluate those operators. The main advantages of the implicit partitioned coupling with sub-iterations are that the convergence is controlled and that it is not prone to added-mass instabilities. Nevertheless, in some cases the number of sub-iterations necessary to satisfy a given convergence criterion might be particularly large [77], increasing the computational cost of the method. In chapter 5, a strong coupling is

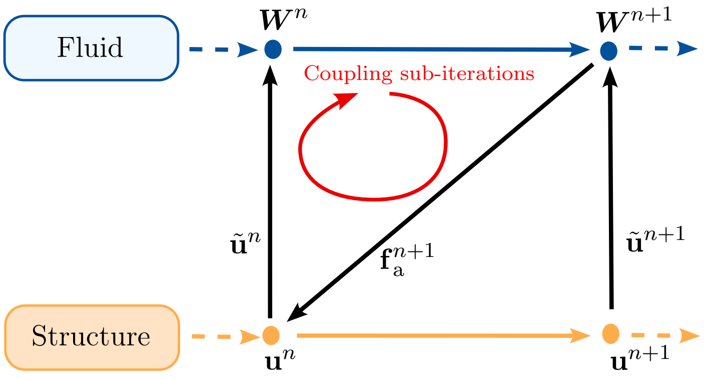

Figure 4.7: Strong parallel coupling between the fluid and structural solvers.

considered with fixed-point sub-iterations between the fluid and structure solvers in a single time step. The different steps of such a partitioned coupling are summarized in flowchart 4.8.

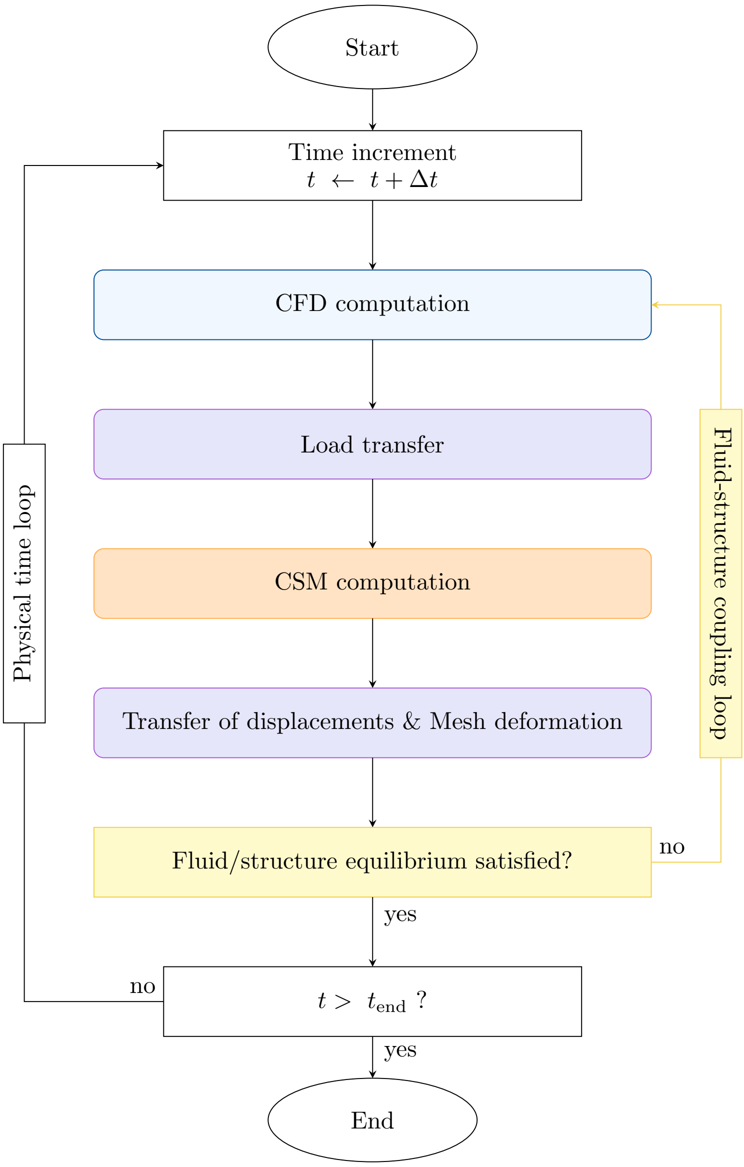

Figure 4.8: The different steps of the partitioned coupling method used in this work.

It is worth mentioning that for both the monolithic and the partitioned approaches, the transmission of the information between the fluid and structural equations is not straightforward since the meshes are different in general. The transfers of loads from the fluid to the structure and of displacements from the structure to the fluid require interpolation techniques between the meshes [13, 33, 52]. Examples of transfer methods are presented in the next section.

4.4 Transfer of the loads and displacements from one mesh to the other

It is common in fluid-structure applications that the meshes for the structure and for the fluid do not match. For instance, one can consider an unstructured tetrahedral mesh for the structure and a structured mesh for the fluid solver. Besides, the local refinements for the structural FE solver and for the Finite Volume fluid solver are different. Thus, the fluid and structural meshes are not coinciding at the interface. The structural displacements at the interface with the fluid should be translated in the fluid mesh boundary. Conversely, the loads of the fluid on the structure's skin have to be transferred to the nodes of the FE structural mesh.

4.4.1 Transfer of the structural displacement of the structural mesh to the aerodynamic mesh

When the fluid and structural meshes do not match at the fluid-structure interface, it is necessary to translate the structural displacements to the fluid mesh to update the boundary condition. To this end, an interpolation via Radial Basis Functions is suitable [10, 14, 169, 206]. We consider N points $\boldsymbol{x}_{s,i} = (x_{s,i}, y_{s,i}, z_{s,i})^T$ in space corresponding to initial position of the structural nodes on the interface and $\hat{\boldsymbol{x}}_{s,i} = (\hat{x}_{s,i}, \hat{y}_{s,i}, \hat{z}_{s,i})^T$ the known displacements at those nodes. Considering a point $\boldsymbol{x} = (x, y, z)^T$ on the fluid boundary, the idea is to interpolate the displacement, for a given direction of space (x, y or z), with a function $f(\boldsymbol{x})$ defined as follows:

$$\begin{cases} f(\boldsymbol{x}) & = \displaystyle\sum_{i=1}^{N} c_i \phi(||\boldsymbol{x} - \boldsymbol{x}_{s,i}||) + p(\boldsymbol{x}), \\ f(\boldsymbol{x}_{s,i}) & = d_i \quad \forall i \in [1, N], \end{cases} \tag{4.23}$$

where d_i is $\hat{x}_{s,i}, \hat{y}_{s,i}$ or $\hat{z}_{s,i}$ according to the direction of space considered, $||\boldsymbol{x} - \boldsymbol{x}_{s,i}||$ is the distance between the point $\boldsymbol{x}$ and the point $\boldsymbol{x}_{s,i}$, ϕ is a radial basis function and $p(\boldsymbol{x})$ is a polynomial. To guarantee the uniqueness of the solution, a constraint on the coefficients c_i is added. For all polynomial p_j of degree inferior or equal to the degree of the polynomial p, the coefficients c_i must satisfy the relation:

$$\sum_{i=1}^{N} c_i p_j(\boldsymbol{x}) = 0. \tag{4.24}$$

Several kernel functions are available for ϕ, the most common are presented in Table 4.1 where r represents the distance.

There are conditions on the degree of the polynomial depending on the positiveness conditions of the kernel function and the uniqueness of the solution. For conditionally positive RBF of second order such as the Thin Plate Spline, the polynomial p has to be linear:

$$p(\boldsymbol{x}) = \alpha_0 + \alpha_1 x + \alpha_2 y + \alpha_3 z. \tag{4.25}$$

Name	Kernel function
Volume Spline	$f(r) = r$
Thin Plate Spline	$f(r) = r^2 \log(r)$
Gaussian	$f(r) = \exp(-r^2)$
Inverse multiquadrics	$f(r) = \dfrac{1}{1+r^2}$
Wendland	$f(r) = \begin{cases} (1-r)^4(4r+1), & 0 \leq r \leq 1 \\ 0 & \text{else} \end{cases}$

Table 4.1: Common radial basis functions.

So far, no direction of space was specified in the description of the method but the coefficients should be computed along the x, y and z directions. In practice, there are different coefficients $\boldsymbol{c}^x = (c_i^x)_{i\in[1,N]}$, $\boldsymbol{c}^y = (c_i^y)_{i\in[1,N]}$, $\boldsymbol{c}^z = (c_i^z)_{i\in[1,N]}$ and $\boldsymbol{\alpha}^x = (\alpha_i^x)_{i\in[1,N]}$, $\boldsymbol{\alpha}^y = (\alpha_i^y)_{i\in[1,N]}$, $\boldsymbol{\alpha}^z = (\alpha_i^z)_{i\in[1,N]}$ to compute in order to recover the total displacement in space. Considering the direction x for instance, the system to solve to determine the coefficients $\boldsymbol{c}^x$ and $\boldsymbol{\alpha}^x$ is the following:

$$\begin{bmatrix} \mathbf{0} & \boldsymbol{P} \\ \boldsymbol{P}^T & \boldsymbol{A} \end{bmatrix} \begin{bmatrix} \boldsymbol{\alpha}^x \\ \boldsymbol{c}^x \end{bmatrix} = \begin{bmatrix} \mathbf{0} \\ \boldsymbol{d}^x \end{bmatrix}, \tag{4.26}$$

where the coefficients of the matrix $\boldsymbol{A} = (A_{ij\,(i,j)\in[1,N]^2})$ are defined by $A_{ij} = \phi(||\boldsymbol{x}_{s,i} - \boldsymbol{x}_{s,j}||)$, the vector $\boldsymbol{d}^x$ in the second member is $\boldsymbol{d}^x = (\hat{x}_{s,1}, \cdots \hat{x}_{s,N})^T$ and the expression of the matrix $\boldsymbol{P}$ is the following:

$$\boldsymbol{P} = \begin{bmatrix} 1 & 1 & \cdots & 1 \\ x_{s,1} & x_{s,2} & \cdots & x_{s,N} \\ y_{s,1} & y_{s,2} & \cdots & y_{s,N} \\ z_{s,1} & z_{s,2} & \cdots & z_{s,N} \end{bmatrix}. \tag{4.27}$$

It is important to mention that the system (4.26) can only be solved if the control points $\boldsymbol{x}$ are not all coplanar. Likewise, the coefficients $(\boldsymbol{c}^y, \boldsymbol{\alpha}^y)$ and $(\boldsymbol{c}^z, \boldsymbol{\alpha}^z)$ are obtained by solving the system (4.26) in which $\boldsymbol{d}^x$ is replaced respectively by $\boldsymbol{d}^y = (\hat{y}_{s,1}, \cdots \hat{y}_{s,N})^T$ and by $\boldsymbol{d}^z = (\hat{z}_{s,1}, \cdots \hat{z}_{s,N})^T$. Finally, the interpolated displacement $\hat{\boldsymbol{x}} = (\hat{x}, \hat{y}, \hat{z})^T$ for any point $\boldsymbol{x}$ on the fluid mesh boundary is obtained by:

$$\hat{\boldsymbol{x}} = \begin{bmatrix} \hat{x} \\ \hat{y} \\ \hat{z} \end{bmatrix} = \begin{bmatrix} x + \sum_{i=1}^{N} c_i^x \phi(||\boldsymbol{x} - \boldsymbol{x}_{s,i}||) + \alpha_0^x + \alpha_1^x + \alpha_2^x + \alpha_3^x \\ y + \sum_{i=1}^{N} c_i^y \phi(||\boldsymbol{x} - \boldsymbol{x}_{s,i}||) + \alpha_0^y + \alpha_1^y + \alpha_2^y + \alpha_3^y \\ z + \sum_{i=1}^{N} c_i^z \phi(||\boldsymbol{x} - \boldsymbol{x}_{s,i}||) + \alpha_0^z + \alpha_1^z + \alpha_2^z + \alpha_3^z \end{bmatrix}. \tag{4.28}$$

Figure 4.9 illustrates the interpolation of the structural displacement to the fluid mesh on an arbitrary displacement. In the example, the structural mesh considered is the tetrahedral mesh while the fluid mesh is built with quadrangle elements. The initial meshes are colored in gray and the deformed meshes in green. The initial positions of the structural nodes are plotted in red (●) and their position after displacement in blue (●). The movement imposed on the structural nodes is arbitrary and voluntarily exaggerated. The interpolation of the displacement on the fluid mesh is performed with Thin Plate Spline RBF functions. This didactic test case shows the ability of RBF methods to interpolate smoothly the fluid mesh displacement from a given structural displacement.

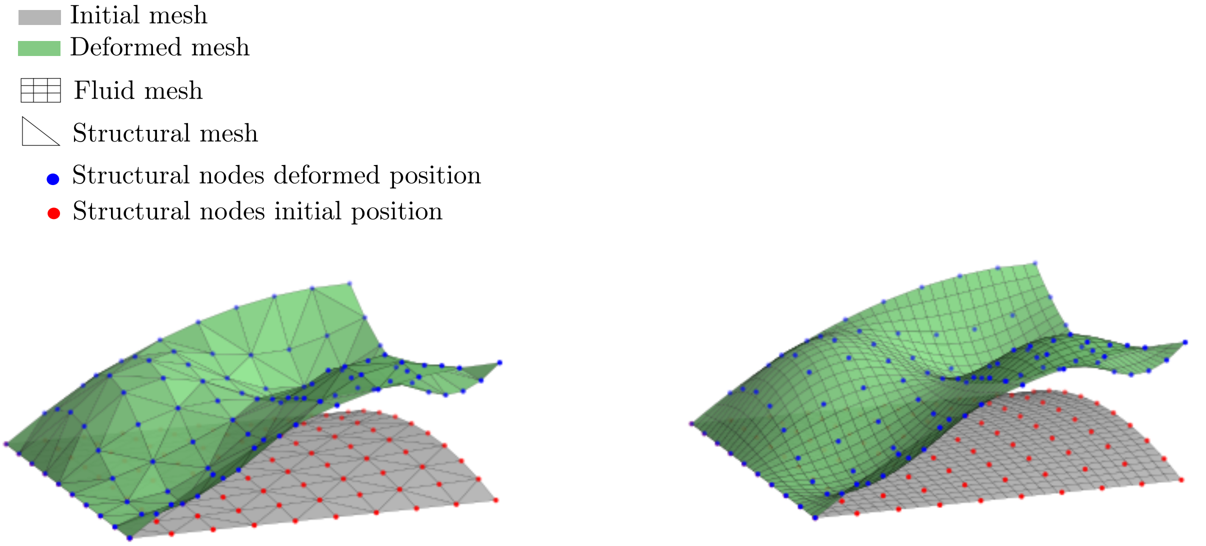

Structural mesh deformation

Fluid mesh interpolation with RBF

Figure 4.9: Example of interpolation of the structural displacement to the fluid mesh with RBF functions (Thin Plate Spline kernel functions here).

4.4.2 Transfer of the fluid loads to the structure

To compute the response of the structure to the fluid loads on the interface, it is necessary to translate those loads to the FE structural mesh as illustrated in Figure 4.10.

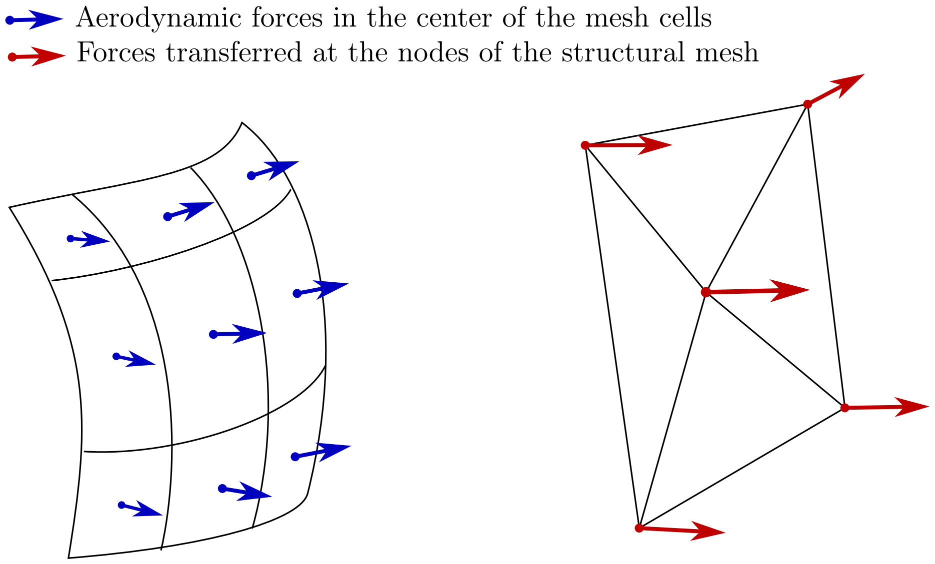

Mesh of the fluid

Mesh of the structure

Figure 4.10: Schematic representation of the load transfer between the fluid and the structural meshes.

Several methods exist in the literature such as projections [115], interpolations or the use of spline functions [10, 186]. The most commonly used for aeroelastic computations are the Nearest-Neighbor Interpolation, the Weighted Residual Method and the RBF interpolation [33, 34, 52]. A conservative transfer consists in preserving the energy over the interface [52], which implies a mathematical relation between the operator transferring the structural displacement to the fluid mesh and conversely the operator transferring the fluid loads to the structural mesh [34]. When the transfer operators do not satisfy this mathematical relation but require constant forces and displacements to be exactly interpolated across the interface, the approach is referred to as consistent [34]. In the present work, the transfer method consists in equalizing the virtual works between the fluid mesh grid $\mathcal{G}_\mathrm{F}$ and the structural grid $\mathcal{G}_\mathrm{S}$. Writing N the number of nodes of the structural grid, we choose a basis of admissible displacement fields $\{\boldsymbol{\delta u}_i\}_{i\in[1,N]}$ and write the equality between the work of the fluid load $\mathbf{f_a}$ and the loads on the structure $\mathbf{f_s}$ for each of the displacement fields $\{\boldsymbol{\delta u}_i\}_{i\in[1,N]}$:

$$\forall i \in [1,N], \quad \delta W_i^{\mathcal{G}_\mathrm{F}} = \delta W_i^{\mathcal{G}_\mathrm{S}}, \tag{4.29}$$

with $\delta W_i^{\mathcal{G}_\mathrm{F}}$ and $\delta W_i^{\mathcal{G}_\mathrm{S}}$ the virtual works associated respectively to the loads on the fluid and structural meshes. The virtual work is the sum of the scalar products between the loads and the virtual displacements at every point of the meshes. The chosen basis of admissible functions $\{\boldsymbol{\delta u}_i\}_{i\in[1,N]}$ consists of RBF functions defined on the structural grid. Each RBF function $\boldsymbol{\delta u}_i$ is built on the structural grid with a unitary displacement at the node P_i of the structural grid and null at the other nodes. Thus, the N functions $\{\boldsymbol{\delta u}_i\}_{i\in[1,N]}$ are built with the N nodes of the structural grid thanks to the resolutions of a smoothing system (4.26). Eventually, the expression of each function $\boldsymbol{\delta u}_i$ is the following:

$$\boldsymbol{\delta u}_i = \begin{pmatrix} \delta u_i^x \\ \delta u_i^y \\ \delta u_i^z \end{pmatrix} = \begin{pmatrix} \displaystyle\sum_{j=1}^{N} c_i^x \phi(||\boldsymbol{x} - \boldsymbol{x}_{s,i}||) + \alpha_0^x + \alpha_1^x x + \alpha_2^x y + \alpha_3^x z \\ \displaystyle\sum_{j=1}^{N} c_i^y \phi(||\boldsymbol{x} - \boldsymbol{x}_{s,i}||) + \alpha_0^y + \alpha_1^y x + \alpha_2^y y + \alpha_3^y z \\ \displaystyle\sum_{j=1}^{N} c_i^z \phi(||\boldsymbol{x} - \boldsymbol{x}_{s,i}||) + \alpha_0^z + \alpha_1^z x + \alpha_2^z y + \alpha_3^z z \end{pmatrix}. \tag{4.30}$$

Those functions are defined analytically. Therefore, the projection of the fluid loads on them is possible at every point of the fluid mesh, leading to the system (4.29) for each function $\boldsymbol{\delta u}_i$. The resolution of those equations provides the interpolation of the loads from the fluid mesh to the nodes of the structural mesh. Besides, it can be shown that this transfer method preserves the total loads and torques.

4.5 Conclusion of the chapter

This chapter presented a brief theoretical background for fluid-structure interaction applications. The equations relative to the fluid were introduced in the frame of a moving mesh via the ALE formulation. Common mesh deformation techniques were subsequently introduced. Then, different coupling procedures were briefly introduced, with a focus on the coupling scheme chosen in this work which is a partitioned strong coupling with fixed-point sub-iterations. Since the fluid and structural meshes do not coincide, transfer methods between the structural and fluid meshes were finally described: the transfer of displacements on one side and of loads on the other. Some theoretical aspects described in this chapter are applied in the following chapter to treat a 2D case of fluid-structure interaction, where the reduced order model developed in section 2.2 is considered for the structural solver.

Chapter 5

Application to the fluid-structure coupling on a two-dimensional example

The purpose of this chapter is to study the efficiency of the ICDual ROM in the frame of fluid-structure interaction. Indeed, aerodynamic forces are complex, distributed and follower loads. The test case of interest consists in placing the beam studied in section 2.3.2 in the wake of a fixed cylinder. The vortex street behind the cylinder triggers the nonlinear vibrations of the beam. First, the vortex street behind an isolated cylinder is analyzed, then the beam is placed behind the cylinder and a partitioned coupling is performed. Finally, the behavior of the system in a range of Reynolds numbers is investigated and a lock-in region is observed both with the full order and the reduced order model. The results of this chapter are published in the following journal paper [58].

Contents

5.1 Numerical setup

The boundary conditions of the test case are depicted in Figure 5.1. A no-slip adiabatic wall condition is imposed to the fluid on the surface of the fixed cylinder and of the flexible beam. Non-reflecting boundary conditions with a constant axial velocity are imposed at the inlet and outlet borders. The upper and lower boundary conditions are chosen far enough from the structure in order to avoid confinement effects that would impact the vortex shedding behind the cylinder. At those walls, slip boundary conditions are imposed unlike in [194] where no-slip boundary conditions are applied. With upper and lower slip boundary conditions, the case without the beam placed behind the cylinder produces the classical von Kármán vortex street. This first case is considered in section 5.2. The Strouhal number associated to this vortex shedding will be compared to Roshko's Strouhal number relation [165] to validate the representativeness of the test case.

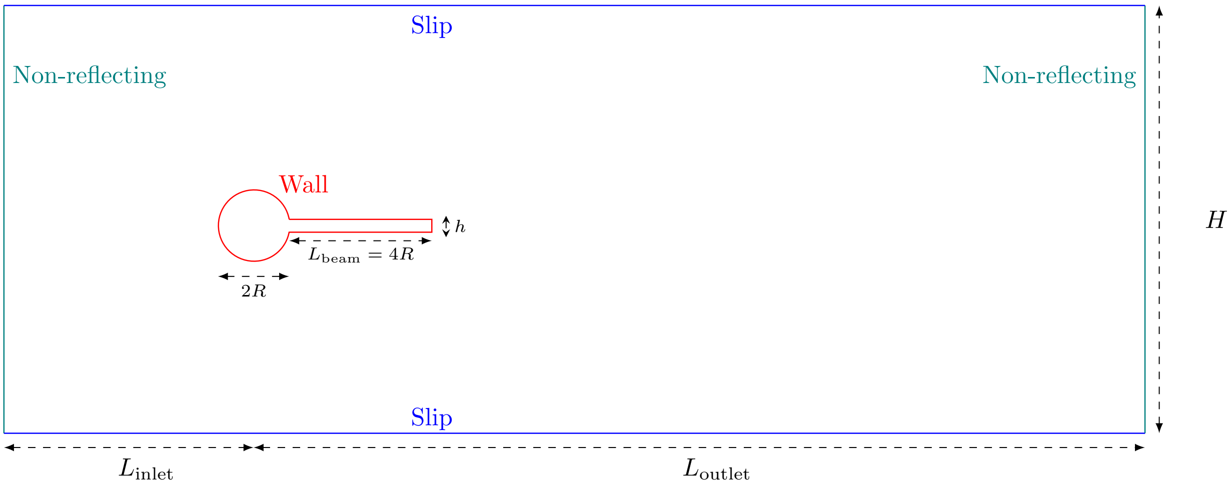

Figure 5.1: Computational domain and boundary condition of the fluid-structure interaction test case.

The structured fluid mesh is illustrated in Figures 5.2 and 5.3. The mesh is refined around the structure and in the near wake, then is progressively coarsened from the structure to the external domain boundaries.

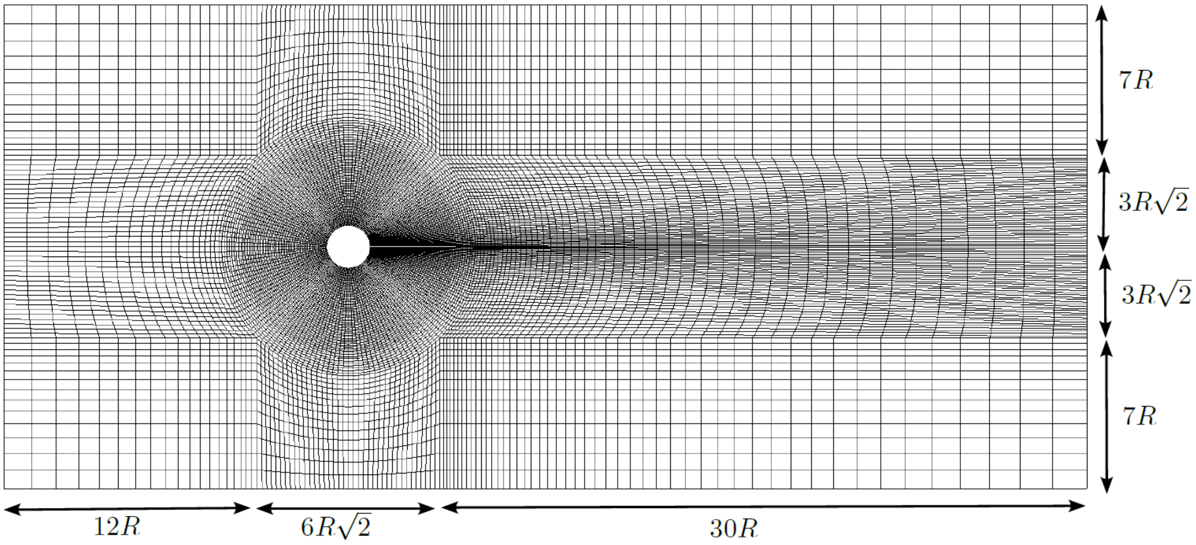

Figure 5.2: Mesh and dimensions of the fluid domain around the cylinder and the beam.

The Finite Volume CFD software *elsA* [19] (ONERA-Safran property) is considered to solve the fluid dynamics. We chose this CFD solver to anticipate industrial aeroelastic applications. A diatomic gas model is chosen, following the perfect gas equations. Its properties are detailed in Table 5.1. The density of the fluid is deduced from the perfect gas equation:

$$\rho_\infty = \frac{p_\infty}{R_{\text{specific}}\, T_\infty} = 1.17 \text{ kg.m}^{-3}. \tag{5.1}$$

The viscosity μ_∞ is set to 0.4 Pa.s to have the targeted Reynolds number with a reasonable inlet velocity (equivalent to Mach number 0.1) and a given diameter D:

$$Re = \frac{\rho_\infty U_\infty D}{\mu_\infty} = 200. \tag{5.2}$$

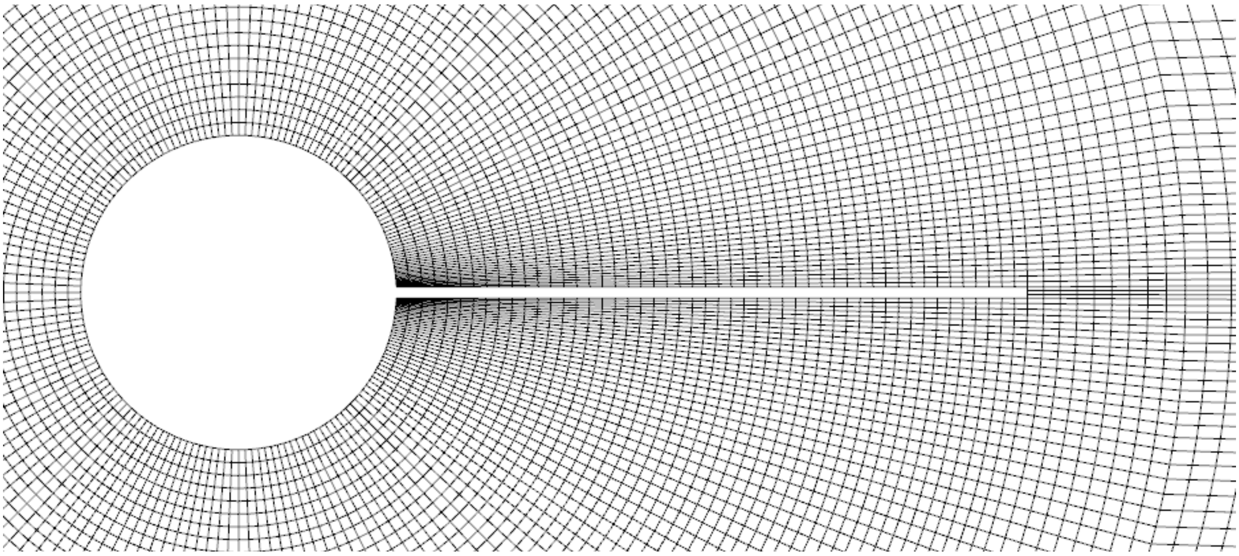

Figure 5.3: Focus of the mesh in the close vicinity of the cylinder and the beam. The beam thickness is discretized with 3 Finite Volumes cells.

Physical quantity	**Value**
T_∞	300 K
p_∞	101,325 Pa
γ	1.4
R_{specific}	287.053 J.kg^{-1}.K^{-1}
$c_v = \frac{5}{2}R_{\text{specific}}$	717 J.kg^{-1}.K^{-1}

Table 5.1: Fluid properties for the flow around the cylinder.

The convective fluxes are approximated by the AUSM+ (P) MiLES scheme [113, 120] to benefit from its low dissipation property and its ability to model low-Mach boundary layer flows. The time step for unsteady simulations is $\mathrm{d}t = 4.11 \times 10^{-3}$ s. The time integration for the fluid is performed with the multi-step Gear method [61, 62].

5.2 Von Kármán vortices in the wake of the cylinder without beam

In this section, we consider only the fixed cylinder, without the beam. This test case is a common application in fluid dynamics. The idea is to check that the CFD solver accurately captures the fluid dynamics at the Reynolds number considered. As illustrated by figure 5.4 a typical von Kármán vortex street develops in the wake of the cylinder. The dimensionless Strouhal number St defined below characterizes the flow periodicity based on the vortex shedding frequency F_s, the characteristic length (diameter cylinder D) and the inflow velocity U_∞ as :

$$St = \frac{F_s D}{U_\infty}. \tag{5.3}$$

For the flow around the cylinder, the Strouhal number can be evaluated by the relation $St = 0.212 - 2.7/Re$ proposed by Roshko [165] based on experimental data in the range $200 \leq Re \leq 2,000$.

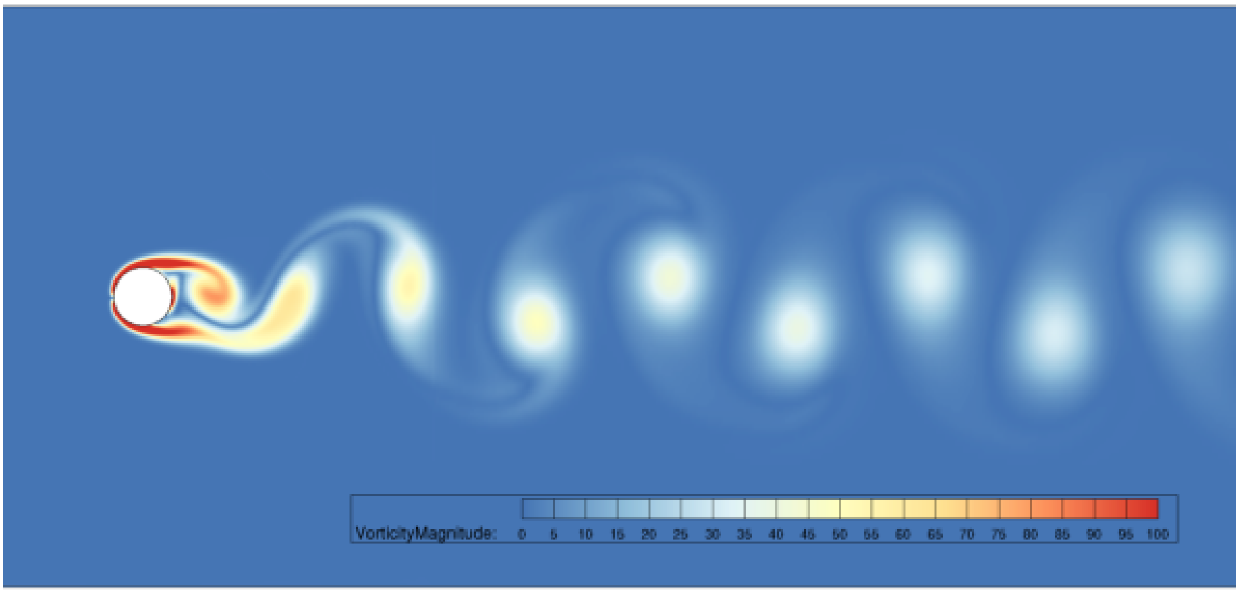

Figure 5.4: Von Kármán vortices in the wake of the fixed cylinder. Visualization of the vorticity magnitude.

Figures 5.5a and 5.5b represent respectively the drag and lift forces that the cylinder undergoes. The periodic oscillations of the vortex emissions can be observed in those figures. For each oscillation of the lift force F_y, two counter-rotating vortices are shed. Thus, the oscillation frequency of the drag force F_x is twice the oscillation frequency of F_y. With the shedding frequency $F_s = 3.42$ Hz evaluated from the lift force, the Strouhal number obtained with the present simulation is St $=$ 0.197 which is very close to the value $St = 0.212 - 2.7/Re = 0.198$ provided by Roshko's relation for Re $=$ 200. This validates the numerical fluid model which is then extended in the next section to a fluid-structure interaction case.

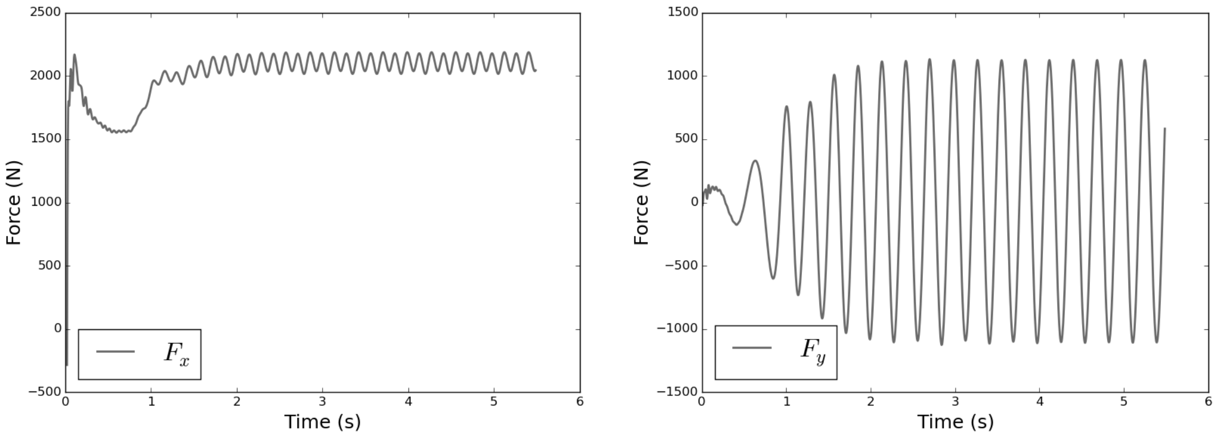

(a) Drag force F_x

(b) Lift force F_y

Figure 5.5: Aerodynamic drag (a) and lift (b) forces on the cylinder resulting from the vortex shedding in the wake.

5.3 Fluid-structure interaction between a flexible beam and the wake of the cylinder

The flexible beam studied in section 2.3.2 is now placed in the wake of the fixed cylinder. The movement of a flexible beam triggered by the vortices has already been studied in [188, 194] on a similar test case. A first approach presented in Appendix A consisted in a monolithic FE computation of the test case considered with an incompressible fluid and a 2D Saint Venant-Kirchhoff formulation for the structure. In the present chapter, the idea is to compute the same fluid-structure interaction application with a partitioned approach, a compressible formulation for the fluid equation and the beam model studied in section 2.3 for the structure. The structural full order model is replaced by the ROM developed previously in order to facilitate the coupling while including a nonlinear effect in the structure. Partitioned approaches are often preferred to monolithic ones to tackle large industrial applications. Indeed, there are dedicated solvers for each physics, which would be difficult to manage in a single monolithic algorithm, the latter requiring tremendous memory resources.

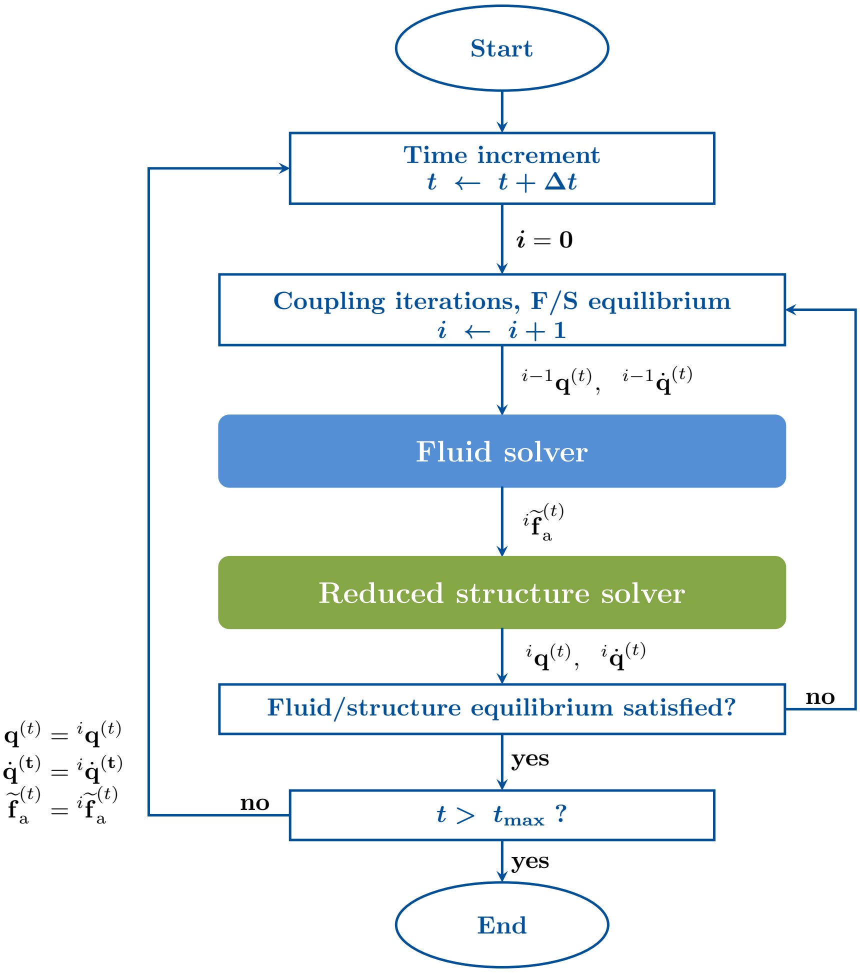

Figure 5.6: Partitioned coupling procedure between the fluid solver and the nonlinear reduced structural solver. The projection of the aerodynamics forces in the reduced basis is denoted here by $\widetilde{\mathbf{f}}_{\mathrm{a}} = \mathbf{V}^T \mathbf{f}_{\mathrm{a}}$.

The displacements on the beam's wet surface are interpolated from the displacements and rotations of the neutral axis. The axial discretization of the beam is the same as the axial local fluid mesh at the skin of the beam. As a result, no specific load transfer method is needed to propagate the aerodynamic forces from the fluid mesh to the structural one. The first linear mode eigenfrequency is equal to 3.37 Hz which is very close to the frequency of the vortex shedding (3.42Hz). No structural damping was introduced in order to reach high amplitudes of deformation. The partitioned coupling procedure between the fluid solver and the structural nonlinear ROM is summarized in the flowchart Figure 5.6. The CFD computation and the mesh deformation are computed by the aeroelastic module of elsA [64]. Developments were made around the code to replace the initial linear ROM by a structural solver to enable the computation of the beam FOM model and the nonlinear ROM.

The time integration of the structural solver is performed with the HHT-α method ($\alpha_{HHT} = 0.01$), including Newton-Raphson iterations during each time step. The HHT-α method which belongs to the one-step Newmark's family of time integration methods is more robust to tackle this coupled problem. Indeed, the approximation of the acceleration in the basic Newmark method may induce perturbations that can destabilize the coupling. This problem has been encountered here (as in [35]) and can be avoided with the HHT-α method. The precision of such methods remains of second-order accuracy (for linear cases) but a light numerical damping [157] is introduced, which stabilizes the coupling. Compared to the previous case without the beam (Figure 5.4), the shed vortices strongly interact with the flexible beam and the wake is significantly modified. This interaction produces a complex unsteady aerodynamic forcing that generates beam's vibration with a significant level of amplitude. The maximum level of amplitude is indeed about of the order of magnitude of the cylinder radius. Figure 5.7 illustrates the unsteady flow during one period in the periodic regime.

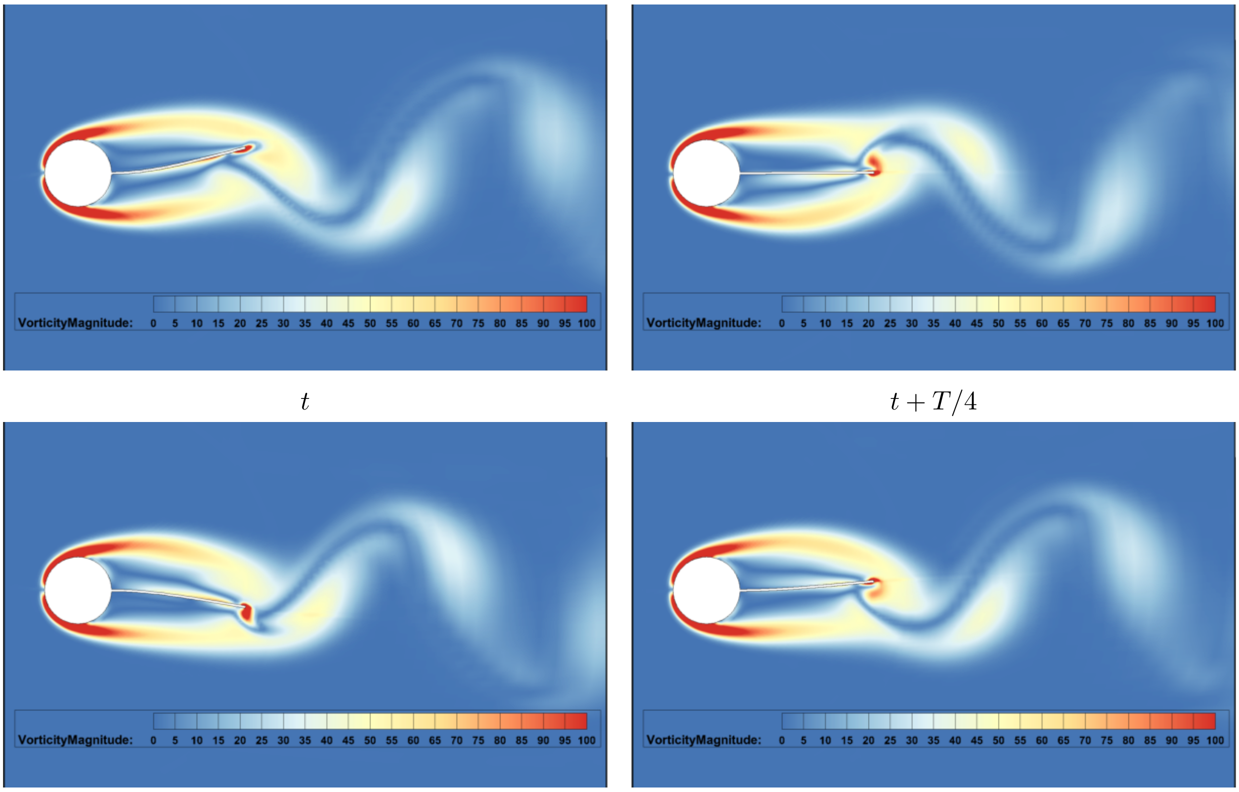

t $t + T/4$

$t + T/2$ $t + 3T/4$

Figure 5.7: Vorticity magnitude field over one period in the periodic regime of the fluid-structure interaction between the vortices in the wake of the cylinder and the flexible beam.

After a quite long transient, the axial and vertical forces on the beam's wet surface reach a periodic regime whose envelope is visible on Figure 5.8. Figure 5.9 illustrates the evolution with time of the vertical and axial displacements at the tip of the beam. The same behavior as for the forces is observed: the displacements converge to a periodic state after a long transient. The maximal vertical displacement reached is about ten times the beam's thickness, i.e. almost the value of the cylinder radius. The maximal axial shortening of the beam is about 1.2 times the beam's thickness: the nonlinearity is therefore significant in this case and has to be properly taken into account in the resolution of the structural dynamics.

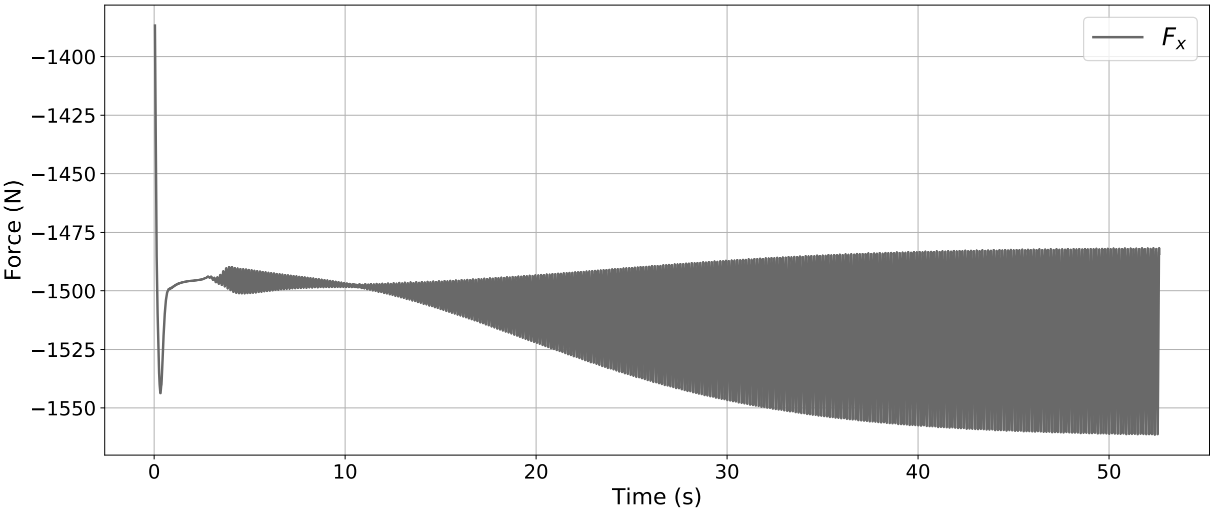

(a) Drag force F_x

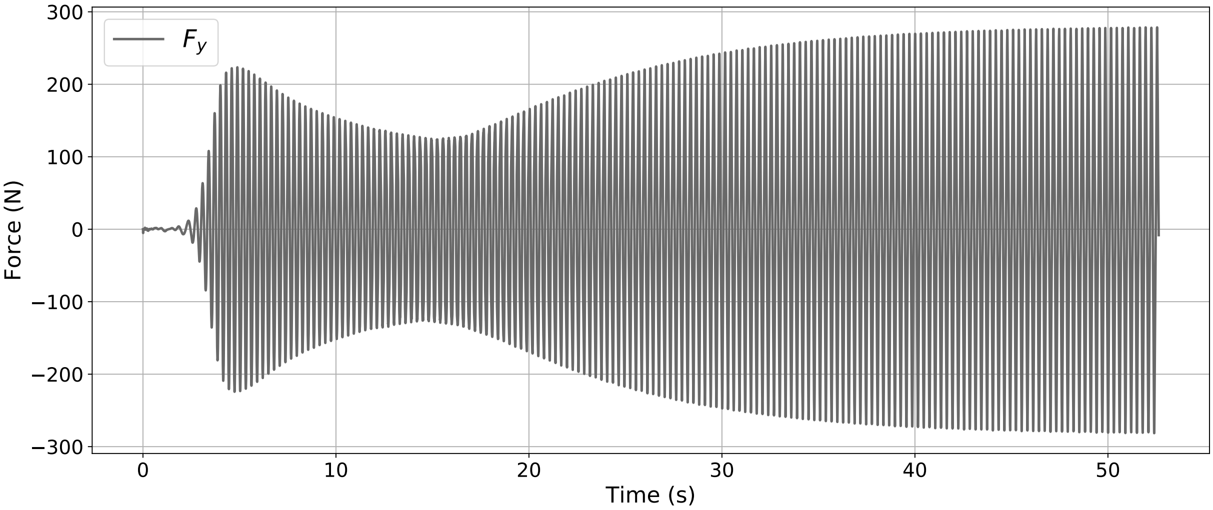

(b) Lift force F_y

Figure 5.8: Time evolution of the aerodynamic forces integrated on the surface of the beam. Drag force F_x (a) and lift force F_y (b).

To satisfy the fluid-structure equilibrium at a given time step before moving to the next one, fixed-point iterations are carried out between the fluid solver and the structural solver. Figures 5.10a and 5.10b represent respectively the evolution of the generalized coordinate of the first mode (resp. the aerodynamic forces projected on the first mode) during the periodic regime. Five fixed-point iterations are performed before moving to the next time step. The generalized coordinate is

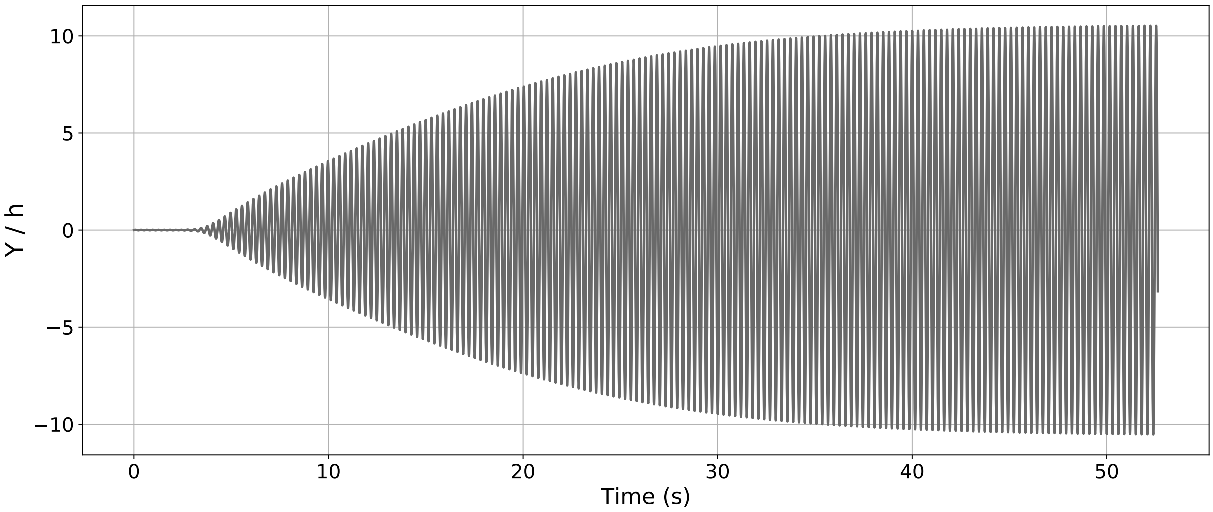

(a) Vertical displacement of the beam tip

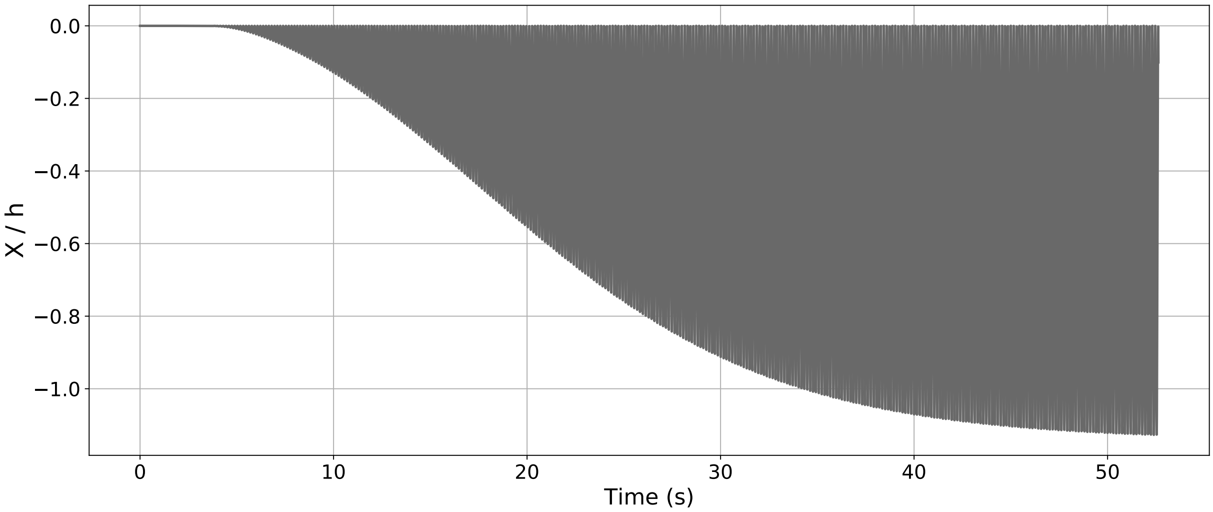

(b) Axial displacement of the beam tip

Figure 5.9: Evolution of the vertical (a) and axial (b) temporal displacements of the tip of the beam.

converged after only one iteration, while five iterations are however needed for the aerodynamic forces to be stabilized.

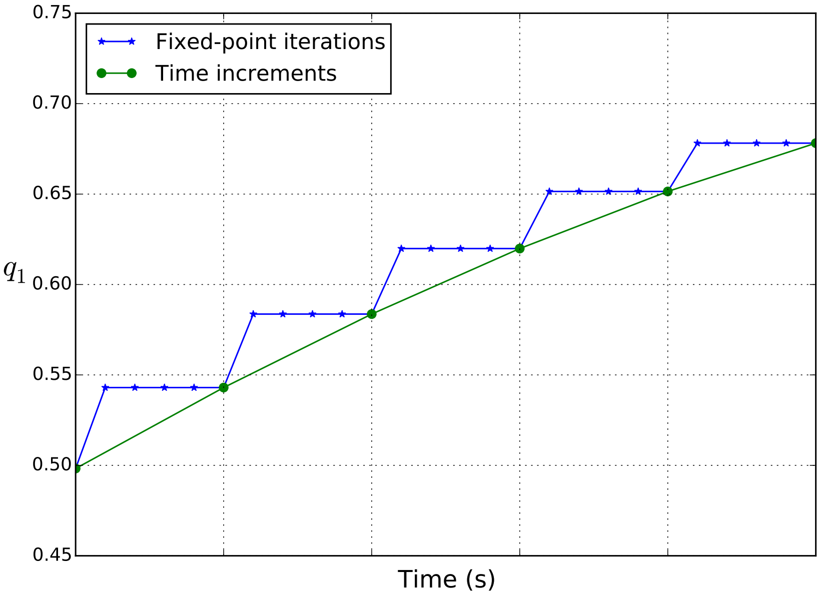

(a) Convergence of the generalized coordinate

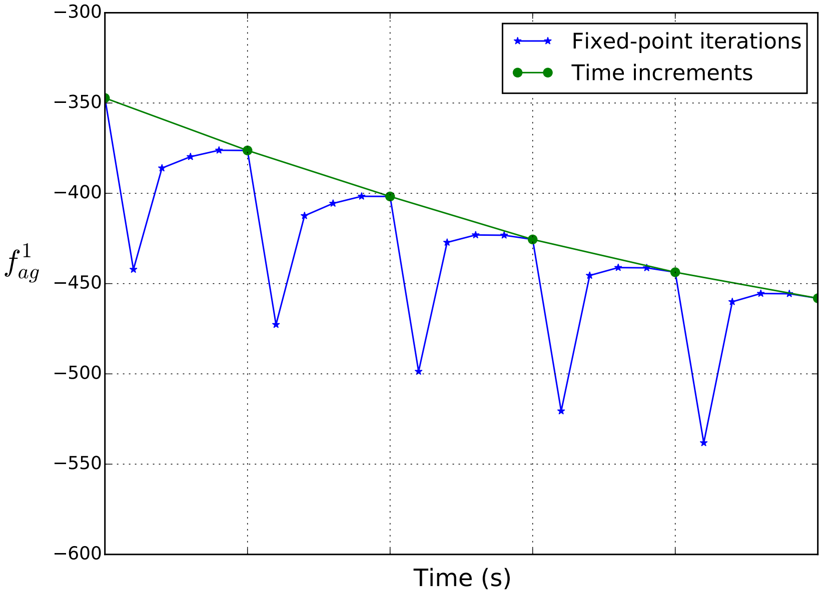

(b) Convergence of the generalized force

Figure 5.10: Convergence of the generalized coordinate (a) and the aerodynamic force (b) associated to the first mode, during the fixed-point equilibrium loop.

The reference solution obtained with the FOM and presented in Figure 5.9 is now compared in Figure 5.11 to the linear solution and to the solution evaluated with the ICDual model for the structure. The ICDual model is the one investigated in section 2.3.2 and includes the first three linear normal modes and the five dual modes determined previously to enrich the projection basis. As already reported in section 2.3.2 with the purely structural test cases, the linear solution introduces a spurious phase shift and the axial shortening is not captured at all. For the time interval shown on Figure 5.11a, the linear response is in advance of two periods with respect to the nonlinear solution: this is illustrated by the horizontal arrow joining the peak values of the linear solution and the corresponding nonlinear solution. On the contrary, the reduced order model captures precisely (though not perfectly) both the vertical and axial displacements during the transient and the periodic regimes.

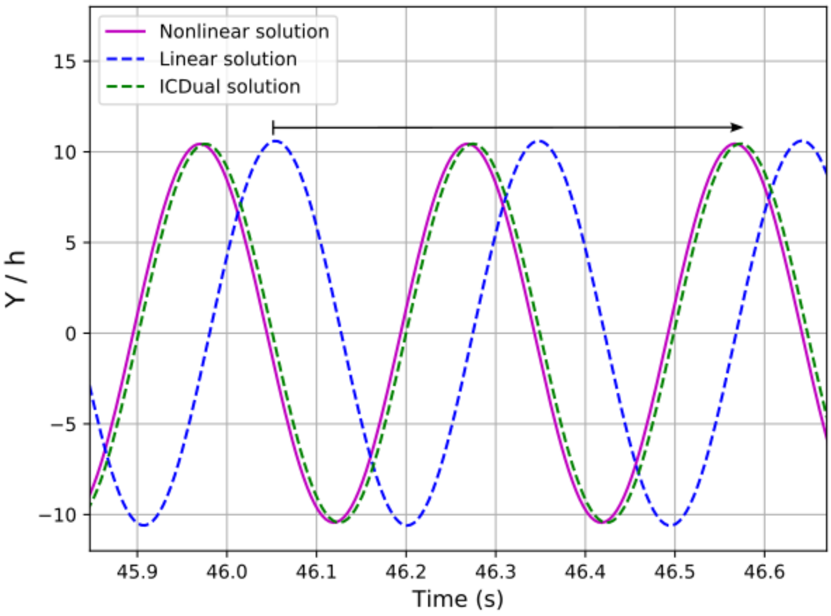

(a) Vertical displacement

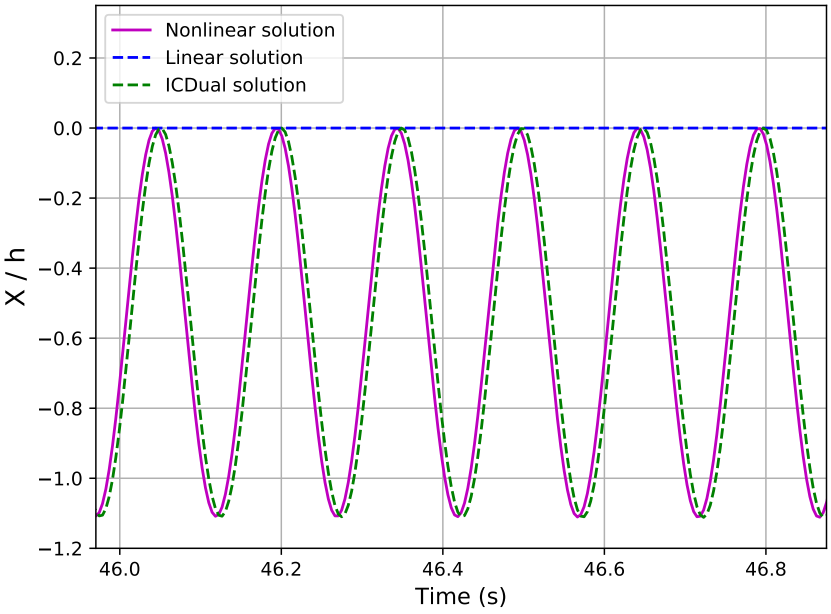

(b) Horizontal displacement

Figure 5.11: Vertical (a) and axial (b) displacements of the tip of the beam during the aeroelastic coupling in the periodic regime. Comparison between the linear and nonlinear FE solutions and the one obtained with the ICDual ROM.

Finally, the coupled behavior of the beam is investigated over a range of Reynolds number around Re $= 200$. Indeed, when both the vortex shedding frequency F_s (corresponding to a given Re with Roshko's relation) and the first eigenmode frequency f_0 of the beam are close, a lock-in phenomenon arises and both frequencies match : $F_s = f_0$ for a certain range of Reynolds number. However, when the Reynold number is sufficiently modified, the vortex shedding frequency deviates progressively from the first eigenmode frequency of the beam and the frequencies are no longer locked.

Figures 5.12 and 5.13 represent respectively the frequency of vibration of the beam and its vertical amplitude of vibration at the tip as a function of the Reynolds number, evaluated from the coupled aeroelastic solutions computed with linear or non-linear beam formulations. When the frequency of the vortex shedding is far from the eigenmode frequency f_0, the amplitudes of vibration are so small that their frequency is imposed by the fluid flow. However, when the frequency of the vortex shedding is close to f_0, the vibration of the structure and the vortex shedding both respond at a unique frequency for a range of Reynolds numbers. Besides, the range of Reynolds numbers of the plateau slightly differs between the linear and nonlinear cases. It is important to note that the ICDual ROM performs very well in the context of this challenging coupled FSI problem: the lock-in region predicted by the full order model is perfectly captured by the coupled solution computed with the ICDual ROM, both in terms of frequency and amplitude of vibration.

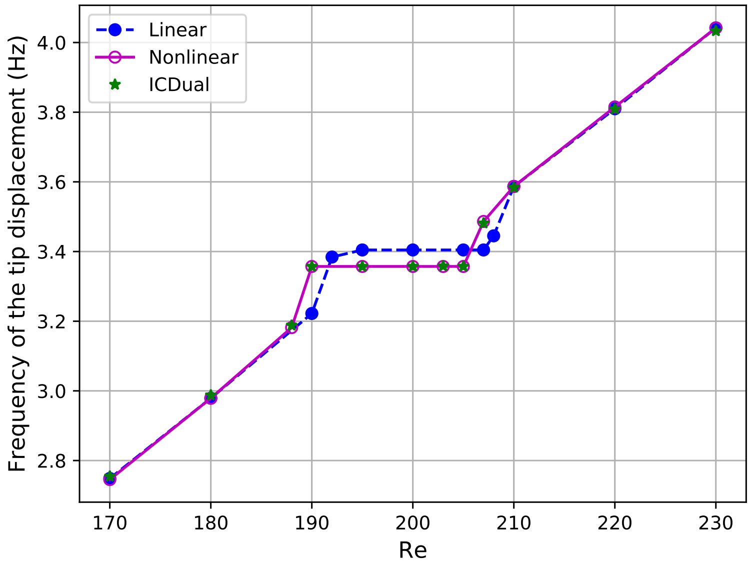

Figure 5.12: Evolution of the frequency of response of the beam with the Reynolds number of the fluid.

Below and after the range of frequencies characterized by the lock-in phenomenon, the beam responds both at the frequency imposed by the fluid flow and to a lesser extent at the eigenmode frequency f_0. It leads to a beating interference pattern visible in Figures 5.14a and 5.14c representing the evolution of the beam tip vertical displacement at Reynolds numbers 180 and 220 respectively. The Fast Fourier Transforms (FFT) of the previous displacements are also illustrated in Figures 5.14a and 5.14c, where both frequencies are distinctly noticeable. On the contrary, in the lock-in region, the unsteady response locks on a single frequency, as shown in Figures 5.14b.

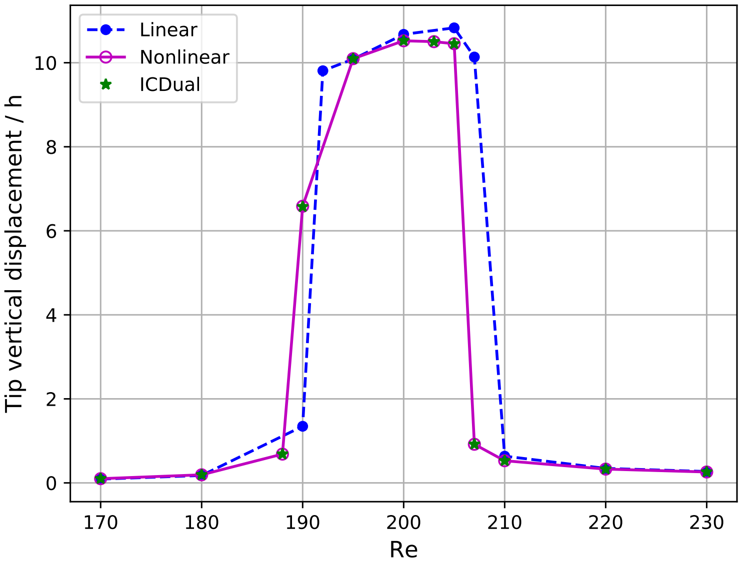

Figure 5.13: Evolution of the amplitude of vertical displacement at the tip of the beam with the Reynolds number of the fluid.

5.4 Conclusion of the chapter

In this chapter, the 2D fluid-structure interaction test case of a flexible beam in the wake of a fixed cylinder is considered. A partitioned coupling has been implemented between the fluid solver elsA and the von Kármán beam model studied in section 2.3. First, a CFD computation of the cylinder alone was performed, then the flexible beam is added in the vortex street of the cylinder. This last test case demonstrates the potential of coupling a structural ROM based on an original formulation with dual modes for aeroelastic problems. The ICDual ROM matches very accurately the FOM solutions and is easily coupled in the framework of a partitioned approach since the reduced order model is independent of any FE solver. The influence of the structural nonlinearity has finally been highlighted in terms of lock-in frequency and the ROM is able to capture this effect very precisely. In this test case, the comparison with the FOM solution was possible because it is a beam model. However, the high-fidelity resolution of a coupled problem is not possible for 3D structures with a large number of degrees of freedom, which justifies the use of the nonlinear ROM. In the next chapter, the precision of the ICDual ROM is investigated on a more complex geometry which is a 3D turbomachine blade.

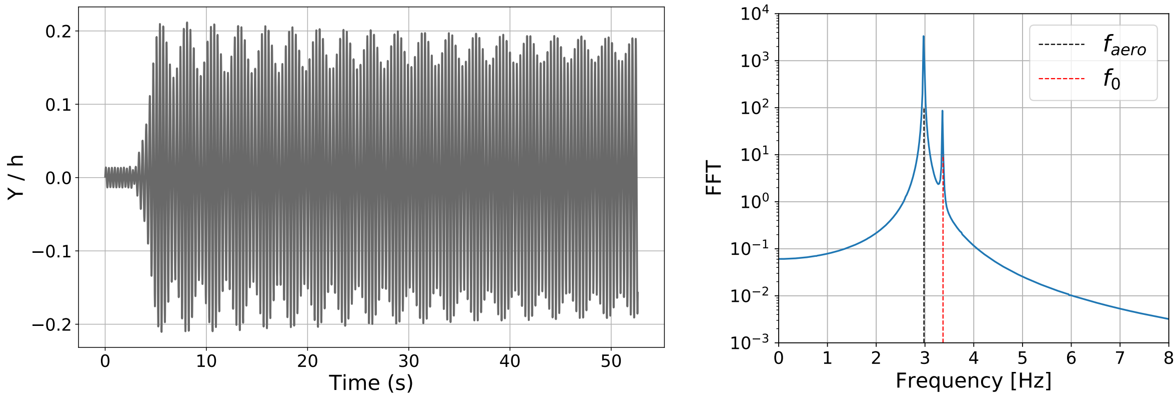

(a) Reynolds numbers 180: time response (left) and FFT (right)

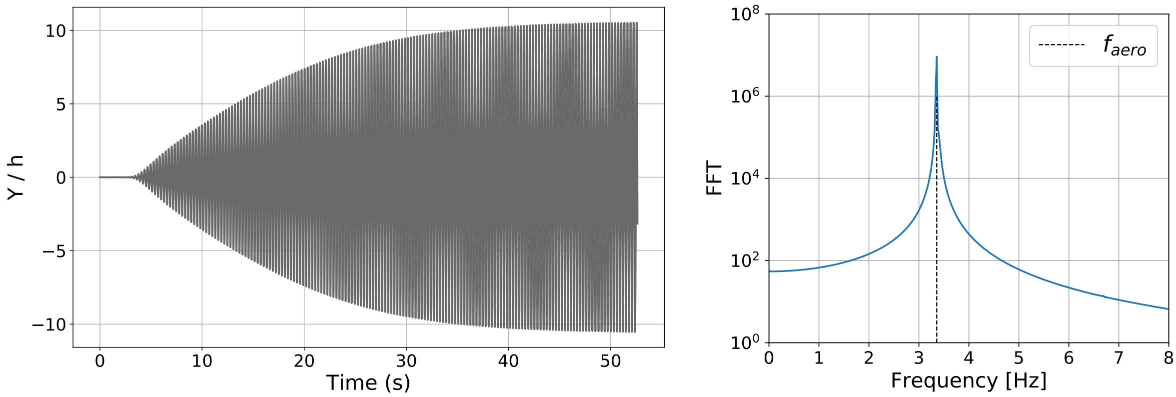

(b) Reynolds numbers 200: time response (left) and FFT (right)

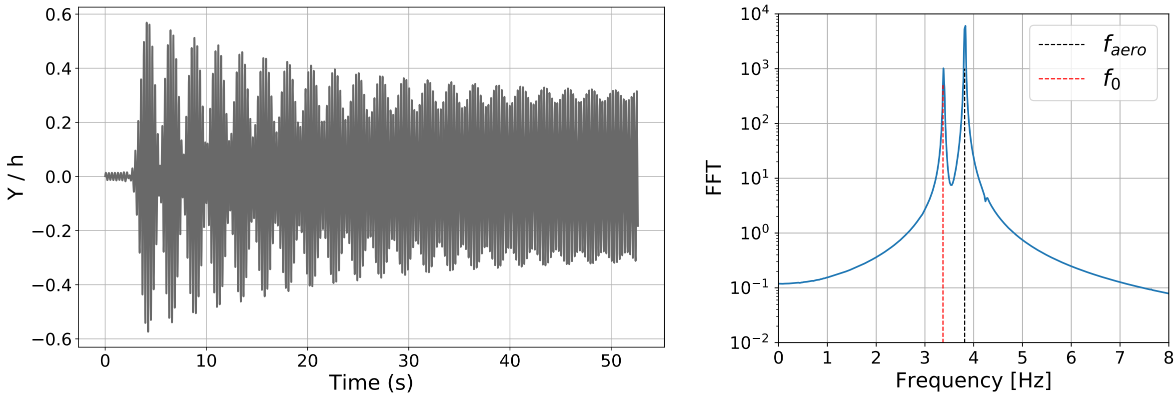

(c) Reynolds numbers 220: time response (left) and FFT (right)

Figure 5.14: Temporal evolution and Fast Fourier Transforms of the beam tip vertical displacements in the fluid flow at Reynolds numbers 180, 200 and 220.

Chapter 6

Application to an industrial test case of a turbomachine blade

---

In this chapter, we consider the complex 3D structure of a fan blade representative of an UHBR turbofan. While the test cases studied in the precedent chapters were symmetric, the geometry of the blade considered in this chapter is more complex leading to geometric nonlinearities involving membrane stretching, bending and torsion together. The objective is to investigate the accuracy of the structural reduced order model for such structures with representative aerodynamic loads. First, the fan configuration is presented. Then the ICDual ROM is built for a selected operating point and tested for a given static load. Subsequently, a CFD computation on the entire fan is performed. Finally, the periodic components of the unsteady aerodynamic loads are determined and the load distribution is applied to the structure to compare the accuracy of the different models. Some results of this chapter are published in the following journal paper [57]. More results and details are provided in this manuscript.

Contents

6.1 Presentation of the fan configuration

In this chapter, a fan configuration from an UHBR turbofan is considered. Such jet engine configuration aims to increase the bypass ratio compared to current engines. It is a shrouded configuration with blades of large dimensions. In the present work, the structure of interest is not the entire wheel but a single fan blade (all blades being the same). Figure 6.1 illustrates the full engine configuration (a) and the fan blade of interest (b).

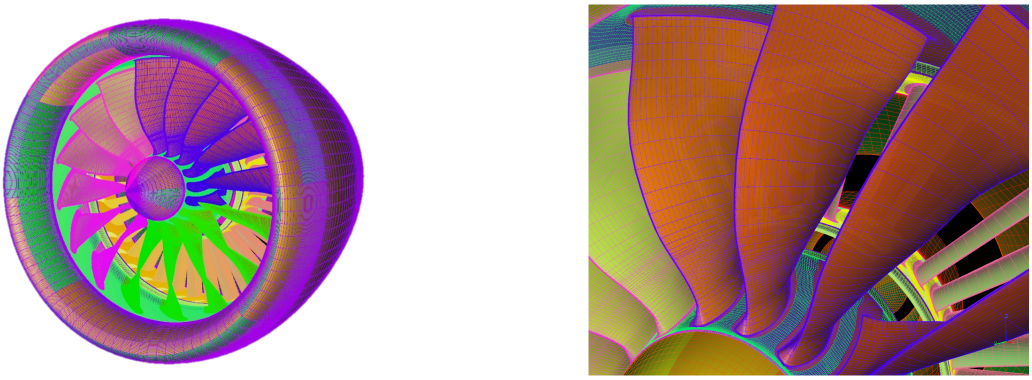

(a) (b)

Figure 6.1: Visualization of the full engine model and the fan blades.

The original blade structural model has been adapted to enable a dynamic analysis restricted to a single fan blade. For that purpose, the blade root was removed and replaced by a clamped boundary condition. The Young's modulus is equal to 110 GPa, the density 4,500 kg.m^{-3} and the Poisson's ratio is equal to 0.318. The blade is discretized in 66,640 HEX8 finite elements, with 6 elements in the blade thickness. The structural mesh of the blade is shown in Figure 6.2 from two different angles of view.

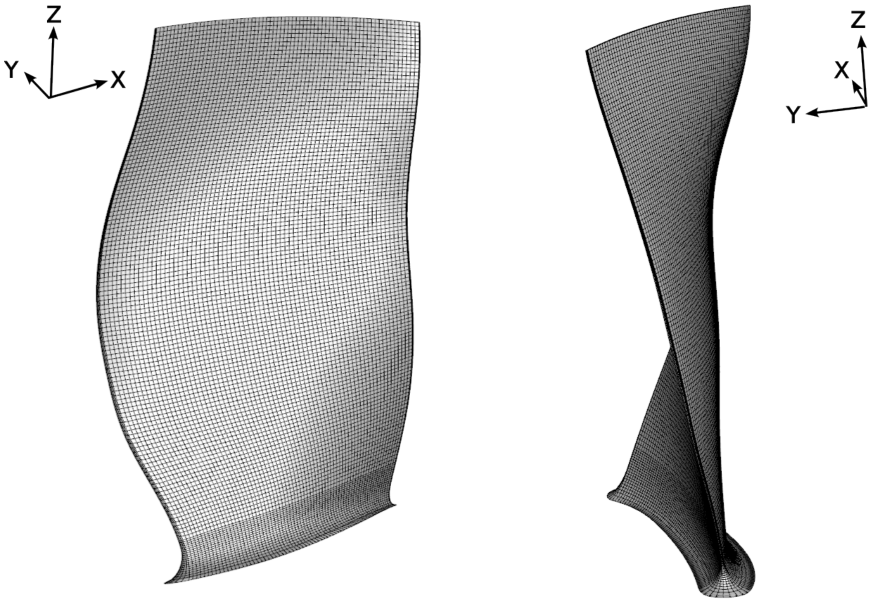

Figure 6.2: Mesh of the blade.

The structure is in rotation around the fixed axis x. Therefore, centrifugal effects are present and the dynamics of the structure is studied around the prestressed position shown in Figure 6.4. The linear normal modes shapes of the structure and their associated modal frequencies are modified by the rotation speed since they are computed relative to the prestressed position. Figure 6.3 is a Campbell diagram showing the evolution of the frequencies of the first three linear normal modes with the rotation speed. The black dotted lines represent the engine orders.

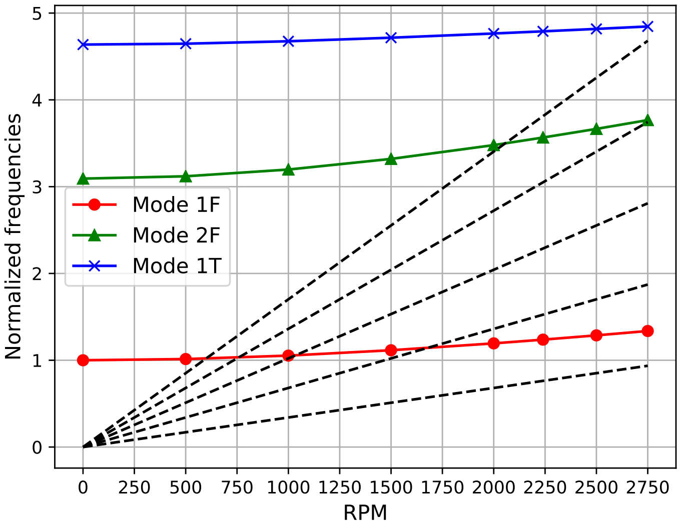

Figure 6.3: Campbell diagram of the blade structure for the first three structural modes.

The first linear normal modes are respectively the first bending mode (named 1F), the second bending mode (2F) and the first torsion mode (1T). It is noticed on the Campbell diagram, that at 2,750 rpm, the modes 2F and 1T are close to multiples of the rotation speed. Resonance can therefore be observed at this rotating speed for those modes, which should be avoided. In what follows, the rotating speed considered is 2,750 rpm in order to study the structural behavior under large displacements. The prestressed position of the blade is shown in Figure 6.4. Due to the centrifugal force, an untwisting of the blade is observed in the present case.

Figure 6.4: Prestressed position (in red) of the blade in rotation at 2,750 rpm. The initial geometry is represented in gray.

In the following section, the reduced order model for the structure is built around the centrifugally prestressed position shown in Figure 6.4.

6.2 Construction of the reduced order model

The linear normal modes considered in the ROM are the first three modes computed around the prestressed position at the rotation speed of 2,750 rpm. Those linear normal modes are respectively the first bending (1F), the second bending (2F) and the first torsion (1T) modes, illustrated in Figure 6.5.

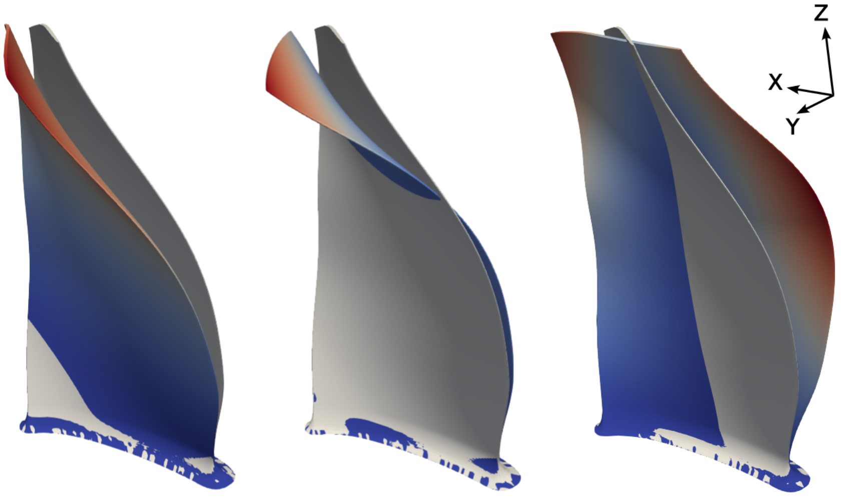

Figure 6.5: First three linear normal modes (1F, 2F and 1T) of the blade at 2,750 rpm.

The dual modes selection process is applied to the blade around the centrifugally prestressed position. The singular values and linearized strain energies are shown in Figure 6.6. As we can observe, there is no clear drop in the singular values due to the strong nonlinearity of the twisted geometry of the blade.

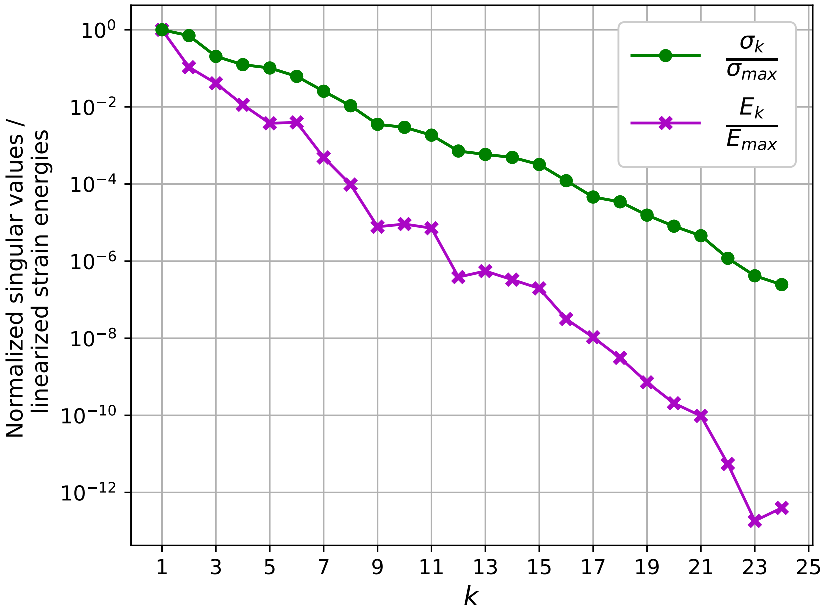

Figure 6.6: Normalized singular values and linearized strain energies of the SVD modes of the blade in rotation at 2,750 rpm.

Figure 6.7 illustrates the first four dual modes candidates corresponding to the four largest singular values and contributors to the linearized strain energy. Their shape is interesting since we recognize bending and torsion but mostly displacements that can be compared to "membrane" contributions. In fact, the dual modes shapes highlight the nonlinear displacement at the points where the blade undergoes a significant stretching due to geometric nonlinearities such as the tip leading and trailing edges. Such displacements are indeed absent from the linear normal modes. For the range of displacement of the applications considered, a first consideration with only one dual mode gives particularly accurate results. The reduction basis is thus enhanced with one additional dual mode, the first one. Its shape is illustrated in Figure 6.7a.

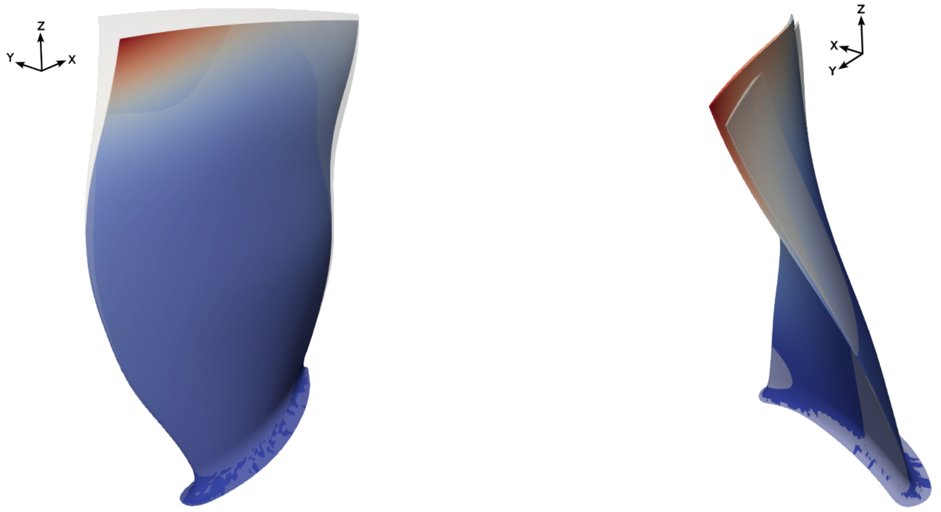

(a) First dual mode

(b) Second dual mode

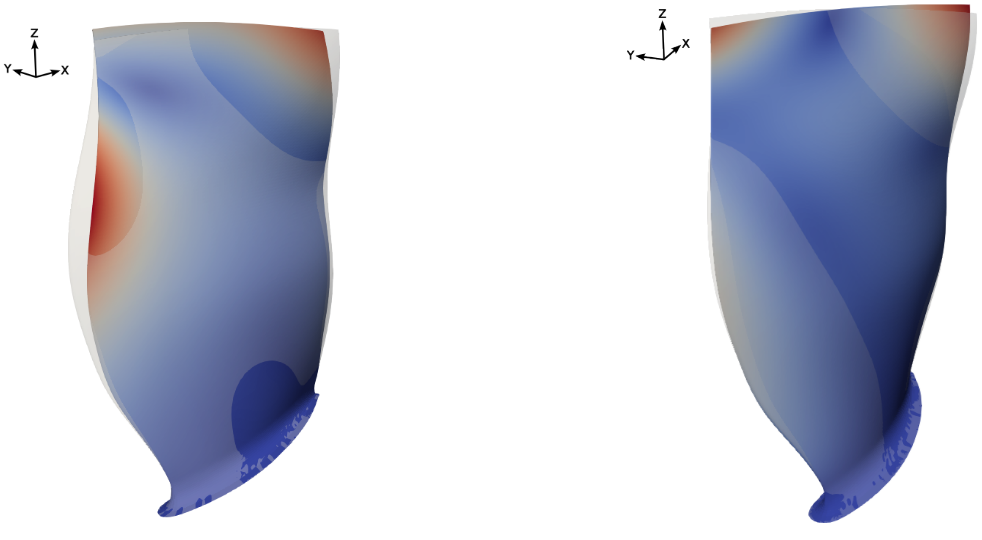

(c) Third dual mode

(d) Fourth dual mode

Figure 6.7: First four dual modes of the blade, determined from the three first linear normal modes around the prestressed position at 2,750 rpm.

The reduction basis consists thus of four modes: the first three linear normal modes and one additional dual mode. The nonlinear force coefficients are then identified from the imposed loads according to the ICDual process. In what follows, the efficiency of such a ROM is first tested with a given static load, then a periodic load based on the distribution of aerodynamic forces.

6.3 Nonlinear response under a static load

In this section, a static load is applied to the structure. The load is based on the shape of the first linear normal mode at $\Omega = 2{,}750$ rpm as follows:

$$\mathbf{f}_{\text{ext}} = -15h\mathbf{K}(\Omega)\frac{\boldsymbol{\phi}_1^{\Omega}}{\max|\boldsymbol{\phi}_1^{\Omega}|}, \tag{6.1}$$

with h the average thickness of the blade tip. For such a load shape, the maximal amplitude of the linear solution is 15 times the thickness of the blade tip. Figure 6.8a represents the solution obtained under the static load of Equation (6.1) and Figure 6.8b under its opposite.

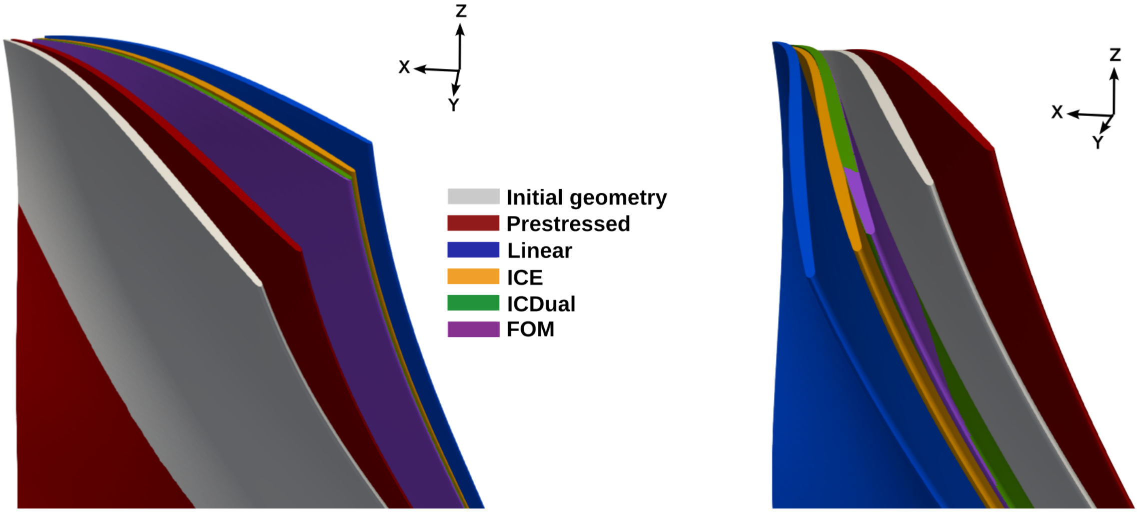

(a) (b)

Figure 6.8: Comparison between the FOM and the ROM solutions under the static load (6.1) (a) and under its opposite (b).

The geometrical nonlinearity is significant for such amplitudes. The nonlinear ICDual solution matches perfectly with the FOM solution but the ICE solution presents a slight deviation at the tip, while the linear ROM solution overestimates the static displacement. In this test case, the external load applied to the structure is arbitrary. To evaluate the efficiency of the ROM on a representative load case, the unsteady aerodynamic loads of the engine are computed.

6.4 Determination of the aerodynamic forces

In this section, a CFD computation of the full 360° fan-OGV-nacelle configuration is performed. First a steady RANS computation, then an unsteady URANS computation starting from the steady solution. The aerodynamic grid consists of roughly 16 million cells. The CFD solver is the finite volume elsA solver (ONERA-Safran property) [19]. Figure 6.1 at the beginning of the chapter illustrates the engine configuration with the nacelle, the fan and OGV blades. Only the secondary flow is computed, the primary flow that crosses the combustion chamber is not computed but imposed as a boundary condition.

6.4.1 Steady aerodynamic forces

The steady aerodynamic computation is performed at Mach 0.8, for a zero angle of attack of the engine and for an altitude of 35,000 feet. The Roe [159] spatial scheme is considered, with the van Albada flux limiter [198]. The turbulence model is the Spalart-Allmaras model [180, 181]. Mixing plane boundary conditions are imposed at the fan/OGV interfaces [39, 81, 168]. Figure 6.9 represents the steady aerodynamic pressure field in the fan and OGV. Some streamlines are also represented to visualize the flow direction in the absolute frame. In the view, the fan blades are moving from bottom to top and the OGV blades are static to redirect the flow.

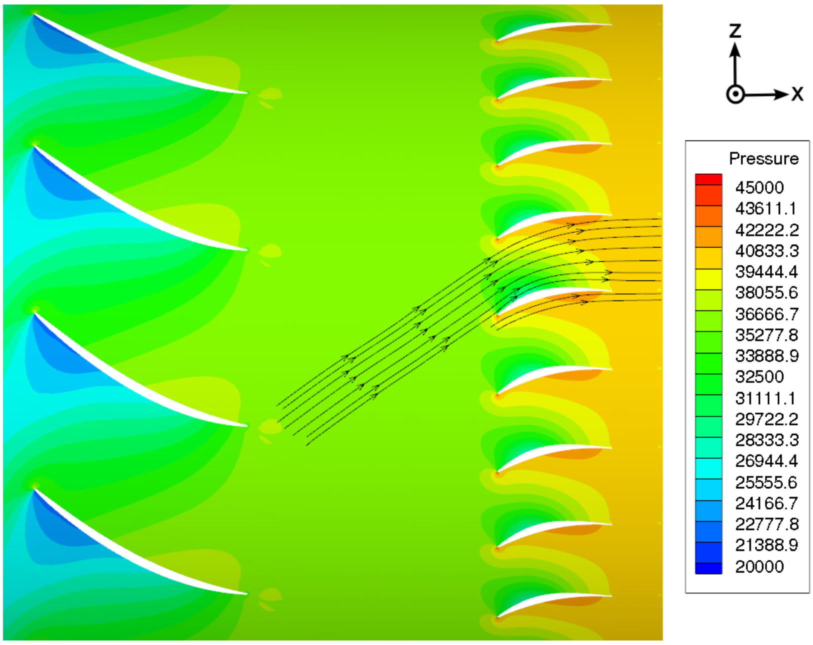

Figure 6.9: Steady aerodynamic pressure field in the fan and OGV at Mach 0.8.

The CFD computation is performed in parallel on 96 processors and 10,000 iterations are needed until a satisfactory convergence is reached (see Figure 6.10).

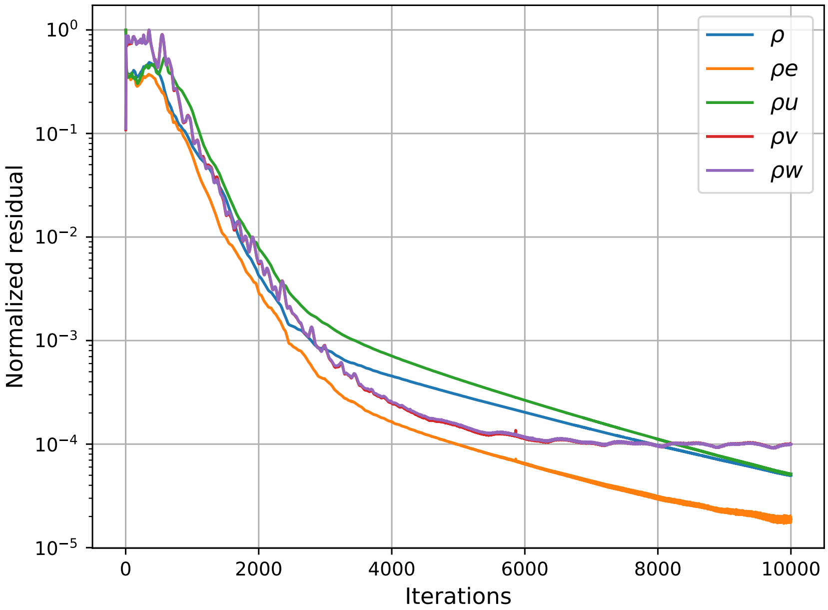

Figure 6.10: Evolution of the residual of the conservative variables. The results are normalized by the respective initial values.

The distribution of the resulting aerodynamic forces on the fan blade considered is represented in Figure 6.11 with different scales for the visualization.

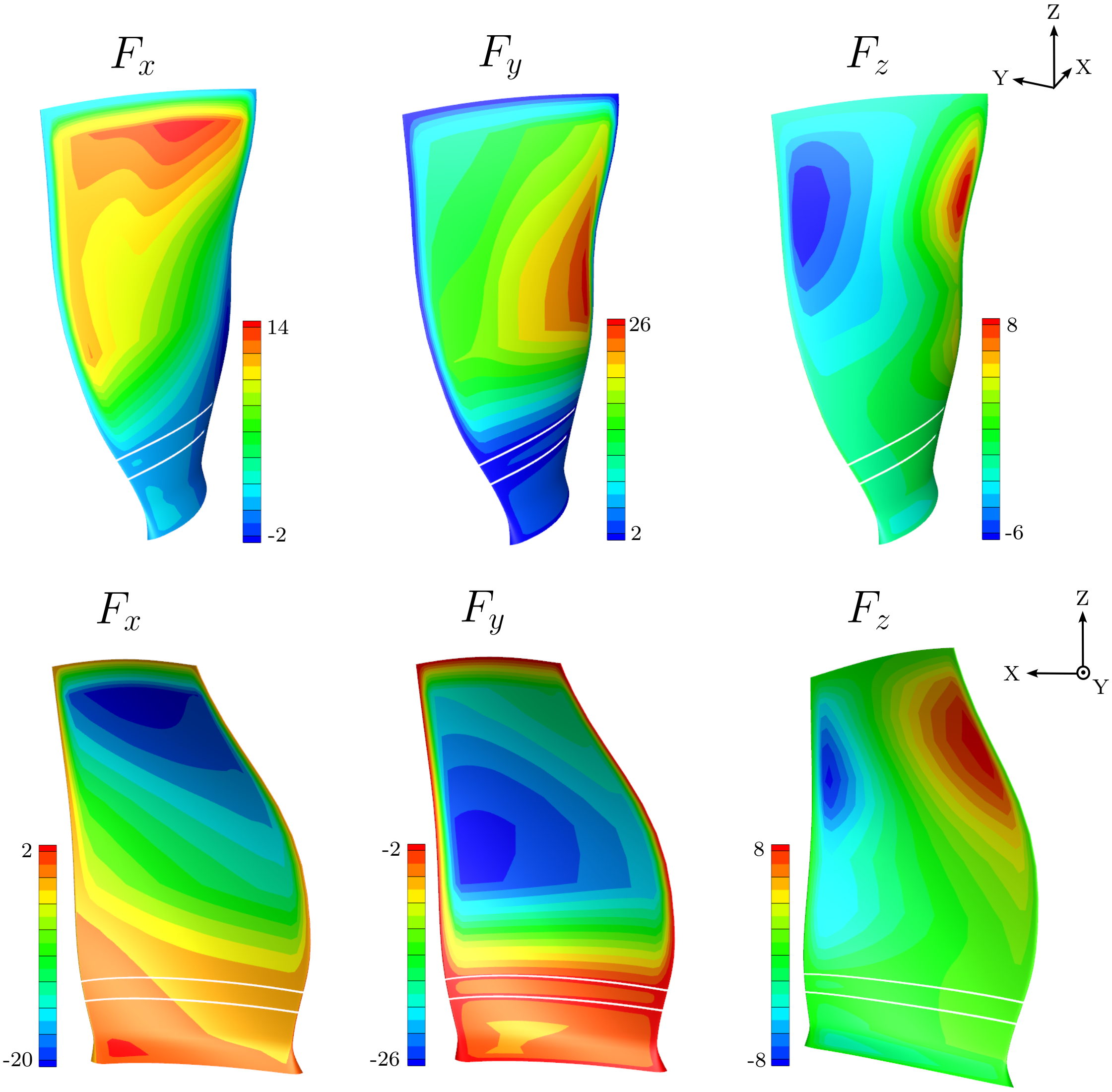

Figure 6.11: Steady aerodynamic forces on the suction side (top) and the pressure side (bottom) of the blade.

Figure 6.12 shows the steady pressure field on the suction and pressure sides of the blade. A pressure decrease is observed on the suction side after the leading edge, while the pressure increases on the pressure side with a maximum near the trailing edge. The evolution of the pressure around the blade at about two-thirds of the span is plotted in Figure 6.13 to highlight the pressure gradients along the profile.

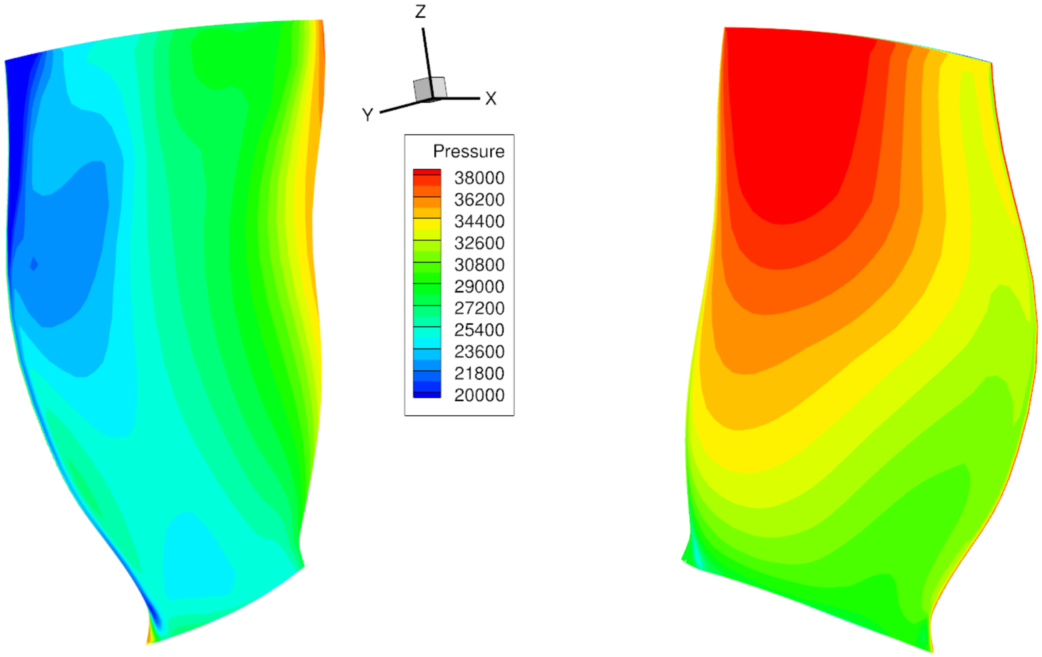

(a) Suction side

(b) Pressure side

Figure 6.12: Steady pressure on the suction (a) and pressure (b) sides.

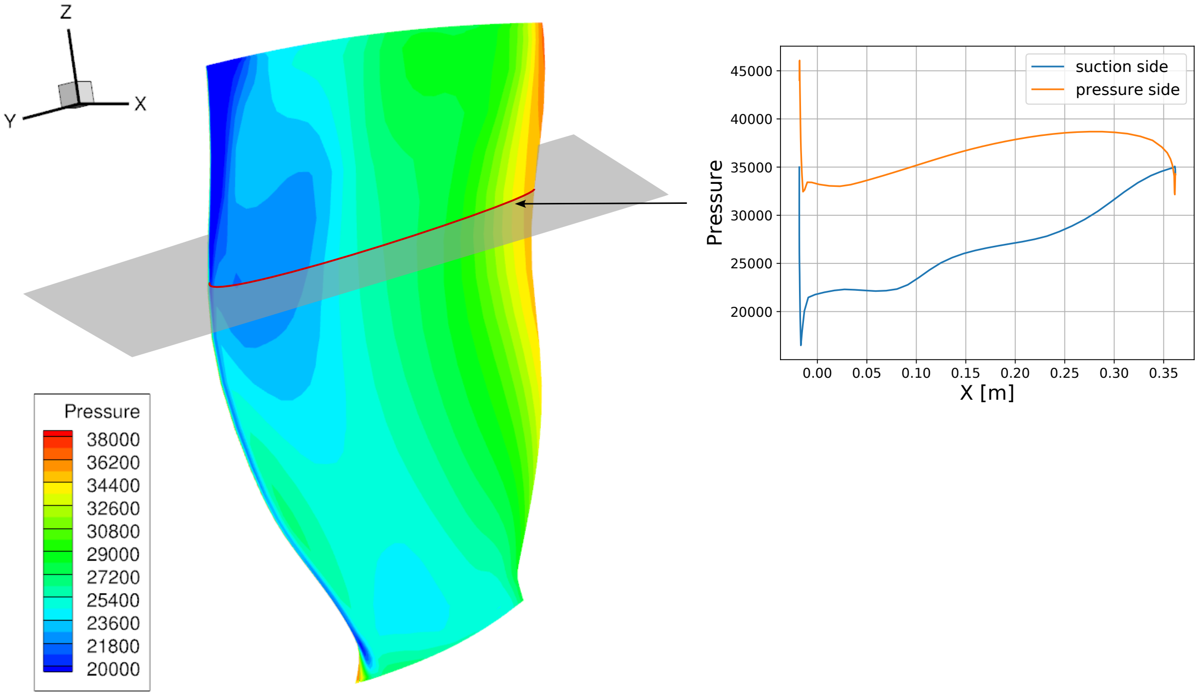

Figure 6.13: Evolution of the pressure along the suction and pressure sides at 2/3 of the blade span.

6.4.2 Unsteady aerodynamic forces

The nacelle inlet presents a dissymmetry. Figure 6.14 is a side view of the nacelle, where the offset between the top and bottom edges is clearly visible. As a result, the inlet flow is subject to a distortion pattern. Figure 6.15 illustrates this distortion pattern by representing the vertical deviation angle in the inlet. During each rotation, a fan blade travels through the distortion pattern and is thus subject to a periodic forcing.

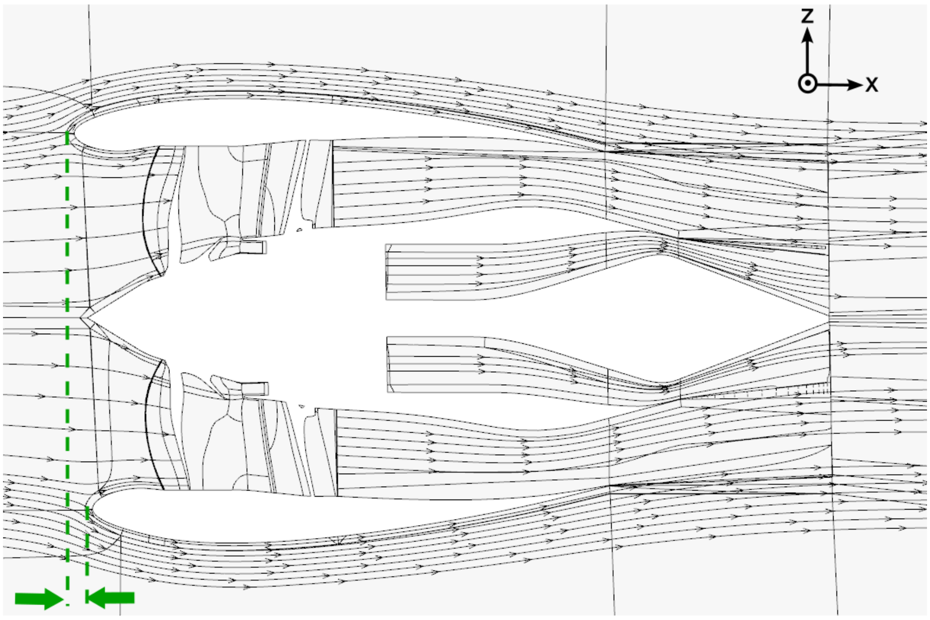

Figure 6.14: Visualization of the dissymetry in the nacelle.

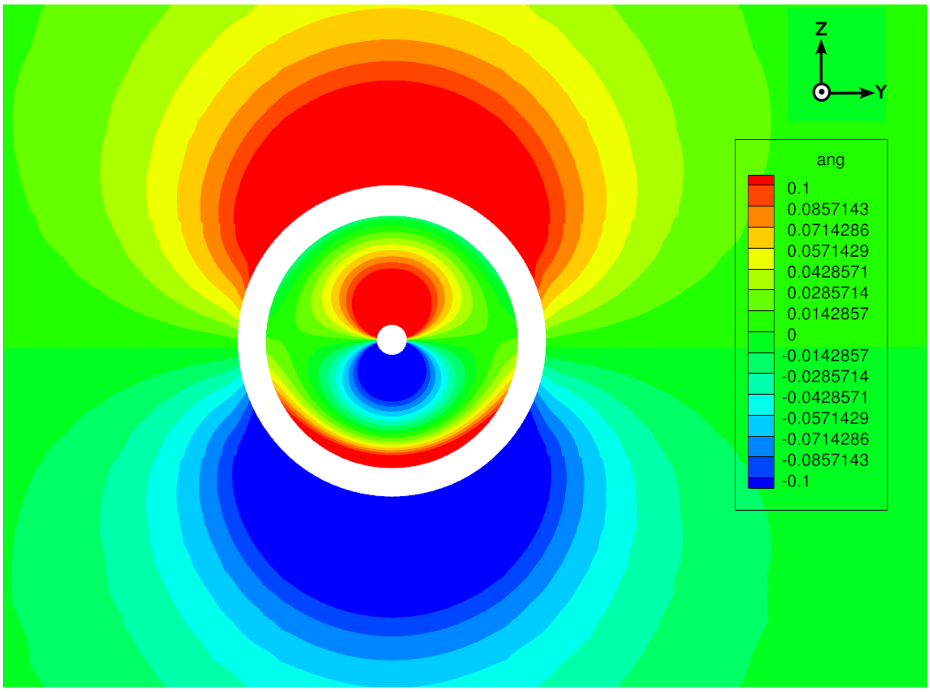

Figure 6.15: Front view of the vertical deviation angle atan2(v_z/v_x) of the velocity in the inlet.

The mixing plane boundary conditions of the steady computation are replaced by sliding mesh conditions. The time discretization consists in 360 time steps for a full rotation of the fan wheel and the time integration is performed with the dual time-stepping method [12, 92]. The temporal evolution of the aerodynamic forces integrated on the blade is represented in Figure 6.16, where the levels of amplitude due to the forced response are significant.

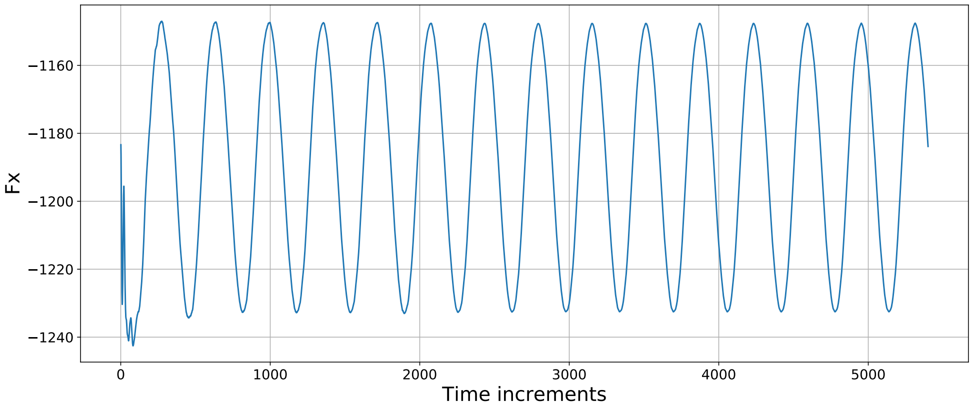

(a) Forces Fx integrated on the blade.

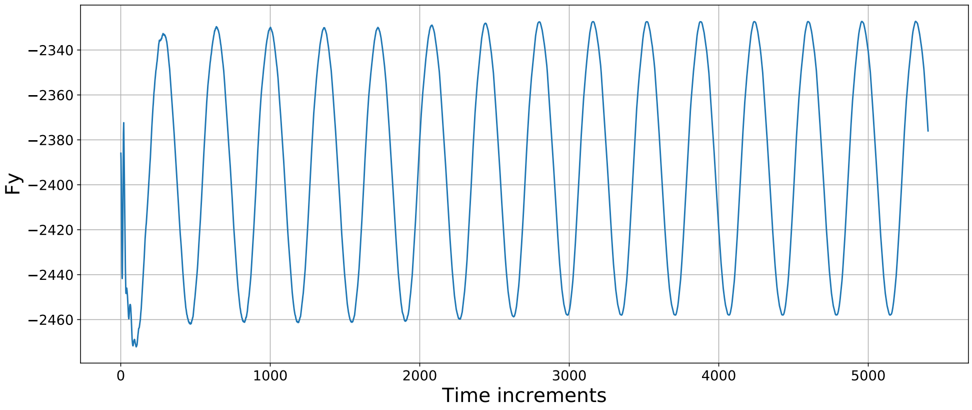

(b) Forces Fy integrated on the blade.

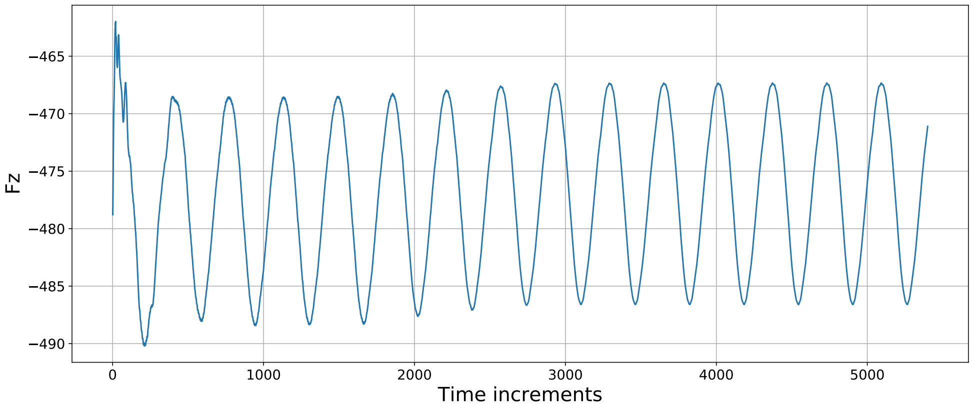

(c) Forces Fz integrated on the blade.

Figure 6.16: Unsteady aerodynamic forces integrated on the entire blade.

Figures 6.17 represent the Fast-Fourier Transform of the integrated forces on the blade in the y direction. The FFT is computed subtracting the mean value of the signal which corresponds to the steady-state solution. The y direction is the direction in which the blade responds the most to the forcing imposed by the inlet distortion. As expected, a peak is observed at the rotation speed as well as a smaller contribution of the harmonics.

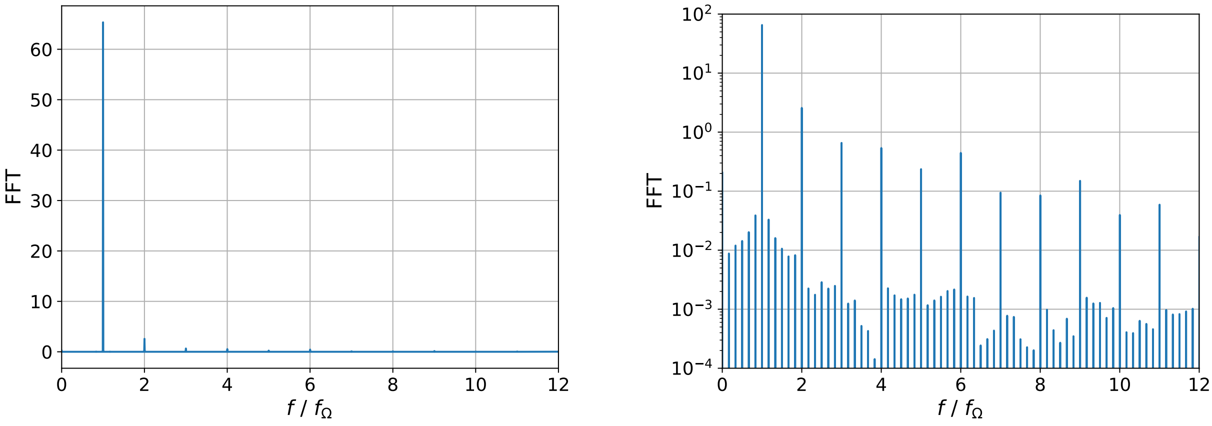

(a) (b)

Figure 6.17: Fast-Fourier Transform in linear (a) and logarithmic (b) scales of the integrated forces on the blade in the y direction. f_Ω represents the frequency of rotation of the fan.

The periodic forcing applies at every point of the blade. Figure 6.18 shows the time evolution of the pressure at two different points of the blade.

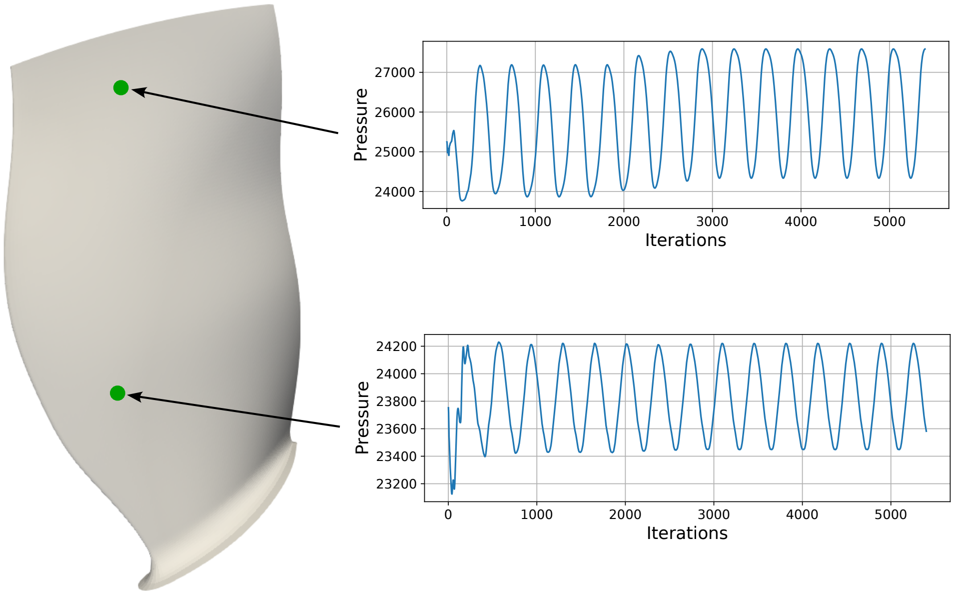

Figure 6.18: Time evolution of the pressure at local points on the suction side.

At every point of the blade surface, we compute the Fourier decomposition of the aerodynamic forces to obtain the amplitudes of the harmonics of the signal. The constant terms correspond to the steady solution shown in Figure 6.11. Only the components of the first harmonics are kept since the amplitudes along the other harmonics are negligible. The amplitudes of the sine F_x^s, F_y^s, F_z^s and cosine F_x^c, F_y^c, F_z^c components of the first harmonics of the unsteady aerodynamic forces are shown on the suction and pressure sides respectively in Figures 6.19 and 6.20.

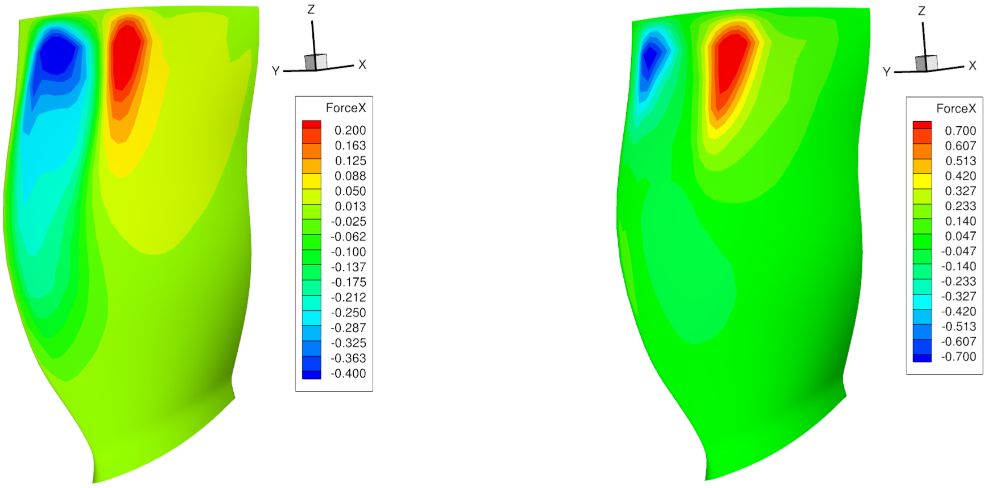

(a) Fourier coefficient F_x^s (b) Fourier coefficient F_x^c

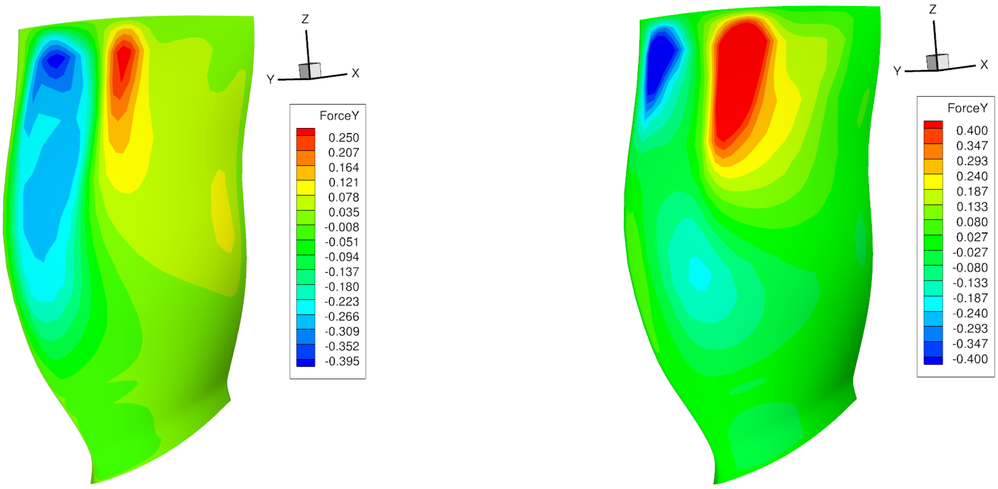

(c) Fourier coefficient F_y^s (d) Fourier coefficient F_y^c

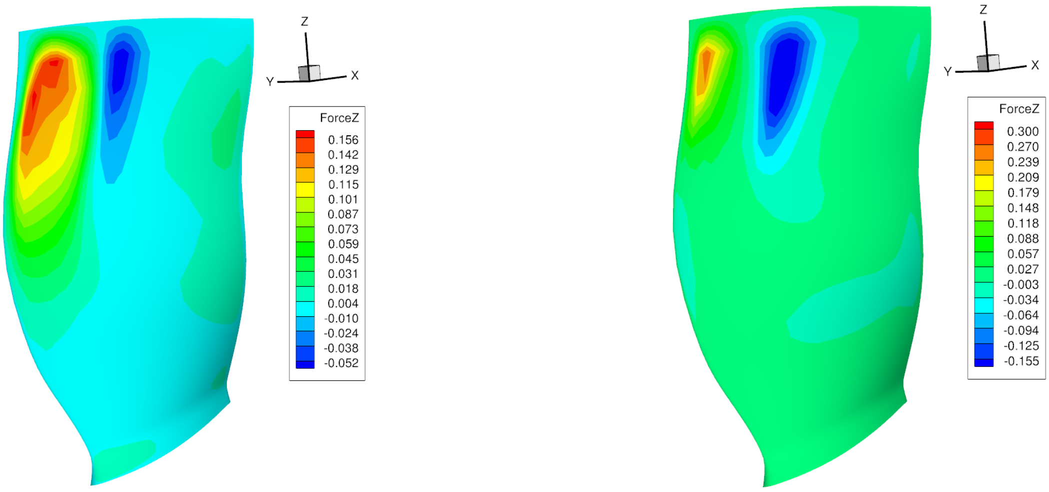

(e) Fourier coefficient F_z^s (f) Fourier coefficient F_z^c

Figure 6.19: Amplitudes of the sine and cosine components of the first harmonics of the unsteady aerodynamic forces on the suction side.

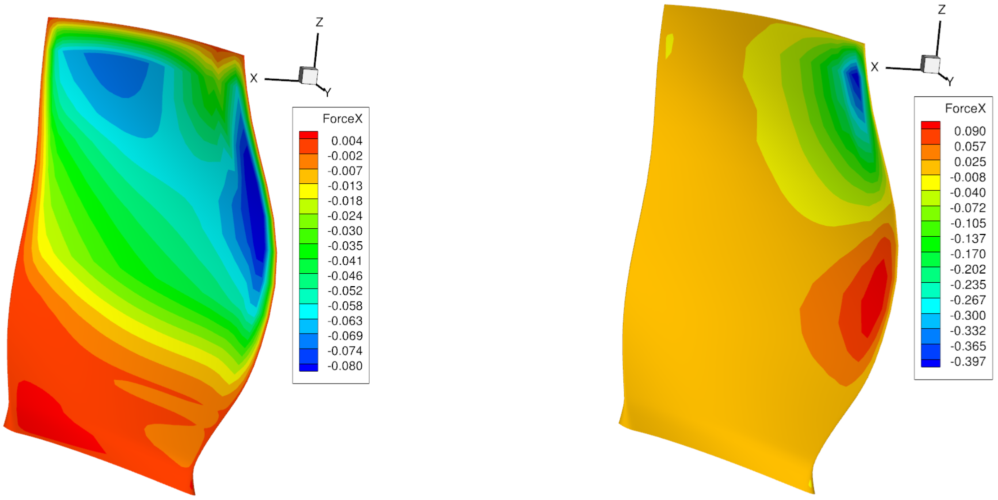

(a) Fourier coefficient F_x^s (b) Fourier coefficient F_x^c

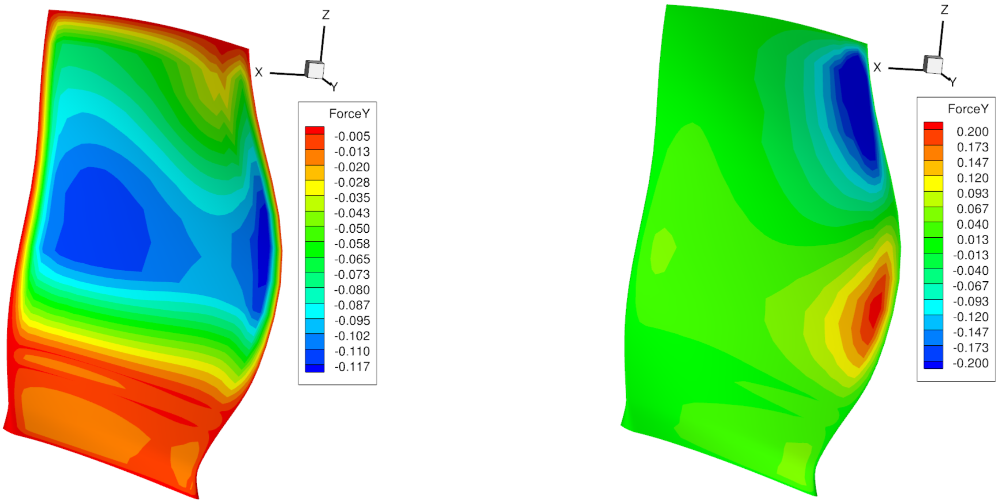

(c) Fourier coefficient F_y^s (d) Fourier coefficient F_y^c

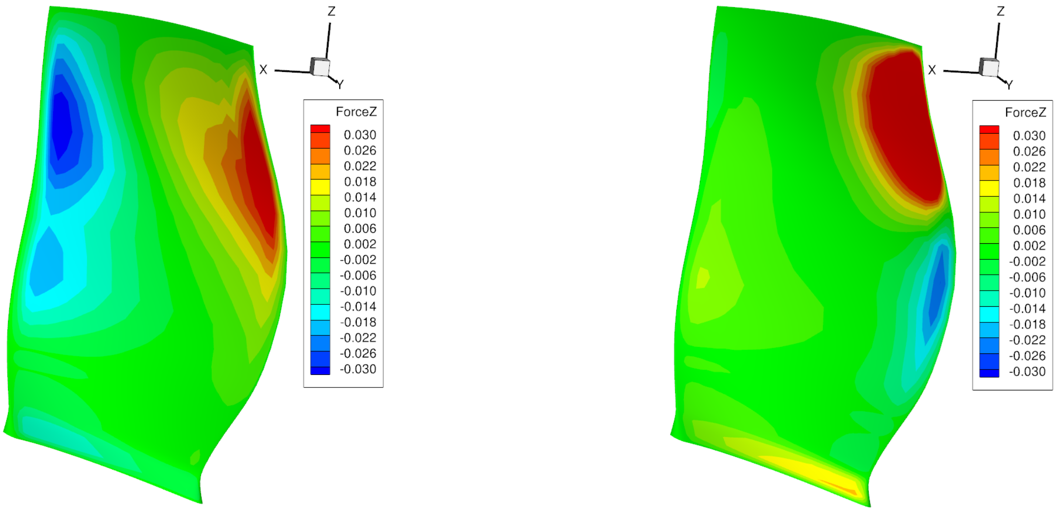

(e) Fourier coefficient F_z^s (f) Fourier coefficient F_z^c

Figure 6.20: Amplitudes of the sine and cosine components of the first harmonics of the unsteady aerodynamic forces on the pressure side.

6.5 Nonlinear response of the structure

The purpose of this section is to compare the FOM solution to the linear and nonlinear reduced solutions under a dynamic load. The Fourier coefficients in the decomposition of the unsteady aerodynamic loads are transferred from the aerodynamic mesh to the neighbouring nodes of the structural mesh. The transfer method is the energy method based on the conservation of the virtual work described in section 4.4.2 to satisfy the equality between the virtual work of the aerodynamic loads and the transferred loads imposed on the structure. Such a load distribution of the fluctuating components is applied to the structure at the frequency of the forcing phenomenon (i.e. the rotation speed) and with the desired amplitude. A Rayleigh damping is also added to the system: $\mathbf{C} = 2\xi\omega_0^{2,750}\mathbf{M}$ with $\xi = 0.05$. Figure 6.21 represents the time evolution of the tip leading edge of the blade along the Y direction and Figure 6.22 shows the maximal positive and negative displacements in the periodic regime for the different models.

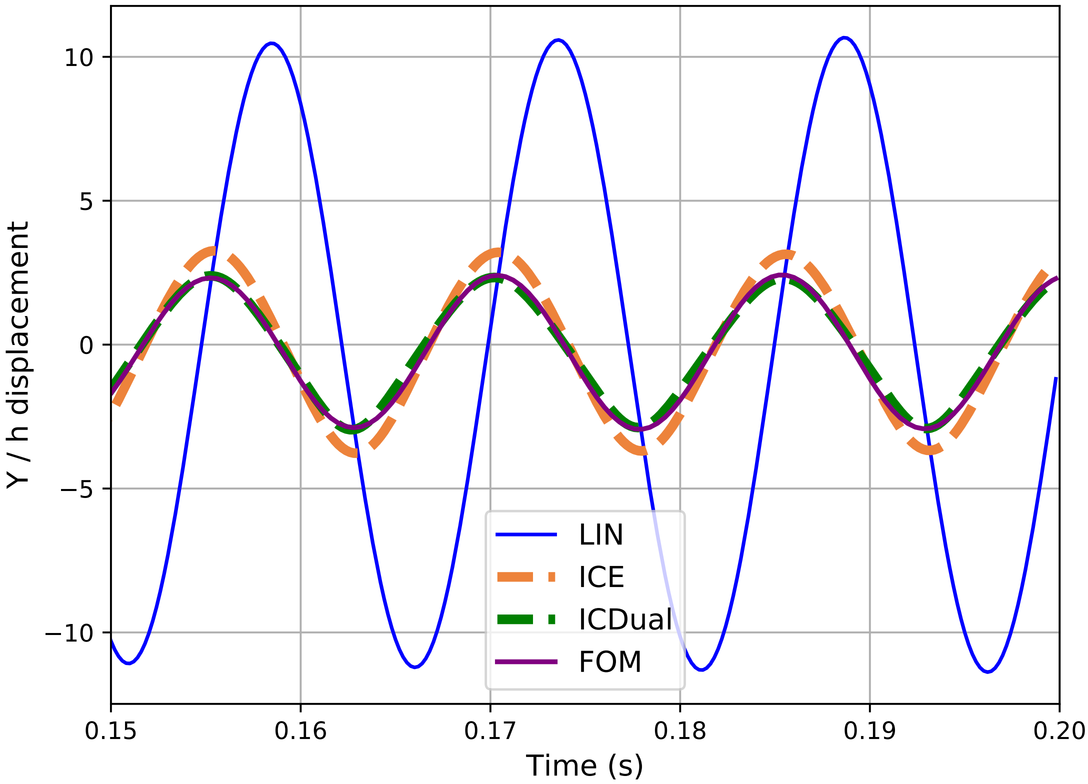

Figure 6.21: Time response of the tip leading edge along the Y direction.

As expected, the levels of vibration of the nonlinear models are much lower than the linear one. There is a significant difference between the ICE and ICDual ROMs, the latter resulting in lower levels of vibrations that are closer to those obtained with the FOM computation. The computations of the FOM dynamic solution take about 10 hours using parallel computing and a significant memory with the solver *Code_Aster*, while the resolution with the ROMs takes less than 10 seconds on a single processor. The ICDual ROM built on the centrifugally prestressed position captures accurately the geometrically nonlinear vibrations of the blade.

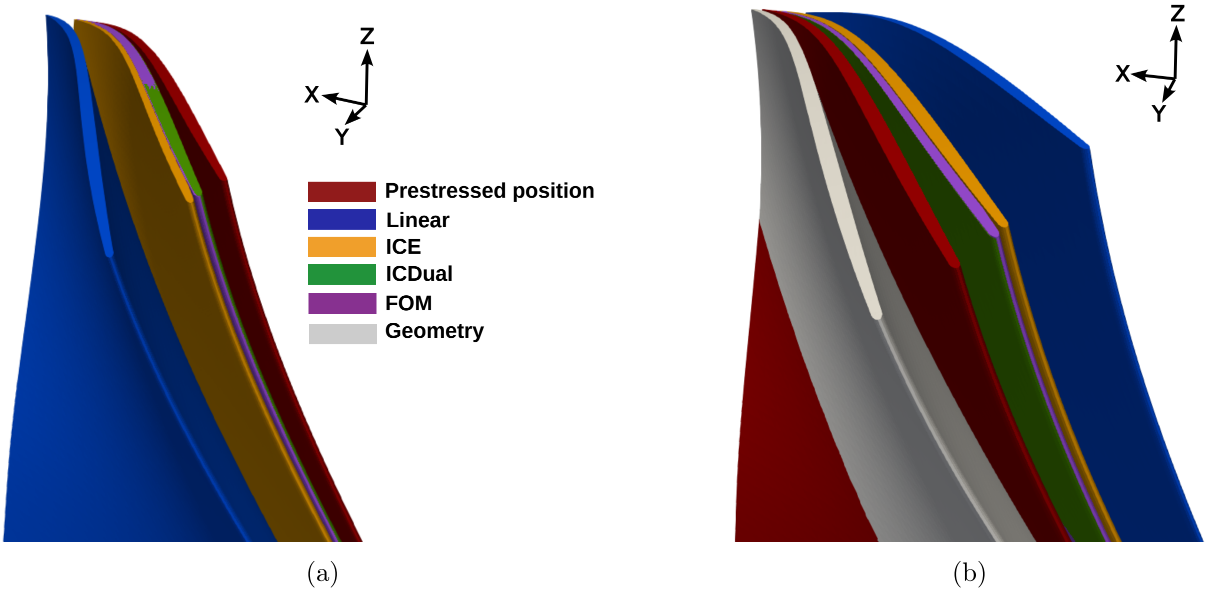

Figure 6.22: Maximal positive (a) and negative (b) displacements in periodic regime of the different models.

6.6 Conclusion of the chapter

In this chapter, the reduction method ICDual is applied to a complex 3D geometry of a turbomachine blade, prestressed due to the centrifugal rotation. An arbitrary static load is first applied, then a dynamic load based on unsteady aerodynamic loads. The shape of the aerodynamic loads was obtained from a CFD computation of the full 360° fan-OGV-nacelle configuration of the UHBR engine. Both for the static and the dynamic load cases, the ICDual ROM captured accurately the nonlinear displacements of the blade. The precision of the ROM opens the perspective of a strong coupling in the future, in particular for open rotor and stator engine configurations with blades of large diameters.

Conclusion and perspectives

The aim of this thesis work was to develop a methodology for the construction of a reduced order model for geometrically nonlinear structures. In addition, this reduced model should enable simple coupling with an external fluid solver to perform fluid-structure computation in order to study aeroelastic applications. We present here the general conclusions of the work carried out in this manuscript, followed by perspectives and a critical look at the work.

Conclusion

In this work we first focused on the formalism of the equations governing the vibration of geometric non-linear structures in rotation, along with temporal and frequency methods of resolution. We then conducted a literature review of reduced order models adapted to geometric nonlinearities. In view of the constraints in terms of coupling, the non-intrusive approach and the reduced number of modes desired in the reduction base, the use of dual modes was considered a relevant candidate. We thus developed a methodology for the construction of the reduced order model based on dual modes and including an innovative way of calculating the coefficients of projected non-linear forces via the application of imposed loads. The advantage is that the imposed loads used to determine the dual modes are reused to calculate the above-mentioned coefficients, thus limiting the number of static calculations required. In addition, the application of loads bypasses a problem encountered with 3D structure for the identification of the coefficients by imposed displacements, which produces numerical artefacts in the resolution due to imposed volume deformations.

A first application was carried out on a von Kármán beam, demonstrating the ability of such a reduced order model to accurately capture the nonlinear dynamic behavior under various loads: punctual, distributed and follower. Both the non-rotating case and the case of the beam in rotation around a fixed axis were tackled. This is followed by an application to the 3D finite element case on the same geometry, where the non-intrusive approach to an external finite element solver makes sense.

The second area of study concerned the fluid-structure coupling based on the ALE formulation along with the issues of mesh deformation and transfer of forces and displacements between non-coincident meshes. The aim being to be able to handle industrial configurations, we chose a partitioned coupling between two separate solvers: one for the fluid and another for the structure. As the scope of this thesis is restricted to model order reduction for the structure only, it is necessary to be able to simply connect ours to any external fluid solver to perform partitioned coupling. A fluid-structure interaction application is performed between the von Kármán beam previously studied and the vortex wake behind a fixed cylinder to which the beam is attached. The results obtained with the reduced model accurately reflect the solutions of the full model and the lock-in phenomenon is very well captured, both in terms of frequency range and amplitude of vibrations observed.

The last study of this work concerns the application to the case of a turbomachine fan blade. This case is complex in terms of number of degrees of freedom and of geometry. We built the reduced order model around an operating point and conducted a first study of the accuracy of the reduced order model on arbitrary static loading cases. Given the good agreement with the high-fidelity solution, we then turned our attention to unsteady aerodynamic loads. To this end, we performed an unsteady CFD calculation on the complete 360° configuration of the engine and recovered the forces acting on the blade. The forces were characterized by a periodic forcing at the engine rotation frequency resulting from nacelle asymmetry. We identified the distribution of the harmonic components of the forces acting on the blade and built an unsteady force on which we based our comparison between the reduced model and the high-fidelity solution. Even though the case studied is complex, the reduced order model accurately retrieves the full order solution.

Discussion and perspectives

The dual modes approach is interesting because it is non-intrusive and independent of a given loading case. It means that the modes obtained can be used for different loading cases. In addition, the singular value decomposition allows control of the desired accuracy regarding the residual of the imposed loading cases. However, it has been observed in some cases that there may be no clear drop in the singular values, which in some cases means that numerous dual modes should be taken into account. For this reason, the additional criterion in terms of linearized strain energy is relevant. It enables to dissociate the dual modes candidates that contribute the most to the linear part of the system's energy from those that contribute the least.

One of the aims of this thesis is to build a reduced model that is non-intrusive. Non-intrusiveness is important because it enables the use of industrial finite element codes. These codes are optimized and rich in complex elements, making them ideally suited to complex aeronautical structures. However, they do not allow intrusive access to the core of the code for reasons of industrial secrecy. The non-intrusive character of the reduced model is therefore necessary. However, it is also a very strong constraint when dealing with the determination of the projected non-linear forces coefficients. A non-intrusive determination of the coefficients of the projected non-linear forces is difficult, both with imposed displacements and with imposed forces. In the first case, the coefficients can be determined one by one, but we have pointed out that imposing displacements leads to erroneous volume deformations which pollute the identification of the coefficients. This is not the case when imposed forces are used. Nevertheless, the identification of the coefficients is no longer done separately in this case, but by solving an often ill-conditioned global system. To limit this, we proposed the determination of quadratic and cubic coefficients separately (when available), as well as a method of determination using the tangent stiffness matrix. In addition, precautions are taken and detailed in section 3.3 to improve the resolution of the system computing the projected non-linear force coefficients. The non-intrusive approach therefore results in a compromise between improved accuracy through the addition of more dual modes, and a possibly less accurate determination of the coefficient in the presence of many modes. It would be interesting to adopt a stochastic approach to assess the uncertainty in determining the coefficients. Work on this subject can be found in the literature, for example in [20, 21, 146].

Regarding the structural reduced order model, an interesting prospect would be the construction of a parametric reduced order model as a function of the rotation velocity to deal with different operating points. Work has already been done to interpolate the matrices in linear cases [105] and for the prestressed displacement in [182]. A Gaussian parametric approach to projected nonlinear coefficients is proposed in [139] for the ICE method, an extension to the reduced model built in this thesis is conceivable. Regarding the parametrization as a function of rotation speed, it is worth mentioning that an intrusive approach based on the parametrization of invariant manifolds is presented in [117].

In the literature, mistuning is one of the problems associated with rotating structures and aeroelasticity. This problem is not dealt with in this thesis and deserves special attention. Indeed, applications to mistuning of geometric nonlinear reduced models can be found in the literature [20, 146, 153]. It is conceivable to use the reduced order model presented in this work to study cases of mistuning, whether it is due to a manufacturing defect or intentional to avoid possible instabilities.

It is true that for a large proportion of aeroelastic applications, the computational cost is mainly driven by the resolution of the fluid rather than the structure. However, for industrial applications involving complex structures, the computational cost of the structure becomes significant. Furthermore, the coupling with a complex fluid solver leads to takes a considerable amount of time due to the coupling sub-iterations and the information transfer between the solvers. It is worth mentioning that simplified fluid dynamics models are also available in the literature, for instance the Theodorsen [185] or lifting line [152] theories. In these cases, it is not the fluid but the structure that requires the most computational resources. The long-term perspective is to use reduced order models both for the structure and the fluid to be efficient in both fields. While the scope of this thesis was restricted solely to the construction of the former, there are reduction methods in the literature for the fluid as well. In this work, a case of strong coupling was performed on a 2D configuration of a flexible beam placed in the vortex wake of a fixed cylinder. An obvious prospect is the study of a strong coupling case in the context of an industrial application. The work presented in this manuscript thus opens the door to many perspectives and improvements. The reduced order model developed in this thesis is not restricted to turbomachine applications. Helicopter blades, aircraft propeller, wind turbines and VTOL aircrafts face the problematic of geometric nonlinearities in rotating structures. Non-rotating structures can also be studied with such reduced order model, for example the large aspect ratio wings of future aircrafts. A partitioned coupling between the reduced order model and a fluid solver enables the study of nonlinear aeroelastic phenomena with strong coupling algorithms and at reasonable costs. Such an approach makes it possible to perform numerical simulations of aeroelastic phenomena encountered in aeronautics, for instance forced response, flutter, lock-in and limit cycles or gust response. One can also think of aeroelastic phenomena specific to turbomachines such as rotating stall or surge.

List of communications

Congress proceedings

- T. Flament, J.-F. Deü, A. Placzek, M. Balmaseda, D.-M. Tran, *Modèle d'ordre réduit pour les vibrations en grande amplitude de structures flexibles sous écoulement fluide.* 15$^{\text{ème}}$ colloque national en calcul des structures, Mai 2022, Giens (Var), France.
- T. Flament, J.-F. Deü, A. Placzek, M. Balmaseda, D.-M. Tran. *Reduced-order model for large amplitude vibrations of flexible structures coupled with a fluid flow.* ECCOMAS (8th European Congress on Computational Methods in Applied Sciences and Engineering), June 2022, Oslo, Norway.
- T. Flament, J.-F. Deü, A. Placzek, M. Balmaseda, D.-M. Tran. *Reduced order model of nonlinear structures for turbomachinery aeroelasticity*, Turbo Expo, June 2023, Boston, USA.
- M. Balmaseda, L. Bernardo Barreda, T. Flament, M.-A. Garcia Bravo *Rapid methods for the aeroelastic analysis of VTOL blades in hover flight*, 79th Annual Forum & Technology Display, West Palm Beach, United States, 2023.

Journal articles

- T. Flament, J.-F. Deü, A. Placzek, M. Balmaseda, D.-M. Tran. *Reduced-order model of geometrically nonlinear flexible structures for fluid-structure interaction applications.* International Journal of Non-Linear Mechanics, 158:104587, 2024.
- T. Flament, J.-F. Deü, A. Placzek, M. Balmaseda, D.-M. Tran. *Reduced order model of nonlinear structures for turbomachinery aeroelasticity*, Journal of Engineering for Gas Turbine and Power, 146(3):031005, 2024.

Appendix

Appendix A

Monolithic coupling between the fluid flow and a flexible beam

In this section, a monolithic approach of the fluid-structure interaction problem presented in chapter 5 is considered. The fluid equation is the incompressible Navier-Stokes equation and the structure follows the Saint Venant-Kirchhoff model. Both the fluid and the solid equations are written in the Lagrangian form in the reference frame. The fluid-structure interface conditions are imposed thanks to Lagrangian multipliers. The associated equations are developed in [145] and not rewritten here for brevity and to avoid the introduction of numerous notations used in this appendix only. As in [145], the equations are scaled with relevant quantities for non-dimensionalization. The difference with the approach in section 5 are thus the monolithic approach, the incompressibility hypothesis and the 2D FE approach for the structure.

The computation is performed with the FEniCSx Finite Element Python library and the systems are solved with PETSc. The time integration scheme considered is the second-order implicit Backward Differentiation scheme (BDF2) [15, 61] and the associated system is solved with a GMRES solver with the usual jacobi preconditioner. It is worth mentioning that the jacobi preconditioner is not particularly relevant for fluid-structure interaction problems due to the particular shape of the system. More relevant preconditioners are for instance proposed in [89, 145]. The time step is equal to 200 iterations per estimated period. The estimated period is based on the strouhal number of the cylinder alone problem and the Roshko formula stipulating: $St = 0.212 - 2.7/R_e$.

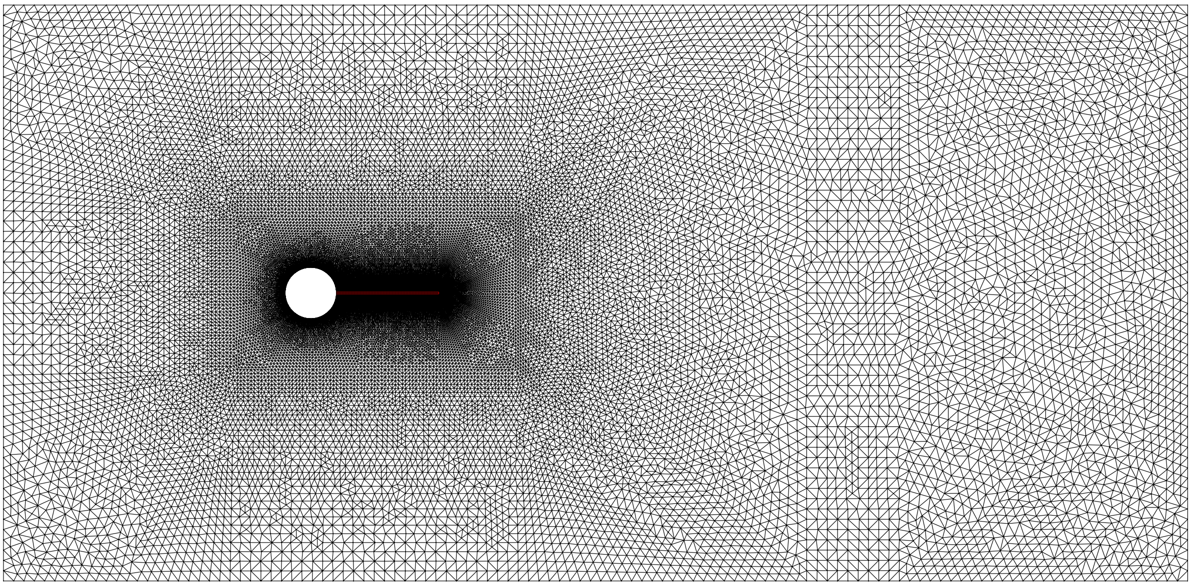

Figure A.1: Unstructured mesh of the FSI problem with the beam and the cylinder.

The mesh is unstructured with 2D tetrahedral elements. The total mesh for both the fluid and the structure consists in 66,141 cells and 33,343 points and is illustrated in Figure A.1. A zoom in the vicinity of the beam is shown in Figure A.2, in which the fluid-structure interface is highlighted in red. The boundary conditions are the same as those in 5.1.

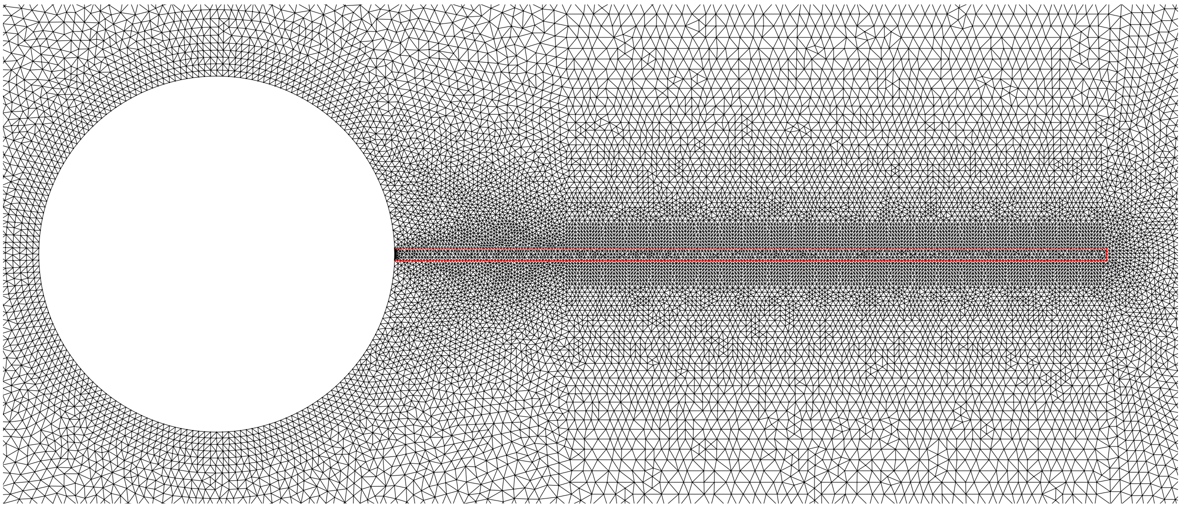

Figure A.2: Zoom of the unstructured mesh in the vicinity of the cylinder and the beam. The fluid-structure interface is highlighted in red (-).

The mesh deformation technique is the solid deformation analogy with variable stiffness based on the cell size. Figure A.3 illustrates the mesh deformation of the beam at a given time.

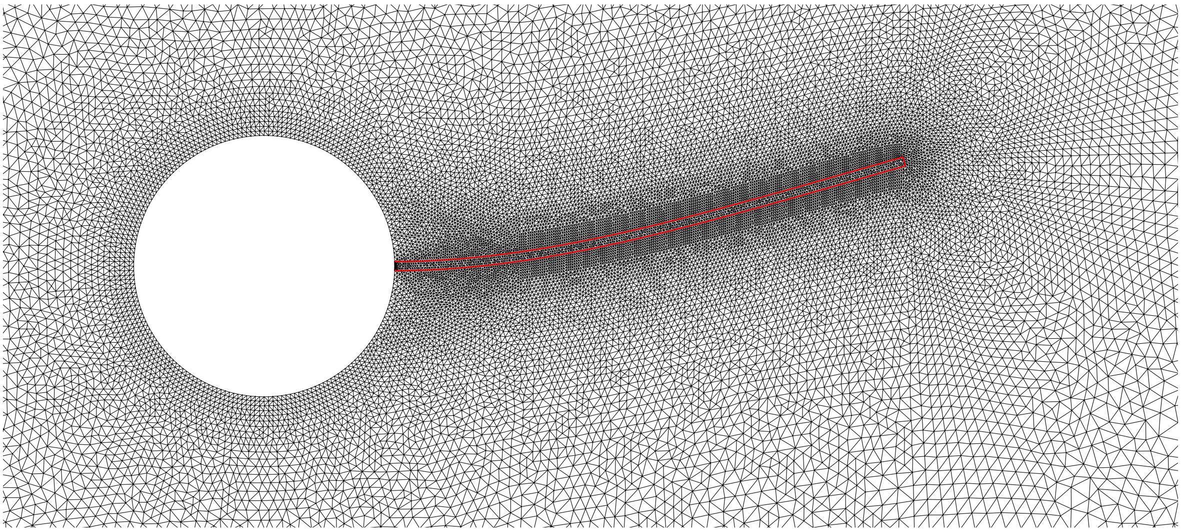

Figure A.3: Visualization of the mesh deformation around the beam.

Figure A.4 shows the velocity field at a given time both in the reference and the deformed configurations. Figure A.5 displays the vorticity field in both configurations at the same time.

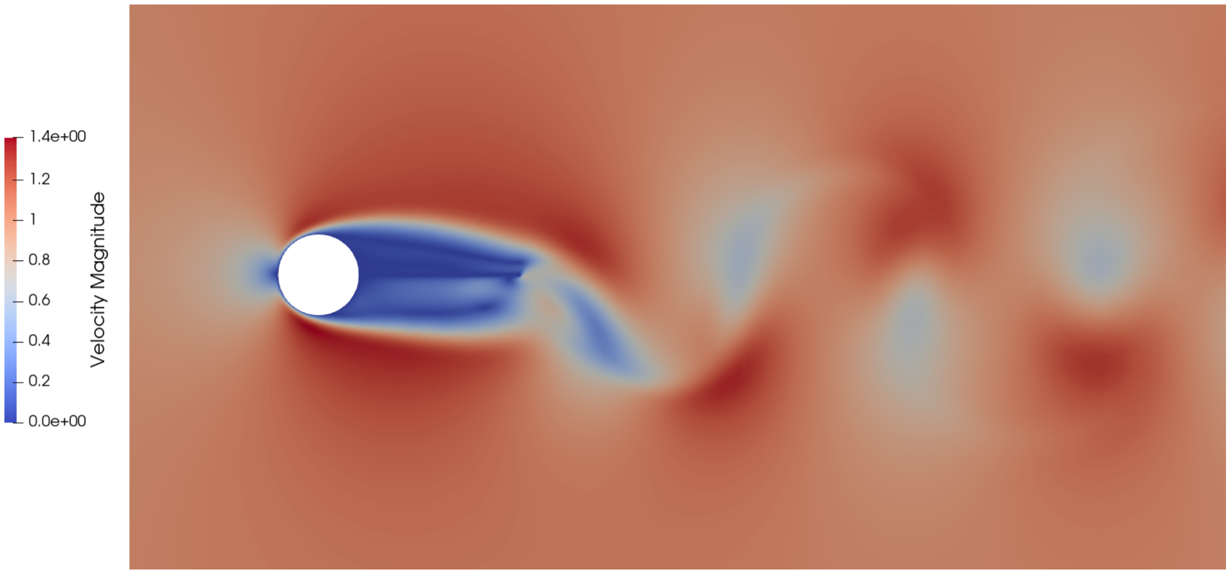

(a) Reference configuration

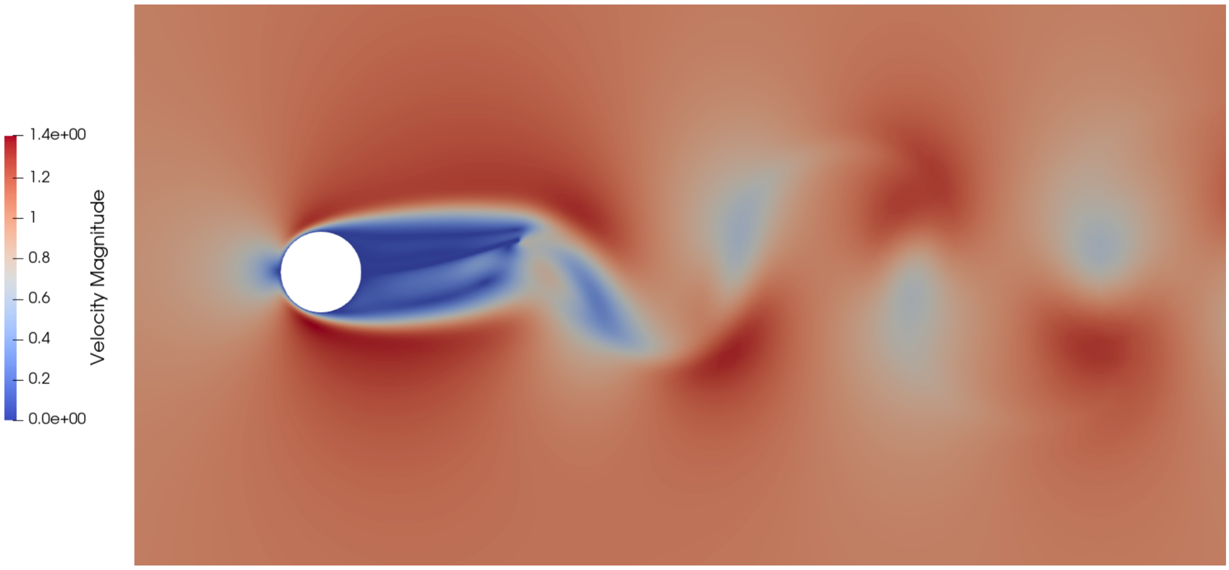

(b) Deformed configuration

Figure A.4: Velocity field of the monolithic cylinder-beam FSI application respectively in the reference (a) and deformed (b) configurations.

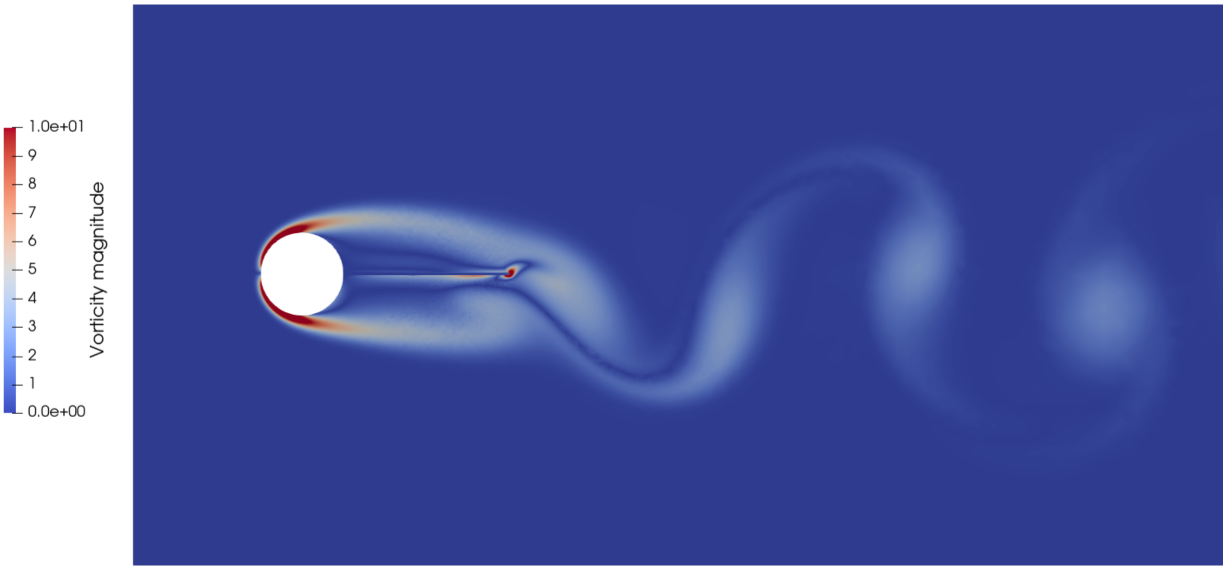

(a) Reference configuration

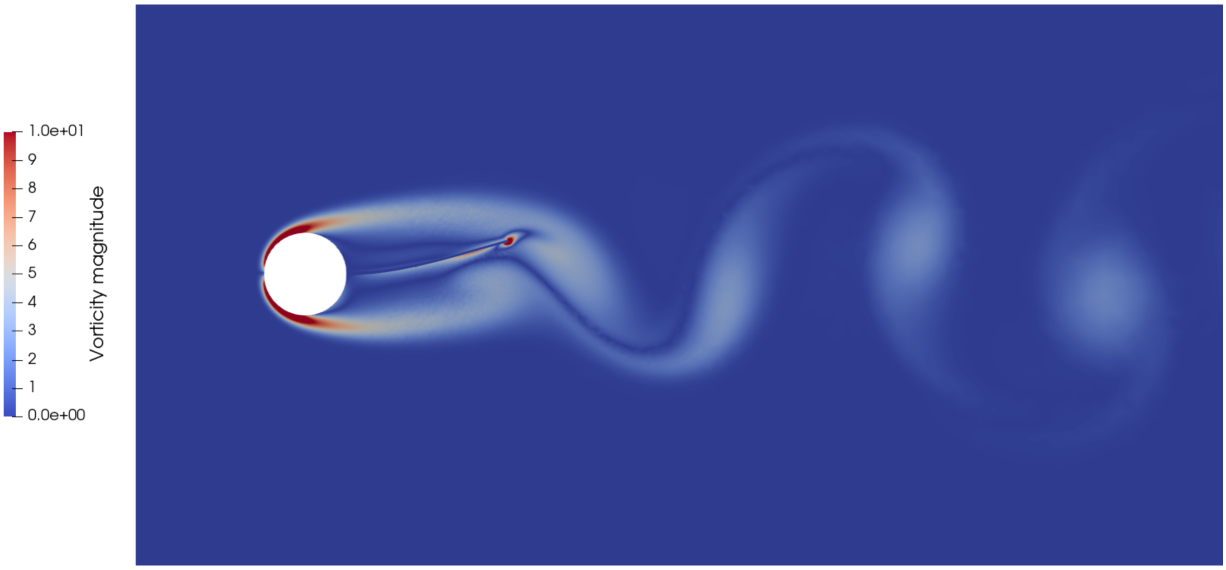

(b) Deformed configuration

Figure A.5: Vorticity field of the monolithic cylinder-beam FSI application respectively in the reference (a) and deformed (b) configurations.

The vertical and axial temporal displacements of the beam's tip are plotted in Figure A.6. The order of magnitude of the amplitudes of displacement are similar as in chapter 5 despite the main differences in implementation that are the incompressibility of the fluid and the FE formulation for the structure.

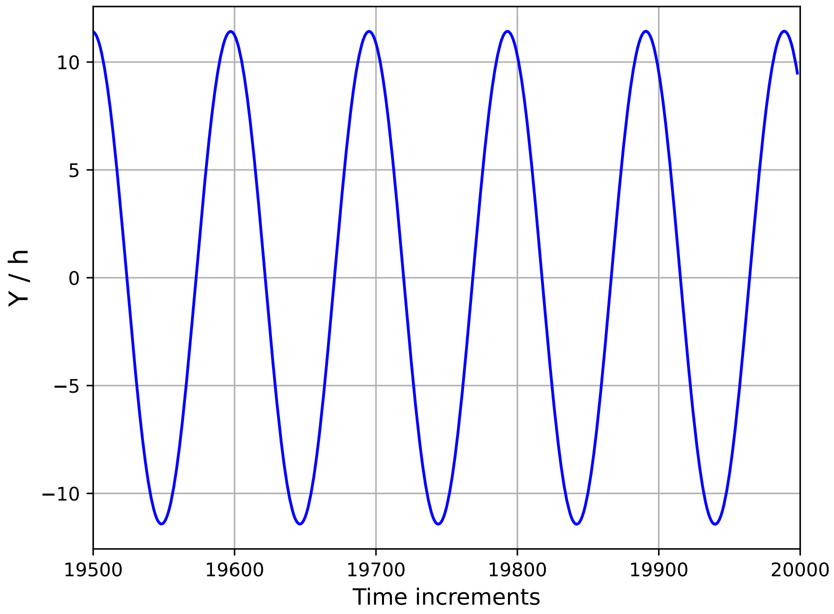

(a)

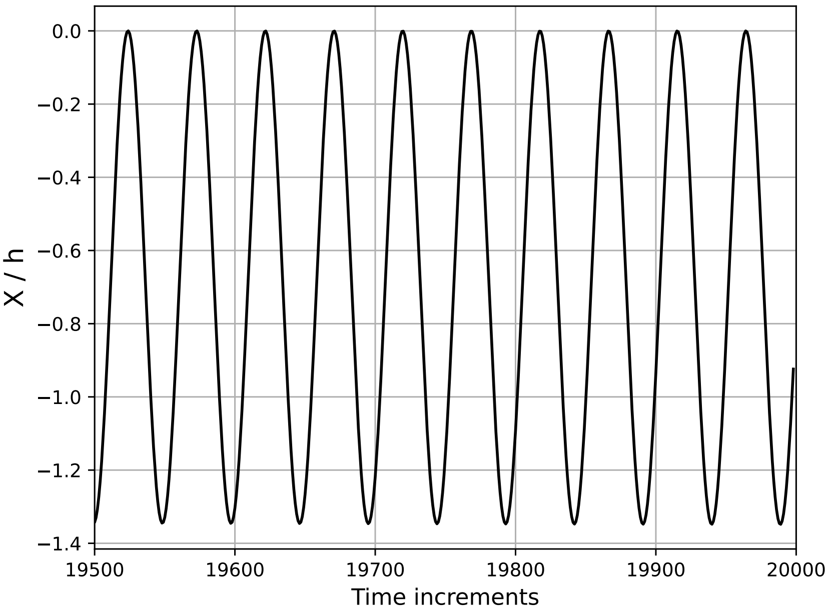

(b)

Figure A.6: Vertical (a) and axial (b) displacement of the beam tip.

APPENDIX B

Comparison of the results with the Direct Normal Form reduction technique

B.1 Direct normal form reduction method with a single master mode and damping

In this appendix, the Direct Normal Form (DNF) reduction method [202] is applied to the von Kármán beam applications and the 3D beam applications. The DNF method is a non-intrusive method to perform a reduction to the normal form up to the third order with an external FE solver. The coefficients of the normal form are computed via imposed displacements. In this section, the reduction to a single master mode is considered, and damping is included. Under such considerations, the reduced dynamics takes the following form:

$$\ddot{R}_1 + (\zeta_m + \zeta_K \omega_1^2)\dot{R}_1 + \omega_1^2 R_1 + (A^1_{111} + h^1_{111})R_1^3 + B^1_{111} R_1 \dot{R}_1^2 + C^1_{111} R_1^2 \dot{R}_1 = 0, \tag{B.1}$$

with R_1 the normal coordinate along the master mode, ω_1 the pulsation of the linear normal associated to the master mode, ζ_m and ζ_K the Rayleigh damping coefficients and A^1_{111}, h^1_{111}, B^1_{111}, C^1_{111} the coefficients of the reduction to the normal form whose expressions will be detailed further. The equation of the dynamics in the normal form (B.1) is defined with no second member. Indeed, the expression of the coefficients and mappings are deduced from the equation without second member. The external load specific to the loading case is then projected on the linear normal master mode and added on the right side of Equation (B.1). It is also possible to include the external load during the construction of the model [138], which leads to a time-dependent manifold. In this section, the notations of the article are kept for a better understanding since only a few details are provided in this appendix.

The physical degrees of freedom are written $\mathbf{X}$ and the velocities $\dot{\mathbf{X}}$. In the damped case, the article [202] provides the formulas for a quadratic mapping between the normal and modal coordinates:

$$\mathbf{X} = \phi_1 R_1 + \bar{\mathbf{a}}_{\mathbf{11}} R_1^2 + \bar{\mathbf{b}}_{\mathbf{11}} \dot{R}_1^2 + \bar{\mathbf{c}}_{\mathbf{11}} R_1 \dot{R}_1, \tag{B.2}$$

$$\dot{\mathbf{X}} = \phi_1 \dot{R}_1 + \bar{\boldsymbol{\alpha}}_{\mathbf{11}} R_1^2 + \bar{\boldsymbol{\beta}}_{\mathbf{11}11} \dot{R}_1^2 + \bar{\boldsymbol{\gamma}}_{\mathbf{11}} R_1 \dot{R}_1, \tag{B.3}$$

with ϕ_1 the linear normal mode considered as master mode, R_1 the normal coordinate of the master mode and $\bar{\mathbf{a}}_{\mathbf{11}}, \bar{\mathbf{b}}_{\mathbf{11}}, \bar{\mathbf{c}}_{\mathbf{11}}, \bar{\boldsymbol{\alpha}}_{\mathbf{11}}, \bar{\boldsymbol{\beta}}_{\mathbf{11}}$, $\bar{\boldsymbol{\gamma}}_{\mathbf{11}}$ the different mappings. The determination of the mappings and normal form coefficients is non-intrusive and incremental. The first step consists in evaluating the quadratic form $\mathbf{G}(\phi_1, \phi_1)$ by imposing to the structure the displacements $q_1\phi_1$ and its opposite and in computing the associated internal nonlinear forces:

$$\mathbf{G}(\phi_1, \phi_1) = \frac{1}{2q_1^2}\left[\mathbf{f_{nl}}(q_1\phi_1) + \mathbf{f_{nl}}(-q_1\phi_1)\right]. \tag{B.4}$$

The amplitude of the displacement imposed along the linear normal mode ϕ_1 is controlled by the chosen amplitude q_1. The vector $\mathbf{G}(\phi_1, \phi_1)$ corresponds to the quadratic part of the internal nonlinear forces resulting from a displacement $\phi_1 q_1$. The cubic part of such a displacement is given by:

$$\mathbf{H}\left(\phi_1,\phi_1,\phi_1\right) = \frac{1}{2q_1^3}\big[\mathbf{f_{nl}}(q_1\phi_1) - \mathbf{f_{nl}}(-q_1\phi_1)\big]. \tag{B.5}$$

The mappings in the expressions (B.2) are all determined thanks to the intermediate vectors $\bar{\mathbf{Z}}_{\mathbf{s11}}, \bar{\mathbf{Z}}_{\mathbf{d11}}$ and $\bar{\mathbf{Z}}_{\mathbf{ss11}}$ defined by:

$$\bar{\mathbf{Z}}_{\mathbf{s11}} = \left[4\omega_1^2\mathbf{M} - \mathbf{K}\right]^{-1}\mathbf{G}\left(\phi_1,\phi_1\right), \tag{B.6}$$
$$\bar{\mathbf{Z}}_{\mathbf{d11}} = -\mathbf{K}^{-1}\mathbf{G}\left(\phi_1,\phi_1\right), \tag{B.7}$$
$$\bar{\mathbf{Z}}_{\mathbf{ss11}} = \left[4\omega_1^2\mathbf{M} - \mathbf{K}\right]^{-1}\mathbf{M}\bar{\mathbf{Z}}_{\mathbf{s11}}, \tag{B.8}$$

with $\mathbf{M}$ and $\mathbf{K}$ the mass and stiffness matrices respectively. From those vectors, the expression of the mappings are:

$$\bar{\mathbf{a}}_{\mathbf{11}} = \frac{1}{2}(\bar{\mathbf{Z}}_{\mathbf{d11}} + \bar{\mathbf{Z}}_{\mathbf{s11}}), \tag{B.9}$$
$$\bar{\mathbf{b}}_{\mathbf{11}} = \frac{1}{2\omega_1^2}(\bar{\mathbf{Z}}_{\mathbf{d11}} - \bar{\mathbf{Z}}_{\mathbf{s11}}), \tag{B.10}$$
$$\bar{\mathbf{c}}_{\mathbf{11}} = \frac{\bar{\mathbf{Z}}_{\mathbf{d11}}}{2}\left(\frac{1}{\omega_1^2}\zeta_M + \zeta_K\right) - \frac{\bar{\mathbf{Z}}_{\mathbf{s11}}}{2}\left(\frac{1}{\omega_1^2}\zeta_M + 5\zeta_K\right) + 2\bar{\mathbf{Z}}_{\mathbf{ss11}}(2\omega_1^2\zeta_K - \zeta_M), \tag{B.11}$$
$$\bar{\boldsymbol{\alpha}}_{\mathbf{11}} = -\omega_1^2\bar{\mathbf{c}}_{\mathbf{11}}, \tag{B.12}$$
$$\bar{\boldsymbol{\beta}}_{\mathbf{11}} = \bar{\mathbf{c}}_{\mathbf{11}} - 2(\zeta_M + \zeta_K\omega_1^2)\bar{\mathbf{b}}_{\mathbf{11}}, \tag{B.13}$$
$$\bar{\boldsymbol{\gamma}}_{\mathbf{11}} = 2\bar{\mathbf{Z}}_{\mathbf{s11}}. \tag{B.14}$$
$$\tag{B.15}$$

Finally, the coefficients $A_{111}^1, B_{111}^1, C_{111}^1$ and h_{111}^1 in the reduced dynamics (B.1) are given by the expressions:

$$A_{111}^1 = 2\phi_1^T\mathbf{G}\left(\phi_1,\bar{\mathbf{a}}_{\mathbf{11}}\right), \tag{B.16}$$
$$B_{111}^1 = 2\phi_1^T\mathbf{G}\left(\phi_1,\bar{\mathbf{b}}_{\mathbf{11}}\right), \tag{B.17}$$
$$C_{111}^1 = 2\phi_1^T\mathbf{G}\left(\phi_1,\bar{\mathbf{c}}_{\mathbf{11}}\right), \tag{B.18}$$
$$h_{111}^1 = 2\phi_1^T\mathbf{H}\left(\phi_1,\phi_1,\phi_1\right), \tag{B.19}$$

where $\mathbf{G}\left(\phi_1,\bar{\mathbf{a}}_{\mathbf{11}}\right), \mathbf{G}\left(\phi_1,\bar{\mathbf{b}}_{\mathbf{11}}\right)$ and $\mathbf{G}\left(\phi_1,\bar{\mathbf{c}}_{\mathbf{11}}\right)$ are quadratic forms evaluated by imposing displacements to the structure. For instance, $\mathbf{G}\left(\phi_1,\bar{\mathbf{a}}_{\mathbf{11}}\right)$ is obtained by first imposing the displacements $q_a\bar{\mathbf{a}}_{\mathbf{11}}$ and its opposite to compute the quadratic part of the nonlinear internal forces associated to the displacement $q_a\bar{\mathbf{a}}_{\mathbf{11}}$: $\mathbf{G}\left(\bar{\mathbf{a}}_{\mathbf{11}},\bar{\mathbf{a}}_{\mathbf{11}}\right)$:

$$\mathbf{G}\left(\bar{\mathbf{a}}_{\mathbf{11}},\bar{\mathbf{a}}_{\mathbf{11}}\right) = \frac{1}{2q_a^2}\big[\mathbf{f_{nl}}(q_a\bar{\mathbf{a}}_{\mathbf{11}}) + \mathbf{f_{nl}}(-q_a\bar{\mathbf{a}}_{\mathbf{11}})\big]. \tag{B.20}$$

Then, the displacement $q_1\phi_1 + q_a\bar{\mathbf{a}}_{\mathbf{11}}$ and its opposite are imposed to the structure to get the resulting internal nonlinear forces and compute the vector $\mathbf{G}\left(\phi_1,\bar{\mathbf{a}}_{\mathbf{11}}\right)$:

$$\mathbf{G}\left(\phi_1,\bar{\mathbf{a}}_{\mathbf{11}}\right) = \frac{1}{4q_1q_a}\big[\mathbf{f_{nl}}(\phi_1q_1 + \bar{\mathbf{a}}_{\mathbf{11}}q_a) + \mathbf{f_{nl}}(-q_1\phi_1 - q_a\bar{\mathbf{a}}_{\mathbf{11}}) - 2q_1^2\mathbf{G}\left(\phi_1,\phi_1\right) - 2q_a^2\mathbf{G}\left(\bar{\mathbf{a}}_{\mathbf{11}},\bar{\mathbf{a}}_{\mathbf{11}}\right)\big] \tag{B.21}$$

The vectors $\mathbf{G}\left(\phi_1,\bar{\mathbf{a}}_{\mathbf{11}}\right), \mathbf{G}\left(\phi_1,\bar{\mathbf{b}}_{\mathbf{11}}\right)$ and $\mathbf{G}\left(\phi_1,\bar{\mathbf{c}}_{\mathbf{11}}\right)$ are obtained with an analogous process.

B.2 Application to the von Kármán beam model

In this section, the DNF reduction technique is applied to the case of the von Kármán beam of section 2.3. Dynamic load cases are considered and the solutions are compared to those obtained with the ICE and ICDual models. First the non-rotating case of the beam considered, then the beam is in rotation around the vertical axis at 500 rpm.

B.2.1 Non-rotating case

The first application consists in the beam from section 2.3 without centrifugal rotation. Three different load cases entitled D1, D2, D3 are considered:

- D1: A vertical load uniformly distributed along the beam of 1,400 N/m.
- D2: A vertical load of amplitude 2,500 N at the tip of the beam.
- D3: A follower load of amplitude 2,500 N at the tip of the beam.

The loads D1 and D3 were already tackled with the linear, ICE and ICDual methods in section 2.3. The results are here compared with those of the DNF method. Figure B.1 illustrates the beam's tip vertical and axial displacements in periodic regime under the load case D2. The relative errors in amplitude regarding the nonlinear FOM solution for the three load cases are gathered in Tables B.1 and B.2.

Table B.1: Relative error, for the different dynamic load cases, of the maximal vertical displacement of the beam tip in periodic regime. Comparison between the reference nonlinear FOM model, the linear FOM, ICE ROM, ICDual ROM and DNF models.

	Relative error of the tip Y displacement (%)		
Load case	D1	D2	D3
Linear FOM	2.63	4.29	2.47
ICE ROM	2.63	4.29	2.47
ICDual ROM	2.02×10^{-4}	3.63×10^{-3}	3.64×10^{-3}
DNF ROM	6.69×10^{-1}	8.07×10^{-1}	8.93×10^{-1}

Table B.2: Relative error, for the different dynamic load cases, of the maximal axial displacement of the beam tip in periodic regime. Comparison between the reference nonlinear FOM model, the linear FOM, ICE ROM, ICDual ROM and DNF models.

	Relative error of the tip X displacement (%)		
Load case	D1	D2	D3
Linear FOM	100	100	100
ICE ROM	5.18	8.67	4.92
ICDual ROM	6.27×10^{-4}	8.04×10^{-3}	8.18×10^{-3}
DNF ROM	1.20	1.55	1.84

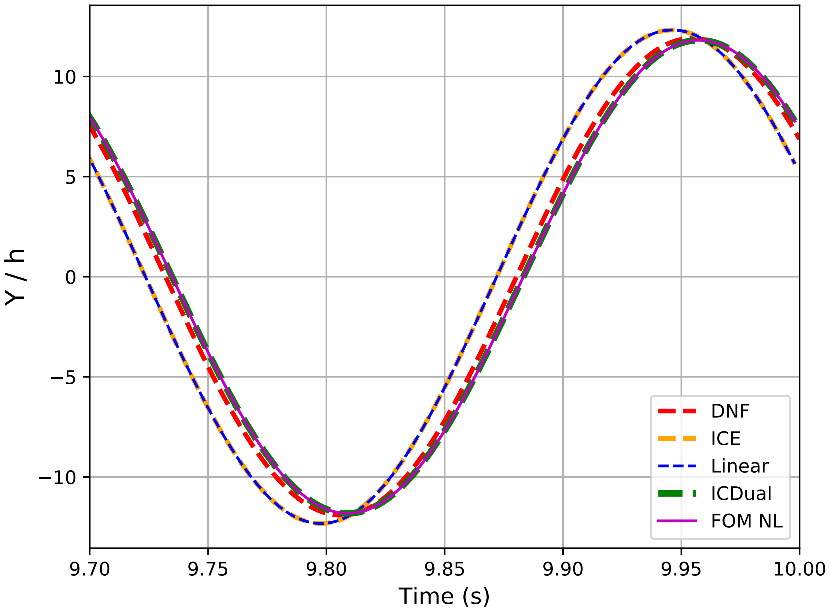

(a) Vertical displacement

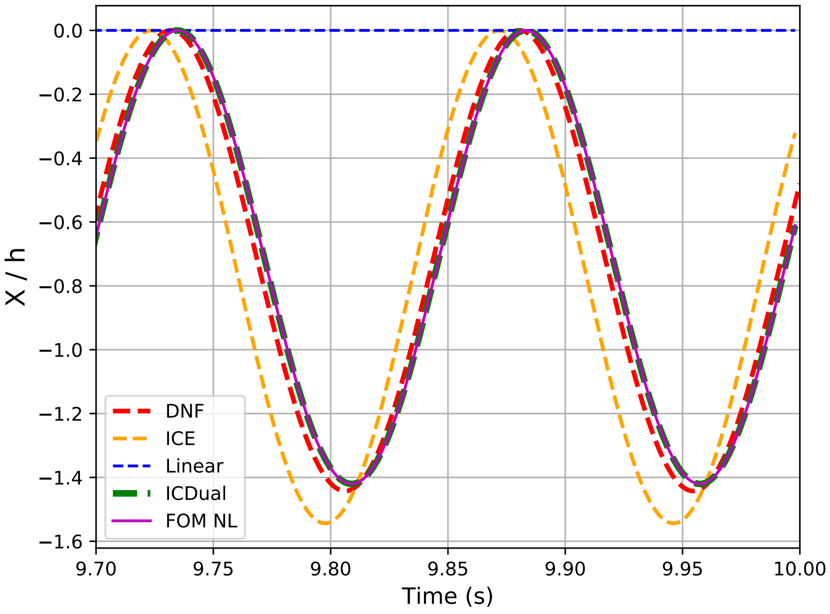

(b) Axial displacement

Figure B.1: Nonlinear dynamic displacement of the clamped-free von Kármán beam under the dynamic load case D2. Comparison of the vertical (a) and axial (b) displacements at the tip of the beam in periodic regime between the nonlinear FE, ICE, ICDual and DNF solutions.

The loads are periodic at the frequency of the first linear normal mode. The DNF ROM considered is thus defined with one master mode which is the first linear normal mode. With only one mode, the results are particularly accurate for the three load cases. An error slightly above the percent is observed for the axial displacement but the result is however still better than the ICE method with 3 modes. The phase shifts of the different models are gathered in Table B.3.

Table B.3: Phase shift in periodic regime at the beam tip for the different dynamic load cases. Comparison between the reference nonlinear FOM model, the linear FOM, ICE ROM, ICDual ROM and DNF models.

	Phase shift (°)		
Load case	D1	D2	D3
Linear FOM	9.7	12.1	12.1
ICE ROM	9.7	12.1	12.1
ICDual ROM	0	0	0
DNF	3.5	2.3	2.3

Vertical load at tip at a different excitation frequency
In the previous test cases, the frequency of excitation of the external loads was exactly the one of the first linear normal mode considered as master mode. Here, the frequency of excitation is slightly shifted to 5 Hz, which is still in the vicinity of the frequency of the first linear normal mode (3.38 Hz) but far from the frequency of the second mode (21.21 Hz). The DNF ROM is not changed and the external load considered is the vertical load at the tip of the beam with amplitude 2,500 N and frequency 5 Hz. It corresponds to the load case D2 with a frequency of 5 Hz. With such excitation, the amplitudes of vertical displacement are close to the linear range, but an axial displacement is observed anyway and absent from the linear solution. Figure B.2 illustrates the vertical and axial displacements of the beam's tip in periodic regime and the quantitative errors are gathered in B.4.

Table B.4: Relative error of the maximal displacement of the beam tip in periodic regime under a vertical load at tip of amplitude 2,500 N and frequency 5 Hz. Comparison between the reference nonlinear FOM model, the linear model, the ICE, ICDual and DNF ROMs.

	Relative error of the tip displacement (%)	
	Y component	X component
Linear	3.24×10^{-2}	100
ICE	2.19×10^{-1}	4.77×10^{-1}
ICDual	1.86×10^{-1}	4.49×10^{-1}
DNF	4.12	12.02

In such a case, the DNF method tends to overestimate the displacements. The latter are small and perfectly captured by the ICE method. The phase shifts are however negligible with all models: 0.18° for the DNF method and 0° for the linear, ICE and ICDual methods. Since the excitation frequency does not correspond to the frequency associated to the master mode, the DNF method is slightly inaccurate. To improve the results, it could be interesting to use several master modes, or higher orders of nonlinear developments in the normal form (via an intrusive approach however).

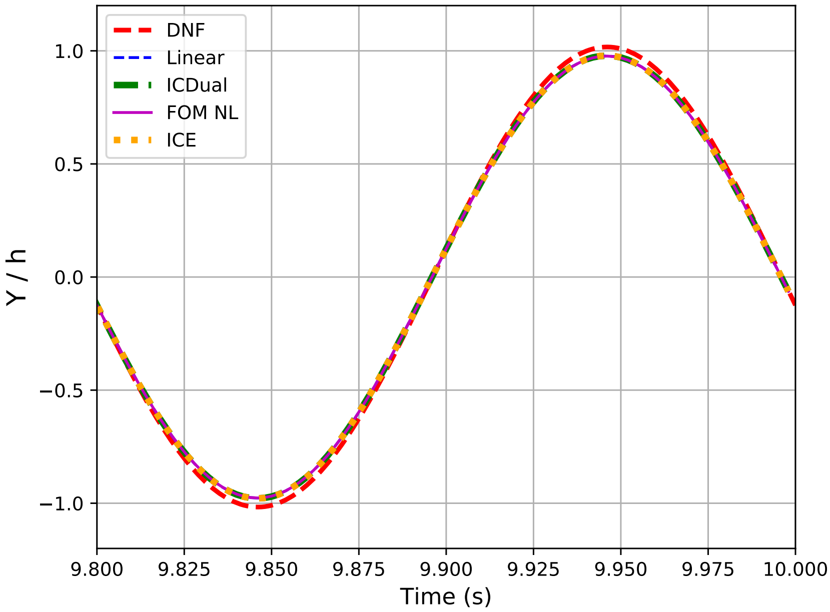

(a) Vertical displacement

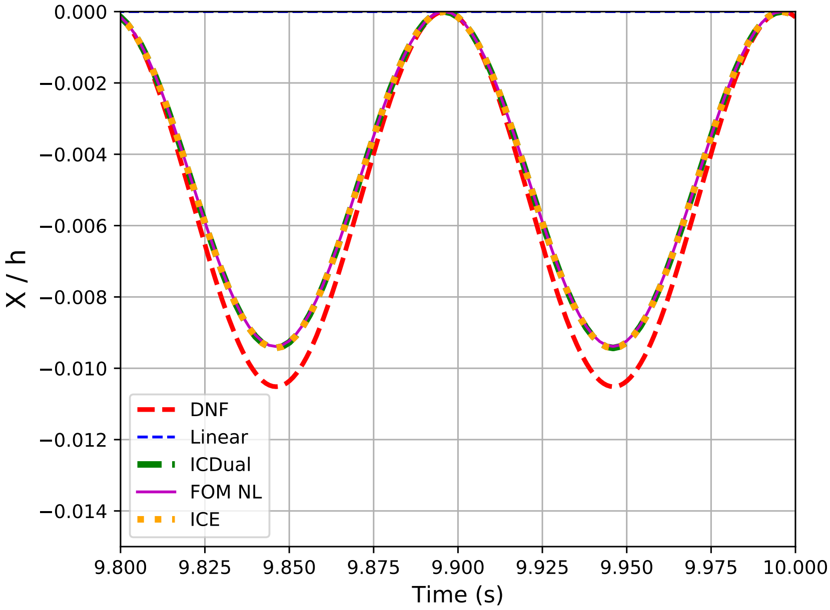

(b) Axial displacement

Figure B.2: Nonlinear dynamic displacement of the clamped-free von Kármán beam under a vertical load at tip of amplitude 2,500 N and frequency 5 Hz. Comparison of the vertical (a) and axial (b) displacements at the tip of the beam in periodic regime between the nonlinear FE, ICE, ICDual and DNF solutions.

Computation of a static case with the DNF method

The principle of the reduction to the normal form is to compute periodic solutions in the vicinity of the linear normal modes. Considering Equation (B.1), it can be interesting to compute static loads by getting rid of the acceleration and velocity terms and solve the equation:

$$\omega_1^2 R_1 + (A_{111}^1 + h_{111}^1) R_1^3 = \phi_1^T \mathbf{f}_{\text{ext}}, \tag{B.22}$$

then rebuild the physical solution with the mapping $\mathbf{X} = \phi_1 R_1 + \bar{\mathbf{a}}_{\mathbf{11}} R_1^2$. The test case considered is a static vertical load of 30,000 N at the tip of the beam. The beam deformation is shown in Figure B.3. The results are inaccurate in the vertical direction for the DNF method while they are inaccurate in the axial direction for the linear solution. Solving Equation (B.22) in itself to compute static load is not appropriate. Indeed, for static cases there is no excitation mode from which the notion of master mode derives. For static linear cases, several modes should be considered in order to retrieve the linear FOM solution. For instance, the linear ROM with only the first linear mode is plotted on Figure B.3 and also shows inaccurate results. The DNF method with several master modes was not tested in this work though it would be interesting to see if it improves the static results.

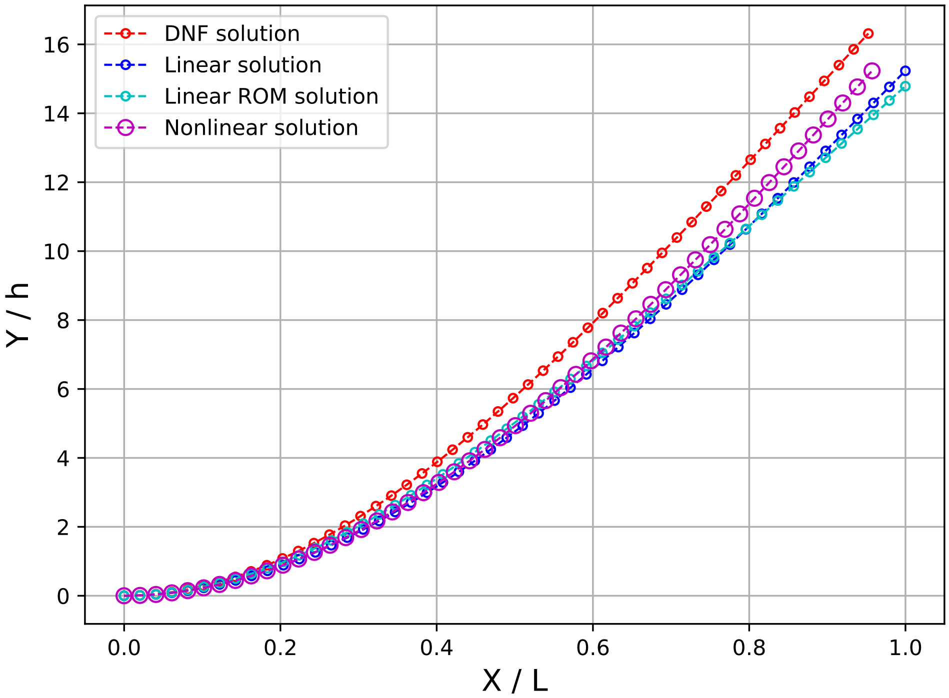

Figure B.3: Nonlinear static displacement of the clamped-free von Kármán beam, loaded vertically at the tip with a load of 30,000 N.

B.2.2 Rotation around the vertical axis at 500 rpm

The beam is now in rotation at 500 rpm around the vertical axis as in section 2.3.3. The following three dynamical load cases are reproduced with the DNF ROM.

- D1_500: A vertical load uniformly distributed along the beam of 4,900 N/m.
- D2_500: A vertical load of amplitude 7,350 N at the tip of the beam.
- D3_500: A follower load of amplitude 7,350 N at the tip of the beam.

Figure B.4 shows the beam's tip vertical and axial displacements in periodic regime under the load case D2_500. The relative errors in vertical and axial amplitudes in periodic regime for the different load cases are gathered respectively in Tables B.5 and B.6.

Table B.5: Relative error of the maximal vertical displacement in periodic regime of the beam tip for the different dynamic load cases of the beam in rotation. Comparison between the reference nonlinear FOM model, the linear FOM, ICE ROM, ICDual ROM and DNF models.

	Relative error of the tip Y displacement (%)		
Load case	D1_500	D2_500	D3_500
Linear FOM	25.22	19.10	17.80
ICE ROM	18.41	14.96	13.78
ICDual ROM	2.99×10^{-3}	2.48×10^{-2}	2.53×10^{-2}
DNF	1.33	7.56×10^{-1}	1.66

Table B.6: Relative error of the maximal axial displacement in periodic regime of the beam tip for the different dynamic load cases of the beam in rotation. Comparison between the reference nonlinear FOM model, the linear FOM, ICE ROM, ICDual ROM and DNF models.

	Relative error of the tip X displacement (%)		
Load case	D1_500	D2_500	D3_500
Linear FOM	100	100	100
ICE ROM	37.93	30.81	28.20
ICDual ROM	2.15×10^{-2}	3.90×10^{-2}	4.05×10^{-2}
DNF	4.46	2.52	4.26

The DNF method with the reduction to the appropriate master mode (the first linear mode) improves significantly the ICE results. Nevertheless, the errors in the rotating case are slightly higher than the errors without rotation. The fact that the amplitude of the external loads are larger than those of the non-rotating case while the model is built for a zero second member may justify the increased errors. The phase shift is equal to 6.5° for all three load cases with the DNF method, 17.2° with the ICE ROM and 0° with the ICDual ROM. The linear FOM solution presents a phase shift of 37.8° for the load case D1 and phase shifts of 34.3° for the load cases D2 and D3.

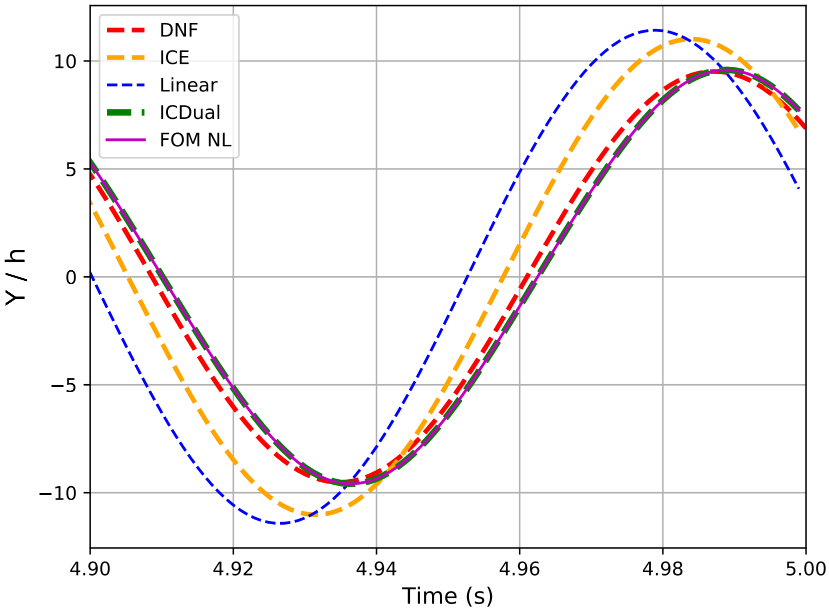

(a) Vertical displacement

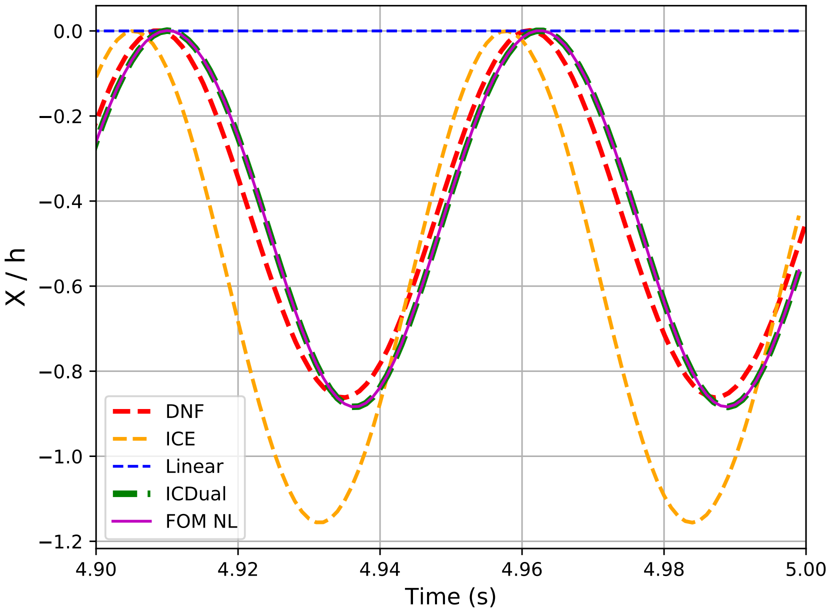

(b) Axial displacement

Figure B.4: Nonlinear dynamic displacement of the clamped-free von Kármán beam in rotation at 500 rpm, subject to the dynamic load case D2. Comparison of the vertical (a) and axial (b) displacements at the tip of the beam in periodic regime between the nonlinear FE, ICE, ICDual and DNF solutions.

In the different examples studied in this section, the DNF reduction method with a single master mode proved to be a good compromise for periodic external loads with a frequency of excitation in the vicinity of a linear normal mode. In such cases, the DNF method improved the ICE solution. However, for a frequency of excitation not corresponding to the frequency associated to the master mode, the accuracy of the DNF method was lower than the ICE method as shown in Figure B.2. The ICDual ROM contains more modes in the reduction basis, leading to very accurate results for the test cases considered. The results of the DNF method are satisfactory but could be improved by taking the external load case into account during the construction of the model. Indeed, the DNF method is not built independently of the external load, it is built regarding an external load that is null. The external load is applied afterwards in the equation where it was supposedly null. Thus, a possibly strong approximation is made, which is accentuated with the amplitude of the load imposed. The ICE and ICDual ROMs are built independently of the external load case. It is taken into account in the projected equation of the dynamics, without stronger approximation than the projection into the reduction basis.

B.3 Application to the 3D beam-like structure

In this section, the DNF method is applied to the non-rotating and rotating cases of the 3D beam-like structure of chapter 3. The fact that a 3D FE structure is considered imposes to carefully compute the DNF coefficients. Indeed, the non-intrusive determination of the coefficients is based on imposed displacements. However, it is well known and explained in [199], that imposing 3D displacements can lead to numerical errors. To limit the issue of volume perturbations, the displacements here are imposed only on the upper skin of the beam, the other elements are free to follow the movement. Besides, each DNF coefficient is computed for several amplitudes of imposed displacements. The values obtained for the different amplitudes are compared to find a range of validity where the values of the coefficients are independent from the amplitude imposed, as they should be according to the theory.

B.3.1 Non-rotating case

In the DNF method, the first step consists in computing accurately the vector $\mathbf{G}\left(\phi_1, \phi_1\right)$. Such a vector is computed via the formula (B.4) using the FE solver. In practice, the mode ϕ_1 is first normalized by its maximal displacement so that its maximal displacement is equal to 1. Then, the normalized mode is multiplied by the amplitude q_G, thus controlling the amplitude of displacement imposed regarding the beam thickness h:

$$\mathbf{G}\left(\phi_1, \phi_1\right) = \frac{1}{2q_G^2}\left[\mathbf{f_{nl}}\left(q_G h \frac{\phi_1}{\max|\phi_1|}\right) + \mathbf{f_{nl}}\left(-q_G h \frac{\phi_1}{\max|\phi_1|}\right)\right]. \tag{B.23}$$

The vector $\mathbf{G}\left(\phi_1, \phi_1\right)$ is computed for several amplitudes of q_G. To control the range of validity of the result obtained, the displacements at the beam tip of the vector $\bar{\mathbf{a}}_{\mathbf{11}}$ are compared for the different values of $\mathbf{G}\left(\phi_1, \phi_1\right)$ obtained with the different amplitudes q_1 imposed. Indeed, $\bar{\mathbf{a}}_{\mathbf{11}}$ depends directly on $\mathbf{G}\left(\phi_1, \phi_1\right)$ and is homogeneous to a displacement. It is more convenient to compare a displacement at a specific point where it is maximal, than compare the values of an arbitrary point in $\mathbf{G}\left(\phi_1, \phi_1\right)$ representing the quadratic part of the internal nonlinear forces associated to the displacement ϕ_1. Figure B.5 represents the displacement at the beam's tip of the vector $\bar{\mathbf{a}}_{\mathbf{11}}$ with the amplitude of the displacement imposed q_G. It can be observed that the displacements obtained for the different amplitudes imposed do not vary more than after the sixth decimal. Thus, the range of validity of imposed displacements for $\mathbf{G}\left(\phi_1, \phi_1\right)$ is large and the amplitude chosen is $q_G = 1$, meaning a displacement imposed with a maximal amplitude equal to the beam's thickness. The vector $\bar{\mathbf{a}}_{\mathbf{11}}$ is a membrane contribution, it is represented in Figure B.6. Now that $\mathbf{G}\left(\phi_1, \phi_1\right)$ is known, all the vectors $\bar{\mathbf{a}}_{\mathbf{11}}, \bar{\mathbf{b}}_{\mathbf{11}}, \bar{\mathbf{c}}_{\mathbf{11}}, \bar{\boldsymbol{\alpha}}_{\mathbf{11}}, \bar{\boldsymbol{\beta}}_{\mathbf{11}}$ and $\bar{\boldsymbol{\gamma}}_{\mathbf{11}}$ can be determined. The scalar coefficients A_{111}^1, B_{111}^1 and C_{111}^1 have yet to be computed. They depend on $\mathbf{G}\left(\phi_1, \bar{\mathbf{a}}_{\mathbf{11}}\right)$, $\mathbf{G}\left(\phi_1, \bar{\mathbf{b}}_{\mathbf{11}}\right)$ and $\mathbf{G}\left(\phi_1, \bar{\mathbf{c}}_{\mathbf{11}}\right)$ respectively. Those vectors need to be correctly evaluated with the FE solver via imposed displacements. To evaluate $\mathbf{G}\left(\phi_1, \bar{\mathbf{a}}_{\mathbf{11}}\right)$, the determination of the vector $\mathbf{G}\left(\bar{\mathbf{a}}_{\mathbf{11}}, \bar{\mathbf{a}}_{\mathbf{11}}\right)$ is required. The latter is computed with the FE solver by:

$$\mathbf{G}\left(\bar{\mathbf{a}}_{\mathbf{11}}, \bar{\mathbf{a}}_{\mathbf{11}}\right) = \frac{1}{2q_a^2}\left[\mathbf{f_{nl}}\left(q_a h \frac{\bar{\mathbf{a}}_{\mathbf{11}}}{\max|\bar{\mathbf{a}}_{\mathbf{11}}|}\right) + \mathbf{f_{nl}}\left(-q_a h \frac{\bar{\mathbf{a}}_{\mathbf{11}}}{\max|\bar{\mathbf{a}}_{\mathbf{11}}|}\right)\right], \tag{B.24}$$

where the amplitude of the imposed displacement is controlled by q_a. Then, the vector $\mathbf{G}\left(\phi_1, \bar{\mathbf{a}}_{\mathbf{11}}\right)$

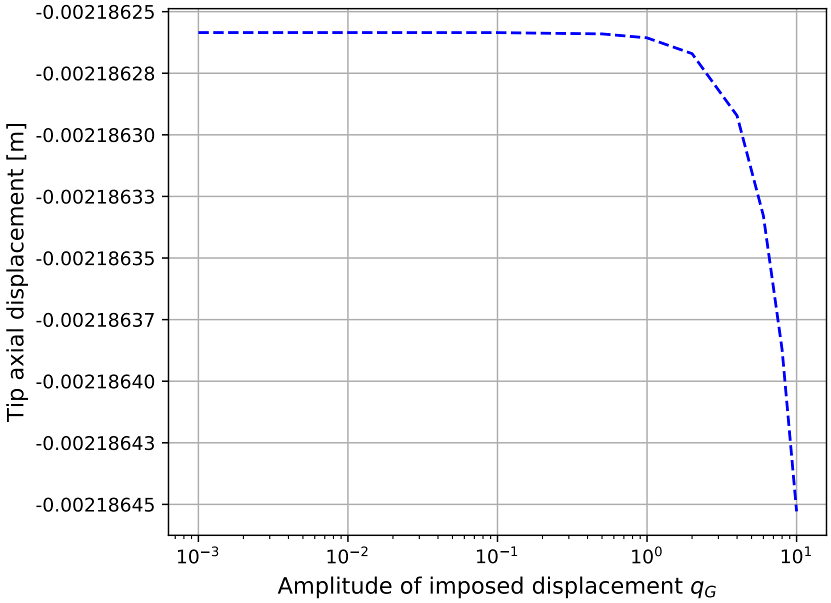

Figure B.5: Dependency of the axial displacement at the beam tip of the vector $\mathbf{\bar{a}_{11}}$ to the imposed amplitude of displacement q_G.

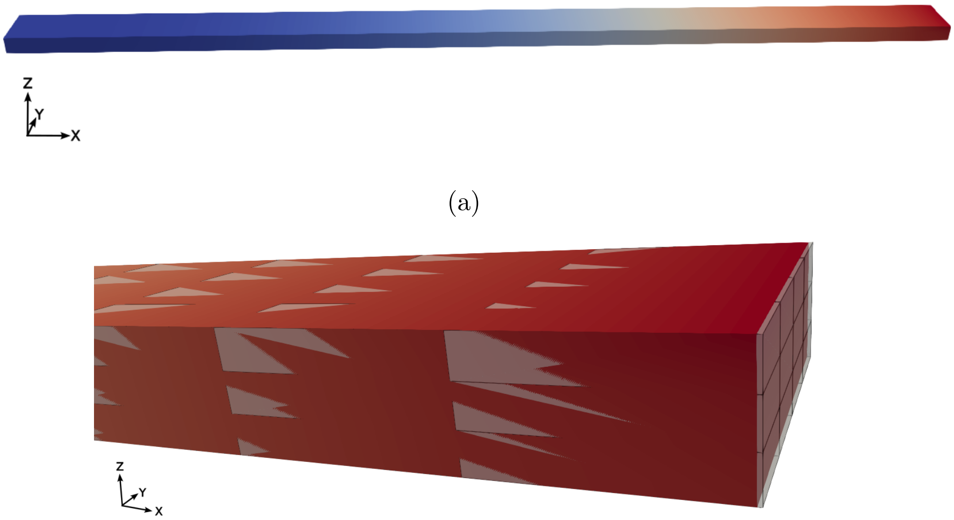

(a)

(b)

Figure B.6: Visualization of the vector $\mathbf{\bar{a}_{11}}$. On the entire beam (a) and at the tip (b).

is evaluated with the FE solver via the formula:

$$\begin{aligned}\mathbf{G}\left(\phi_1, \mathbf{\bar{a}_{11}}\right) = \frac{1}{4 q_G q_a} \Bigg[& \mathbf{f_{nl}} \left(q_G h \frac{\phi_1}{\max|\phi_1|} + q_a h \frac{\mathbf{\bar{a}_{11}}}{\max|\mathbf{\bar{a}_{11}}|} \right) \\ & + \mathbf{f_{nl}} \left(-q_G h \frac{\phi_1}{\max|\phi_1|} - q_a h \frac{\mathbf{\bar{a}_{11}}}{\max|\mathbf{\bar{a}_{11}}|} \right) \\ & - 2 q_G^2 \mathbf{G}\left(\phi_1, \phi_1\right) - 2 q_a^2 \mathbf{G}\left(\mathbf{\bar{a}_{11}}, \mathbf{\bar{a}_{11}}\right) \Bigg]. \end{aligned} \tag{B.25}$$

Finally the coefficient A^1_{111} is obtained by projection: $A^1_{111} = 2\phi_1^T \mathbf{G}\left(\phi_1, \bar{\mathbf{a}}_{\mathbf{11}}\right)$. The amplitude q_G taken is $q_G = 1$ chosen previously for the evaluation of $\mathbf{G}\left(\phi_1, \phi_1\right)$ and several values of q_a are considered. Figure B.7 illustrates the values of the coefficient A^1_{111} for different amplitudes of q_a. A plateau is observed in the range $q_a \in [10^{-3}, 10^{-1}]$, where A^1_{111} is constant and equal to $-5{,}008.218$.

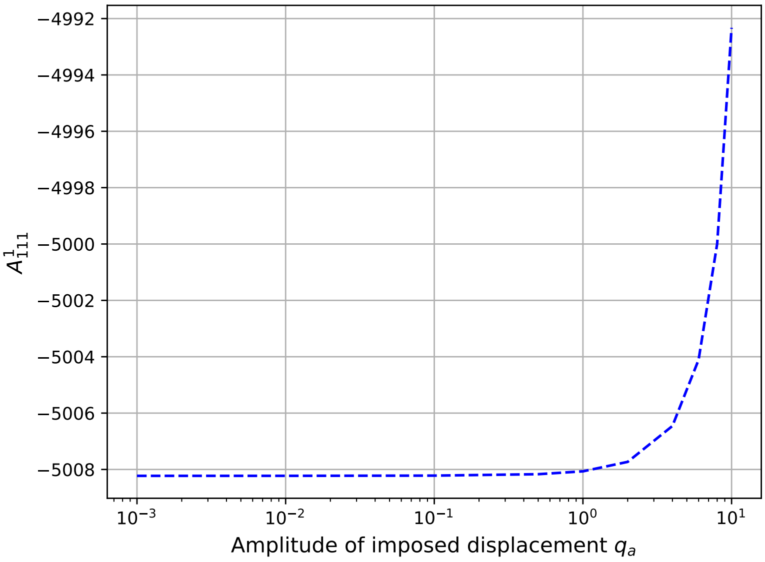

Figure B.7: Dependency of the coefficient A^1_{111} to the imposed amplitude of displacement q_a.

A similar procedure is applied to compute the coefficients B^1_{111} and C^1_{111}, with imposed amplitudes written respectively q_b and q_c. Figure B.8 shows the dependency of the coefficient B^1_{111} to the amplitude q_b of the imposed displacement. A plateau is observed for $q_b \in [10^{-3}, 10^{-1}]$ and the value of B^1_{111} for $q_b = 0.1$ is equal to 1.113×10^{-3}. Regarding the coefficient C^1_{111}, its value is constant for $q_c \in [10^{-3}, 10^{-2}]$ as shown in Figure B.9. The value of C^1_{111} for an imposed amplitude $q_c = 0.01$ is equal to -4.029×10^{-6}.

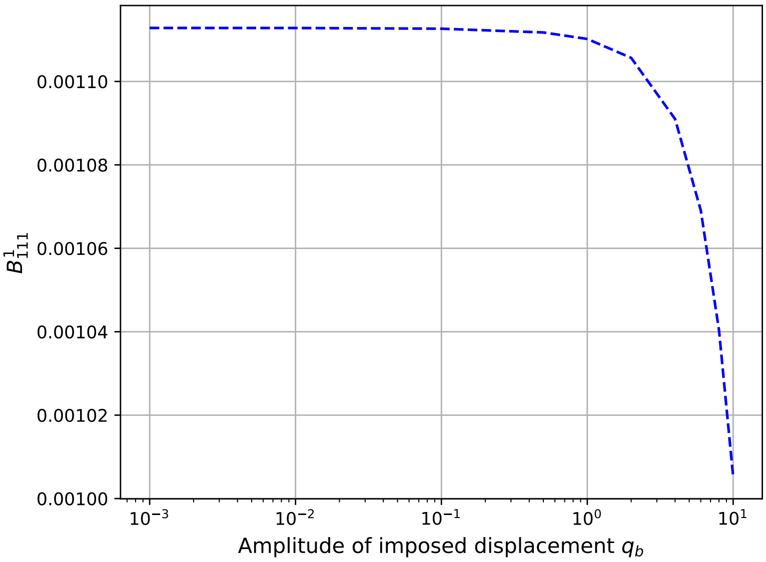

Figure B.8: Dependency of the coefficient B^1_{111} to the imposed amplitude of displacement q_b.

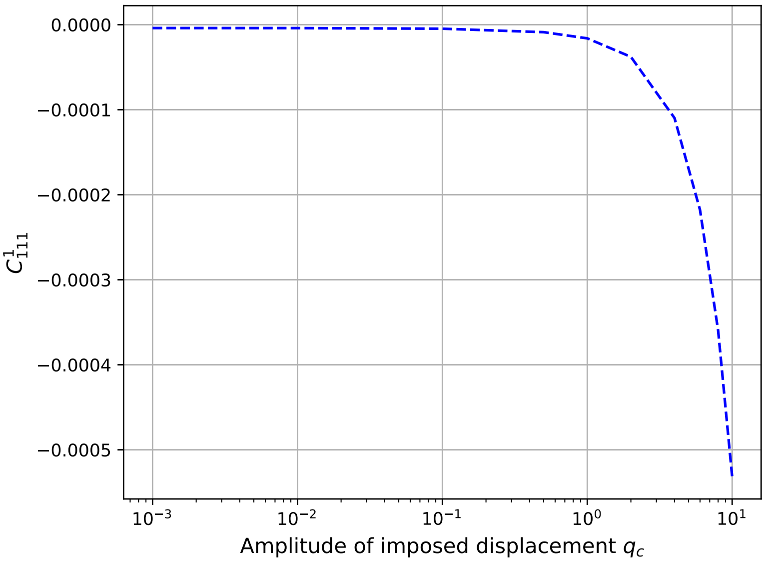

Figure B.9: Dependency of the coefficient C^1_{111} to the imposed amplitude of displacement q_c.

The last coefficient to determine is h^1_{111}. It is evaluated by imposing a displacement along the mode ϕ_1 to the beam to compute the vector $\mathbf{H}\left(\phi_1,\phi_1,\phi_1\right)$, then project this vector to evaluate $h^1_{111} = 2\phi_1^T \mathbf{H}\left(\phi_1,\phi_1,\phi_1\right)$. Due to the numerical perturbations of imposing displacements to compute internal forces, the amplitude to impose for computing $\mathbf{G}\left(\phi_1,\phi_1\right)$ and $\mathbf{H}\left(\phi_1,\phi_1,\phi_1\right)$ are not a priori equal. The vector $\mathbf{H}\left(\phi_1,\phi_1,\phi_1\right)$ is evaluated with the FE solver by imposing a displacement of amplitude q_H as follows:

$$\mathbf{H}\left(\phi_1,\phi_1,\phi_1\right) = \frac{1}{2q_H^3}\left[\mathbf{f_{nl}}\left(q_H h \frac{\phi_1}{\max|\phi_1|}\right) - \mathbf{f_{nl}}\left(-q_H h \frac{\phi_1}{\max|\phi_1|}\right)\right]. \tag{B.26}$$

The coefficient h^1_{111} is computed for several amplitudes q_H. Figure B.10 illustrates the dependency of the coefficient h^1_{111} to the amplitude q_H of the imposed displacement. A plateau is observed for $q_H \in [10^{-2}, 10^0]$, where h^1_{111} is equal to 5,008.037. The coefficients B^1_{111} and C^1_{111} are very small whereas the coefficients A^1_{111} and h^1_{111} have a much larger contribution and are of opposed signs. Those coefficients are partly compensating one another in the factor $(A^1_{111} + h^1_{111})$ of R^3 in the expression of the dynamics in the normal form B.1.

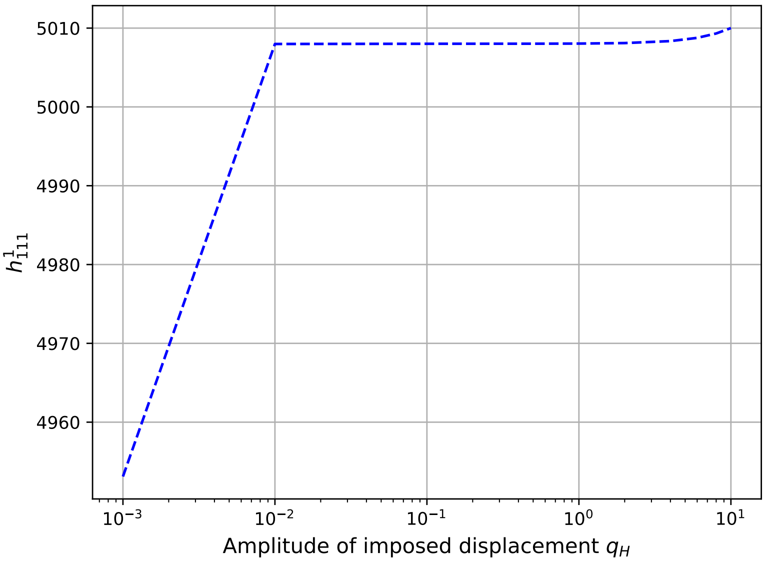

Figure B.10: Dependency of the coefficient h^1_{111} to the imposed amplitude of displacement.

The test case for the application is a vertical periodic load at the tip of the beam of amplitude 2,500 N at the frequency of the first linear mode. The temporal vertical and axial tip displacements in periodic regime are plotted in Figure B.11. The relative errors regarding the FOM solution of the different models are gathered in Table B.7. The relative errors in the vertical and axial displacements are lower than those of the ICE solution and higher than those of the ICDual solution. The phase shifts are 0° for the linear solution, 14.6° for the ICE solution, 9.7° for the ICDual solution and 19.3° for the DNF solution.

Table B.7: Relative error of the maximal displacement of the beam tip in periodic regime under a vertical load at tip of amplitude 2,500 N and frequency 3.38 Hz. Comparison between the reference nonlinear FOM model, the linear model, the ICE, ICDual and DNF ROMs.

	Relative error of the tip displacement (%)	
	Y component	X component
Linear	1.91	100
ICE	3.05	5.20
ICDual	0.48	1.27
DNF	1.62	2.25

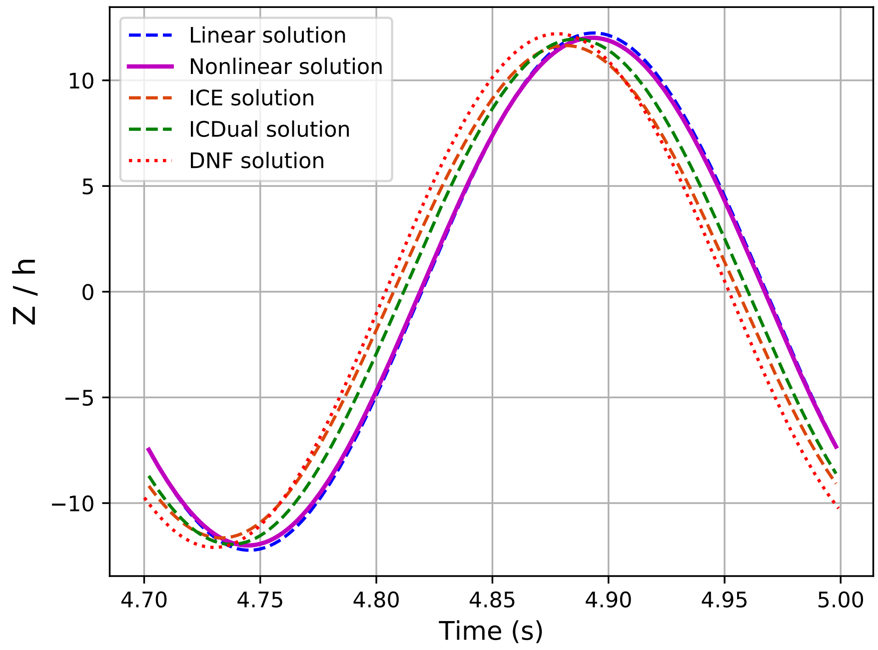

(a) Vertical displacement

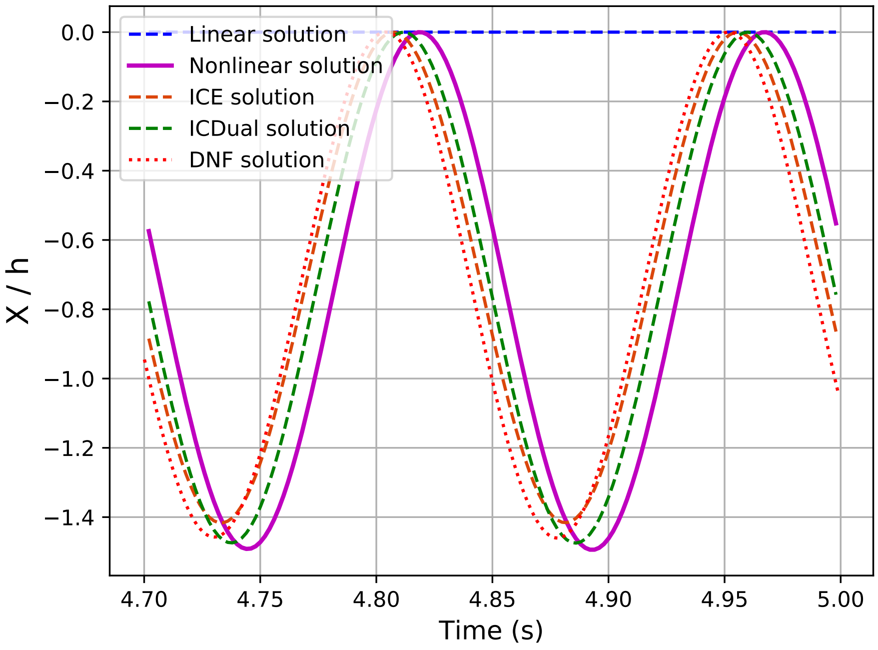

(b) Axial displacement

Figure B.11: Nonlinear dynamic displacement of the clamped-free 3D beam-like structure subject to a vertical load at the tip of amplitude 2,500 N and frequency 3.38 Hz.

B.3.2 Rotating around the vertical axis at 500 rpm

The beam is now in rotation at 500 rpm around the vertical axis. In the DNF formulations, the stiffness matrix $\mathbf{K}$ is now the total stiffness in rotation $\mathbf{K}(\Omega)$ and the internal nonlinear forces $\mathbf{f_{nl}}$ are replaced by $\mathbf{g_{nl}}$. Figure B.12 represents the displacement of the vector $\bar{\mathbf{a}}_{\mathbf{11}}$ at the beam tip according to the amplitude q_G of the imposed displacement. Like the case without rotation, the variations are observed after the sixth decimal and are thus negligible. Thus, the range of validity for the imposed displacements to compute $\mathbf{G}(\phi_1, \phi_1)$ is large and the amplitude chosen is $q_G = 1$, meaning an imposed displacement in the order of magnitude of the thickness of the beam. Similarly to the non-rotating case, the vector $\bar{\mathbf{a}}_{\mathbf{11}}$ is a membrane contribution and its deformation is similar to the one illustrated in Figure B.6 for the non-rotating case.

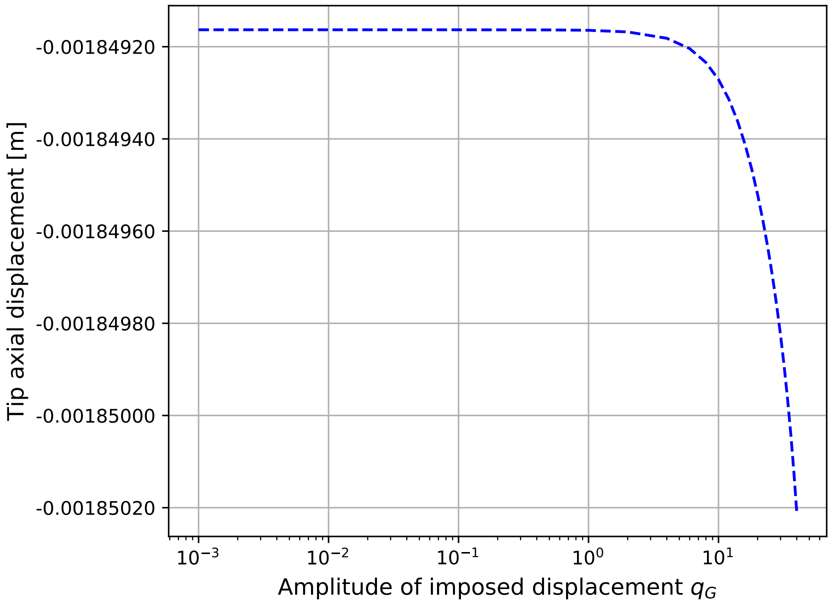

Figure B.12: Dependency of the axial displacement of the vector $\bar{\mathbf{a}}_{\mathbf{11}}$ at the beam tip to the imposed amplitude of displacement q_G. The beam is in rotation around the vertical axis at 500 rpm.

The vector $\mathbf{G}(\phi_1, \phi_1)$ determined, the mappings $\bar{\mathbf{a}}_{\mathbf{11}}, \bar{\mathbf{b}}_{\mathbf{11}}, \bar{\mathbf{c}}_{\mathbf{11}}, \bar{\boldsymbol{\alpha}}_{\mathbf{11}}, \bar{\boldsymbol{\beta}}_{\mathbf{11}}$ and $\bar{\boldsymbol{\gamma}}_{\mathbf{11}}$ are deduced. With the same process as for the non-rotating case, the coefficients A^1_{111}, B^1_{111} and C^1_{111} are determined by imposing the adequate displacements along respectively $\bar{\mathbf{a}}_{\mathbf{11}}, \bar{\mathbf{b}}_{\mathbf{11}}$ and $\bar{\mathbf{c}}_{\mathbf{11}}$ with the amplitudes q_a, q_b and q_c respectively. Figure B.13 represents the variations of the coefficient A^1_{111} with the amplitude q_a of the imposed displacement. A plateau is observed for $q_a \in [10^{-3}, 10^{-1}]$, where A^1_{111} is constant equal to $-3{,}149.644$.

The coefficients B^1_{111} and C^1_{111} are evaluated with imposed displacements via the amplitudes respectively q_b and q_c. Figures B.14 and B.15 show respectively the dependency of the coefficient B^1_{111} and C^1_{111} to the respective amplitudes q_b and q_c of the imposed displacements. For both cases, constant values are obtained for q_b and q_c in the range $[10^{-3}, 10^{-1}]$. For q_b and q_c equal to 0.1, the coefficient B^1_{111} is equal to 9.232×10^{-4} and C^1_{111} is equal to -1.879×10^{-5}.

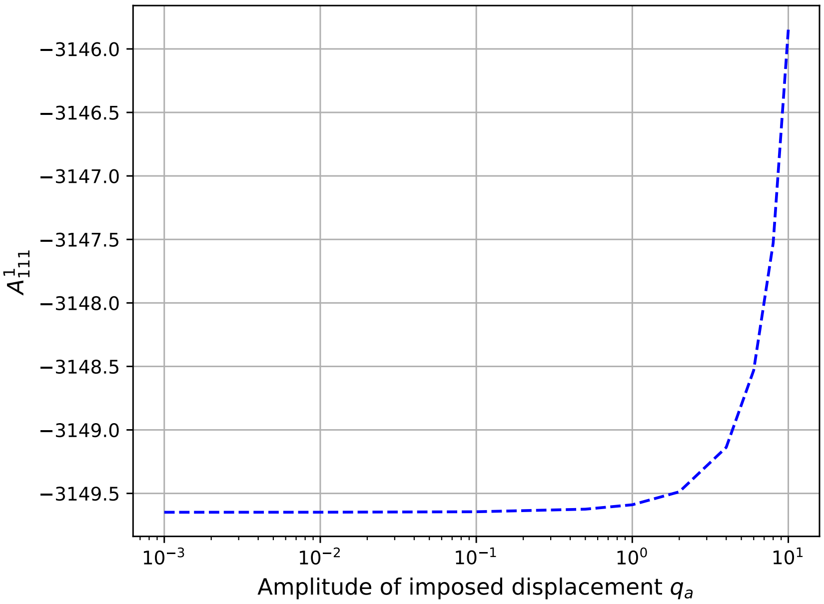

Figure B.13: Dependency of the coefficient A^1_{111} to the imposed amplitude q_a of displacement. The beam is in rotation around the vertical axis at 500 rpm.

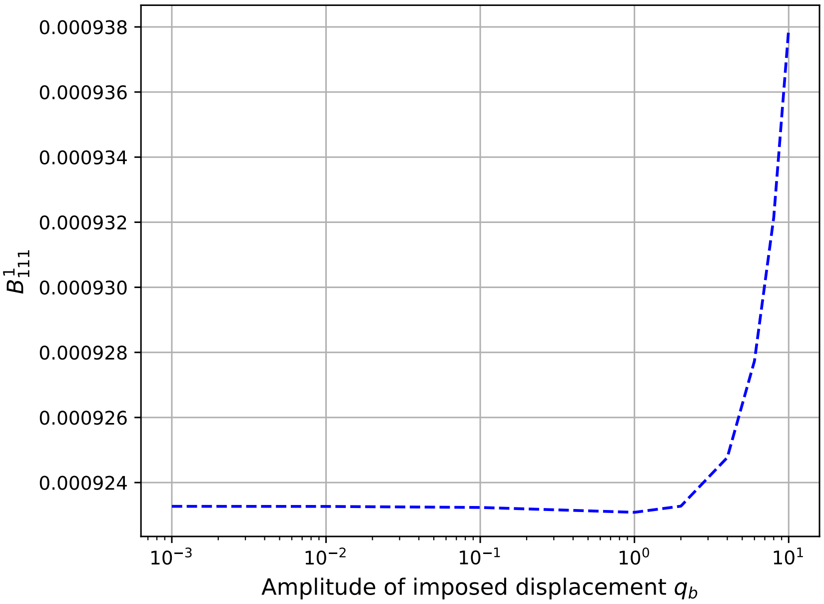

Figure B.14: Dependency of the coefficient B^1_{111} to the imposed amplitude q_b of displacement. The beam is in rotation around the vertical axis at 500 rpm.

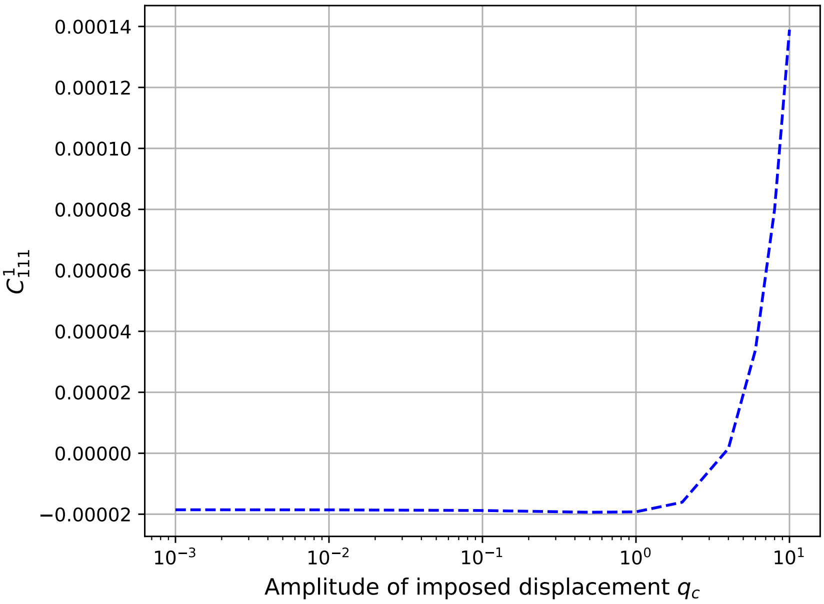

Figure B.15: Dependency of the coefficient C^1_{111} to the imposed amplitude q_c of displacement. The beam is in rotation around the vertical axis at 500 rpm.

The DNF coefficient h^1_{111} is also evaluated from imposed displacements of several amplitudes q_H. Figure B.16 represents the dependency of the coefficient h^1_{111} to the amplitude q_H of imposed displacement. Contrary to the other coefficients and to the non-rotating case, the coefficient h^1_{111} is very sensitive to the amplitude of displacement imposed. In Figure B.16 (a), a plateau is observed for $q_H \in [10^{-1}, 40]$. However, looking closer in Figure B.16 (b), there is no such plateau. The value chosen for the moment corresponds to $q_H = 26$ and gives $h^1_{111} = 3{,}148, 167$. In Figure B.16 (b), the value of the coefficient $-A^1_{111}$ is plotted on the graph. In the normal form, the coefficients A^1_{111} and h^1_{111} are summed in factor of R^3. The value of the sum $A^1_{111} + h^1_{111}$ determines the cubic nonlinearity of the normal form and the softening or hardening behavior of the dynamics. Since no clear plateau is observed in the dependency of h^1_{111} to q_H, both a hardening and a softening behavior are possible according to the value chosen. In the present case with the value $q_H = 26$ chosen, the behavior is softening.

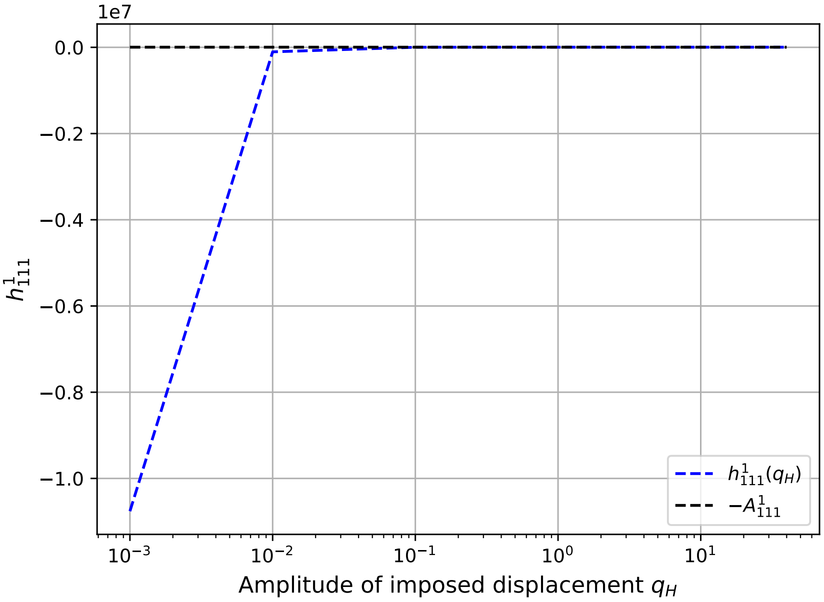

(a) q_H in the range $[10^{-3}, 40]$

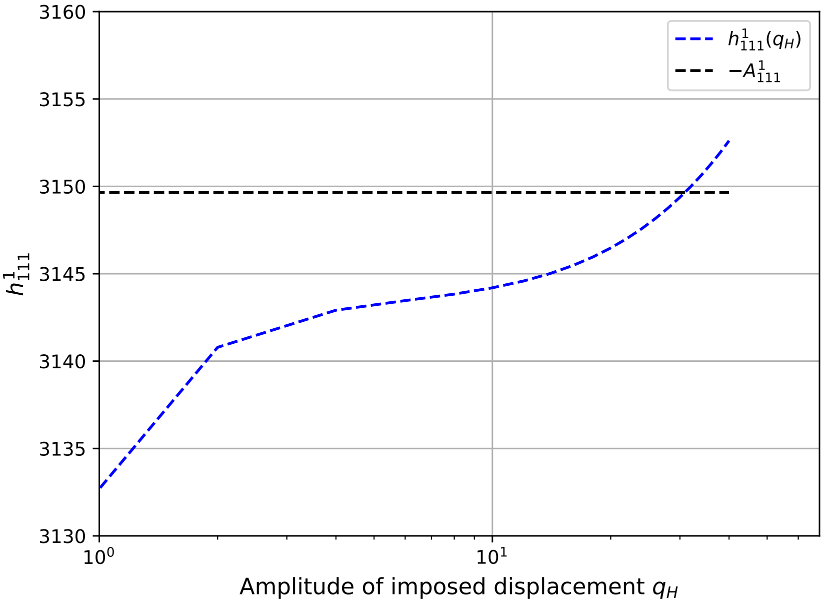

(b) q_H in the range $[1, 40]$

Figure B.16: Dependency of the coefficient h^1_{111} to the imposed amplitude q_H of displacement. The beam is in rotation around the vertical axis at 500 rpm.

Figure B.17 represents the temporal solutions with the different ROMs and the nonlinear FOM model for the test case of a vertical periodic load at the tip of the beam of amplitude 7,350 N and frequency 9.67 Hz. This test case was already tackled in section 3.2. The ICE and ICDual ROMs are those built with the 3 first linear normal modes in the (x,z) plane. The reader may refer to section 3.2 for more details about the ICE and ICDual ROMs considered. The relative errors of the maximal vertical and axial displacements with the different ROMs are gathered in Table B.8. The DNF ROM is particularly precise regarding the vertical displacement and has a relative error lower than 3% for the axial displacement. The phase shifts are 7.0° for the linear and ICDual solutions, 27.8° for the ICE solution and 3.1° for the DNF solution.

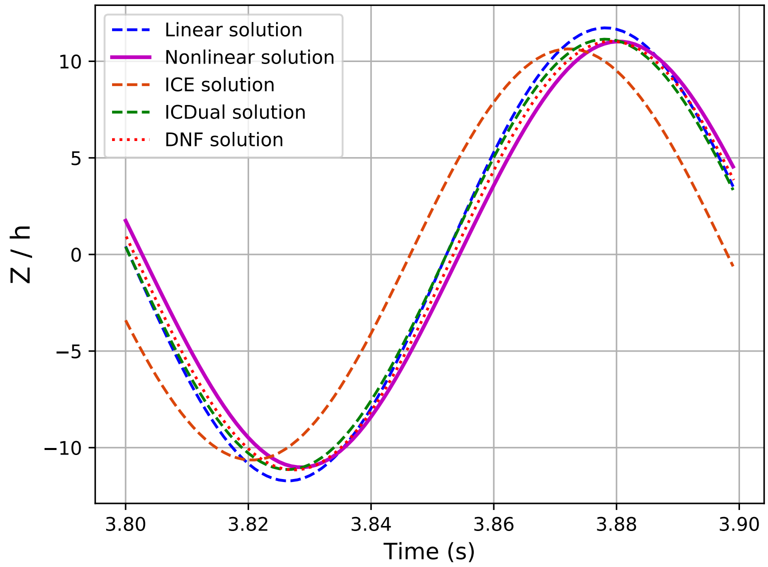

(a) Vertical displacement

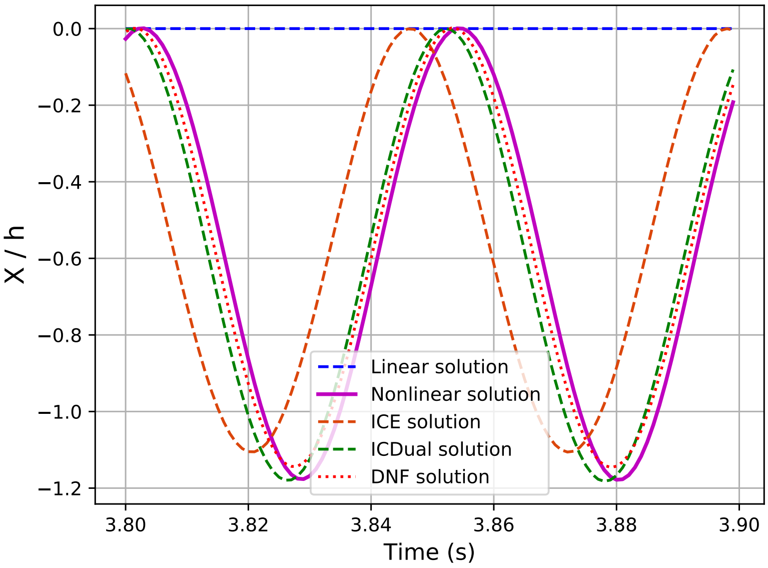

(b) Axial displacement

Figure B.17: Nonlinear dynamic displacement of the clamped-free 3D beam-like structure subject to a vertical load at the tip of amplitude 7,350 N and frequency 9.67 Hz.

Table B.8: Relative error of the maximal displacement of the beam tip in periodic regime under a vertical load at tip of amplitude 7,350 N and frequency 9.67 Hz. Comparison between the reference nonlinear FOM model, the linear model and the ICE, ICDual and DNF ROMs.

	Relative error of the tip displacement (%)	
	Y component	X component
Linear	6.41	100
ICE	3.48	6.15
ICDual	1.08	0.34
DNF	0.13	2.73

Nevertheless, has shown in Figure B.16, the determination of the coefficient h^1_{111} is not clear since such a coefficient varies in a non-negligible range with the amplitude of displacement imposed. The imposed amplitude $q_H = 26$ provides good results. Figure B.18 shows the results of the abovementioned test case with DNF ROMs built with a coefficient h^1_{111} obtained with the imposed amplitudes $q_H = 20$ and $q_H = 32$. For $q_H = 20$ and $q_H = 26$, the behavior is softening since $A^1_{111} + h^1_{111} < 0$. However, for $q_H = 32$, $A^1_{111} + h^1_{111} > 0$ and the behavior is hardening. It is observed in Figure B.18 that the value of the coefficient h^1_{111} strongly affects the phases and amplitudes obtained.

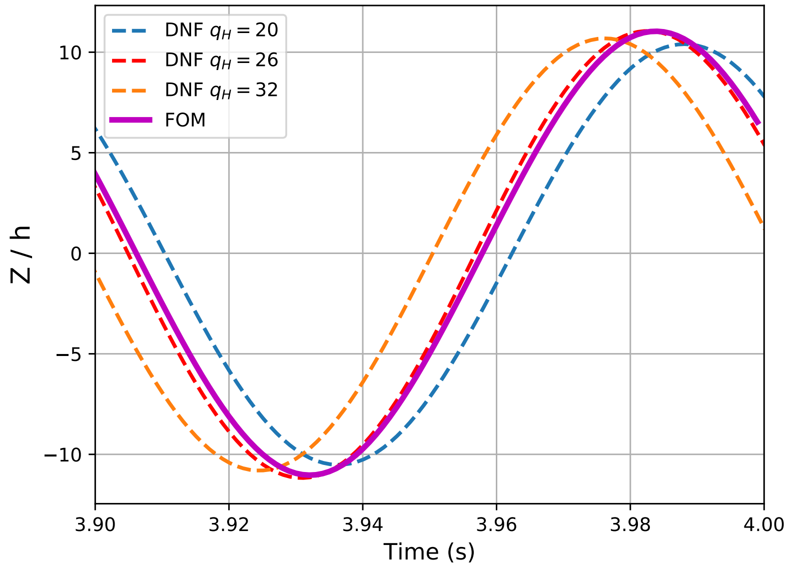

(a) Vertical displacement

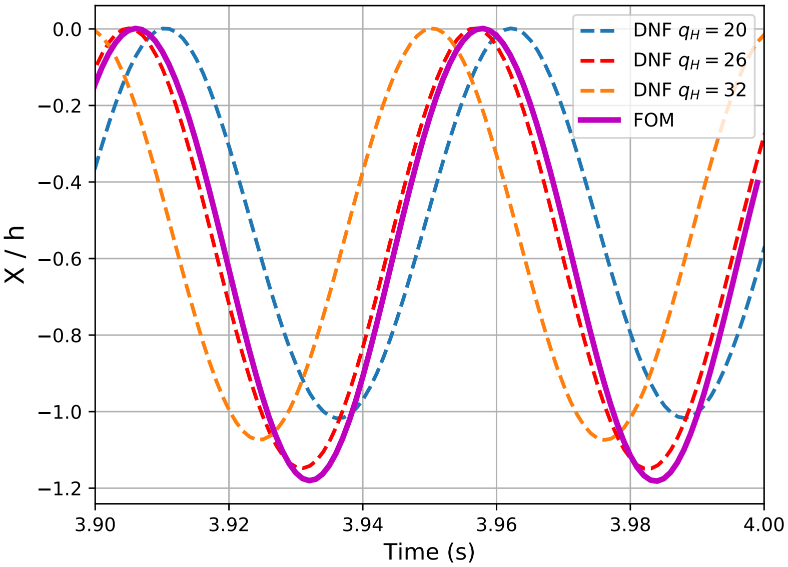

(b) Axial displacement

Figure B.18: Nonlinear dynamic displacement of the clamped-free 3D beam-like structure subject to a vertical load at the tip of amplitude 7,350 N and frequency 9.67 Hz. Comparison between the FOM solution and the DNF ROMs with different coefficients C^1_{111} obtained from imposed displacements of different amplitudes q_H.

B.4 Conclusion

In this appendix, the Direct Normal Form reduction method with only one master mode is presented and evaluated on some test cases tackled in the manuscript that are the von Kármán beam and the 3D beam-like structure, both with and without rotation. The results obtained capture accurately though not exactly the nonlinear FOM solutions. For 3D structures, a sensitivity investigation to the amplitude of imposed displacement is necessary in order to build an accurate DNF model. It was seen for the rotating case that some coefficients are highly sensitive to the amplitude of imposed displacement.

Appendix C

Jacobian of the reduced nonlinear forces

The expression of the projected nonlinear forces in the reduced space is a third-order polynomial of the generalized coordinates. Let $k \in [1, n]$ and $n \geq 3$, the projected non-linear forces in the IC method are:

$$\widetilde{f}^k_{\mathrm{nl}}(\mathbf{q}) = \sum_{i=1}^{n}\sum_{j=i}^{n} \beta^k_{ij} q_i q_j + \sum_{i=1}^{n}\sum_{j=i}^{n}\sum_{m=j}^{n} \gamma^k_{ijm} q_i q_j q_m \tag{C.1}$$

For the resolution of the nonlinear problems, an explicit expression of the jacobian matrix of those internal nonlinear forces is required for the iterative Newton procedure. The coefficient at the line k and the column ℓ of the jacobian matrix of the non-linear forces is equal to:

$$\begin{aligned} \left(\frac{\partial \widetilde{f}^k_{\mathrm{nl}}(\mathbf{q})}{\partial q_\ell}\right) &= \frac{\partial}{\partial q_\ell}\left(\sum_{i=1}^{n}\sum_{j=i}^{n} \beta^k_{ij} q_i q_j\right) + \frac{\partial}{\partial q_\ell}\left(\sum_{i=1}^{n}\sum_{j=i}^{n}\sum_{m=j}^{n} \gamma^k_{ijm} q_i q_j q_m\right) \\ &= \sum_{i=1}^{n} \mathrm{B}^{k,\ell}_i q_i + \sum_{i=1}^{n}\sum_{j=i}^{n} \mathrm{G}^{k,\ell}_{ij} q_i q_j \end{aligned} \tag{C.2}$$

with

$$\mathrm{B}^{k,\ell}_i = \begin{cases} \beta^k_{i\ell} & \text{if } i < \ell \\ 2\beta^k_{\ell\ell} & \text{if } i = \ell \\ \beta^k_{\ell i} & \text{if } i > \ell \end{cases} \tag{C.3}$$

and

$$\mathrm{G}^{k,\ell}_{ij} = \begin{cases} \text{if } \; j < \ell & \gamma^k_{ij\ell} \\ \text{if } \; j = \ell & \begin{cases} 2\gamma^k_{i\ell\ell} & \text{if } \; i < \ell \\ 3\gamma^k_{\ell\ell\ell} & \text{if } \; i = \ell \end{cases} \\ \text{if } \; j > \ell & \begin{cases} \gamma^k_{i\ell j} & \text{if } \; i < \ell \\ 2\gamma^k_{\ell\ell j} & \text{if } \; i = \ell \\ \gamma^k_{\ell ij} & \text{if } \; i > \ell \end{cases} \end{cases} \tag{C.4}$$

Appendix D

Application of the reduced order model to a bi-clamped Bernoulli/von Kármán beam

---

The applications considered in section 2.3 are cantilevered examples. Those examples were addressed because cantilever beams are challenging for reduced order models of geometrically nonlinear structures. It is nevertheless interesting to evaluate the efficiency of the ICDual ROM in a clamped-clamped configuration. The non-linearity is indeed stronger for the clamped-clamped beam and the ICDual ROM is accurate as well. Figure D.1 represents the displacement of the beam of 2.3, this time clamped-clamped, and subjected to a vertical load at the center of amplitude $300,000$ N. Figure D.2 shows the vertical displacement at the center of the clamped-clamped beam, subjected to a vertical sinusoidal load at the center of amplitude $60,000$ N and at the frequency of the first linear mode. For both the static and dynamic test cases, the ICDual ROM matches with the full order model. It is worth mentioning that the coefficients of the projected nonlinear forces obtained with the forced-based method are in agreement with those obtained with a displacement-based method as well as those with a symbolic computations.

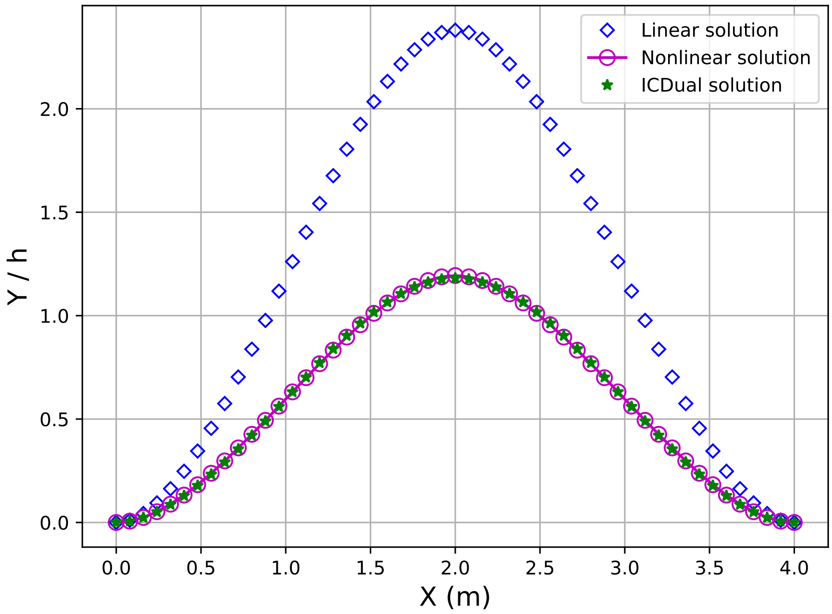

Figure D.1: Displacement of a clamped-clamped subjected to a vertical load at the center of amplitude $300,000$ N.

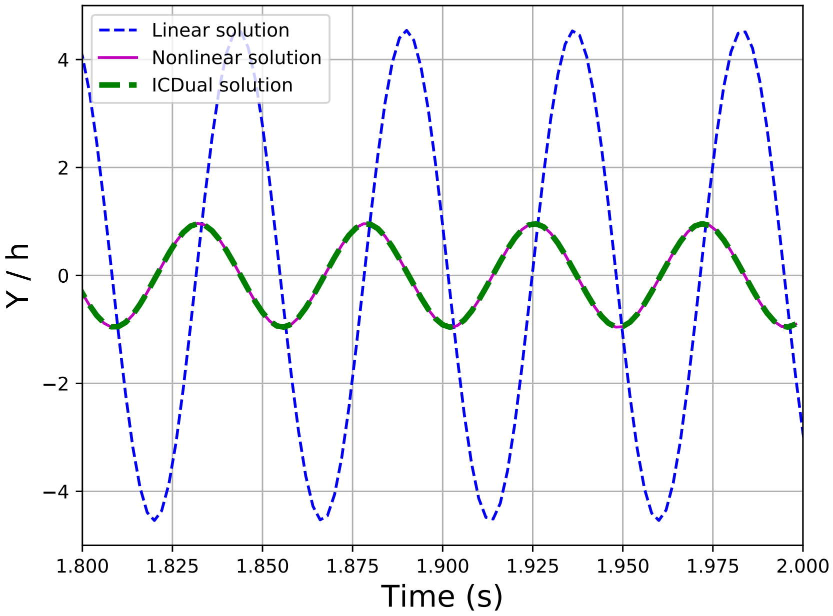

Figure D.2: Vertical displacement at the center of the clamped-clamped beam, subjected to a vertical sinusoidal load at the center of amplitude $60,000$ N and at the frequency of the first linear mode.

Bibliography

[1] M. Amabili, A. Sarkar, and M. Païdoussis. Chaotic vibrations of circular cylindrical shells: Galerkin versus reduced-order models via the proper orthogonal decomposition method. *Journal of Sound and Vibration*, 290(3-5):736–762, 2006. (Cited page 199.)

[2] M. Amabili and C. Touzé. Reduced-order models for nonlinear vibrations of fluid-filled circular cylindrical shells: Comparison of POD and asymptotic nonlinear normal modes methods. *Journal of Fluids and Structures*, 23(6):885–903, 2007. (Cited pages 42 and 201.)

[3] S. S. An, T. Kim, and D. L. James. Optimizing Cubature for Efficient Integration of Subspace Deformations. *ACM Transactions on Graphics*, 27(5), Dec. 2008. (Cited pages 36 and 200.)

[4] M. Arnold and O. Brüls. Convergence of the generalized-α scheme for constrained mechanical systems. *Multibody System Dynamics*, 18(2):185–202, 2007. (Cited pages 18, 20 and 198.)

[5] S. Badia, F. Nobile, and C. Vergara. Fluid-structure partitioned procedures based on Robin transmission conditions. *Journal of Computational Physics*, 227(14):7027–7051, 2008. (Cited pages 102 and 209.)

[6] E. M. Baily. *Steady State Harmonic Analysis of Nonlinear Networks.* PhD thesis, Stanford University, 1968. (Cited pages 21 and 198.)

[7] M. Balmaseda, G. Jacquet-Richardet, A. Placzek, and D.-M. Tran. Reduced Order Models for Nonlinear Dynamic Analysis with Application to a Fan Blade. *Journal of Engineering for Gas Turbine and Power*, 142(4):041002, 2020. (Cited page 44.)

[8] M. Balmaseda Aguirre. *Reduced order models for nonlinear dynamic analysis of rotating structures : Application to turbomachinery blades.* PhD thesis, Université de Lyon, 2019. (Cited pages 31 and 34.)

[9] K. Bathe. *Finite Element Procedures.* Prentice Hall, 2006. (Cited pages 14, 18 and 198.)

[10] A. Beckert and H. Wendland. Multivariate interpolation for fluid-structure-interaction problems using radial basis functions. *Aerospace Science and Technology*, 5(2):125–134, 2001. (Cited pages 104, 107 and 209.)

[11] S. Bellizzi and R. Sampaio. POMs analysis of randomly vibrating systems obtained from karhunen–loève expansion. *Journal of Sound and Vibration*, 297(3):774–793, 2006-11. (Cited page 25.)

[12] A. Belov, L. Martinelli, and A. Jameson. A new implicit algorithm with multigrid for unsteady incompressible flow calculations. In *33rd Aerospace Sciences Meeting and Exhibit.* American Institute of Aeronautics and Astronautics, 1995. (Cited page 133.)

[13] M. Breuer, G. D. Nayer, M. Münsch, T. Gallinger, and R. Wüchner. Fluid-structure interaction using a partitioned semi-implicit predictor-corrector coupling scheme for the application of large-eddy simulation. *Journal of Fluids and Structures*, 29:107–130, 2012. (Cited pages 102, 104 and 209.)

[14] M. D. Buhmann. *Radial Basis Functions.* Cambridge University Press, July 2003. (Cited pages 104 and 209.)

[15] J. C. Butcher. *Numerical methods for ordinary differential equations.* John Wiley & Sons, Nashville, TN, June 2003. (Cited page 147.)

[16] X. Cabré, E. Fontich, and R. de la Llave. The Parameterization Method for Invariant Manifolds I: Manifolds Associated to Non-resonant Subspaces. *Indiana University Mathematics Journal*, 52(2):283–328, 2003. (Cited pages 40 and 200.)

[17] X. Cabré, E. Fontich, and R. de la Llave. The Parameterization Method for Invariant Manifolds II: Regularity with Respect to Parameters. *Indiana University Mathematics Journal*, 52(2):329–360, 2003. (Cited pages 40 and 200.)

[18] X. Cabré, E. Fontich, and R. de la Llave. The parameterization method for invariant manifolds III: overview and applications. *Journal of Differential Equations*, 218(2):444–515, 2005. (Cited pages 40 and 200.)

[19] L. Cambier, S. Heib, and S. Plot. The Onera elsA CFD software: input from research and feedback from industry. *Mechanics Industry*, 14(3):159–174, 2013. (Cited pages 42, 110, 128, 210 and 214.)

[20] E. Capiez-Lernout, C. Soize, and M. Mbaye. Mistuning analysis and uncertainty quantification of an industrial bladed disk with geometrical nonlinearity. *Journal of Sound and Vibration*, 356:124–143, 2015. (Cited pages 140, 217 and 218.)

[21] E. Capiez-Lernout, C. Soize, and M. P. Mignolet. Computational stochastic statics of an uncertain curved structure with geometrical nonlinearity in three-dimensional elasticity. *Computational Mechanics*, 49(1):87–97, 2011. (Cited pages 140 and 218.)

[22] J. Carr. *Applications of Centre Manifold Theory.* Springer US, 1981. (Cited page 37.)

[23] M. Casoni and E. Benini. A Review of Computational Methods and Reduced Order Models for Flutter Prediction in Turbomachinery. *Aerospace*, 8(9):242, 2021. (Cited page 42.)

[24] P. Causin, J. Gerbeau, and F. Nobile. Added-mass effect in the design of partitioned algorithms for fluid-structure problems. *Computer Methods in Applied Mechanics and Engineering*, 194(42-44):4506–4527, 2005. (Cited pages 102 and 209.)

[25] T. Chapman, P. Avery, P. Collins, and C. Farhat. Accelerated mesh sampling for the hyper reduction of nonlinear computational models. *International Journal for Numerical Methods in Engineering*, 109(12):1623–1654, 2017. (Cited page 36.)

[26] S. Chaturantabut and D. C. Sorensen. Nonlinear Model Reduction via Discrete Empirical Interpolation. *SIAM Journal on Scientific Computing*, 32(5):2737–2764, 2010. (Cited pages 35 and 200.)

[27] J. Chung and G. M. Hulbert. A Time Integration Algorithm for Structural Dynamics with Improved Numerical Dissipation: The Generalized-α Method. *Journal of Applied Mechanics*, 60(2):371–375, 1993. (Cited pages 18, 20 and 198.)

[28] Clean Sky 2 Joint Undertaking. *Clean aviation highlights 2022: clean aviation takes off.* Publications Office, 2023. (Cited page 1.)

[29] B. Cochelin. A path-following technique via an asymptotic-numerical method. *Computers & Structures*, 53(5):1181–1192, 1994. (Cited pages 21 and 198.)

[30] A. R. Collar. The expanding domain of aeroelasticity. *The Journal of the Royal Aeronautical Society*, 50(428):613–636, 1946. (Cited page 42.)

[31] N. Damil and M. Potier-Ferry. A new method to compute perturbed bifurcations: Application to the buckling of imperfect elastic structures. *International Journal of Engineering Science*, 28(9):943–957, 1990. (Cited pages 21 and 198.)

[32] A. de Boer, M. van der Schoot, and H. Bijl. Mesh deformation based on radial basis function interpolation. *Computers & Structures*, 85(11):784–795, 2007. Fourth MIT Conference on Computational Fluid and Solid Mechanics. (Cited pages 99 and 208.)

[33] A. de Boer, A. van Zuijlen, and H. Bijl. Review of coupling methods for non-matching meshes. *Computer Methods in Applied Mechanics and Engineering*, 196(8):1515–1525, 2007. (Cited pages 104, 107 and 209.)

[34] A. de Boer, A. van Zuijlen, and H. Bijl. Comparison of conservative and consistent approaches for the coupling of non-matching meshes. *Computer Methods in Applied Mechanics and Engineering*, 197(49-50):4284–4297, 2008. (Cited pages 107 and 209.)

[35] G. De Nayer. *Interaction Fluide-Structure pour les corps élancés*. PhD thesis, Ecole Centrale de Nantes (ECN), Dec. 2008. (Cited page 114.)

[36] E. Delhez, F. Nyssen, J.-C. Golinval, and A. Batailly. Assessment of Geometric Nonlinearities Influence On NASA Rotor 37 Response to Blade Tip/Casing Rubbing Events. *Journal of Engineering for Gas Turbines and Power*, 2021. (Cited page 29.)

[37] E. Delhez, F. Nyssen, J.-C. Golinval, and A. Batailly. Reduced order modeling of blades with geometric nonlinearities and contact interactions. *Journal of Sound and Vibration*, 500:116037, 2021. (Cited page 29.)

[38] E. Delhez, F. Nyssen, J.-C. Golinval, and A. Batailly. Numerical study of bladed structures with geometric and contact nonlinearities. *Journal of Sound and Vibration*, 544:117382, 2023. (Cited page 29.)

[39] J. D. Denton. The calculation of three-dimensional viscous flow through multistage turbomachines. *Journal of Turbomachinery*, 114(1):18–26, 1992. (Cited page 129.)

[40] S. Deparis, D. Forti, G. Grandperrin, and A. Quarteroni. FaCSI: A block parallel preconditioner for fluid-structure interaction in hemodynamics. *Journal of Computational Physics*, 327:700–718, 2016. (Cited pages 101 and 208.)

[41] Deparis, Simone, Fernández, Miguel Angel, and Formaggia, Luca. Acceleration of a fixed point algorithm for fluid-structure interaction using transpiration conditions. *ESAIM: M2AN*, 37(4):601–616, 2003. (Cited pages 102 and 209.)

[42] C. Descelier. *Dynamique non linéaire en déplacements finis des structures tridimensionnelles viscoélastiques en rotation*. PhD thesis, Châtenay-Malabry, Ecole centrale Paris, 2001. (Cited page 6.)

[43] J. Donea, A. Huerta, J.-P. Ponthot, and A. Rodríguez-Ferran. *Arbitrary Lagrangian–Eulerian Methods*, chapter 14. John Wiley & Sons, Ltd, 2004. (Cited page 96.)

[44] E. H. Dowell. *A Modern Course in Aeroelasticity*. Springer International Publishing, 2015. (Cited page 42.)

[45] A. Dugeai, A. Madec, and A.-S. Sens. Numerical unsteady aerodynamics for turbomachinery aeroelasticity. In *9th International Symposium of Unsteady Aerodynamics, Aeroacoustics and Aeroelasticity of Turbomachines*, Lyon (France), Sept. 2000. (Cited pages 97 and 208.)

[46] H. Dulac. Solutions d'un système d'équations différentielles dans le voisinage de valeurs singulières. *Bulletin de la Société Mathématique de France*, 40:324–383, 1912. (Cited page 39.)

[47] EDF. Finite element *code_aster*, Analysis of Structures and Thermomechanics for Studies and Research. Open source on www.code-aster.org. Open source on www.code-aster.org, 1989–2017. (Cited pages 77 and 92.)

[48] European Commission, Directorate General for Research and Innovation, Directorate General for Mobility and Transport. *Flightpath 2050:Europe's vision for aviation: maintaining global leadership and serving society's needs.* Publications Office, 2011. (Cited page 1.)

[49] C. Farhat, P. Avery, T. Chapman, and J. Cortial. Dimensional reduction of nonlinear finite element dynamic models with finite rotations and energy-based mesh sampling and weighting for computational efficiency. *International Journal for Numerical Methods in Engineering*, 98(9):625–662, 2014. (Cited page 36.)

[50] C. Farhat, T. Chapman, and P. Avery. Structure-preserving, stability, and accuracy properties of the energy-conserving sampling and weighting method for the hyper reduction of nonlinear finite element dynamic models. *International Journal for Numerical Methods in Engineering*, 102(5):1077–1110, 2015. (Cited page 36.)

[51] C. Farhat, M. Lesoinne, P. Stern, and S. Lantéri. High performance solution of three-dimensional nonlinear aeroelastic problems via parallel partitioned algorithms: methodology and preliminary results. *Advances in Engineering Software*, 28(1):43–61, 1997. (Cited pages 102 and 209.)

[52] C. Farhat, M. Lesoinne, and P. L. Tallec. Load and motion transfer algorithms for fluid/structure interaction problems with non-matching discrete interfaces: Momentum and energy conservation, optimal discretization and application to aeroelasticity. *Computer Methods in Applied Mechanics and Engineering*, 157(1-2):95–114, 1998. (Cited pages 104, 107 and 209.)

[53] C. Farhat, K. G. van der Zee, and P. Geuzaine. Provably second-order time-accurate loosely-coupled solution algorithms for transient nonlinear computational aeroelasticity. *Computer Methods in Applied Mechanics and Engineering*, 195(17-18):1973–2001, 2006. (Cited pages 101, 102 and 209.)

[54] B. F. Feeny and R. Kappagantu. On the Physical Interpretation of Proper Orthogonal Modes in Vibrations. *Journal of Sound and Vibration*, 211(4):607–616, 1998. (Cited pages 25 and 199.)

[55] C. A. Felippa, K. Park, and C. Farhat. Partitioned analysis of coupled mechanical systems. *Computer Methods in Applied Mechanics and Engineering*, 190(24-25):3247–3270, 2001. (Cited pages 102 and 209.)

[56] M. Á. Fernández and M. Moubachir. A Newton method using exact jacobians for solving fluid-structure coupling. *Computers & Structures*, 83(2-3):127–142, 2005. (Cited page 102.)

[57] T. Flament, J.-F. Deü, A. Placzek, M. Balmaseda, and D.-M. Tran. Reduced Order Model of Nonlinear Structures for Turbomachinery Aeroelasticity. *Journal of Engineering for Gas Turbines and Power*, 146(3):031005, 2023. (Cited page 123.)

[58] T. Flament, J.-F. Deü, A. Placzek, M. Balmaseda, and D.-M. Tran. Reduced-order model of geometrically nonlinear flexible structures for fluid–structure interaction applications. *International Journal of Non-Linear Mechanics*, 158:104587, 2024. (Cited pages 66 and 109.)

[59] C. Förster, W. A. Wall, and E. Ramm. Artificial added mass instabilities in sequential staggered coupling of nonlinear structures and incompressible viscous flows. *Computer Methods in Applied Mechanics and Engineering*, 196(7):1278–1293, 2007. (Cited pages 102 and 209.)

[60] A. L. Gaitonde and S. P. Fiddes. A Comparison of a Cell-Centre Method and a Cell-Vertex Method for the Solution of the Two-Dimensional Unsteady Euler Equations on a Moving Grid. *Proceedings of the Institution of Mechanical Engineers, Part G: Journal of Aerospace Engineering*, 209(3):203–213, 1995. (Cited pages 99 and 208.)

[61] C. W. Gear. The numerical integration of ordinary differential equations. *Mathematics of Computation*, 21(98):146–156, 1967. (Cited pages 111 and 147.)

[62] C. W. Gear. *Numerical initial value problems in ordinary differential equations.* Automatic Computation S. Longman Higher Education, Harlow, England, 1971. (Cited pages 18, 111 and 198.)

[63] M. W. Gee, U. Küttler, and W. A. Wall. Truly monolithic algebraic multigrid for fluid-structure interaction. *International Journal for Numerical Methods in Engineering*, 85(8):987–1016, 2010. (Cited pages 101 and 208.)

[64] P. Girodroux-Lavigne. Progress in steady/unsteady fluid-structure coupling with Navier-Stokes equations. *IFASD*, 2007. (Cited page 114.)

[65] A. Givois, A. Grolet, O. Thomas, and J.-F. Deü. On the frequency response computation of geometrically nonlinear flat structures using reduced-order finite element models. *Nonlinear Dyn. (97)*, pages 1747–1781, 2019. (Cited page 33.)

[66] A. Grolet and F. Thouverez. Free and forced vibration analysis of a nonlinear system with cyclic symmetry: Application to a simplified model. *Journal of Sound and Vibration*, 331(12):2911–2928, 2012. (Cited page 37.)

[67] M. Gruin. *Dynamique non-linéaire d'une roue de turbine Basse Pression soumise à des excitations structurales d'un turboréacteur.* PhD thesis, Ecole Centrale de Lyon, 2012. (Cited page 6.)

[68] J. Guckenheimer and P. Holmes. *Nonlinear Oscillations, Dynamical Systems, and Bifurcations of Vector Fields.* Springer New York, 1983. (Cited page 37.)

[69] G. P. Guruswamy. Integrated approach for active coupling of structures and fluids. *AIAA Journal*, 27(6):788–793, 1989. (Cited page 42.)

[70] G. P. Guruswamy. Unsteady aerodynamic and aeroelastic calculations for wings using Euler equations. *AIAA Journal*, 28(3):461–469, 1990. (Cited page 42.)

[71] G. P. Guruswamy and P. M. Goorjian. Unsteady transonic aerodynamics and aeroelastic calculations at low-supersonic freestreams. *Journal of Aircraft*, 25(10):955–961, 1988. (Cited page 42.)

[72] G. Guskov. *Dynamique non-linéaire des systèmes multi-rotors. Études numérique et expérimentale.* PhD thesis, Ecole Centrale de Lyon, 2007. (Cited page 6.)

[73] G. Haller and S. Ponsioen. Nonlinear normal modes and spectral submanifolds: existence, uniqueness and use in model reduction. *Nonlinear Dynamics*, 86(3):1493–1534, 2016. (Cited pages 37 and 200.)

[74] À. Haro, M. Canadell, J.-L. Figueras, A. Luque, and J. M. Mondelo. *The Parameterization Method for Invariant Manifolds.* Springer International Publishing, 2016. (Cited pages 40 and 200.)

[75] C. Hayashi. *Nonlinear oscillations in physical systems.* Princeton Legacy Library. Princeton University Press, Princeton, NJ, Apr. 2016. (Cited pages 21 and 198.)

[76] M. Heil. An efficient solver for the fully coupled solution of large-displacement fluid-structure interaction problems. *Computer Methods in Applied Mechanics and Engineering*, 193(1-2):1–23, 2004. (Cited pages 100, 101 and 208.)

[77] M. Heil, A. L. Hazel, and J. Boyle. Solvers for large-displacement fluid-structure interaction problems: segregated versus monolithic approaches. *Computational Mechanics*, 43(1):91–101, 2008. (Cited page 102.)

[78] H. M. Hilber, T. J. R. Hughes, and R. L. Taylor. Improved numerical dissipation for time integration algorithms in structural dynamics. *Earthquake Engineering Structural Dynamics*, 5(3):283–292, 1977. (Cited pages 18, 20 and 198.)

[79] J. Hollkamp and R. Gordon. Reduced-Order Models for Nonlinear Response Prediction: Implicit Condensation and Expansion. *Journal of Sound and Vibration*, 318:1139–1153, 2008. (Cited pages 31, 35 and 200.)

[80] J. J. Hollkamp, R. W. Gordon, and S. M. Spottswood. Nonlinear modal models for sonic fatigue response prediction: a comparison of methods. *Journal of Sound and Vibration*, 284(3):1145–1163, 2005. (Cited page 35.)

[81] D. G. Holmes. Mixing Planes Revisited: A Steady Mixing Plane Approach Designed to Combine High Levels of Conservation and Robustness. volume 6: Turbomachinery, Parts A, B, and C of *Turbo Expo: Power for Land, Sea, and Air*, pages 2649–2658, 2008. (Cited page 129.)

[82] G. Hou, J. Wang, and A. Layton. Numerical Methods for Fluid-Structure Interaction — A Review. *Communications in Computational Physics*, 12(2):337–377, 2012. (Cited pages 100, 102, 208 and 209.)

[83] B. Hübner, E. Walhorn, and D. Dinkler. A monolithic approach to fluid-structure interaction using space-time finite elements. *Computer Methods in Applied Mechanics and Engineering*, 193(23-26):2087–2104, 2004. (Cited pages 100 and 208.)

[84] T. J. R. Hughes. A note on the stability of Newmark's algorithm in nonlinear structural dynamics. *International Journal for Numerical Methods in Engineering*, 11(2):383–386, 1977. (Cited page 18.)

[85] S. Ibrahim, B. Patel, and Y. Nath. Modified shooting approach to the non-linear periodic forced response of isotropic/composite curved beams. *International Journal of Non-Linear Mechanics*, 44(10):1073–1084, 2009. (Cited pages 21 and 198.)

[86] S. Idelsohn and Cardona. A load-dependent basis for reduced nonlinear structural dynamics. *Computers & Structures*, 20(1-3):203–210, Jan. 1985. (Cited pages 27 and 28.)

[87] S. R. Idelsohn and A. Cardona. A load-dependent basis for reduced nonlinear structural dynamics. *Computers & Structures*, 20(1):203–210, 1985. Special Issue: Advances and Trends in Structures and Dynamics. (Cited page 199.)

[88] S. R. Idelsohn and A. Cardona. A reduction method for nonlinear structural dynamic analysis. *Computer Methods in Applied Mechanics and Engineering*, 49(3):253–279, 1985-06. (Cited pages 27 and 28.)

[89] M. Jadoui. *Efficient Monolithic Solution Algorithms for High-Fidelity Aerostructural Analysis and Optimization.* PhD thesis, Sorbonne université, 2023. (Cited page 147.)

[90] S. Jain, P. Tiso, and G. Haller. Exact nonlinear model reduction for a von kármán beam: Slow-fast decomposition and spectral submanifolds. *Journal of Sound and Vibration*, 423:195–211, 2018. (Cited page 200.)

[91] S. Jain, P. Tiso, J. B. Rutzmoser, and D. J. Rixen. A quadratic manifold for model order reduction of nonlinear structural dynamics. *Computers & Structures*, 188:80–94, 2017. (Cited pages 29 and 199.)

[92] A. Jameson. Time dependent calculations using multigrid, with applications to unsteady flows past airfoils and wings. In *10th Computational Fluid Dynamics Conference*. American Institute of Aeronautics and Astronautics, 1991. (Cited page 133.)

[93] L. Jezequel and C. Lamarque. Analysis of non-linear dynamical systems by the normal form theory. *Journal of Sound and Vibration*, 149(3):429–459, 1991. (Cited page 37.)

[94] C. Joannin, B. Chouvion, F. Thouverez, M. Mbaye, and J.-P. Ousty. Nonlinear Modal Analysis of Mistuned Periodic Structures Subjected to Dry Friction. *Journal of Engineering for Gas Turbines and Power*, 138(7), 2015. (Cited pages 37 and 201.)

[95] C. Joannin, B. Chouvion, F. Thouverez, J.-P. Ousty, and M. Mbaye. A nonlinear component mode synthesis method for the computation of steady-state vibrations in non-conservative systems. *Mechanical Systems and Signal Processing*, 83:75–92, 2017. (Cited pages 37 and 201.)

[96] C. Kassiotis, A. Ibrahimbegovic, R. Niekamp, and H. G. Matthies. Nonlinear fluid-structure interaction problem. Part I: implicit partitioned algorithm, nonlinear stability proof and validation examples. *Computational Mechanics*, 47(3):305–323, 2010. (Cited page 102.)

[97] A. Kelley. The stable, center-stable, center, center-unstable, unstable manifolds. *Journal of Differential Equations*, 3(4):546–570, 1967. (Cited page 37.)

[98] G. Kerschen and J. C. Golinval. Physical interpretation of the proper orthogonal modes using the singular value decomposition. *Journal of Sound and Vibration*, 249(5):849–865, 2001. (Cited pages 25 and 199.)

[99] E. Kim and M. Cho. Equivalent model construction for a non-linear dynamic system based on an element-wise stiffness evaluation procedure and reduced analysis of the equivalent system. *Computational Mechanics*, pages 709–724, 2017. (Cited page 34.)

[100] K. Kim, A. Radu, X. Wang, and M. Mignolet. Nonlinear Reduced Order Modeling of Isotropic and Functionally Graded Plates. *International Journal of Non-Linear Mechanics*, 49:100–110, 2013. (Cited pages 29, 30, 199 and 202.)

[101] M. Krack. Nonlinear modal analysis of nonconservative systems: Extension of the periodic motion concept. *Computers & Structures*, 154:59–71, 2015. (Cited pages 37 and 201.)

[102] M. Krack, L. P. von Scheidt, J. Wallaschek, C. Siewert, and A. Hartung. Reduced Order Modeling Based on Complex Nonlinear Modal Analysis and Its Application to Bladed Disks With Shroud Contact. *Journal of Engineering for Gas Turbines and Power*, 135(10), 2013. (Cited pages 37 and 201.)

[103] N. M. Krylov and N. N. Bogoliubov. *Introduction to non-linear mechanics. (AM-11), volume 11*. Annals of Mathematics Studies. Princeton University Press, Princeton, NJ, Dec. 1949. (Cited pages 21 and 198.)

[104] K. Kunisch and S. Volkwein. Galerkin proper orthogonal decomposition methods for parabolic problems. *Numerische Mathematik*, 90(1):117–148, 2001. (Cited page 25.)

[105] E. Kurstak, R. Wilber, and K. D'Souza. Parametric Reduced Order Models for Bladed Disks With Mistuning and Varying Operational Speed. *Journal of Engineering for Gas Turbines and Power*, 141(5), 2019. (Cited pages 140 and 218.)

[106] W. Lacarbonara and G. Rega. Resonant non-linear normal modes. Part II: activation/orthogonality conditions for shallow structural systems. *International Journal of Non-Linear Mechanics*, 38(6):873–887, 2003. (Cited page 37.)

[107] W. Lacarbonara, G. Rega, and A. Nayfeh. Resonant non-linear normal modes. Part I: analytical treatment for structural one-dimensional systems. *International Journal of Non-Linear Mechanics*, 38(6):851–872, 2003. (Cited page 37.)

[108] D. Laxalde. *Étude d'amortisseurs non-linéaires appliqués aux roues aubagées et aux systèmes multi-étages*. PhD thesis, École Centrale de Lyon, 2007. (Cited pages 37 and 201.)

[109] D. Laxalde and F. Thouverez. Complex non-linear modal analysis for mechanical systems: Application to turbomachinery bladings with friction interfaces. *Journal of Sound and Vibration*, 322(4):1009–1025, 2009. (Cited pages 37 and 201.)

[110] M. Li, H. Yan, and L. Wang. Nonlinear model reduction for a cantilevered pipe conveying fluid: A system with asymmetric damping and stiffness matrices. *Mechanical Systems and Signal Processing*, 188:109993, 2023. (Cited pages 42 and 201.)

[111] Y. Liang, H. Lee, S. Lim, W. Lin, K. Lee, and C. Wu. Proper Orthogonal Decomposition and its Applications. *Journal of Sound and Vibration*, 252(3):527–544, 2002. (Cited pages 25 and 199.)

[112] A. M. Liapounoff. *Probleme General de la Stabilite du Mouvement. (AM-17), Volume 17*. Annals of Mathematics Studies. Princeton University Press, Princeton, NJ, July 1947. (Cited page 37.)

[113] M.-S. Liou and C. J. Steffen. A New Flux Splitting Scheme. *Journal of Computational Physics*, 107(1):23–39, 1993. (Cited pages 111 and 210.)

[114] M. K. Mahdiabadi, P. Tiso, A. Brandt, and D. J. Rixen. A non-intrusive model-order reduction of geometrically nonlinear structural dynamics using modal derivatives. *Mechanical Systems and Signal Processing*, 147:107126, 2021. (Cited pages 27, 28, 29 and 199.)

[115] N. Maman and C. Farhat. Matching fluid and structure meshes for aeroelastic computations: A parallel approach. *Computers & Structures*, 54(4):779–785, 1995. (Cited pages 106 and 209.)

[116] J. Marshall and M. Imregun. A review of aeroelasticity methods with emphasis on turbomachinery applications. *Journal of Fluids and Structures*, 10(3):237–267, 1996. (Cited page 42.)

[117] A. Martin, A. Opreni, A. Vizzaccaro, M. Debeurre, L. Salles, A. Frangi, O. Thomas, and C. Touzé. Reduced-order modeling of geometrically nonlinear rotating structures using the direct parametrisation of invariant manifolds. *Journal of Theoretical, Computational and Applied Mechanics*, 2023. (Cited pages 140 and 218.)

[118] A. Martin and F. Thouverez. Dynamic Analysis and Reduction of a Cyclic Symmetric System Subjected to Geometric Nonlinearities. *Journal of Engineering for Gas Turbines and Power*, 141(4), 2018. (Cited page 33.)

[119] D. Maruyama, D. Bailly, and G. Carrier. High-Quality Mesh Deformation Using Quaternions for Orthogonality Preservation. *AIAA Journal*, 52(12):2712–2729, 2014. (Cited page 99.)

[120] I. Mary, P. Sagaut, and M. Deville. An algorithm for unsteady viscous flows at all speeds. *International Journal for Numerical Methods in Fluids*, 34(5):371–401, 2000. (Cited pages 111 and 210.)

[121] H. G. Matthies and J. Steindorf. Partitioned but strongly coupled iteration schemes for nonlinear fluid-structure interaction. *Computers & Structures*, 80(27-30):1991–1999, 2002. (Cited pages 102 and 209.)

[122] M. McEwan, J. Wright, J. Cooper, and A. Leung. A combined modal/finite element analysis technique for the dynamic response of a non-linear beam to harmonic excitation. *Journal of Sound and Vibration 243*, 243(4):601–624, 2001. (Cited pages 31, 34, 42 and 200.)

[123] R. Medeiros, C. E. Cesnik, and E. Coetzee. Nonlinear aeroelastic reduced order models using modal coordinates. In *31st Congress of the International Council of the Aeronautical Sciences*, Belo Horizonte, Brazil, 2018. (Cited page 42.)

[124] M. Mignolet, A. Przekop, S. Rizzi, and S. Spottswood. A Review of indirect/non-intrusive reduced order modeling of nonlinear geometric structures. *Journal of Sound and Vibration*, 332(10):2437–2460, 2013. (Cited pages 29 and 199.)

[125] M. P. Mignolet and C. Soize. Stochastic reduced order models for uncertain geometrically nonlinear dynamical systems. *Computer Methods in Applied Mechanics and Engineering*, 197(45):3951–3963, 2008. (Cited pages 31 and 200.)

[126] A. A. Muravyov and S. A. Rizzi. Determination of nonlinear stiffness with application to random vibration of geometrically nonlinear structures. *Computers & Structures*, 81:1513–1523, 2003-07. (Cited pages 31, 59 and 200.)

[127] A. Najah, B. Cochelin, N. Damil, and M. Potier-Ferry. A critical review of asymptotic numerical methods. *Archives of Computational Methods in Engineering*, 5(1):31–50, 1998. (Cited pages 21 and 198.)

[128] M. Nakhla and J. Vlach. A piecewise harmonic balance technique for determination of periodic response of nonlinear systems. *IEEE Transactions on Circuits and Systems*, 23(2):85–91, 1976. (Cited pages 21 and 198.)

[129] M. S. Nakhla and F. H. Branin. Determining the periodic response of nonlinear systems by a gradient method. *International Journal of Circuit Theory and Applications*, 5(3):255–273, 1977. (Cited pages 21 and 198.)

[130] A. H. Nayfeh and B. Balachandran. *Applied Nonlinear Dynamics*. Wiley, 1995. (Cited pages 21 and 198.)

[131] A. H. Nayfeh, C. Chin, and S. A. Nayfeh. On Nonlinear Normal Modes of Systems With Internal Resonance. *Journal of Vibration and Acoustics*, 118(3):340–345, 1996. (Cited page 37.)

[132] A. H. Nayfeh and S. A. Nayfeh. On Nonlinear Modes of Continuous Systems. *Journal of Vibration and Acoustics*, 116(1):129–136, 1994. (Cited page 37.)

[133] R. B. Nelson. Simplified calculation of eigenvector derivatives. *AIAA Journal*, 14(9):1201–1205, 1976. (Cited pages 27 and 199.)

[134] N. M. Newmark. A Method of Computation for Structural Dynamics. *Journal of the Engineering Mechanics Division*, 85(3):67–94, 1959. (Cited pages 18 and 198.)

[135] E. Nicolaidou, T. L. Hill, and S. A. Neild. Nonlinear mapping of non-conservative forces for reduced-order modelling. *Proceedings of the Royal Society A: Mathematical, Physical and Engineering Sciences*, 478(2268), 2022. (Cited page 63.)

[136] N. Ombret. *Prédiction du flottement de soufflante avec prise en compte des nonlinéarités en pied d'aube*. PhD thesis, École Centrale de Lyon, 2022. (Cited page 42.)

[137] A. Opreni, A. Vizzaccaro, A. Frangi, and C. Touzé. Model order reduction based on direct normal form: application to large finite element MEMS structures featuring internal resonance. *Nonlinear Dynamics*, 105(2):1237–1272, 2021. (Cited page 201.)

[138] A. Opreni, A. Vizzaccaro, C. Touzé, and A. Frangi. High-order direct parametrisation of invariant manifolds for model order reduction of finite element structures: application to generic forcing terms and parametrically excited systems. *Nonlinear Dynamics*, 111(6):5401–5447, 2022. (Cited pages 40, 153 and 201.)

[139] K. Park and M. S. Allen. A Gaussian process regression reduced order model for geometrically nonlinear structures. *Mechanical Systems and Signal Processing*, 184:109720, 2023. (Cited pages 140 and 218.)

[140] F. Pedregosa, G. Varoquaux, A. Gramfort, V. Michel, B. Thirion, O. Grisel, M. Blondel, P. Prettenhofer, R. Weiss, V. Dubourg, J. Vanderplas, A. Passos, D. Cournapeau, M. Brucher, M. Perrot, and Édouard Duchesnay. Scikit-learn: Machine Learning in Python. *Journal of Machine Learning Research*, 12(85):2825–2830, 2011. (Cited page 91.)

[141] M. Peeters, R. Viguié, G. Sérandour, G. Kerschen, and J.-C. Golinval. Nonlinear normal modes, Part II: Toward a practical computation using numerical continuation techniques. *Mechanical Systems and Signal Processing*, 23(1):195–216, 2009. Special Issue: Non-linear Structural Dynamics. (Cited page 37.)

[142] R. Perez, X. Q. Wang, and M. P. Mignolet. Nonintrusive Structural Dynamic Reduced Order Modeling for Large Deformations: Enhancements for Complex Structures. *Journal of Computational and Nonlinear Dynamics*, 9(3), 02 2014. (Cited pages 29, 44 and 199.)

[143] R. Perez, X. Q. Wang, and M. P. Mignolet. Nonintrusive Structural Dynamic Reduced Order Modeling for Large Deformations: Enhancements for Complex Structures. *Journal of Computational and Nonlinear Dynamics*, 9(3), 2014. (Cited pages 42, 44 and 59.)

[144] E. Pesheck, C. Pierre, and S. Shaw. A new galerkin-based approach for accurate non-linear normal modes through invariant manifolds. *Journal of Sound and Vibration*, 249(5):971–993, 2002. (Cited page 37.)

[145] J.-L. Pfister. *Instabilities and optimization of elastic strutures interacting with laminar flows*. PhD thesis, Université Paris Saclay, June 2019. (Cited page 147.)

[146] A. Picou, E. Capiez-Lernout, C. Soize, and M. Mbaye. Robust dynamic analysis of detuned-mistuned rotating bladed disks with geometric nonlinearities. *Computational Mechanics*, 65(3):711–730, 2019. (Cited pages 140, 217 and 218.)

[147] S. Piperno and C. Farhat. Partitioned procedures for the transient solution of coupled aeroelastic problems - part II: energy transfer analysis and three-dimensional applications. *Computer Methods in Applied Mechanics and Engineering*, 190(24-25):3147–3170, 2001. (Cited pages 102 and 209.)

[148] A. Placzek, D.-M. Tran, and R. Ohayon. Nonlinear POD-based reduced-order models for aeroelastic compressible flows. In *International Forum on Aeroelasticity and Structural Dynamics*, Seattle, Washington, USA, June 2009. (Cited page 25.)

[149] A. Placzek, D.-M. Tran, and R. Ohayon. A nonlinear POD-Galerkin reduced-order model for compressible flows taking into account rigid body motions. *Computer Methods in Applied Mechanics and Engineering 200 (49-52)*, pages 3497–3514, 2011. (Cited page 25.)

[150] H. Poincare. *Les Methodes Nouvelles De La Mecanique Celeste*. Gauthiers-Villars, 1892. (Cited page 39.)

[151] S. Ponsioen, S. Jain, and G. Haller. Model reduction to spectral submanifolds and forced-response calculation in high-dimensional mechanical systems. *Journal of Sound and Vibration*, 488:115640, 2020. (Cited page 40.)

[152] L. Prandtl. *Tragflügeltheorie*. 1918. (Cited pages 141 and 217.)

[153] S. Quaegebeur, B. Chouvion, F. Thouverez, and L. Berthe. On a new nonlinear reduced-order model for capturing internal resonances in intentionally mistuned cyclic structures. In *ASME Turbo Expo 2020: Turbomachinery Technical Conference and Exposition, GT 2020*, volume 11. American Society of Mechanical Engineers (ASME), 2020. (Cited pages 140 and 217.)

[154] R. H. Rand. A direct method for non-linear normal modes. *International Journal of Non-Linear Mechanics*, 9(5):363–368, 1974. (Cited page 37.)

[155] J. N. Reddy. *An Introduction to nonlinear Finite Element Analysis Ed. 2*. Oxford university press, NY, 2015. (Cited page 52.)

[156] T. Richter. A monolithic geometric multigrid solver for fluid-structure interactions in ALE formulation. *International Journal for Numerical Methods in Engineering*, 104(5):372–390, 2015. (Cited pages 101 and 208.)

[157] D. J. Rixen and M. Géradin. *Mechanical Vibrations, third edition*. John Wiley & Sons, 2015. (Cited pages xiii, 18, 19 and 114.)

[158] A. Rizzi and A. Muravyov. Improved Equivalent Linearization Implementations Using Nonlinear Stiffness Evaluation. *NASA/TM-2001-210838*, 2001. (Cited page 31.)

[159] P. Roe. Approximate Riemann solvers, parameter vectors, and difference schemes. *Journal of Computational Physics*, 43(2):357–372, Oct. 1981. (Cited page 128.)

[160] R. Rosenberg. On Nonlinear Vibrations of Systems with Many Degrees of Freedom. In *Advances in Applied Mechanics*, pages 155–242. Elsevier, 1966. (Cited page 37.)

[161] R. M. Rosenberg. Normal Modes of Nonlinear Dual-Mode Systems. *Journal of Applied Mechanics*, 27(2):263–268, 1960. (Cited page 37.)

[162] R. M. Rosenberg. On Normal Vibrations of a General Class of Nonlinear Dual-Mode Systems. *Journal of Applied Mechanics*, 28(2):275–283, June 1961. (Cited page 37.)

[163] R. M. Rosenberg. The Normal Modes of Nonlinear n-Degree-of-Freedom Systems. *Journal of Applied Mechanics*, 29(1):7–14, 1962. (Cited page 37.)

[164] R. M. Rosenberg and J. K. Kuo. Nonsimilar Normal Mode Vibrations of Nonlinear Systems Having Two Degrees of Freedom. *Journal of Applied Mechanics*, 31(2):283–290, 1964. (Cited page 37.)

[165] A. Roshko. *On the development of turbulent wakes from vortex streets*. PhD thesis, California Institute of Technology, 1952. (Cited pages 109 and 111.)

[166] J. Rutzmoser. *Model Order Reduction for Nonlinear Structural Dynamics*. PhD thesis, Technische Universität München, 2018. (Cited pages 27 and 199.)

[167] R. Sampaio and C. Soize. Remarks on the efficiency of POD for model reduction in nonlinear dynamics of continuous elastic systems. *International Journal for numerical methods in Engineering*, 2007. (Cited page 25.)

[168] A. P. Saxer and M. B. Giles. Predictions of three-dimensional steady and unsteady inviscid transonic stator/rotor interaction with inlet radial temperature nonuniformity. *Journal of Turbomachinery*, 116(3):347–357, 1994. (Cited page 129.)

[169] R. Schaback. Creating Surfaces from Scattered Data Using Radial Basis Functions. In *Mathematical Methods in CAGD III*. M. Daehlen, T.Lyche, and L.L. Schumacher (eds.), 1995. (Cited pages 104 and 209.)

[170] J. S. Schotte. *Influence de la gravité sur les vibrations linéaires d'une structure élastique partiellement remplie par un liquide incompressible.* PhD thesis, Conservatoire national des arts et metiers-CNAM, 2001. (Cited page 6.)

[171] A. Sénéchal. *Réduction de vibrations de structure complexe par shunts piézoélectriques : application aux turbomachines.* PhD thesis, Conservatoire national des arts et metiers - CNAM, 2011. (Cited pages xiii, 23 and 66.)

[172] R. Seydel. *Practical Bifurcation and Stability Analysis.* Springer New York, 2010. (Cited pages 21 and 198.)

[173] S. Shaw and C. Pierre. Non-linear normal modes and invariant manifolds. *Journal of Sound and Vibration*, 150(1):170–173, 1991. (Cited pages 37 and 200.)

[174] S. Shaw and C. Pierre. Normal Modes for Non-Linear Vibratory Systems. *Journal of Sound and Vibration*, 164(1):85–124, 1993. (Cited pages 37 and 200.)

[175] S. Shaw and C. Pierre. Normal Modes of Vibration for Non-Linear Continuous Systems. *Journal of Sound and Vibration*, 169(3):319–347, 1994. (Cited pages 37 and 200.)

[176] Y. Shen, N. Béreux, A. Frangi, and C. Touzé. Reduced order models for geometrically nonlinear structures: Assessment of implicit condensation in comparison with invariant manifold approach. *European Journal of Mechanics - A/Solids*, 86:104165, 2021. (Cited pages xiii and 38.)

[177] K. Sinha, F. Alijani, W. R. Krüger, and R. D. Breuker. Koiter-Newton Based Model Reduction for Large Deflection Analysis of Wing Structures. *AIAA Journal*, 61(8):3608–3617, 2023. (Cited page 35.)

[178] P. Slaats, J. de Jongh, and A. Sauren. Model reduction tools for nonlinear structural dynamics. *Computers & Structures*, 54(6):1155–1171, 1995-03. (Cited pages 27, 28 and 199.)

[179] J. C. Slater. A numerical method for determining nonlinear normal modes. *Nonlinear Dynamics*, 10(1):19–30, 1996. (Cited page 37.)

[180] P. Spalart. Trends in turbulence treatments. In *Fluids 2000 Conference and Exhibit*. American Institute of Aeronautics and Astronautics, June 2000. (Cited page 129.)

[181] P. R. Spalart and C. L. Rumsey. Effective Inflow Conditions for Turbulence Models in Aerodynamic Calculations. *AIAA Journal*, 45(10):2544–2553, Oct. 2007. (Cited page 129.)

[182] A. Sternchüss. *Multi-level parametric reduced models of rotating bladed disk assemblies.* PhD thesis, Ecole Centrale de Paris, 2009. (Cited pages 140 and 218.)

[183] P. Sundararajan and S. T. Noah. Dynamics of Forced Nonlinear Systems Using Shooting/Arc-Length Continuation Method, Application to Rotor Systems. *Journal of Vibration and Acoustics*, 119(1):9–20, 1997. (Cited pages 21 and 198.)

[184] P. L. Tallec and J. Mouro. Fluid structure interaction with large structural displacements. *Computer Methods in Applied Mechanics and Engineering*, 190(24-25):3039–3067, 2001. (Cited pages 102 and 209.)

[185] T. Theodorsen. General theory of aerodynamic instability and the mechanism of flutter. *Aerodynamic Flutter, American Institute of Aeronautics and Astronautics*, (496), 1935. (Cited pages 141 and 217.)

[186] P. Thevenaz, T. Blu, and M. Unser. Interpolation revisited [medical images application]. *IEEE Transactions on Medical Imaging*, 19(7):739–758, 2000. (Cited pages 107 and 209.)

[187] O. Thomas, A. Sénéchal, and J.-F. Deü. Hardening/Softening Behavior and Reduced Order Modeling of Nonlinear Vibrations of Rotating Cantilever Beams. *Nonlinear Dynamics*, 2(86):1293–1318, 2016. (Cited pages 17 and 56.)

[188] F.-B. Tian, H. Dai, H. Luo, J. F. Doyle, and B. Rousseau. Fluid-structure interaction involving large deformations: 3D simulations and applications to biological systems. *Journal of Computational Physics*, 258:451–469, Feb. 2014. (Cited page 113.)

[189] R. Tibshirani. Regression Shrinkage and Selection via the Lasso. *Journal of the Royal Statistical Society Series B: Statistical Methodology*, 58(1):267–288, 1996. (Cited pages 44, 91 and 203.)

[190] P. Tiso. Optimal second order reduction basis selection for nonlinear transient analysis. In *Conference Proceedings of the Society for Experimental Mechanics Series*, pages 27–39. Springer New York, 2011. (Cited page 29.)

[191] P. Tiso and D. Rixen. Discrete empirical interpolation method for finite element structural dynamics. In G. Kerschen, D. Adams, and A. Carrella, editors, *Topics in Nonlinear Dynamics, Volume 1 - Proceedings of the 31st IMAC, A Conference on Structural Dynamics, 2013*, Conference Proceedings of the Society for Experimental Mechanics Series, pages 203–212. Springer, 2013. (Cited pages 36 and 200.)

[192] C. Touzé and M. Amabili. Nonlinear normal modes for damped geometrically nonlinear systems: Application to reduced-order modelling of harmonically forced structures. *Journal of Sound and Vibration*, 298(4-5):958–981, 2006. (Cited page 39.)

[193] C. Touzé and M. Amabili. Nonlinear normal modes for damped geometrically nonlinear systems: Application to reduced-order modelling of harmonically forced structures. *Journal of Sound and Vibration*, 298(4):958–981, 2006. (Cited pages 42 and 201.)

[194] S. Turek and J. Hron. Proposal for numerical benchmarking of fluid–structure interaction between an elastic object and laminar incompressible flow. In *Fluid–Structure Interaction: Modelling, Simulation, Optimisation, Springer-Verlag*, pages 371–385, Berlin, Heidelberg, Netherlands, 2006. H.J. Bungartz, M. Schäfer (Eds.). (Cited pages 100, 109, 113 and 208.)

[195] A. Vakakis, T. Nayfeh, and M. King. A Multiple-Scales Analysis of Nonlinear, Localized Modes in a Cyclic Periodic System. *Journal of Applied Mechanics*, 60(2):388–397, 1993. (Cited page 37.)

[196] A. F. Vakakis. Dynamics of a nonlinear periodic structure with cyclic symmetry. *Acta Mechanica*, 95(1-4):197–226, 1992. (Cited page 37.)

[197] A. F. Vakakis and C. Cetinkaya. Mode Localization in a Class of Multidegree-of-Freedom Nonlinear Systems with Cyclic Symmetry. *SIAM Journal on Applied Mathematics*, 53(1):265–282, 1993. (Cited page 37.)

[198] G. D. van Albada, B. van Leer, and W. W. Roberts Jr. A comparative study of computational methods in cosmic gas dynamics. *Astronomy and Astrophysics*, 108(1):76–84, Apr. 1982. (Cited page 129.)

[199] A. Vizzaccaro, A. Givois, P. Longobardi, Y. Shen, J.-F. Deü, L. Salles, C. Touzé, and O. Thomas. Non-intrusive reduced order modelling for the dynamics of geometrically nonlinear flat structures using three-dimensional finite elements. *Computational Mechanics*, 66(6):1293–1319, 2020-12. (Cited pages 31, 34, 44, 90, 163 and 200.)

[200] A. Vizzaccaro, A. Opreni, L. Salles, A. Frangi, and C. Touzé. High order direct parametrisation of invariant manifolds for model order reduction of finite element structures: application to large amplitude vibrations and uncovering of a folding point. *Nonlinear Dynamics*, 110(1):525–571, 2022. (Cited pages 40 and 201.)

[201] A. Vizzaccaro, L. Salles, and C. Touzé. Comparison of nonlinear mappings for reduced-order modelling of vibrating structures: normal form theory and quadratic manifold method with modal derivatives. *Nonlinear Dynamics*, 103(4):3335–3370, 2020. (Cited page 200.)

[202] A. Vizzaccaro, Y. Shen, L. Salles, J. Blahoš, and C. Touzé. Direct computation of nonlinear mapping via normal form for reduced-order models of finite element nonlinear structures. *Computer Methods in Applied Mechanics and Engineering*, 384:113957, 2021. (Cited pages 40, 153 and 201.)

[203] S. Volkwein. *Proper orthogonal decomposition and singular value decomposition*. Karl-Franzens-Univ. Graz & Techn. Univ. Graz, 1999. (Cited page 25.)

[204] X. Wang and M. P. Mignolet. Toward a systematic construction of the basis for nonlinear geometric reduced order models. *Proceedings of the International Conference on Structural Dynamic , EURODYN*, 1:335 – 354, 2020. (Cited pages 29 and 199.)

[205] X. Q. Wang, V. Khanna, K. Kim, and M. Mignolet. Nonlinear reduced-order modeling of flat cantilevered structures: identification challenges and remedies. *Journal of Aerospace Engineering*, 34(6):04021085, 2021. (Cited pages 29 and 199.)

[206] H. Wendland. *Konstruktion und Untersuchung radialer Basisfunktionen mit kompaktem Träger*. PhD thesis, Universität Göttingen, 1996. (Cited pages 104 and 209.)

[207] J. Witteveen. Explicit and Robust Inverse Distance Weighting Mesh Deformation for CFD. In *48th AIAA Aerospace Sciences Meeting Including the New Horizons Forum and Aerospace Exposition*. American Institute of Aeronautics and Astronautics, 2010. (Cited pages 99 and 208.)

[208] L. Xuanang. *Backbone Curve Analysis of Nonlinear Mechanical Systems*. PhD thesis, University of Sheffield, 2018. (Cited page 21.)

[209] O. C. Zienkiewicz and R. L. Taylor. *The finite element method: Solid mechanics vol. 2*. Butterworth-Heinemann, 5 edition, 2000. (Cited page 14.)

[210] H. Zou and T. Hastie. Regularization and Variable Selection Via the Elastic Net. *Journal of the Royal Statistical Society Series B: Statistical Methodology*, 67(5):768–768, 11 2005. (Cited pages 44, 91 and 203.)

Résumé du mémoire (en français)

Introduction

La recherche de meilleures performances pour les futurs moteurs d'avion conduit à des hélices et des pales plus grandes, et donc à des structures plus flexibles. Cette flexibilité engendre des amplitudes de déformation plus importantes, nécessitant une modélisation prenant en compte les non-linéarités géométriques pour évaluer précisément les niveaux de vibrations et caractériser les phénomènes aéroélastiques tels que le flottement et la réponse forcée. L'étude de ces phénomènes requière la résolution d'un problème couplé prenant en compte à la fois les domaines fluide et structure. Une approche pour résoudre les problèmes aéroélastiques consiste à coupler deux solveurs non-linéaires différents pour le fluide et pour la structure. Néanmoins, dans le cadre d'applications industrielles, les ressources de calcul en temps et en mémoire d'un tel couplage sont souvent trop importantes. En outre, la plupart des solveurs fluides et structures ne sont pas conçus pour communiquer entre eux, rendant le transfert d'informations d'un solveur à l'autre laborieux.

Afin de faciliter le couplage et réduire les temps de calcul, une approche efficace consiste à coupler un solveur non-linéaire pour la partie fluide avec un modèle d'ordre réduit non-linéaire de la structure. Pour être efficace, le modèle d'ordre réduit doit être conçu de manière non intrusive, indépendant du modèle d'éléments finis complet pendant le calcul, ne nécessitant pas de solveur extérieur mais seulement la connaissance des composantes réduites. Il est à noter que la dynamique du fluide peut également être représentée par des modèles de moindre fidélité (par exemple les théories de Theodorsen et de Lifting-line) ou par des modèles d'ordre réduit s'appuyant sur des approches haute-fidélité comme des formulation hybrides ou data-driven. Dans ce travail, la dynamique du fluide n'est pas réduite et calculée à l'aide d'un solveur CFD haute fidélité. Notre travail se concentre uniquement sur l'élaboration d'un modèle d'ordre réduit pour la structure, sous la contrainte d'un couplage avec un solveur fluide externe.

Dans la littérature, l'étude des phénomènes aéroélastiques sur des configurations industrielles est généralement effectuée en couplant un solveur fluide avec un modèle d'ordre réduit linéaire pour la structure. Or nous avons évoqué le fait qu'une modélisation linéaire n'est plus suffisante pour rendre compte de ces phénomènes sur les structures élancées. Des modèles réduits non-linéaires pour la structure sont courants dans la littérature et nous en détaillons certains dans ce travail, mais ils ne sont généralement pas élaborés dans une optique de couplage.

C'est ce qui justifie cette étude qui consiste à développer un modèle d'ordre réduit pour la structure dans le cadre de non-linéarités géométriques et sous la contrainte d'un couplage simple avec un quelconque solveur fluide externe. Ce modèle d'ordre réduit doit pouvoir être construit de manière non-intrusive à partir d'un solveur éléments finis industriel afin d'être en mesure de traiter des structures aéronautiques complexes.

Les contributions de cette thèse résident dans l'élaboration d'une méthode innovante de construction du modèle d'ordre réduit non-linéaire de manière non intrusive par rapport à un solveur éléments finis, ainsi que dans le couplage de ce modèle réduit avec un solveur fluide industriel pour caractériser des phénomènes d'interaction fluide-structure.

Chapitre 1: Réduction de modèle pour des structures non-linéaires géométriques en rotation

Le premier chapitre de ce manuscrit établit le contexte théorique relatif à la modélisation de la structure. Nous considérons une loi de comportement élastique linéaire pour le matériau, se traduisant par la loi de Hooke liant les tenseurs des contraintes de Piola-Kirchhoff $\boldsymbol{S}$ et celui de Green-Lagrange $\boldsymbol{E}$ des déformations : $\boldsymbol{S} = \boldsymbol{\mathcal{H}} : \boldsymbol{E}$, ainsi qu'une cinématique de grands déplacements pour ce dernier:

$$\boldsymbol{E} = \frac{1}{2}\left[\boldsymbol{\nabla_X u} + (\boldsymbol{\nabla_X u})^T + (\boldsymbol{\nabla_X u})^T \boldsymbol{\nabla_X u}\right]. \tag{6.1}$$

La dynamique de la structure est étudiée dans son repère mobile en rotation à vitesse constante autour d'un axe fixe. Une discrétisation de Galerkin par éléments finis est adoptée. Notant $\mathbf{u}$ les degrés de liberté de la structure, ces derniers sont solutions de l'équation:

$$\mathbf{M}\ddot{\mathbf{u}} + \mathbf{C}\dot{\mathbf{u}} + \underbrace{\left[\mathbf{K_{mat}} - \mathbf{K_c} + \mathbf{K_{nl}}(\mathbf{u_s})\right]}_{\mathbf{K}(\Omega)} \mathbf{u} + \mathbf{g_{nl}}(\mathbf{u}) = \mathbf{f}_{\mathrm{a}}, \tag{6.2}$$

avec $\mathbf{M}$ la matrice de masse, $\mathbf{C}$ l'amortissement de Rayleigh, $\mathbf{K_{mat}}$ la matrice de raideur matériaux, $\mathbf{K_c}$ la matrice d'assouplissement centrifuge, $\mathbf{K_{nl}}(\mathbf{u_s})$ la partie non-linéaire de la matrice tangente de raideur (jacobienne des efforts internes non-linéaires) évaluée en la solution précontrainte $\mathbf{u_s}$, $\mathbf{g_{nl}}$ les efforts internes non-linéaires et $\mathbf{f}_{\mathrm{a}}$ l'effort aérodynamique extérieur imposé en supplément des efforts centrifuges. Les expressions de ces matrices et vecteurs sont données dans le chapitre et il est important pour la suite de préciser que la composante purement non-linéaire des efforts internes $\mathbf{g_{nl}}$ est cubique en les degrés de liberté.

La résolution de l'équation de la dynamique est possible selon deux approches. La première est une résolution temporelle, intégrant l'équation (6.2) à partir de conditions initiales, du régime transitoire jusqu'à l'établissement d'un régime permanent. Les schémas d'intégration temporelle sont abondants dans la littérature tels que les schémas de différentiation d'Euler (explicites et implicites), les méthodes de Runge-Kutta, les schémas multi-pas comme ceux de Gear [62] ou de Bathe [9] et ses variantes Bathe-β_1/β_2, ρ_∞-Bathe. Pour résoudre la dynamique de la structure, les méthodes à un pas de la famille des méthodes de Newmark [134] et ses variantes HHT-α [78] et α-generalized [4, 27] sont habituellement privilégiées.

La seconde approche pour résoudre les équations dynamiques de la structure est dite fréquentielle. L'idée est que le calcul temporel du régime transitoire avant l'établissement du régime permanent est parfois long et bien souvent non exploité par la suite. Les méthodes fréquentielles permettent de ne calculer que le régime permanent établi. Cela permet également de déterminer ce dernier pour différentes fréquences d'excitation via des techniques de continuation telles que les méthodes dites de tir (Shooting) [85, 129, 130, 172, 183], d'équilibrage harmonique [6, 75, 103, 128] ou asymptotiques numériques [29, 31, 127]. Les méthodes de continuations temporelles sont en effet très coûteuses du fait de l'intégration des régimes transitoires et les parties instables sont difficilement accessibles contrairement à l'utilisation des méthodes fréquentielles.

L'équation de la dynamique (6.2) constitue le modèle dit "complet" et comporte un nombre conséquent de degrés de libertés. Comme précisé en introduction, la résolution du système complet et le couplage de ce dernier avec un autre code de calcul nécessite des ressources numériques et des temps de calcul souvent inabordables. C'est pourquoi des méthodes dites de réduction de modèle sont développées afin de réduire la dimension du système à résoudre et de ce fait les ressources nécessaires.

Les modèles réduits dits par projection consistent à projeter les équations de la dynamique dans une base de dimension réduite $\mathbf{V}$ judicieusement choisie. Les degrés de liberté des déplacements sont approximés par $\mathbf{u} \approx \mathbf{Vq}$ où $\mathbf{q}$ est le vecteur des coordonnées dites généralisées. Après projection, l'equation de la dynamique devient:

$$\underbrace{\mathbf{V}^T\mathbf{M}\mathbf{V}}_{\widetilde{\mathbf{M}}}\ddot{\mathbf{q}} + \underbrace{\mathbf{V}^T\mathbf{C}\mathbf{V}}_{\widetilde{\mathbf{C}}}\dot{\mathbf{q}} + \underbrace{\mathbf{V}^T\mathbf{K}\mathbf{V}}_{\widetilde{\mathbf{K}}}\mathbf{q} + \underbrace{\mathbf{V}^T\mathbf{g}_{\mathbf{nl}}(\mathbf{Vq})}_{\widetilde{\mathbf{g}}_{\mathbf{nl}}(\mathbf{q})} = \underbrace{\mathbf{V}^T\mathbf{f}_{\mathrm{a}}}_{\widetilde{\mathbf{f}}_{\mathrm{a}}}. \tag{6.3}$$

La base de réduction $\mathbf{V}$ ne contient que peu de vecteurs, ce qui conduit à des matrices projetées $\widetilde{\mathbf{M}}$, $\widetilde{\mathbf{C}}$ et $\widetilde{\mathbf{K}}$ de dimensions négligeables au regard du problème initial. L'enjeu est donc de déterminer une base de réduction capable de rendre compte du comportement non-linéaire de la structure. Une seconde contrainte que nous détaillerons plus loin consiste à déterminer une expression explicite des efforts non-linéaires projetés $\widetilde{\mathbf{g}}_{\mathbf{nl}}(\mathbf{q})$. En effet, la projection $\mathbf{V}^T\mathbf{g}_{\mathbf{nl}}(\mathbf{Vq})$ est intrusive car elle nécessite un calcul dans le domaine complet par un solveur éléments finis, ce qui n'est pas souhaitable.

Les vibrations de la structure peuvent être caractérisées par les modes normaux linéaires de celle-ci: $\mathbf{\Phi} = \{\boldsymbol{\phi}_1, \cdots, \boldsymbol{\phi}_N\}$ avec N le nombre de degrés de liberté de la structure. Les modes normaux linéaires sont solutions de l'équation aux valeurs propres:

$$\left(\mathbf{K} - \omega_i^2\mathbf{M}\right)\boldsymbol{\phi}_i = \mathbf{0} \quad \forall i \in [1, N], \tag{6.4}$$

avec ω_i les pulsations dont dérivent les fréquences propres de ces modes. Lorsque les amplitudes de déplacement sont faibles et que les non-linéarités géométriques peuvent de ce fait être négligées, le problème devient linéaire. Dans un tel cas, le choix d'une base de réduction exclusivement constituée d'un nombre réduit de modes normaux linéaires est un choix pertinent pour représenter le comportement dynamique de la structure. Il suffit de prendre les modes de la structure dont la fréquence propre est contenue dans la gamme de fréquences des excitations externes. En revanche, en présence de non-linéarités géométriques, un couplage apparait entre des modes basse et haute fréquence. Par conséquent, les premiers modes linéaires ne sont plus suffisants pour capturer la dynamique et la base de réduction doit être enrichie par des modes additionnels prenant en compte le couplage non-linéaire des modes.

Une possibilité est l'exploitation de résultats de simulations haute-fidélité déjà calculées par des méthodes POD [1, 54, 98, 111]. Le problème majeur est d'une part que les calculs préliminaires sont très coûteux et d'autre part qu'ils dépendent du cas de chargement. Une autre possibilité est l'utilisation de dérivées modales [87, 91, 114, 133, 166, 178], qui sont une expansion de Taylor des modes linéaires afin de capturer la non-linéarité proche. Le nombre de dérivés modales évolue de manière quadratique avec celui des modes linéaires. Bien qu'il existe des méthodes pour sélectionner les plus pertinentes [114], une telle pluralité peut être problématique. La littérature propose également un enrichissement de la base de réduction par modes duaux [100, 124, 142, 204, 205]. Ces derniers sont obtenus à partir d'une décomposition en valeurs singulières de solutions statiques résultant d'efforts imposés avec une forme particulière. Les efforts sont en effet construits en s'appuyant sur les modes linéaires de la structure afin que les modes duaux enrichissant la base de réduction ne privilégient pas de cas de chargement spécifique. Nous reviendrons sur les modes duaux dans le Chapitre 2.

Dans le cadre d'un couplage fluide-structure partitionné, le solveur fluide intéragit avec un solveur éléments finis qui calcule, à chaque sous-itération de couplage, le déplacement de la structure soumise au chargement aérodynamique. L'échange d'informations entre les solveurs fluide et structure n'est pas trivial, d'où l'intérêt d'utiliser un modèle d'ordre réduit non-intrusif et autonome dans le sens où le solveur éléments finis n'est pas appelé pendant le calcul. Or, l'évaluation des efforts projetés $\widetilde{\mathbf{g}}_{\mathbf{nl}}(\mathbf{q}) = \mathbf{V}^T\mathbf{g}_{\mathbf{nl}}(\mathbf{Vq})$ dans l'équation (6.3) nécessite des aller-retours entre les variables réduites et celles du modèle complet. En effet, le déplacement physique $\mathbf{u} \approx \mathbf{Vq}$ doit dans un premier temps être assemblé puis évalué dans le domaine complet par le solveur éléments finis (calcul de $\mathbf{g}_{\mathbf{nl}}(\mathbf{Vq})$), pour être ensuite projeté à nouveau dans l'espace réduit. Nous comprenons que l'intérêt serait de connaitre une expression explicite de $\widetilde{\mathbf{g}}_{\mathbf{nl}}(\mathbf{q})$ en fonction des coordonnées généralisées, ce qui permettrait d'évaluer cette quantité directement dans l'espace réduit. Notre travail se plaçant dans le cadre de problèmes d'élasticité en petites déformations locales et grands déplacements et rotations, régi par un modèle de comportement de Saint Venant-Kirchhoff, les efforts non-linéaires internes $\mathbf{g}_{\mathbf{nl}}(\mathbf{u})$ sont cubiques en les degrés de liberté $\mathbf{u}$ [125, 126]. L'introduction de l'approximation linéaire $\mathbf{u} \approx \mathbf{Vq}$ dans leur expression conduit à des efforts non-linéaires projetés $\widetilde{\mathbf{g}}_{\mathbf{nl}}(\mathbf{q})$ cubiques en les coordonnées généralisées $\mathbf{q}$. Notant $\widetilde{g}^k_{\text{nl}}(\mathbf{q})$ la $k^{\text{ième}}$ coordonnée de $\widetilde{\mathbf{g}}_{\mathbf{nl}}(\mathbf{q})$, nous pouvons écrire son expression de manière explicite de la manière suivante:

$$\widetilde{g}^k_{\text{nl}}(\mathbf{q}) = \sum_{i=1}^{n}\sum_{j=i}^{n}\beta^k_{ij}q_iq_j + \sum_{i=1}^{n}\sum_{j=i}^{n}\sum_{m=j}^{n}\gamma^k_{ijm}q_iq_jq_m, \tag{6.5}$$

avec n le nombre de modes dans la base de réduction, alors que β^k_{ij} et γ^k_{ijm} sont les coefficients respectivement quadratiques et cubiques de l'expression polynomiale. Ces coefficients restent à déterminer. Pour cela deux méthodes se distinguent dans la littérature. La première consiste à déterminer ces coefficients un par un en imposant à la structure des déplacements astucieusement choisis, cette méthode est appelée STEP [126]. Il faut toutefois garder en mémoire qu'évaluer des efforts internes sur ces déplacements imposés avec des structures 3D peut entrainer des artefacts numériques [199]. La seconde méthode est basée non pas sur des déplacements mais sur des efforts imposés à la structure, avec une forme particulière issue des modes normaux linéaires. Une telle méthode est connue sous le nom de *Implicit Condensation* (IC) [122]. Elle se restreint à ne considérer que les premiers modes linéaires de la structure, identifier les coefficients des efforts non-linéaires projetés par efforts imposés, puis une étape de reconstruction a posteriori du calcul appelée *Expansion* [79] est proposée pour rendre compte du couplage non-linéaire entre les modes. Dans le chapitre 2 nous proposons une méthode innovante s'affranchissant de cette reconstruction a posteriori peu précise, et qui ne se restreint pas à uniquement des modes linéaires dans la base de réduction, tout en gardant des efforts imposés similaires.

Il existe d'autres approches pour construire des modèles d'ordres réduits pour des structures non-linéaires géométriques. Une famille de méthodes appelées Hyper-réduction consistent à évaluer les efforts internes non-linéaires toujours dans le domaine complet, mais seulement pour un nombre réduit de degrés de libertés judicieusement choisis. Nous pouvons citer par exemple les méthodes DEIM [26] et ses dérivées UDEIM [191] et ECSW [3]. Ces méthodes restant intrusives elles peuvent ne pas être évidentes à mettre en pratique et sont moins compatibles avec un couplage fluide-structure.

Afin d'étudier la réponse non-linéaire de la structure autour de résonances, la théorie des modes non-linéaires est très présente dans la littérature. Elle ne consiste pas en une projection dans une base de dimension réduite mais en un changement de variable non-linéaire pour passer des variables réduites aux physiques. La dynamique de la structure évolue dans une variété tangente aux modes linéaires à l'origine et est pilotée par des modes dits maitres alors que les autres modes, appelés esclaves, ont un comportement fonction de ces modes maitres [173–175, 201]. L'unicité de la variété sous certaines conditions est prouvée dans [90], conduisant à la théorie des sous-variétés spectrales [73]. Auparavant limitée à des changements de variables d'ordre faibles, la méthode de paramétrisation des variétés invariantes [16–18, 74] a permis l'application de la théorie à des systèmes de grande dimension avec des développements à ordre arbitraire et de traiter les résonnance internes [200]. La prise en compte de l'effort extérieur dans la construction du modèle est également possible [137, 138]. La construction du modèle étant intrusive dans le code source éléments finis, une approche non-intrusive limitée à l'ordre 3 est également proposée dans [202]. Des applications en interaction fluide-structure sont présentes dans la littérature [2, 110, 193] mais l'approche n'est pas prévue dans sa construction pour des efforts extérieurs dépendants de la position, ce que sont les efforts aérodynamiques. Il est également utile de mentionner les modes complexes non-linéaires proposés dans [108, 109], basés sur une variation pseudo-périodique des modes non-linéaires, qui permettent également de traiter des non-linéarités de frottement aux contacts [94, 95, 101, 102].

Chapitre 2: Développement d'un modèle réduit non-intrusif pour le couplage aéroélastique

Ce chapitre détaille la construction du modèle réduit proposé et traite une première application à un cas de poutre de von Kármán.

Construction du modèle réduit: Le couplage du modèle réduit structure avec un solveur fluide et les applications aéronautiques imposent plusieurs contraintes. La première est que les structures étant complexes, nous nous imposons que la construction du modèle puisse faire appel de manière non-intrusive à un logiciel éléments finis industriel. De plus, une fois construit, le modèle réduit ne doit plus avoir à faire appel au solveur éléments finis et est entièrement déterminé par les matrices réduites et coordonnées généralisées, notamment pour les efforts non-linéaires internes projetés $\widetilde{\mathbf{g}}_{\mathbf{nl}}(\mathbf{q})$. La seconde contrainte vient des applications aéroélastiques qui ont pour particularité que les efforts aérodynamiques extérieurs s'exerçant sur la structure sont suiveurs donc dépendent de la position et qu'ils ont également un contenu fréquentiel très riche. Ces deux points posent problème vis à vis d'une réduction par modes non-linéaires et la littérature manque de recul sur ce point. Dans ce chapitre nous proposons un modèle réduit par projection, que nous appellerons ICDual, avec enrichissement de la base de réduction par modes duaux et une expression des efforts non-linéaires projetés identifiée par efforts imposés.

Le base de modes propres de la structure est enrichie par des modes duaux. La détermination de ces derniers nécessite le calcul de solutions statiques à des efforts imposés de la forme suivante:

$$\forall \ell \in [1, n_{\mathrm{L}}] \quad \mathbf{f}_{\mathrm{ext}}^{(\ell)} = \mathbf{K}\left(\sum_{i=1}^{n_{\mathrm{b}}} \alpha_i^{(\ell)} \boldsymbol{\phi}_i\right), \tag{6.6}$$

où $(\boldsymbol{\phi})_{i\in[1,n_{\mathrm{b}}]}$ sont les modes normaux linéaires de la structure considérés et $\alpha_i^{(\ell)}$ des coefficients de pondération. Les efforts imposés de la sorte sont intéressants car ils sont basés exclusivement sur la forme des modes linéaires et non sur des cas de chargements particuliers qui seraient alors privilégiés par le modèle dans certaines applications au détriment d'autres. Les solutions non-linéaires statiques résultant de ces chargements sont solutions des équations:

$$\forall \ell \in [1, n_{\mathrm{L}}] \quad \mathbf{K}\mathbf{u}_{\mathbf{s}}^{(\ell)} + \mathbf{f}_{\mathbf{nl}}(\mathbf{u}_{\mathbf{s}}^{(\ell)}) = \mathbf{f}_{\mathrm{ext}}^{(\ell)}. \tag{6.7}$$

L'idée est ensuite d'extraire les coordonnées généralisées $\mathbf{q}^{(\ell)}$ associées aux projections sur les modes de ces solutions statiques. En effet, comme $\mathbf{u}_{\mathbf{s}}^{(\ell)} \approx \boldsymbol{\Phi}\mathbf{q}^{(\ell)}$, les coordonnées $\mathbf{q}^{(\ell)}$ sont calculées par moindres carrés et les résidus de l'approximation sont écrits $\mathbf{r}^{(\ell)}$ ce qui donne:

$$\forall \ell \in [1, n_{\mathrm{L}}] \quad \mathbf{u}_{\mathbf{s}}^{(\ell)} = \boldsymbol{\Phi}\mathbf{q}^{(\ell)} + \mathbf{r}^{(\ell)}. \tag{6.8}$$

Les résidus $\mathbf{r}^{(\ell)}$ sont ensuite rassemblés dans une matrice dont une décomposition en valeurs singulières est effectuée:

$$\left[\mathbf{r}^{(1)}, \quad \cdots, \quad \mathbf{r}^{(n_\mathrm{L})}\right] = \left[\mathbf{d}_1, \quad \cdots, \quad \mathbf{d}_{n_\mathrm{p}}\right] \mathrm{diag}(\sigma_1, \sigma_2, \cdots, \sigma_{n_\mathrm{p}})\mathbf{W}^T, \tag{6.9}$$

où $(\sigma_i)_{i \in [1, n_\mathrm{p}]}$ sont les valeurs singulières non nulles, ordonnées de la plus élevée à la plus faible, $(\mathbf{d}_i)_{i \in [1, n_\mathrm{p}]}$ sont les vecteurs singuliers à gauche de la décomposition et $\mathbf{W}^T$ les vecteurs singuliers à droite. La projection des vecteurs des résidus sur les vecteurs de la décomposition en valeur singulière est la suivante:

$$\mathbf{r}^{(\ell)} = \sum_{k=1}^{n_\mathrm{p}} \beta_k^\ell \mathbf{d}_k, \tag{6.10}$$

avec $\beta_k^\ell = \sigma_k W_{\ell k}$. La somme $\mathcal{E}_r$ des énergies de déformation linéarisées associées à chaque résidu a pour expression:

$$\mathcal{E}_r = \sum_{\ell=1}^{n_\mathrm{L}} \mathbf{r}^{(\ell)^T} \mathbf{K} \mathbf{r}^{(\ell)} = \sum_{k=1}^{n_\mathrm{p}} \underbrace{\left(\sum_{\ell=1}^{n_\mathrm{L}} {\beta_k^\ell}^2 \mathbf{d}_k^T \mathbf{K} \mathbf{d}_k \right)}_{E_k}, \tag{6.11}$$

car $\forall (k, j) \in [1, n_\mathrm{p}]^2, \mathbf{d}_k^T \mathbf{d}_j = \delta_{kj}$. Comme expliqué dans [100], les modes duaux choisis pour compléter la base de réduction sont les vecteurs $\left(\mathbf{d}_i\right)_{i \in [1, n_\mathrm{p}]}$ associés d'une part aux valeurs singulières σ_k les plus élevées, et d'autre part ceux contribuant le plus à l'énergie de déformation linéarisée, c'est-à-dire ceux pour lesquels E_i est le plus élevé. La base de réduction est finalement la concaténation entre les modes propres linéaires choisis et les modes duaux sélectionnés $\mathbf{V} = [\mathbf{\Phi}, \mathbf{\Phi}_\mathrm{dual}]$.

L'étape suivante consiste à déterminer l'expression explicite de $\widetilde{\mathbf{g}}_\mathbf{nl}(\mathbf{q})$ comme développement cubique en les coordonnées généralisées $\mathbf{q}$, selon l'expression donnée en équation (6.5). Les coefficients de la décomposition polynomiale des efforts sont déterminés par efforts imposés selon la forme (6.6). En ce sens la méthode est similaire à la méthode IC. Nous imposons des efforts construits uniquement à partir des modes linéaires mais nous considérons une base de réduction plus riche du fait des modes duaux. Les modes duaux ne sont en effet pas utilisés pour imposer les efforts car ils génèrent des efforts internes dont l'amplitude diffère de plusieurs ordres de grandeurs par rapport à leurs homologues linéaires, ce qui entraine des difficultés numériques. D'autant que cela n'est pas nécessaire car l'application d'efforts selon l'expression (6.6) conduit à des déplacements pour lesquels les modes duaux sont eux aussi mis à contribution. Un avantage non négligeable est également que les solutions statiques calculées pour déterminer les modes duaux peuvent être réutilisées pour la détermination des coefficients de $\widetilde{\mathbf{g}}_\mathbf{nl}(\mathbf{q})$, ce qui réduit le nombre de calculs à effectuer en comparaison avec une détermination par déplacements imposés. De plus, l'application d'efforts pour déterminer les coefficients permet d'éviter les éventuels problèmes numériques résultant de l'imposition de déplacements modaux sur les structures tridimensionnelles.

Comme pour la détermination des modes duaux, les n_L solutions statiques sont notées $\mathbf{u}_\mathbf{s}^{(\ell)}$. Les coordonnées généralisées associées sont déterminées par moindres carrés en utilisant la pseudo-inverse de la base de réduction $\mathbf{V}$:

$$\mathbf{q}^{(\ell)} = (\mathbf{V}^T \mathbf{V})^{-1} \mathbf{V}^T \mathbf{u}_\mathbf{s}^{(\ell)}. \tag{6.12}$$

A ce stade, n_L couples $\left(\mathbf{q}^{(\ell)}, \mathbf{f}_\mathbf{nl}(\mathbf{u}_\mathbf{s}^{(\ell)})\right)$ sont déterminés et satisfons les systèmes suivants (pour chaque mode k) aux inconnues β_{ij}^k and γ_{ijm}^k:

$$\widetilde{f}_\mathrm{nl}^k(\mathbf{q}^{(\ell)}) = \mathbf{V}_k^T \mathbf{f}_\mathbf{nl}(\mathbf{V}\mathbf{q}^{(\ell)}) = \sum_{i=1}^{n} \sum_{j=i}^{n} \beta_{ij}^k q_i^{(\ell)} q_j^{(\ell)} + \sum_{i=1}^{n} \sum_{j=i}^{n} \sum_{m=j}^{n} \gamma_{ijm}^k q_i^{(\ell)} q_j^{(\ell)} q_m^{(\ell)}. \tag{6.13}$$

En fonction du nombre de cas de chargements utilisés, le système est soit carré, soit sur ou sous-déterminé, auquel cas une résolution par moindres carrés est nécessaire. Le conditionnement du système étant parfois élevé, des méthodes de régressions pénalisées telles que Ridge, Lasso [189] ou Elastic Net [210] peuvent être préférées.

Application à une poutre de Bernoullli/von Kármán: Dans ce chapitre, une première application du modèle réduit présenté consiste en une poutre de Bernoulli/von Kármán. Le modèle réduit ICDual présenté en début de chapitre est dans un premier temps construit. La figure 6.3 représente les critères en valeurs singulières et énergie pour la sélection des modes duaux. Cinq modes duaux sont retenus pour enrichir la base de réduction contenant les trois premiers modes normaux linéaires.

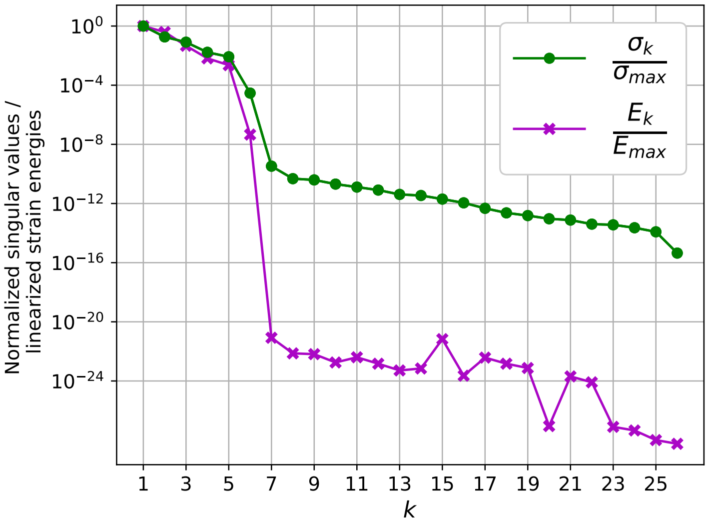

Figure 6.3: Valeurs singulières et énergies de déformations linéarisées des résidus des solutions statiques pour la détermination des modes duaux.

Différents cas de chargement sont étudiés, dans un premier temps statiques, puis dynamiques. Le premier chargement est distribué le long de la poutre et le second est pontuel et suiveur en son extrémité. Les figures 6.4a et 6.4b illustrent les déformées statiques de la poutre soumise aux chargements respectivement distribué et suiveur. Les solutions linéaires et non-linéaires du modèle complet sont comparées aux solutions réduites IC, ICE et ICDual. Pour rappel, la solution IC est la solution ICE avant l'étape de post-traitement appelée *Expansion*. Dans le cas de l'effort distribué les solutions ICE et ICDual sont en très bon accord avec le modèle non-linéaire complet. Il est important de mentionner qu'il en est de même pour un effort vertical à l'extrémité non-suiveur. En revanche, pour un effort suiveur, seule la solution ICDual capture précisément la solution exacte. Ce cas test identifie une première limitation de la méthode ICE et l'intérêt des modes duaux dans la base de réduction. En effet, l'effort est suiveur mais la base de projection linéaire pour la méthode ICE ne contient que des modes de flexion caractérisés par une composante axiale nulle. Ainsi, la composante axiale de l'effort suiveur est tronquée par la projection et seule celle verticale est prise en compte. Dans le cadre de la méthode ICDual, les modes duaux, dotés d'une composante axiale, permettent de prendre en considération l'effort suiveur dans sa totalité.

Les réponses de la poutre à des sollicitations dynamiques sont ensuite étudiées. La figure 6.5 illustre les déplacements verticaux et axiaux de l'extrémité de la poutre soumise à un chargement suiveur. Un comportement analogue est observé pour un chargement non suiveur ainsi

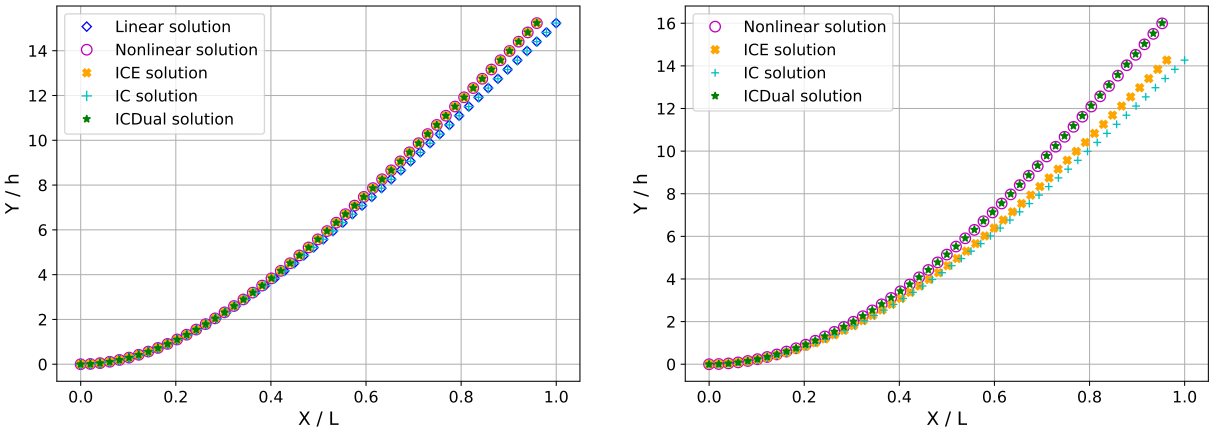

(a) Effort vertical distribué uniformément le long de la poutre de densité 20,000 N/m

(b) Effort suiveur en bout de poutre d'amplitude 30,000 N.

Figure 6.4: Déformée non-linéaire statique de la poutre de Bernoullli/von Kármán encastrée-libre soumise à un chargement distribué (a) et suiveur (b).

qu'un chargement distribué. Pour une telle configuration, les réponses verticales linéaires et non-linéaires sont proches, moyennant un déphasage. En revanche, la formulation non-linéaire de la poutre traduit un raccourcissement axial, ce que le calcul linéaire ne prend pas en compte. Le modèle réduit ICDual capture parfaitement la dynamique dans les directions verticales et axiales ainsi que le déphasage. Au contraire, le modèle réduit ICE est déphasé et ne capture que approximativement les déplacements non-linéaires. La raison est que le couplage membrane-flexion n'est que reconstruit en post-traitement à partir de considérations statiques. Au contraire, le couplage dynamique entre membrane et flexion est directement calculé (plutôt que reconstruit) via les modes duaux avec le modèle ICDual.

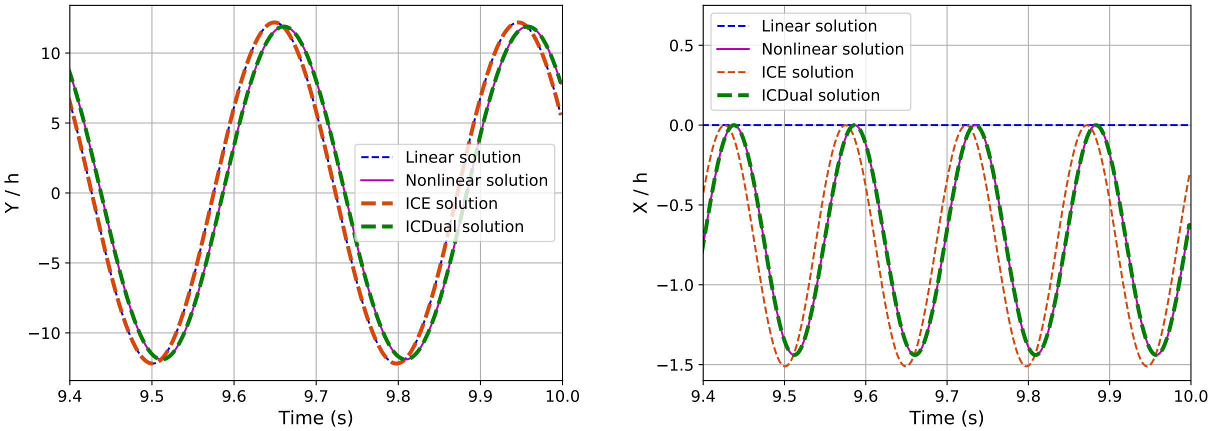

(a) Déplacement vertical

(b) Déplacement axial

Figure 6.5: Déplacement non-linéaire dynamique à l'extrémité de la poutre de Bernoulli/von Kármán encastrée-libre soumise à un chargement suiveur sinusoidal en bout de poutre d'amplitude 2,500 N et de fréquence $f_0 = 3.37$ Hz. Comparaison des résultats des différents modèles.

Le cas de la poutre en rotation centrifuge à 500 tr/min autour d'un axe fixe est également étudié pour des cas de chargements analogues. Les conclusions des cas statiques sont les mêmes avec un bon accord des solutions ICE et ICDual dans les cas non-suiveurs alors que seule la méthode ICDual est efficace dans le cas suiveur pour les raisons détaillées précédemment. Les conclusions des cas dynamiques sont également similaires à celles des cas sans rotation dans le sens où la limitation du post-traitement ICE est mis en évidence alors que la méthode ICDual capture parfaitement la solution de référence. La figure 6.6 illustre les déplacements verticaux et axiaux de l'extrémité de la poutre soumise à un chargement suiveur dans le cas en rotation. Ici encore les conclusions sont simillaires avec le chargement non-suiveur et celui distribué. Il est intéressant de préciser que la non-linéarité du modèle est plus riche dans le cas en rotation, ce qui accentue les erreurs du modèle ICE sans affecter la précision de la méthode ICDual.

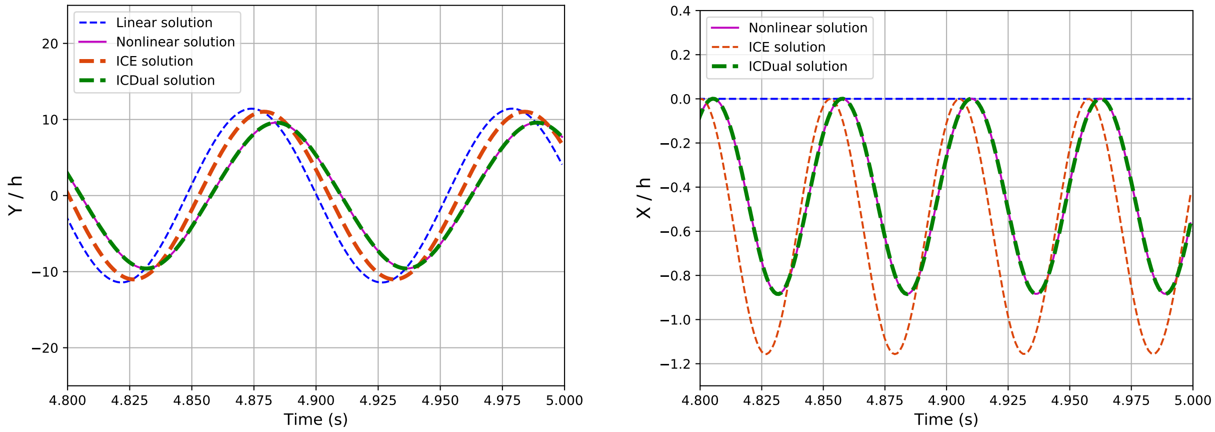

(a) Déplacement vertical (b) Déplacement axial

Figure 6.6: Déplacement non-linéaire dynamique à l'extrémité de la poutre de Bernoulli/von Kármán encastrée-libre en rotation à 500 tr/min soumise à un chargement suiveur sinusoidal en bout de poutre d'amplitude 7,350 N et de fréquence correspondant à celle du premier mode en rotation. Comparaison des résultats des différents modèles.

Dans ce chapitre, nous avons proposé un modèle réduit, ICDual, s'appuyant sur les modes duaux et innovant dans la façon d'évaluer les coefficients des efforts non-linéaires projetés. Un premier cas d'étude consistant en une poutre de Bernoulli/von Kármán donne des résultats très satisfaisants.

Chapitre 3: Application à des éléments finis 3D à l'aide un solveur éléments finis externe

Le troisième chapitre de ce manuscrit de thèse a pour but d'appliquer notre méthode de réduction dans le cadre d'éléments finis 3D avec l'utilisation non-intrusive d'un solveur industriel, ici *Code_Aster*. Nous reprenons la géométrie de la poutre du chapitre précédent, désormais maillée avec des éléments finis 3D HEX20. Une première configuration sans rotation puis une seconde à 500 tr/min sont considérées. Les cas de chargements sont un effort vertical en bout de poutre, dans un premier temps statique, puis dynamique.

Le modèle réduit est construit à partir des trois premiers modes linéaires. Ces modes sont illustrés sur la figure 6.7. On peut remarquer que le second mode n'est pas dans le même plan que le premier et le troisième.

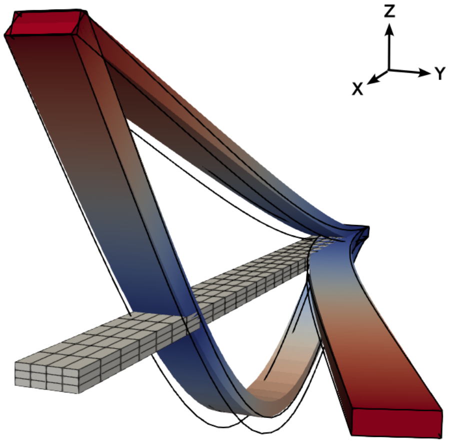

Figure 6.7: Visualisation des 3 premiers modes normaux de la poutre en rotation centrifuge à 500 tr/min. La configuration maillée correspond à la géométrie initiale et les traits continus illustrent les modes correspondants du cas sans rotation.

Nous ne retenons que les deux premiers modes duaux dans le processus de sélection afin d'avoir un nombre faible de coefficients à déterminer mais également car nous ne souhaitons pas enrichir la dynamique dans la direction Y. Ces modes sont illustrés en figure 6.8.

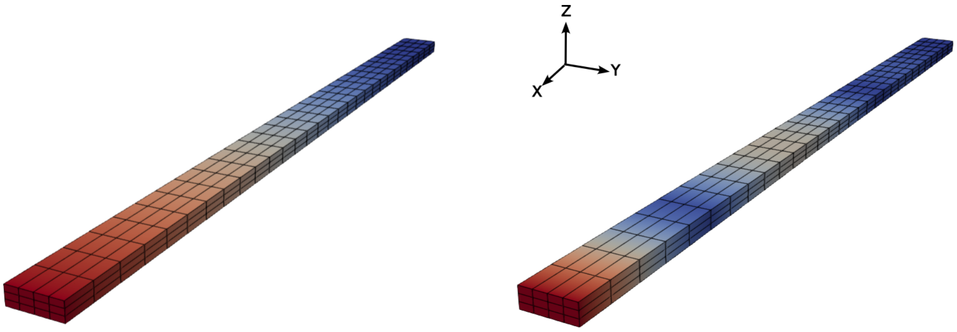

Figure 6.8: Représentation des deux premiers modes duaux obtenus à partie des trois premiers modes linéaires.

La réponse non-linéaire de la poutre à un chargement statique vertical en son extrémité est notamment caractérisée par un raccourcissement axial. Comme pour l'application du chapitre précédent, un bon accord est observé entre la solution éléments finis et les solutions obtenues avec les modèles ICE et ICDual pour les chargements statiques. La solution ICDual est toutefois plus précise que la solution ICE dans le cas en rotation. En ce qui concerne les réponses aux chargements dynamiques, la reconstruction en post-traitement de la méthode ICE est approximative comme dans le chapitre précédent. La méthode ICDual permet elle une meilleure prise en compte du couplage membrane-flexion et donne de meilleurs résultats, moyennant un léger déphasage. La figure 6.9 illustre le déplacement maximal en régime permanent de la poutre soumise à un chargement vertical sinusoidal. Le déplacement est illustré sur la ligne moyenne de la poutre 3D et un zoom sur le bout de la poutre est associé à la figure, mettant en évidence le raccourcissement axial dû à la non-linéarité.

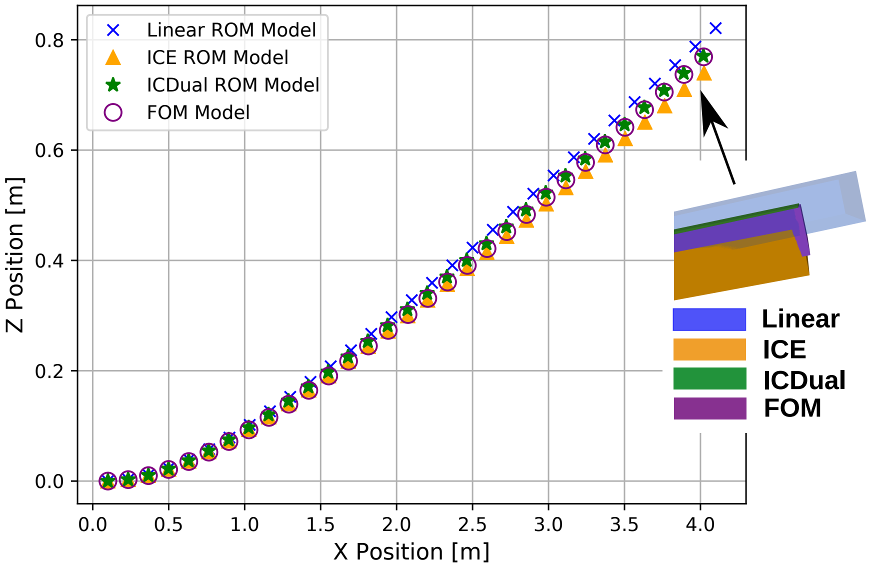

Figure 6.9: Comparaison du déplacement maximal en régime permanent entre le modèle éléments finis complet et les modèles réduits. La poutre est soumise à un chargement vertical sinusoidal en son extrémité, d'amplitude 7350 N et de fréquence 9.67 Hz.

Dans ce chapitre nous avons mis en évidence qu'avec seulement deux modes duaux supplémentaires et aucun calcul statique additionel, l'utilisation du modèle réduit ICDual permet une amélioration significative des résultats par rapport à une approche ICE classique.

Chapitre 4: Procédure de couplage partitionné entre le solveur fluide et le modèle réduit structure

Ce chapitre présente des éléments théoriques nécessaires au couplage fluide-structure tels que celui effectué dans le chapitre suivant. La dynamique du fluide est régie par les équations de Navier-Stokes. En l'absence de terme source, ces équations prennent la forme suivante:

$$\frac{\partial \boldsymbol{W}}{\partial t} + \nabla \cdot \boldsymbol{\mathcal{F}}(\boldsymbol{W}) = 0. \tag{6.14}$$

avec $\boldsymbol{W} = \begin{bmatrix} \rho & \rho \boldsymbol{v} & \rho E \end{bmatrix}^T$ le vecteur des variables conservatives et $\boldsymbol{\mathcal{F}}$ leur flux. Dans le cadre d'un couplage fluide-structure, le déplacement de la structure en raison des efforts aérodynamiques conduit au mouvement de la condition limite pour le fluide. Par propagation de la condition limite, le maillage est mis en mouvement dans son ensemble. Pour rendre compte de la dynamique du fluide dans un maillage mobile il est courant d'écrire les équations de Navier-Stokes en formulation ALE (Arbitrary Lagrangian-Eulerian). La forme intégrale des équations de Navier-Stokes appliquée à un élément de volume Ω_F de surface $S_F(t)$ en formulation ALE est la suivante:

$$\frac{\mathrm{d}}{\mathrm{d}t} \int_{\Omega_F} \boldsymbol{W} \, \mathrm{d}\Omega_F + \int_{S_F(t)} \boldsymbol{\mathcal{F}}(\boldsymbol{W}, \hat{\boldsymbol{v}}) \cdot \boldsymbol{n} \, \mathrm{d}S_F(t) = 0, \tag{6.15}$$

où le flux à travers la surface a pour expression:

$$\boldsymbol{\mathcal{F}}(\boldsymbol{W},\hat{\boldsymbol{v}}) = \begin{bmatrix} \rho(\boldsymbol{v}-\hat{\boldsymbol{v}}) \\ \rho\boldsymbol{v}\otimes(\boldsymbol{v}-\hat{\boldsymbol{v}}) + p\mathbf{I} - \boldsymbol{\tau} \\ \rho E(\boldsymbol{v}-\hat{\boldsymbol{v}}) + p\boldsymbol{v} - \boldsymbol{\tau}\boldsymbol{v} + \boldsymbol{q} \end{bmatrix}. \tag{6.16}$$

dans laquelle $\boldsymbol{\tau}$ est le tenseur des contraintes visqueuses et $\boldsymbol{q}$ le flux de chaleur.

Comme évoqué précédemment, la déformation de la structure à l'interface doit être propagée dans le domaine de calcul et le maillage fluide est ainsi déformé au cours du couplage. Il existe différentes méthodes de déformation du maillage. Par exemple, une méthode consiste en une analogie structurale. Le domaine fluide est assimilé à un matériau linéaire élastique auquel un déplacement est prescrit à l'interface [45]. Le matériau est caractérisé par un module d'Young E et un coefficient de Poisson ν. La déformation de maillage est alors calculée comme un problème classique éléments finis. Toutefois, le module d'Young et le coefficient de Poisson ne sont pas uniformes dans le maillage mais dépendent des tailles locales des cellules. Le but est d'augmenter la rigidité dans les régions de maillage fortement raffinées telles que les couches limites proches parois. Cette méthode de déformation de maillage est celle utilisée dans ce travail. Il existe également d'autres méthodes de déformation de maillage telles que la méthode TFI (TransFinite Interpolation) [60] qui est une méthode analytique basée sur des fonctions d'interpolation, dépendant des coordonnées curvilignes du maillage, et satisfaisant le déplacement à l'interface. Cette méthode étant analytique, elle est très rapide. Toutefois elle ne s'applique qu'aux maillages structurés. Il est également possible d'utiliser des fonctions de bases radiales (RBF) [32] pour déformer le maillage ou la méthode IDW (Inverse Distance Weighting) [207] basée sur la distance à des points de contrôle. Une déformation du maillage impliquant de très grandes rotations pouvant parfois poser problème, il existe des méthodes de déformation utilisant les quaternions.

Le calcul numérique des problèmes d'interaction fluide-structure est difficile car la dynamique de la structure et celle du fluide sont imbriquées. En effet, la condition limite pour le fluide est le déplacement de la structure et les conditions limites pour la structure sont les charges aérodynamiques du fluide. Dans la littérature, deux approches fondamentalement différentes existent pour résoudre un problème d'interaction fluide-structure [82]. D'une part, l'idée est de résoudre toute la physique simultanément dans un unique système, cette approche est appelée l'approche monolithique. D'autre part, l'approche partitionnée consiste en deux solveurs différents pour le fluide et la structure, qui s'échangent les informations nécessaires avec un schéma spécifique.

Comme mentionné ci-dessus, l'approche monolithique consiste en la résolution implicite d'un système unique regroupant les équations du fluide, de la structure, de la déformation du maillage et des transferts. Ainsi, toutes les composantes du couplage sont résolues simultanément dans une seule boucle d'incrémentation temporelle, ce qui garantit la stabilité et la convergence du couplage. La formulation implicite du système permet également des pas de temps qui ne sont pas excessivement petits. Des exemples de problèmes d'interaction fluide-structure résolus avec l'approche monolithique peuvent être trouvés dans [76, 82, 83, 194]. L'inconvénient des approches monolithiques est qu'elles conduisent à des systèmes non linéaires de grandes dimensions dont la résolution est parfois difficile [40, 63, 76, 156].

Dans le cadre d'un couplage partitionné, des solveurs différents sont considérés pour le fluide et la structure. Cela permet une plus grande modularité. En outre, un autre avantage est qu'il existe un solveur dédié pour chaque physique, dans lequel toute la complexité souhaitée peut être intégrée plus facilement, ce qui est plus difficile à mettre en oeuvre dans une approche monolithique.

Le couplage partitionné le plus simple consiste à alterner les calculs du fluide et de la structure à chaque pas de temps, on appelle cela le couplage faible. Chaque solveur communique à son homologue des valeurs prédites selon un schéma particulier. Avec des schémas de prédiction et d'intégration bien choisis, il est possible de garantir une précision temporelle de second ordre [53]. Des exemples de couplage faible se trouvent par exemple dans [55, 82, 184] et [51, 53, 147] avec des applications aux configurations aéroélastiques dans ces derniers. Toutefois, les schémas de couplage faible entraînent un décalage temporel entre les deux solveurs [147] et les conditions à l'interface fluide-structure en termes de vitesse, de déplacement et de contraintes ne correspondent pas exactement entre les deux solveurs à chaque pas de temps du couplage. La convergence de l'ensemble du problème fluide-structure n'est pas garantie, ce qui peut entraîner une perte de stabilité et de précision et faire diverger la solution numérique de la solution physique. En outre, le décalage temporel entre les solveurs peut se traduire par un ajout purement numérique d'énergie au système puisque le travail échangé entre les deux solveurs n'est pas parfaitement équilibré [147], ce qui conduit à des instabilités de masse ajoutée [24, 59]. La littérature propose également des schémas de couplage parallèles [51, 55]. Lors de tels couplages, les solveurs fluide et structure n'attendent pas que leur homologue actualise ses variables en fonction des informations tout juste fournies, les deux solveurs fonctionnent en même temps. Ils ne communiquent entre eux qu'à des intervalles de temps spécifiques. Ces méthodes de couplage réduisent considérablement le temps de calcul au prix d'une légère perte de précision.

Pour satisfaire les conditions à l'interface fluide-structure et contrôler la convergence du problème global, un couplage partitionné implicite (également appelé couplage fort) est courant. Cette approche consiste à ajouter des sous-itérations de couplage au cours du même pas de temps. Il est courant que ces sous-itérations soient des itérations de point fixe entre les solveurs, c'est ce qui est fait par exemple dans [5, 13, 41, 121]. Les principaux avantages du couplage partitionné implicite avec sous-itérations sont que la convergence est contrôlée et qu'elle n'est pas sujette à des instabilités de masse ajoutée. Néanmoins, dans certains cas, le nombre de sous-itérations nécessaires pour satisfaire un critère de convergence donné peut être particulièrement élevé, ce qui augmente le coût de calcul de la méthode. Dans le chapitre suivant, un couplage fort est considéré avec des sous-itérations de point fixe entre les solveurs fluide et structure au sein d'un même pas de temps. Les différentes étapes d'un tel couplage partitionné sont résumées dans la figure 6.10.

Que ce soit avec une approche monolithique ou partionnée, il est nécessaire de garder en mémoire que les maillages fluide et structure sont dans la majorité des cas non-coincidents et que la transmission des informations d'un maillage à l'autre n'est pas trivialle. Le transfert des efforts du maillage fluide vers le maillage structure et le transfert des déplacements du maillage structure au maillage fluide ont recours à des techniques d'interpolation entre les maillages. Une interpolation par fonctions de bases radiales est souvent utilisée pour interpoler la déformation de la structure dans le maillage fluide [10, 14, 169, 206]. Inversement, les efforts aérodynamiques peuvent être reportés sur le maillage fluide à l'aide de différentes méthodes comme des projections [115] ou l'utilisation de fonctions Splines [10, 186], les méthodes les plus courantes étant toutefois des méthodes de plus proches voisins, de RBF ou la méthode Weighted Residual Method [33, 34, 52].

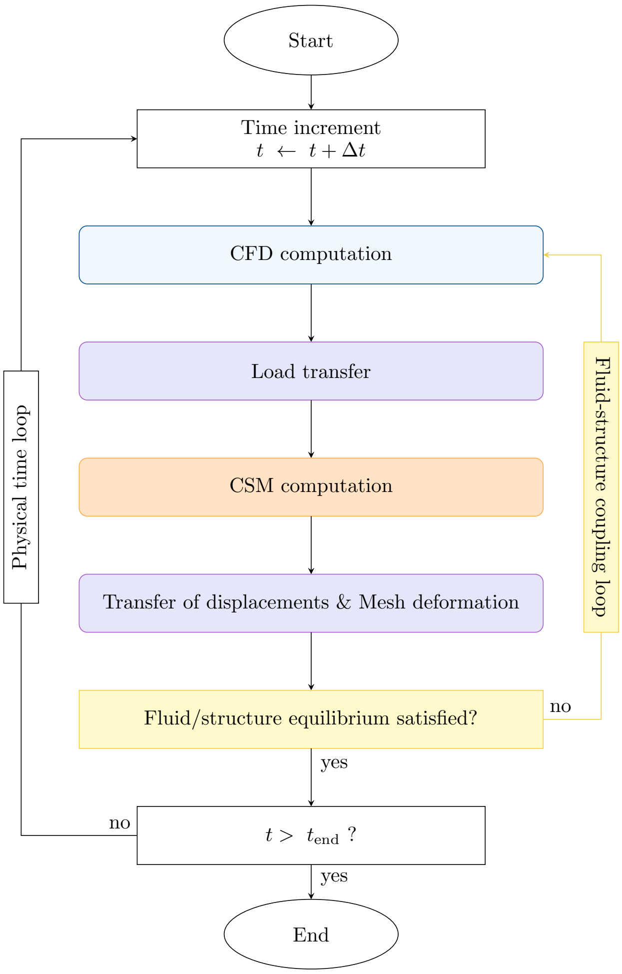

Figure 6.10: Les différentes étapes du couplage partitionné utilisé dans ce travail.

Chapitre 5: Application du couplage fluide-structure à un exemple bidimensionnel

Le but de ce chapitre est d'étudier l'efficacité du modèle réduit ICDual dans un cas d'interaction fluide-structure. En effet, les forces aérodynamiques sont des efforts complexes, à la fois distribués et suiveurs. Le cas test d'intérêt consiste à placer la poutre étudiée au chapitre 2 dans le sillage tourbillonnaire en aval d'un cylindre fixe.

Un couplage partitionné est mis en oeuvre. La dynamique du fluide est calculée au moyen du solveur volumes finis *elsA* [19] (propriété de conjointe de l'ONERA et Safran). Le choix de ce solveur en particulier est d'anticiper de futures applications aéroélastiques industrielles. Les flux convectifs sont approximés avec le schéma AUSM+ (P) MiLES [113, 120], afin de bénéficier d'une faible dissipation et sa bonne précision pour des écoulements à basse vitesse. En ce qui concerne le solveur structure, un schéma d'intégration temporelle HHT-α est utilisé, incluant à chaque pas de temps des sous-itérations de Newton-Raphson pour la convergence des équations non-linéaires. La figure 6.11 illustre le couplage au cours d'une période, l'écoulement du fluide est à Reynolds 200. Les déplacements verticaux et axiaux de l'extrémité de la poutre en régime permanent sont représentés en figure 6.12. La solution obtenue avec le modèle réduit ICDual est comparée à celles des modèles complets linéaires et non-linéaires. Le modèle réduit ICDual est celui de l'application sans rotation du chapitre 2 avec les trois modes linéaires et les cinq modes duaux. On remarque

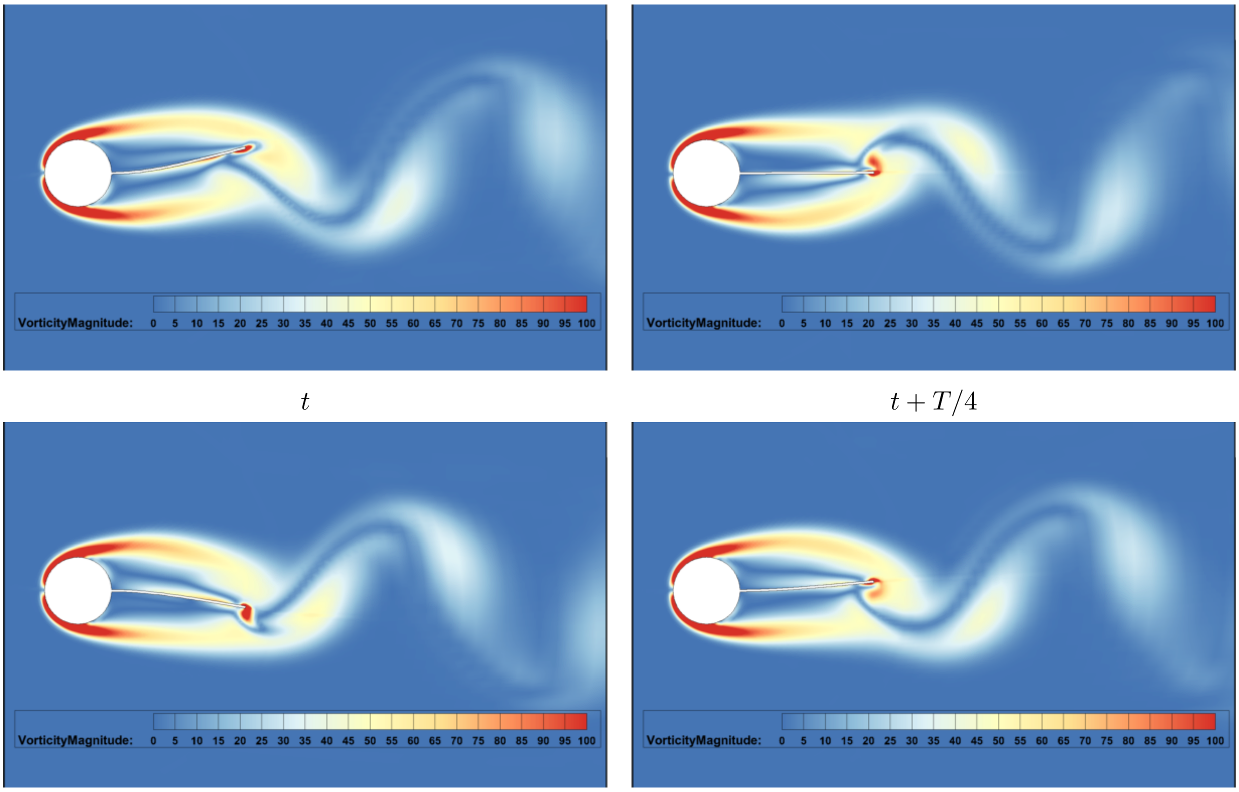

t $t + T/4$

$t + T/2$ $t + 3T/4$

Figure 6.11: Visualisation du champ de l'amplitude de la vorticité au cours d'une période en régime permanent, dans le cas de l'interaction fluide-structure entre le détachement de vortex dans le sillage d'un cylindre fixe et la poutre flexible.

que le raccourcissement axial n'est pas capturé par le calcul linéaire et le déplacement vertical présente un déphasage vis à vis de la solution exacte. Sur la durée de calcul considérée, la réponse linéaire est en avance de presque deux périodes sur la solution exacte. Au contraire, le modèle réduit ICDual capture très précisément la solution non-linéaire, tant lors du régime transitoire que du régime permanent.

Le comportement couplé de la poutre est ensuite étudié sur une gamme de nombres de Reynolds autour de $Re = 200$. En effet, lorsque la fréquence du détachement tourbillonnaire et la fréquence propre de la poutre sont proches, un phénomène de verrouillage en fréquence apparait appelé lock-in. Les figures 6.13a et 6.13b représentent respectivement la fréquence de vibration de la poutre et son amplitude de déplacement vertical à l'extrémité, en fonction du nombre de Reynolds. Lorsque la fréquence du détachement tourbillonnaire est éloignée de la fréquence du mode propre, les amplitudes de vibration sont si faibles que leur fréquence est imposée par l'écoulement du fluide. Cependant, lorsque la fréquence du détachement tourbillonnaire est proche de la fréquence propre, la vibration de la structure et le détachement tourbillonnaire répondent tous deux à une fréquence unique, sur toute une gamme de nombres de Reynolds. En outre, l'étendue du plateau diffère légèrement entre les cas linéaires et non linéaires. Avant et après la plage de fréquences caractérisée par le phénomène de verrouillage, la poutre répond à la fois à la fréquence imposée par l'écoulement du fluide et, dans une moindre mesure, à la fréquence du mode propre. Il en résulte une phénomène de battement.

On remarque que le modèle réduit ICDual donne des résultats très bons pour ce problème complexe d'interaction fluide-structure: la région de verrouillage en fréquence prédite par le modèle

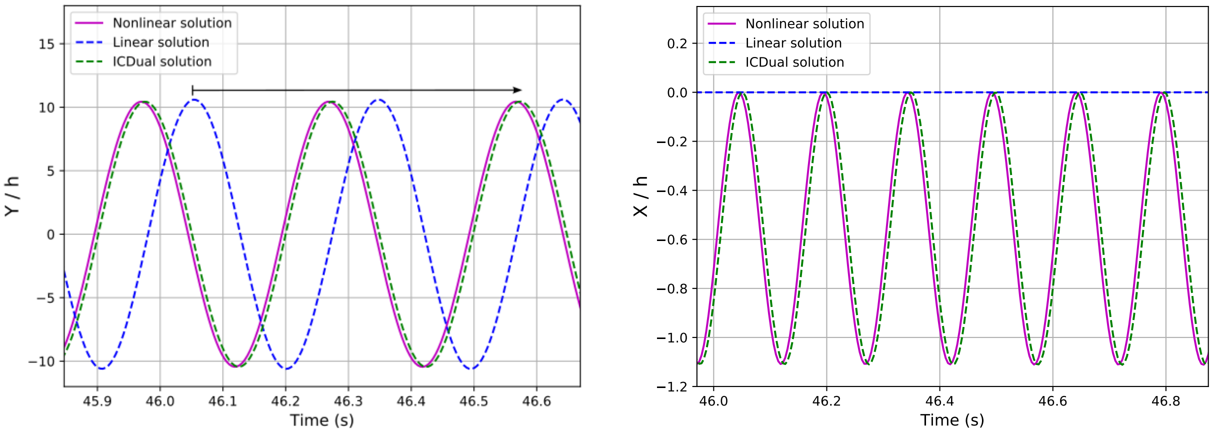

(a) Déplacement vertical

(b) Déplacement axial

Figure 6.12: Déplacement vertical (a) et axial (b) du bout de la poutre lors du couplage aéroélastique en régime permanent établi.

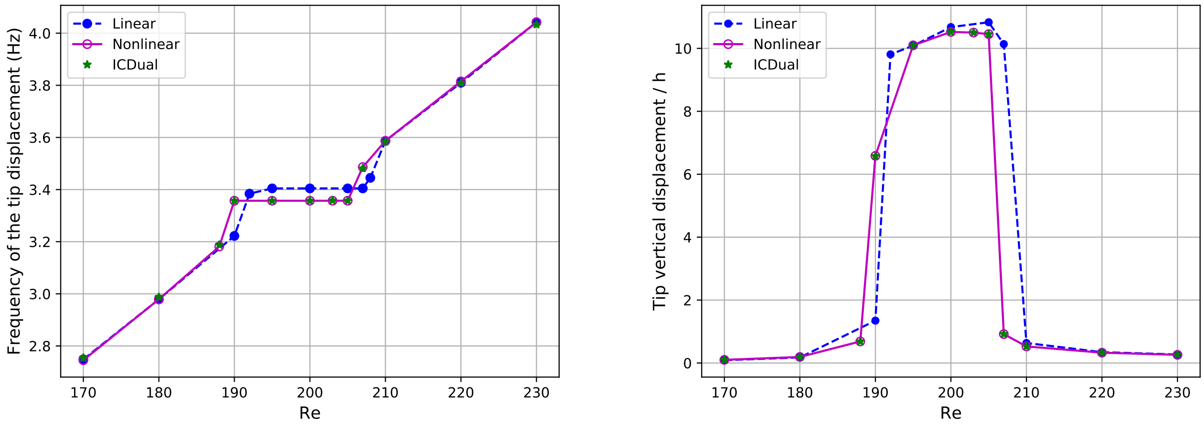

(a) Evolution de la fréquence de vibration de la poutre pour différents nombres de Reynolds.

(b) Evolution de l'amplitude du déplacement vertical en bout de poutre pour différents nombres de Reynolds.

Figure 6.13: Mise en évidence du phénomène aéroélastique de lock-in pour les différents modèles, en terme de fréquence (a) et d'amplitude (b).

complet est parfaitement capturée lors des calculs couplés avec le modèle réduit, à la fois en terme de fréquences et d'amplitudes de vibration. Ce dernier cas test démontre le potentiel d'un couplage entre un modèle réduit de structure basé sur une formulation originale avec des modes duaux pour les problèmes aéroélastiques. Le modèle réduit ICDual rend très précisément compte de la solution non-linéaire de référence et est facilement couplé dans le cadre d'une approche partitionnée, car il est indépendant de tout solveur éléments finis. L'influence de la non-linéarité géométrique a été mise en évidence en termes de fréquence d'accrochage et le modèle réduit a été capable de capturer cet effet de manière très précise. Pour ce cas test, la comparaison avec la solution du modèle complet a été possible car il s'agit d'un modèle de poutre. Cependant, la résolution haute fidélité d'un problème couplé est très coûteuse et difficile à mettre en oeuvre pour les structures 3D avec un grand nombre de degrés de liberté, ce qui justifie l'utilisation d'un modèle réduit non linéaire. Dans le chapitre suivant, la précision du modèle réduit ICDual est étudiée sur une géométrie plus complexe, à savoir une aube de turbomachine en éléments finis 3D.

Chapitre 6: Application à un cas test industriel d'aube de turbomachine

Dans ce chapitre, nous considérons une structure 3D complexe d'une aube de soufflante représentative d'un turboréacteur UHBR. L'objectif est d'étudier la précision et la robustesse du modèle d'ordre réduit pour de telles structures avec des charges aérodynamiques représentatives.

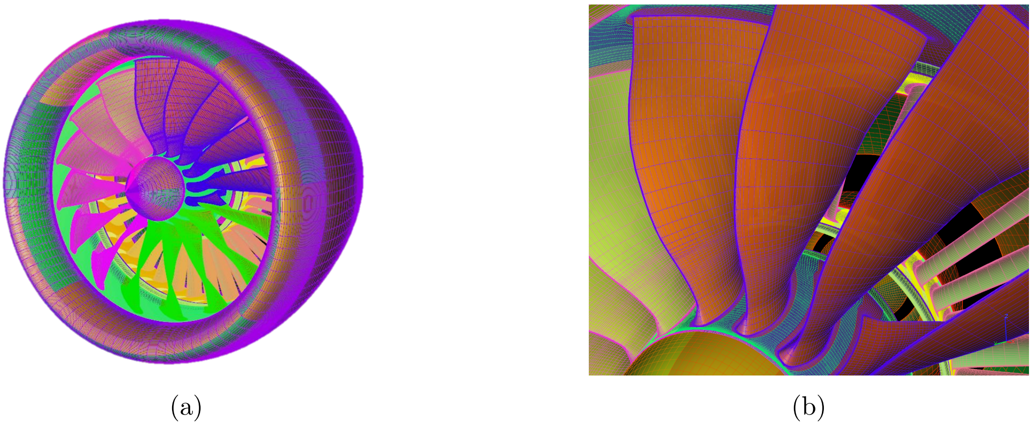
(a)

(b)

Figure 6.14: Visualisation du moteur complet (a) et zoom sur des aubes du fan (b).

La figure 6.14 illustre la configuration complète du moteur (à gauche) et l'aube de soufflante qui nous intéresse (à droite). Nous ne considérons qu'une seule aube de soufflante (toutes les aubes étant identiques). Le modèle structurel original de l'aube a été adapté pour permettre une analyse dynamique limitée à une seule aube : à cette fin, le pied de l'aube a été supprimé et remplacé par une condition limite d'encastrement. Le module d'Young est égal à 110 GPa, la densité à 4500 kg.m^{-3} et le coefficient de Poisson à $0,318$. L'aube est discrétisée en 66640 éléments finis HEX8, avec 6 éléments dans l'épaisseur.

La structure est en rotation autour d'un axe fixe à une vitesse de 2,750 tr/min. Les effets centrifuges sont présents et la dynamique de la structure est étudiée autour de la position précontrainte qui correspond à un léger dévrillage de l'aube. Les formes des modes normaux linéaires de la structure et leurs fréquences modales associées sont modifiées par la vitesse de rotation puisqu'elles sont calculées par rapport à la position précontrainte. Les premiers modes normaux linéaires sont respectivement le premier mode de flexion (appelé 1F), le deuxième mode de flexion (2F) et le premier mode de torsion (1T). La base de réduction est enrichie avec un mode dual. Les modes constituant la base de réduction sont représentés en figure 6.15.

Dans un premier temps, un effort statique arbitraire est considéré, puis un effort dynamique issu d'efforts aérodynamiques instationnaires. La Figure 6.16 illustre les solutions des différents modèles dans le cas du chargement statique, défini par $\mathbf{f}_{\text{ext}} = 15h\mathbf{K}(\Omega)\boldsymbol{\phi}_1^{2750}/\max|\boldsymbol{\phi}_1^{2750}|$. La non-linéarité géométrique est significative pour de telles amplitudes. La solution non linéaire ICDual est en très bon accord avec la solution FOM, mais la solution ICE présente une légère déviation à l'extrémité du bord d'attaque alors que la solution linéaire surestime fortement le déplacement statique.

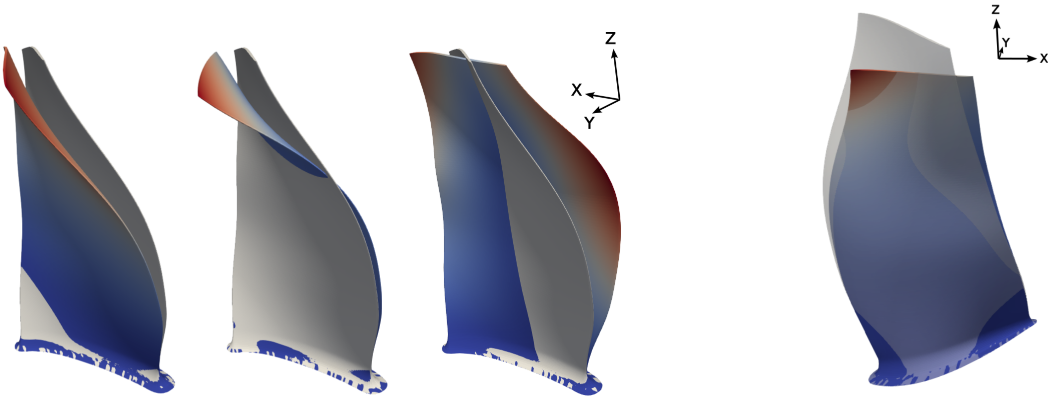

(a) Trois premiers modes linéaires à 2,750 tr/min.

(b) Premier mode dual.

Figure 6.15: Modes de la base de réduction. Trois premiers modes linéaires (a) à 2,750 tr/min et premier mode dual (b) construit à partir de ces modes.

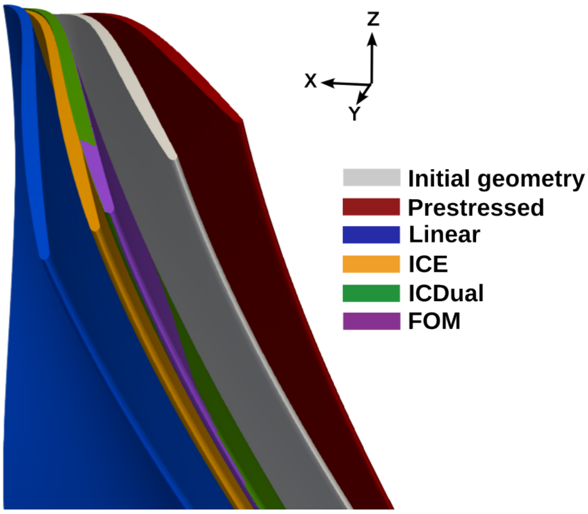

Figure 6.16: Comparaison entre la solution du modèle complet et celles des modèles réduits pour la structure soumise au chargement $\mathbf{f}_{\text{ext}} = 15h\mathbf{K}(\Omega)\boldsymbol{\phi}_1^{2750}/\max|\boldsymbol{\phi}_1^{2750}|$.

Un calcul CFD de la configuration 360° fan-OGV-nacelle (illustrée en figure 6.14) est ensuite effectué, premièrement un calcul stationnaire, puis instationnaire à partir de ce premier. Le maillage aérodynamique est constitué d'environ 16 millions de cellules. Le solveur CFD est le solveur de volumes finis elsA [19]. Les distributions des efforts aérodynamiques résultants sur l'aube considérée sont représentées sur la figure 6.17.

L'entrée de la nacelle présente une dissymétrie. En conséquence, le flux d'entrée est soumis à un motif de distorsion. A chaque tour, une aube fan traverse le motif de distorsion et est donc soumise à un forçage périodique. Un calcul CFD instationnaire est effectué et la décomposition de Fourier des forces aérodynamiques instationnaires est calculée pour obtenir les amplitudes et les phases en chaque point de la surface de l'aube. Le terme constant de la décomposition de Fourier correspond à la solution stationnaire illustrée en figure 6.17. En ce qui concerne les harmoniques, seules les premières harmoniques sont conservées car les amplitudes le long des suivantes sont négligeables. Les coefficients de Fourier locaux sont ensuite transférés du maillage aérodynamique aux noeuds voisins du maillage structurel avec une méthode énergétique basée sur la conservation du travail virtuel.

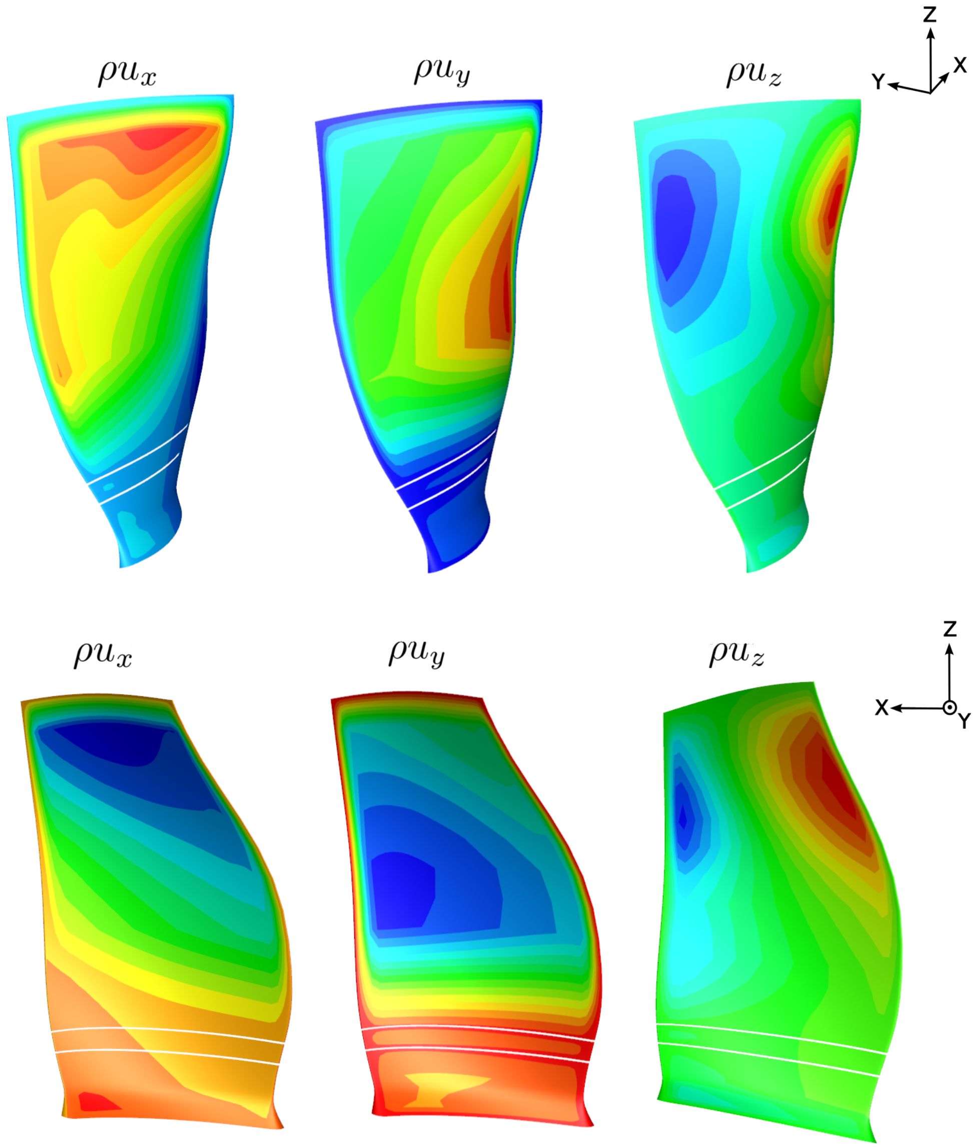

Figure 6.17: Efforts aérodynamiques stationnaires sur l'extrados (en haut) et sur l'intrados (en bas) de l'aube.

La répartition des composantes fluctuantes des efforts est ensuite appliquée à la structure à la fréquence du phénomène de forçage (i.e. la vitesse de rotation) et à l'amplitude souhaitée, en plus de la composante constante. Un amortissement de Rayleigh est également considéré dans le système : $\mathbf{C} = 2\xi\omega_0^{2750}\mathbf{M}$ avec $\xi = 0.05$. La figure 6.18 représente l'évolution temporelle au bord d'attaque en bout d'aube dans la direction Y.
Comme attendu, les niveaux de vibration des modèles non linéaires sont beaucoup plus faibles que ceux du modèle linéaire. Il existe une différence non négligeable entre les modèles réduits ICE et ICDual, ce dernier présente des niveaux de vibration plus faibles et plus proches de ceux obtenus avec le calcul éléments finis de référence. Le calcul de la solution dynamique du modèle éléments finis complet prend environ 10 heures en utilisant du calcul parallèle et une utilisation mémoire importante alors que la résolution avec les modèles réduits s'effectue en moins de 10 secondes sur un seul processeur.

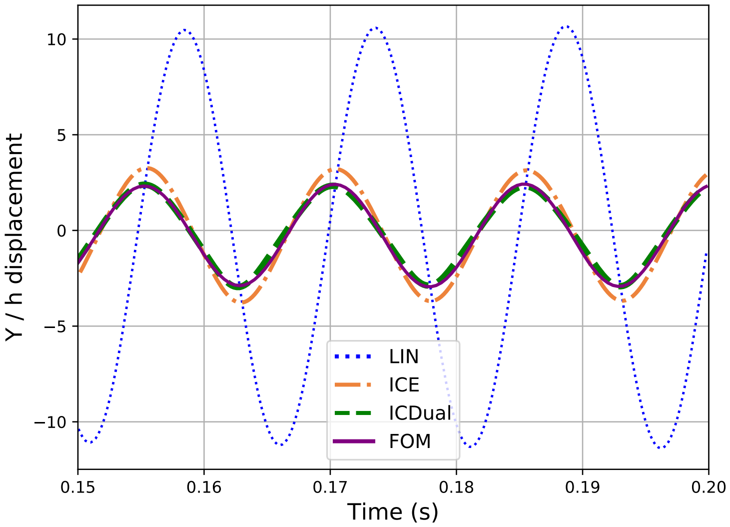

Figure 6.18: Réponse temporelle dans la direction Y à l'extrémité du bord d'attaque en bout d'aube.

Conclusion

Dans cette étude, nous nous sommes dans un premier temps concentrés sur le formalisme des équations régissant la vibration des structures géométriques non linéaires en rotation, ainsi que sur les méthodes de résolution temporelle et fréquentielle. Ensuite, une revue de la littérature sur les modèles d'ordre réduit adaptés aux non-linéarités géométriques a été effectuée. En tenant compte des contraintes en termes de couplage, de l'approche non intrusive et du nombre réduit de modes souhaités dans la base de réduction, l'utilisation de modes duaux a été considérée comme un candidat pertinent. Nous avons ainsi développé une méthodologie de construction du modèle d'ordre réduit basée sur les modes duaux et incluant une manière innovante de calculer les coefficients des forces non linéaires projetées via l'application de charges imposées. Cette approche présente l'avantage de réutiliser les charges imposées pour déterminer les modes duaux dans le calcul des coefficients des efforts non-linéaires projetés, limitant ainsi le nombre de calculs statiques nécessaires. En outre, l'application d'efforts contourne une difficulté rencontrée avec les structures 3D en ce qui concerne l'identification des coefficients par des déplacements imposés, pouvant générer des artefacts numériques dans la résolution en raison des déformations volumiques imposées. Une première application à une poutre de von Kármán à démontré la capacité d'un tel modèle d'ordre réduit à capturer avec précision le comportement dynamique non linéaire sous différents cas de chargement : des efforts ponctuels et distribués, suiveurs ou non. Les cas sans et avec rotation autour d'un axe fixe ont été abordés. Cette première étude à été suivie d'une application aux éléments finis 3D sur la même géométrie, où l'approche non intrusive avec un solveur d'éléments finis externe prend tout son sens. Le deuxième axe d'étude se concentre sur le couplage fluide-structure, les problèmes de déformation du maillage et le transfert des forces et déplacements qui en découlent. Avec pour objectif de traiter des configurations industrielles, nous avons choisi un couplage partitionné entre deux solveurs distincts (un pour le fluide et un autre pour la structure). Bien que le champ d'application de cette thèse soit limité à la réduction de modèle pour la structure, il est nécessaire de pouvoir connecter simplement notre modèle réduit à n'importe quel solveur fluide externe pour réaliser le couplage partitionné. Une application en interaction fluide-structure a ensuite été menée entre la poutre de von Kármán précédemment étudiée et le sillage tourbillonnaire en aval d'un cylindre fixe auquel la poutre est attachée. Les résultats obtenus avec le modèle réduit sont en excellent accord avec les solutions du modèle complet, capturant parfaitement le phénomène de verrouillage en fréquence, tant en termes de gamme de fréquences que d'amplitude des vibrations observées. La dernière étude de ce travail concerne l'application à une aube de soufflante de turbomachine. Ce cas est complexe tant par sa géométrie que par le nombre de degrés de liberté le constituant. Nous avons construit le modèle d'ordre réduit autour d'un point de fonctionnement et mené une première étude de la précision du modèle d'ordre réduit sur des cas de chargement statique arbitraires. Après avoir confirmé la bonne concordance avec la solution haute-fidélité, nous nous sommes penchés sur des efforts aérodynamiques instationnaires. À cette fin, des calculs CFD instationnaires ont été effectués sur la configuration complète du moteur et récupéré les efforts agissant sur l'aube. Ces efforts sont caractérisés par un forçage périodique à la fréquence de rotation du moteur résultant de l'asymétrie de la nacelle. Nous avons identifié la distribution des composantes harmoniques des efforts agissant sur l'aube et construit un chargement instationnaire représentatif à partir duquel nous avons basé notre comparaison entre le modèle réduit et la solution haute-fidélité. Malgré la complexité du cas étudié, la solution du modèle complet à été capturée avec précision par le modèle d'ordre réduit proposé.

Perspectives

Le modèle réduit proposé est non intrusif, permettant ainsi d'être construit à partir d'un solveur éléments finis industriel. Ces codes, optimisés et riches en éléments sophistiqués, conviennent parfaitement aux structures aéronautiques complexes. Cependant, en raison du secret industriel, un accès intrusif au cœur du code n'est pas possible, justifiant le caractère non intrusif du modèle réduit. L'ajout de modes duaux à la base de réduction enrichit cette dernière. La décomposition en valeurs singulières permet de contrôler la précision souhaitée en ce qui concerne le résidu des cas de charge imposés. Dans certains cas, l'absence de chute nette des valeurs singulières indique la nécessité de prendre en compte de nombreux modes duaux, justifiant l'ajout du critère d'énergie de déformation linéarisée pour distinguer les contributions les plus et moins significatives. Toutefois, il a été observé dans certains cas qu'il n'y a pas de chute nette des valeurs singulières, ce qui signifie dans certains cas que de nombreux modes duaux doivent être pris en compte. C'est pourquoi le critère supplémentaire en termes d'énergie de déformation linéarisée est pertinent car il permet de distinguer les modes duaux candidats qui contribuent le plus à la partie linéaire de l'énergie du système de ceux qui y contribuent le moins. Dans ce travail, un cas de couplage fort a été réalisé sur une configuration 2D d'une poutre flexible placée dans le sillage tourbillonnaire d'un cylindre fixe. Une perspective évidente est l'étude d'un cas de couplage fort dans le contexte d'une application industrielle. Bien que le temps de calcul pour de nombreuses applications aéroélastiques soit principalement dû à la résolution du fluide, pour des structures complexes en contexte industriel, le coût de calcul de la structure devient significatif. Il faut également mentionner que des modèles simplifiés de dynamique des fluides sont également disponibles dans la littérature, par exemple les théories de Theodorsen [185] ou de la ligne portante [152]. Dans ces cas, ce n'est pas le fluide mais la structure qui nécessite le plus de ressources informatiques. Il existe dans la littérature des modèles réduits pour les fluides, la perspective à long terme est d'utiliser des modèles d'ordre réduit à la fois pour la structure et le fluide afin d'être efficace dans les deux domaines. Dans la littérature, le désaccordage est l'un des problèmes associés aux structures tournantes et à l'aéroélasticité. Ce problème n'est pas traité dans cette thèse et mérite une attention particulière. En effet, des applications de modèles réduits non linéaires géométriques pour traiter des phénomènes de désaccordage peuvent être trouvées dans [20, 146, 153]. L'étude de tels phénomènes avec le modèle réduit proposé est une perspective envisageable. Comme axes d'amélioration du modèle réduit proposé il serait intéressant de développer une version paramétrique en fonction de la vitesse de rotation afin de pouvoir considérer plusieurs points de fonctionnement. On trouve dans la littérature des travaux au sujet d'une telle paramétrisation [105, 117, 139, 182]. L'adoption d'une approche stochastique pour évaluer l'incertitude dans la détermination des coefficients d'efforts non linéaires projetés, basée sur les travaux [20, 21, 146], serait une perspective également pertinente. Le modèle réduit présenté dans ce manuscrit ouvre la porte à de nombreuses perspectives et améliorations. Son utilisation n'est pas limitée aux applications relatives aux turbomachines, mais s'étend aux pales d'hélicoptères, aux hélices d'avions, aux éoliennes et aux véhicules VTOL, confrontés aux défis des non-linéarités géométriques. Des applications non tournantes, telles que les ailes à grand allongement des futurs avions, peuvent également être étudiées avec ce modèle d'ordre réduit.